Conjugated polymer nanoparticles for eco-efficient processing of organic photovoltaic cells

Maxime Mohammad Rammal

UNIVERSITÉ DE STRASBOURG

ÉCOLE DOCTORALE DE PHYSIQUE ET CHIMIE PHYSIQUE

Institut de Chimie et Procédés pour l'Énergie, l'Environnement et la Santé

(ICPEES – UMR 7515)

THÈSE présentée par :

Maxime Mohammad RAMMAL

Soutenue le : 10/06/2021

pour obtenir le grade de : **Docteur de l'université de Strasbourg**

Discipline/ Spécialité : Chimie et physicochimie des polymères

Conjugated polymer nanoparticles for eco-efficient processing of organic photovoltaic cells

THÈSE dirigée par :

Dr HEBRAUD Anne	Maitre de conférences, Université de Strasbourg

RAPPORTEURS :

Pr VIGNAU Laurence	Professeur des universités, Université de Bordeaux
Pr CHASSENIEUX Christophe	Professeur des universités, Le Mans Université

AUTRE MEMBRE DU JURY :

Pr HEISER Thomas	Professeur des universités, Université de Strasbourg

MEMBRE INVITÉ :

Dr LECLERC Nicolas	Directeur de recherche, Université de Strasbourg

- AKNOWLEDGMENT -

No one who achieves success does so without acknowledging the help of others.
The wise and confident acknowledge this help with gratitude.

Alfred North Whitehead

Je voudrais exprimer, tout d'abord, ma profonde reconnaissance aux membres de mon jury de thèse : Pr. Laurence VIGNAU, Pr. Christophe CHASSENIEUX et Pr. Thomas HEISER pour avoir accepté de juger ce travail de trois ans. Merci également à ma directrice de thèse, Dr Anne HEBRAUD, ainsi qu'au responsable du notre équipe « PolyFun » Dr Nicolas LECLERC, pour m'avoir encadré et guidé durant toute cette période. De même, Je remercie le directeur de l'ICPEES, Pr. Guy SCHLATTER avec toute son équipe administrative, pour m'avoir accueilli chaleureusement durant toute cette période.

Mes remerciements sont ensuite tournés vers les chercheurs et les enseignants-chercheurs avec lesquels j'ai collaboré au cours de cette thèse. Merci, donc, aux Drs Amparo RUIZ et Stéphane MERY pour avoir bien voulu juger de mon travail à l'occasion de mes deux soutenances à mi-parcours et m'avoir, à ces occasions, fait profiter de leurs expériences afin de me proposer de nouvelles idées. Un grand merci au Dr. Benoît HEINRICH pour les analyses de polymères par DSC, par ATG et par GIWAXS, je le remercie aussi pour l'adorable humeur dont il a fait preuve lorsque nous avons partagé les repas à l'occasion de la conférences SPIC en 2019 ou bien durant les analyses STXM au synchrotron soleil en 2020. J'en profite aussi pour remercier le Dr. Sufal SWARAJ pour les mesures STXM ainsi que l'aide apportée dans leurs interprétations. Sa motivation et bien évidement sa patience m'ont énormément motivé et encouragé. Je témoigne ma reconnaissance au Dr Patrick LEVEQUE qui a enrichie la patrie « optoélectronique » de la revue publiée récemment et du manuscrit ici présent. Je remercie de même le Dr. Pascal HEBRAUD qui m'a autorisé à réaliser les mesures DLS au sein de l'IPCMS, la Dr. Émilie STEVELER pour les mesures de photoluminescence résolue en temps ainsi que le Dr. Gilles ULLRICH pour la spectroscopie de fluorescence. J'adresse aussi mes remerciements aux Drs. Sadiara FALL et Olzhas IBRAIKULOV ainsi que pour Jiang JING pour le partage d'idées, d'informations et de connaissances durant le processus de la préparation de cellules photovoltaïques à l'ICUBE.

Que soient également remerciés tous les membres administratifs et techniques de l'ICPEES ou de l'ICUBE qui m'ont toujours apporté leur aide lorsque je les ai sollicité : Julien BERTRAND, Christophe MELART, Christophe SUTTER, Céline PIRAS, Dr. Géraldine LAYRAC (que je remercie tout particulièrement pour son aide lors de la préparation des suspensions de nanoparticules pendant que j'étais bien occupé par la rédaction de ce manuscrit), Stéphanie FERRY, Catherine KIENTZ, Alexandra SUTTER, Sabine SIEGWALD, Alain RACH, Dr. Thierry DINTZER, Thierry ROMERO et Nicolas ZIMMERMAN.

Mes plus sincères remerciements s'adressent à Dr Catherine JEUNESSE et Dr. Sébastien GALLETS pour l'excellent accueil qu'ils m'ont fait durant mon passage à l'IUT Robert Schuman – Illkirch en tant qu'enseignant.

Un grand merci au personnel du Resto-U Cronenbourg pour « la bonne qualité » des plats du midi et bien sûr aux personnes avec qui j'ai partagé ces repas !

Mes plus chaleurs remerciements s'adressent ensuite à mes collègues (ICPEES – ICS -IPCMS & ICBUE) avec qui j'ai partagés le travail, mon bureau, le repas du midi, les pause-café, les sorties et surtout les soirées (avant corona): Agate, Alix, Alexis, Alfred, Amina, Antoine, Audrey, Carole, Cassandra, Cédric, Chaïma, Claudia, Connie, Domitille, Fabien, Florence, Gianni, Jiang, Jing, Julien, Kim, Lili, Liza, Lotfi, Marine, Marion, Matteo, Nicolas, Pablo, Paul, Pierre, Raymond, Ricardo, Sael, Sébastien, Sophie, Theodore et Wenziz.

Rien de tout cela ne serait arrivé si je n'avais pas eu le soutien de ma famille et mes amis fidèles. Merci pour votre présence, votre soutien et votre amour incessant qui m'ont permis d'être ce que je suis aujourd'hui. Aucun mot n'est assez fort pour vous dire : Merci !

Direction de la **recherche**
et de la **valorisation**
Collège **doctoral**
Université de Strasbourg

Déclaration sur l'honneur

Declaration of Honour

J'affirme être informé que le plagiat est une faute grave susceptible de mener à des sanctions administratives et disciplinaires pouvant aller jusqu'au renvoi de l'Université de Strasbourg et passible de poursuites devant les tribunaux de la République Française.

Je suis conscient(e) que l'absence de citation claire et transparente d'une source empruntée à un tiers (texte, idée, raisonnement ou autre création) est constitutive de plagiat.

Au vu de ce qui précède, **j'atteste sur l'honneur que le travail décrit dans mon manuscrit de thèse est un travail original et que je n'ai pas eu recours au plagiat ou à toute autre forme de fraude.**

I affirm that I am aware that plagiarism is a serious misconduct that may lead to administrative and disciplinary sanctions up to dismissal from the University of Strasbourg and liable to prosecution in the courts of the French Republic.

I am aware that the absence of a clear and transparent citation of a source borrowed from a third party (text, idea, reasoning or other creation) is constitutive of plagiarism.

In view of the foregoing, ***I hereby certify that the work described in my thesis manuscript is original work and that I have not resorted to plagiarism or any other form of fraud.***

Nom : Prénom : RAMMAL Maxime Mohammad

Ecole doctorale : ED 182

Laboratoire : ICPEES - ECPM

Date : 10/06/2021

Signature :

The greatest enemy of knowledge is not ignorance, it is the illusion of knowledge

-Steven HAWKING-

to my father , the man I owe everything,

to my mother for whom I have not been very available the last few years

I dedicate this work ...

- ABBREVIATIONS -

AFM	Atomic Force Microscopy
Ag	Silver
Al	Aluminum
BHJ	Bulk heterojunction
C	Speed of light
Ca	Calcium
CB	Chloro-benzene
$CDCl_3$	Deuterated Chloroform
CE	Charge Extraction
$CHCl_3$	Chloroform
CMC	Critical Micelle Concentration
CV	Cyclic voltammetry
D	Electron Donor
DLS	Dynamic light scattering
DMSO	Dimethyl sulfoxide
DOBS	disodium 4-dodecyl-2,4'-oxydibenzenesulfonate
DSC	Differential Scanning Calorimetry
eh-IDTBR	5,5'-[[4,4,9,9-tetrakis(2-ethylhexyl)-4,9-dihydro-s-indaceno[1,2-b:5,6-b']dithiophene-2,7-diyl]bis(2,1,3-benzothiadiazole-7,4-diylmethylidyne)]bis[3-ethyl-2-thioxo-4-thiazolidinone]
EPBT	Energy Payback Time
ETL	electron transporting layer
eV	Electron Volt
FF	Fell Factor
GIWAXS	Grazing-Incidence Wide-Angle X-ray Scattering
HOMO	Highest Occupied Molecular Orbital
HTL	hole transporting layer
ICBA	1',1'',4',4''-Tetrahydro-di[1,4]methanonaphthaleno[1,2:2',3',56,60:2'',3''][5,6]fullerene-C60

ITIC	3,9-bis(2-methylene-(3-(1,1-dicyanomethylene)-indanone))-5,5,11,11-tetrakis(4-hexylphenyl)-dithieno[2,3-d:2',3'-d']-s-indaceno[1,2-b:5,6-b']dithiophene
ITO	Indium tin oxide
Jsc	Current density
LBG	Low bandgap
LUMO	Lowest Unoccupied Molecular Orbital
MoO_3	Molybdenum oxide
Mw	Molecular weight
NBS	N-Bromosuccimide
n-Buli	n-Butyllithium
NEXAFS	near-edge X-ray absorption fine structure
nm	Nanometer
NPs	Nanoparticles
o-DCB	ortho-dichlorobenzen
OFET	Organic field-effect transistor
OFET	Organic field-effect transistor
o-IDTBR	(5Z,5'Z)-5,5'-((7,7'-(4,4,9,9-tetraoctyl-4,9-dihydro-s-indaceno[1,2-b:5,6-b']dithiophene-2,7-diyl)bis(benzo[c][1,2,5]thiadiazole-7,4-diyl))bis(methanylylidene))bis(3-ethyl-2-thioxothiazolidin-4-one)
OPV	Organic Photovoltaic
OSC	Organic Semi-Conductor
P-(o-Tolyl)$_3$	Tri(o-tolyl)phosphine
P3HT	Poly(3-hexylthiophene-2,5-diyl)
PC61BM	3'H-cyclopropa[1,9][5,6]fullerene-C60-Ih-3'-butanoic acid 3'-phenyl methyl ester
PC71BM	[6,6]-Phenyl-C71-butyric acid methyl ester
PCDTBT	poly[N-9'-heptadecanyl-2,7-carbazole-alt-5,5-(4,7-di-2-thienyl-2',1',3'-benzothiadiazole]
PCE	Power Conversion Efficency
$Pd(PPh_3)_4$	Palladium-tetrakis(triphenylphosphine)
Pd_2dba_3	Tris(dibenzylideneacetone)dipalladium(0)
PEDOT-PSS	Poly(3,4-éthylènedioxythiophène) -Poly(styrène sulfonate) de sodium
PEG	polyethylene glycol
PF127	Pluorinic F127

PF2	Difluorinated - polymer
PL	Photoluminescence
PSBTBT	Poly[(4,4-bis(2-ethylhexyl)-dithieno[3,2-b:2’,3’-d]silole)-2,6-diyl-alt-(2,1,3-benzothiadiazole)-4,7-diyl]
PTB7-th	Poly[4,8-bis(5-(2-ethylhexyl)thiophen-2-yl)benzo[1,2-b;4,5-b']dithiophene-2,6-diyl-alt-(4-(2-ethylhexyl)-3-fluorothieno[3,4-b]thiophene-)-2-carboxylate-2-6-diyl)]
RCP	Random close-packed
SANS	Small-angle neutron scattering
SCLC	Space Charge Limited Current
SDBS	Dodecylbenzenesulfonate
SDS	Sodium dodecyl sulfate
SEC	Size-exclusion chromatography
SEM	Scanning Electron Microscopy
Si	Silicium
SiO_2	Silica
STXM	Scanning Transmission X-ray Microscopy
Tb	Boiling Temperature
TEBS	2-(3-thienyl)ethyloxybutylsulfonate sodium salt
TEM	Transmission Electron Microscopy
TEM	Transmission Electron Microscopy
Tg	Glass transition temperature
TGA	Thermogravimetric analysis
THF	TertraHydroFuran
TOF-SIMS	Time of Flight - Secondary Ion Mass
TPV	Transient photovoltage
TQ1	poly[2,3-bis-(3-octyloxyphenyl)quinoxaline-5,8-diyl-alt-thiophene-2,5-diyl]
UV-O_3	Ultraviolet-Ozone
V	Voltage
Voc	Open-circuit voltage
ZnO	Zinc oxide
λ	Lambda (wavelength)
θ	Teta (angle °)
Đ	polymer Dispersity

μ_{h+}	holes mobility
μ_{e-}	electron mobility
µm	micrometer
π	3.14

- SUMMARY -

GENERAL INTRODUCTION

En raison du développement industriel et de la croissance démographique, la demande mondiale d'énergie a augmenté de manière exponentielle ces dernières décennies. En plus d'être à l'origine d'une crise environnementale sans précédent, les énergies fossiles et carbonées atteignent aujourd'hui la limite des ressources énergétiques disponibles. Il est donc urgent de réfléchir à une alternative à l'énergie fossile afin de résoudre ce problème particulier.

L'énergie solaire est une énergie infinie et très abondante. Ainsi, la quantité captée par la Terre pendant 1 heure pourrait suffire à la consommation énergétique mondiale annuelle. Elle est de fait une énergie particulièrement attractive. Il existe deux façons d'utiliser cette énergie : sous forme d'énergie thermique directement ou sous l'effet photovoltaïque permettant la production d'électricité.

Le marché du photovoltaïque est dominé par le silicium cristallin en raison de sa grande efficacité et de sa durabilité. Les cellules solaires commerciales affichent aujourd'hui une durée de vie supérieure à 25 ans avec un rendement d'environ 20 %[(1)]. En revanche, la production des cellules solaires inorganique à base de silicium est à la fois exigeante en termes de coût et d'énergie. Pour économiser les coûts et les matériaux, les chercheurs ont développé des concepts dits émergents, incluant entre autres des cellules basées sur l'utilisation de couches minces de matériaux semi-conducteurs organiques comme couche active. Cette approche est censée diminuer les coûts de fabrication et répondre à des critères nouveaux tels que la flexibilité, l'esthétisme ou encore la semi-transparence.

Les cellules solaires organiques sont constituées de matériaux semi-conducteurs organiques qui peuvent être des polymères conjugués (P3HT[(2)], PTB7-Th[(3)],…) ou des petites molécules conjuguées (famille des fullerène [(4)], IDTBR[(5)], ITIC[(6)], …)

La recherche scientifique dans ce domaine n'a cessé de progresser au cours des dernières décennies et des efficacités de l'ordre de 18% sont aujourd'hui annoncées[(7)]. En revanche, la mise en œuvre de ces matériaux requiert principalement l'utilisation de solvants toxiques, souvent chlorés, tel que le chloroforme ou l'*ortho*-dichlorobenzène. Un défi afin de permettre l'industrialisation de cette technologie, consiste à éviter la manipulation directe sur les chaînes de production des solvants toxiques.

Afin d'éviter l'utilisation de ces solvant toxiques, une solution consiste à modifier chimiquement ces polymères conjugués en ajustant les chaines alkyles pour améliorer leur solubilité dans des solvants verts et inoffensifs, idéalement l'eau ou les alcools. L'inconvénient de cette solution repose sur la modification des propriétés optoélectroniques de ces polymères associés aux propriétés électroniques (effet inductif donneur par exemple) ou structurales (encombrement stérique, auto-assemblage …) des nouvelles chaînes solubilisantes. Afin d'éviter ceci, une deuxième approche vise

à disperser les matériaux semi-conducteurs organiques sous la forme de nanoparticules solides dans l'eau ou les alcools. Pour élaborer ces particules, deux méthodes peuvent être utilisées, la miniémulsion et la nanoprécipitation.

Dans les deux cas, les solvants organiques initialement utilisés pour solubiliser les matériaux semi-conducteurs organiques sont éliminés de la dispersion par évaporation. Les vapeurs peuvent alors être piégées et recyclées. Les suspensions de nanoparticules peuvent ensuite être utilisées comme des encres à base aqueuse pour déposer les couches actives sur les substrats par des techniques d'impression classiques.

Ce projet de thèse s'inscrit dans cette thématique. Cette thèse est financée dans le cadre d'un projet ANR « Jeune chercheur » obtenue par ma directrice de thèse le Dr. Anne Hébraud. Ce projet ambitieux vise à élaborer et étudier des dispersions de NPs de semi-conducteurs organiques en vue de les utiliser comme matériaux actifs de cellules solaires organiques. Outre les compétences d'A. Hébraud dans les colloïdes, ce projet s'appuie également sur les compétences du Dr. N. Leclerc, de l'ICPEES, en synthèse de matériaux semi-conducteurs organiques et des collègues physiciens, P. Lévêque et T. Heiser, de l'ICube pour l'élaboration des dispositifs optoélectroniques.

Le premier chapitre bibliographique se présente sous la forme d'une revue qui a été publiée en 2020 dans le journal *Material Chemistry Frontiers* de la RSC. Cette revue résume les différentes méthodes d'élaboration des nanoparticules ainsi que leurs caractérisations et leur utilisation dans l'élaboration des cellules solaires organiques.

Le deuxième chapitre présente les matériaux utilisés ainsi que les modes opératoires associés aux différentes mesures réalisées.

L'élaboration de nanoparticules par la technique de miniemulsion est abordée dans le troisième chapitre. Différents types de nanoparticules, contenant un seul matériau (donneur ou accepteur d'électron) ou les deux à la fois, ont été préparées. La caractérisation de ces dernières par différentes mesures optiques fait l'objet de la fin de ce chapitre.

Le quatrième chapitre décrit l'utilisation des nanoparticules précédemment élaborées par miniémulsion au sein de couches actives de cellules photovoltaïques.

L'approche nanoprécipitation permettant également l'élaboration de nanoparticules fait l'objet du chapitre V. La première partie de ce chapitre décrit la conception et la synthèse de nouveaux copolymères semi-conducteurs *ad hoc*, plus solubles et permettant de stabiliser la dispersion de nanoparticules dans l'eau.

Nous avons choisi de présenter tous les chapitres en anglais en vue de leur soumission sous forme de publications. En revanche, un résumé récapitulatif en Français apparait à la fin de ce manuscrit.

Références :

1. Green, M. A. Silicon photovoltaic modules: a brief history of the first 50 years. Prog. Photovolt. Res. Appl. 13, 447–455 (2005).
2. Vanlaeke, P. et al. P3HT/PCBM bulk heterojunction solar cells: Relation between morphology and electro-optical characteristics. Sol. Energy Mater. Sol. Cells 90, 2150–2158 (2006).
3. Liao, S.-H., Jhuo, H.-J., Cheng, Y.-S. & Chen, S.-A. Fullerene Derivative-Doped Zinc Oxide Nanofilm as the Cathode of Inverted Polymer Solar Cells with Low-Bandgap Polymer (PTB7-Th) for High Performance. Adv. Mater. 25, 4766–4771 (2013).
4. Zimmermann, B., Würfel, U. & Niggemann, M. Longterm stability of efficient inverted P3HT:PCBM solar cells. Sol. Energy Mater. Sol. Cells 93, 491–496 (2009).
5. Holliday, S. et al. High-efficiency and air-stable P3HT-based polymer solar cells with a new non-fullerene acceptor. Nat. Commun. 7, (2016).
6. Doumon, N. Y. et al. Energy level modulation of ITIC derivatives: Effects on the photodegradation of conventional and inverted organic solar cells. Org. Electron. 69, 255–262 (2019).
7. Liu, Q. et al. 18% Efficiency organic solar cells. Sci. Bull. 65, 272–275 (2020).

CHAPTER I BIBLIOGRAPHY

This chapter has been published as a review article with following reference: "Recent advances in the green elaboration of organic photovoltaic devices from nanoparticle dispersions" M. Rammal, P. Lévêque, G. Schlatter, N. Leclerc, A. Hébraud. Mater. Chem. Front. 4, 2904 (2020).

I. Introduction:

The development of renewable energies reducing CO_2 emissions and natural resources consumption is a key challenge to limit the global warming. In this context, major efforts are being made to increase the performance of photovoltaic panels and improve their life cycle in term of energy payback time (EPBT) and environmental loads[(1)]. Among the different photovoltaic technologies, organic photovoltaics (OPV) looks appealing.

OPV performances, now reaching 18% at laboratory scale[(2)], are still below those of mono- and poly-crystalline based silicon photovoltaics. OPV has nevertheless several advantages as OPV modules are light weight and flexible, their shape and color can easily be tuned, and they can be produced at low cost by solution processes requiring lower energy.

An OPV solar cell is multilayer device composed of an organic semiconducting materials-based active layer sandwiched between two electrodes. One transparent electrode is usually made up of Indium tin oxide (ITO). The second electrode is commonly based on metals such as calcium (Ca), aluminum (Al) or silver (Ag). Most often, an OPV device also contains interfacial layers tuning the electrode work function and improving the charge carriers collection(**Figure 1 a & b**).

To understand the following bibliographic developments, a short note on the working principle of organic solar cells is necessary at this point. In contrast to inorganic semiconductors, organic semiconductors have a dielectric constant that is too low to dissociate the exciton (a neutral particle consisting of a hole and an electron bound by coulomb forces) into free charges at room temperature. An active layer of an OPV device is therefore made up of two materials with electron-donor and electron-acceptor nature respectively, mixed on a nanometric scale within a thin film. In fact, the morphology of this D/A blend is a key parameter that impacts the performance of the device. The process of converting solar light into electricity in OPV cells is generally described as a succession of 4 major steps: i) Photoexcitation of semiconductors by absorption of an incident photon. This creates coulombically bound electron–hole pair, called exciton ; ii) Diffusion of this exciton (diffusion length is typically on the order of 10-20 nm) to a near D/A interface ; iii) Exciton dissociation at the D/A interface into a free hole and a free electron ; iv) which can then migrate towards the anode and the cathode, respectively. These collected charges at the electrodes will generate electrical power. The performance of a solar cell is generally determined by its power conversion efficiency (PCE), defined as the ratio of the maximum power delivered by the cell (I_{pmax} V_{pmax}) to the incident light power (P_{in}). The PCE is generally extracted from the characteristic curves of current density (J) versus voltage (V) measured under illumination (**Figure 1 c**).

It is constituted of three main parameters, the open circuit voltage (V_{OC}), the short-circuit current (J_{SC}) and the fill factor (*FF*) following the **equation 1** below.

$$PCE = \frac{FF\ V_{oc}\ J_{sc}}{P_{in}} \qquad \textbf{(equation 1)}$$

The V_{OC} is the maximum voltage that a current-free device can produce . It is strongly related to the organic semiconducting materials energy levels. The J_{SC} is the maximum current that passes through the device under illumination when the voltage is zero. It is strongly related to the mobility and lifetime of the charge carriers. The *FF* allows to evaluate the quality of the cell by comparing the largest possible collection of charges for a perfect cell with the quantity of charges actually collected. This factor reflects the competition between the charge transport and their recombination.

$$FF = \frac{I_{pmax}\ V_{pmax}}{J_{sc}\ V_{oc}} \qquad \textbf{(equation 2)}$$

In recent years, the increase of Power Conversion Efficiencies (PCE) of OPV devices has been mainly achieved thanks to the evolution of photoactive material design on the one hand and the improvement of the different device interfacial layers on the other hand.

Regarding the photoactive materials, in order to meet the industrial criteria, two key concerns remain to be addressed: i) their synthesis cost, closely related to the number of steps and reagents used, and ii) their processing in thin films. If the first point starts to be well documented with in particular the recent introduction of the following new indexes: the synthetic complexity (SC) and the figure of merit (FOM)[3,4], the second point still needs to be addressed as high PCE organic semiconductors (OSC) are less and less soluble and require not only the use of toxic organic solvents but also moderate temperature (above 80°C) processing where the amount of generated vapors is critical[5,6]. Therefore, the development of alternative eco-friendly processing allowing the use of green solvents, appears as a key step towards industrialization of OPV technology. Three main solutions are currently being developed consisting in i) the research of alternative and less toxic solvents [7], ii) the design of water-soluble materials [8] and iii) the dispersion of OSCs nanoparticles (NP) in water or alcohols, resulting in an eco-friendly active layer ink.

Two recent reviews have been published discussing these three different strategies [9,10], but none of them described thoroughly all the aspects of the NP dispersion route. Our review focuses on the NP dispersion strategy and aims at describing its different steps, from the elaboration of the NPs to their assembly in the active layer, the OPV device characterization and its optimization. It also highlights the essential parameters that can be tuned at each step to improve the performance of the final device.

Regarding the device sub-layers optimization, The NP approach also allows to specifically address the control of the active-layer thin film morphology in an innovative way. Indeed, the photoactive layer of efficient solution-processed OPV devices is made of phase-separated domains of electron-acceptor (A) and electron-donor (D) materials known as bulk heterojunction. Two different levels of organization should be considered. First, the structuration of the materials in each domain at the molecular scale (crystallinity, self-assembling properties...) is a major parameter to obtain high charge-carriers mobilities. Then, at the mesoscale, the morphology of the phase separation is critical as it simultaneously enable both exciton dissociation and free-charges collection. The ideal structure is an interpenetrating network of the two phases with typical length scale of the order of the exciton diffusion length, i.e., 10-20 nm. The two levels of organisation of the active-layer are depending on the materials physico-chemical properties (solubility, planarity, self-assembling properties …) and on the film preparation process. The elaboration of separate electron-donor NPs and electron-acceptor NPs or composite NPs containing both materials is an attractive way to address these issues, because it provides the possibility to control the morphology of the molecules and their phase separation at the scale of the nanoparticles. These NPs are then assembled to form the active layer. Accordingly, the NP approach offers an additional control degree on the active-layer morphology.

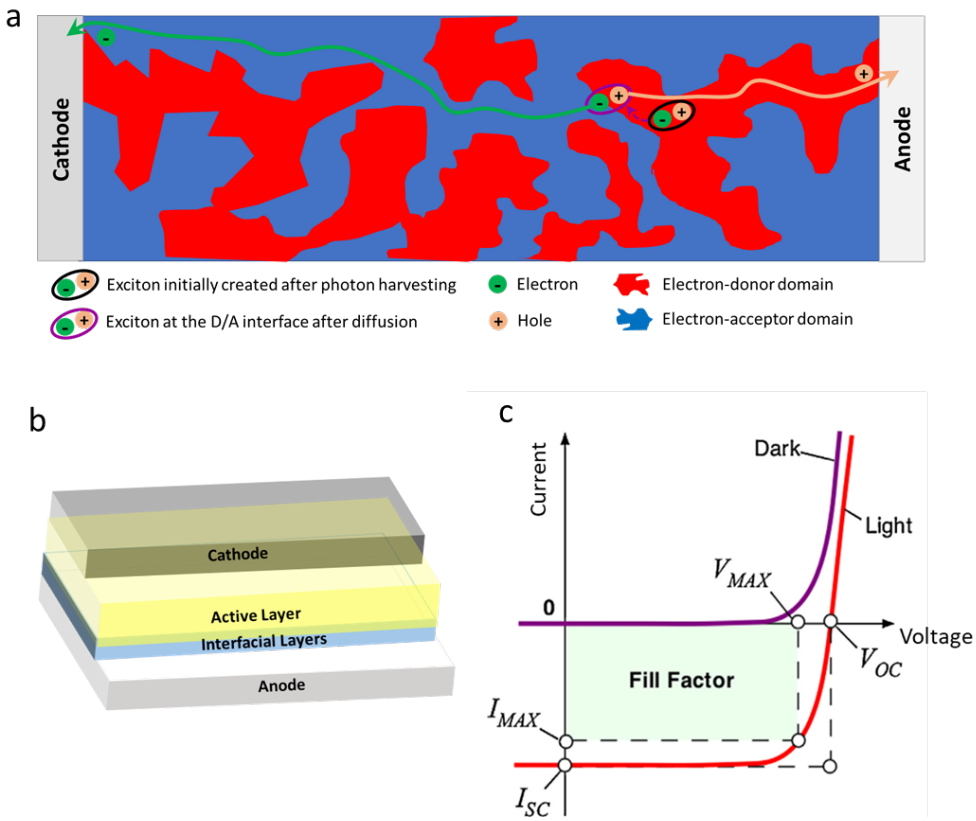

Figure 1: a)Typical BHJ scheme for a donor:acceptor blend in organic solar cell, b) OPV cell architecture and c) J-V curve of a solar cell under illumination / dark

In this review, we aim at providing an up-to-date overview of this field by focusing on the different steps that make up the development of an OPV device, from the preparation of nanoparticles to the characterization of the device (**Figure 2**). Thus, in a first part of the review, we focus on the elaboration of separate and composite OSC NP by the two main post-polymerization processes: miniemulsion and nanoprecipitation. We then discuss the impact of the materials and different processing parameters on the diameter and internal morphology of these NPs. In the second part, we present the different NP deposition processes and their optimization from the spin-coating at lab scale, to roll-to-roll processing allowing the preparation of large-scale devices. The morphology of the active layer obtained from the assembly of the NPs is then described in details and the influence of thermal annealing on the purity and size of the segregated donor and acceptor domains are discussed. Finally, the last part of the review focuses on the performances of OPV devices obtained by this strategy. The charge-carrier generation and recombination dynamics that may limit NP OPV devices as well as the optimization processes are extensively discussed.

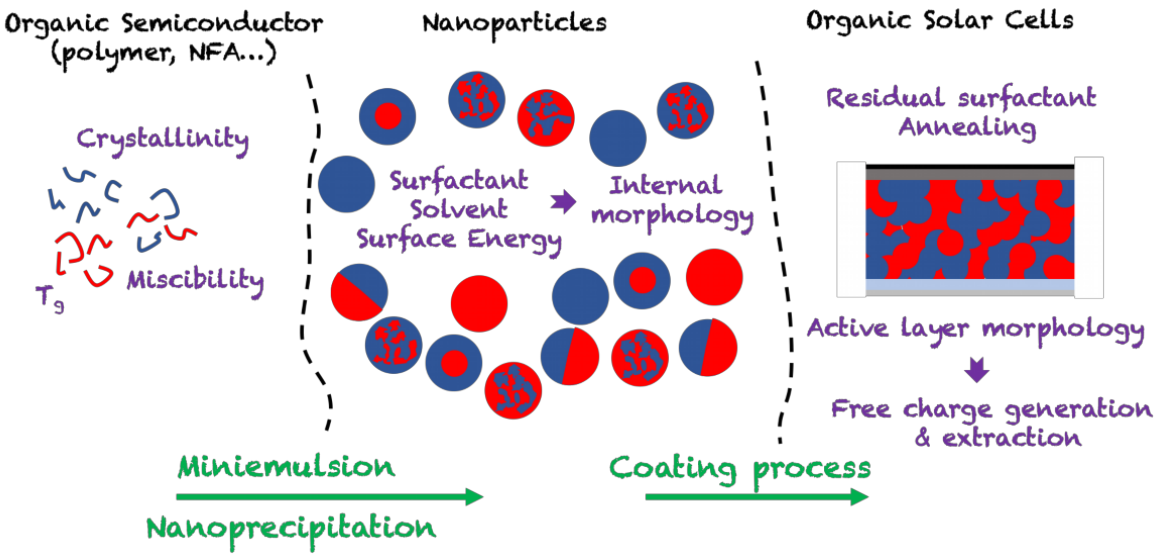

Figure 2: Scheme of the NP dispersion route to OPV cell

II. Elaboration of nanoparticle dispersions in green solvents:

Different ways have been used to synthesize semiconducting polymer NPs by polymerization in heterophase systems or post-polymerization methods [11,12]. We focus here on the post-polymerization preparation methods because they are very versatile, allowing the preparation of NPs from most recent organic semiconducting materials. Readers interested in the heterophase polymerization strategy can refer the review of Pecher *et al* [11].

Two main post-polymerization processes can be used to prepare semiconducting NPs with diameters in the range of a 20 to 200 nm: miniemulsion and nanoprecipitation.

II.1 Miniemulsion:

Preparation of aqueous dispersions of semiconducting polymer NPs by the miniemulsion process was first demonstrated by Landfester *et al*[13]. In this process, two non-miscible phases are prepared: an organic phase composed of the polymer in a good solvent and an aqueous phase containing a surfactant (**Figure 3**). The organic phase is then dispersed in the aqueous phase by ultrasonication giving a metastable miniemulsion *i.e.* a dispersion of very small organic droplets into an aqueous phase. After evaporation of the organic solvent, a polymer dispersion is obtained. The diameter of the obtained NPs, typically between 50 and 250 nm, depends on the surfactant concentration, an increase of the surfactant concentration resulting in a decrease of the NP size [13]. Moreover, as the NPs are obtained after evaporation of the solvent from the miniemulsion droplets, the NP size also increases with the initial polymer concentration in the organic phase[14]. If low boiling temperature (T_b) solvents such as chloroform (T_b = 61°C) are usually preferred for the miniemulsion technique, it was also possible to prepare NPs from high boiling point solvents such as *ortho*-dichlorobenzene (*o*-DCB, T_b = 178°C)[15] or *o*-xylene (T_b = 144°C)[16], thus expanding the range of semi-conducting polymer that can be processed by this technique. In this case, evaporation of the solvent is completed after several hours at 60 or 75°C and water had to be regularly added into the flask in order to compensate for water loss through evaporation. Using this process, composite NPs containing two different materials in the same particle can also be prepared, by mixing the two materials in the initial organic phase, prior to emulsification [17,18].

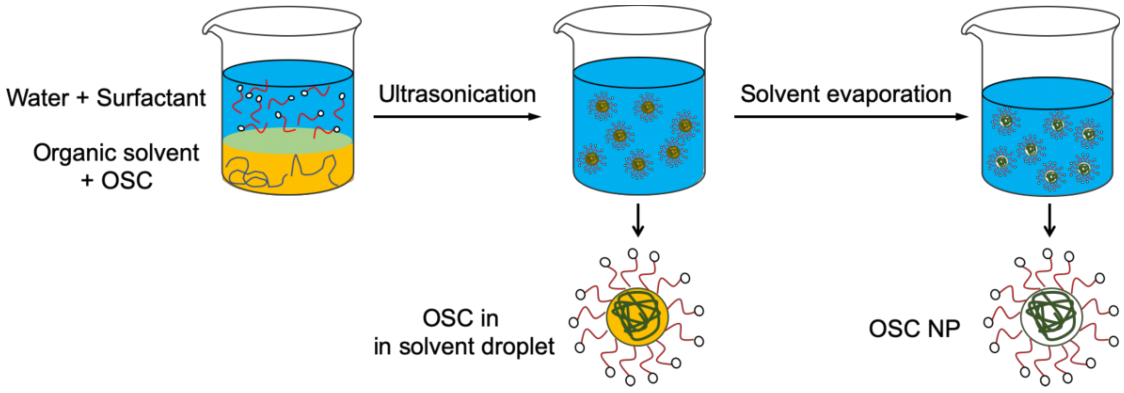

Figure 3: Elaboration of NP by the miniemulsion process.

Materials segregation in the NPs

During the solvent evaporation step in the miniemulsion process, a phase separation then occurs inside the NPs leading to core-shell[19], Janus [20], or more complex structures [21]. The morphology of the NPs can be inferred from Small Angle Neutron Scattering (SANS) [14,21] or Scanning Transmission X-ray Microscopy (STXM) for large particles (**Figure 4**) [22]. This latter, based on the measurement of the near-edge X-ray absorption fine structure (NEXAFS) characteristic of the molecular structures of the materials, also allows to quantitatively determine the chemical composition of the two segregated phases. Its resolution is of 30 nm approximatively.

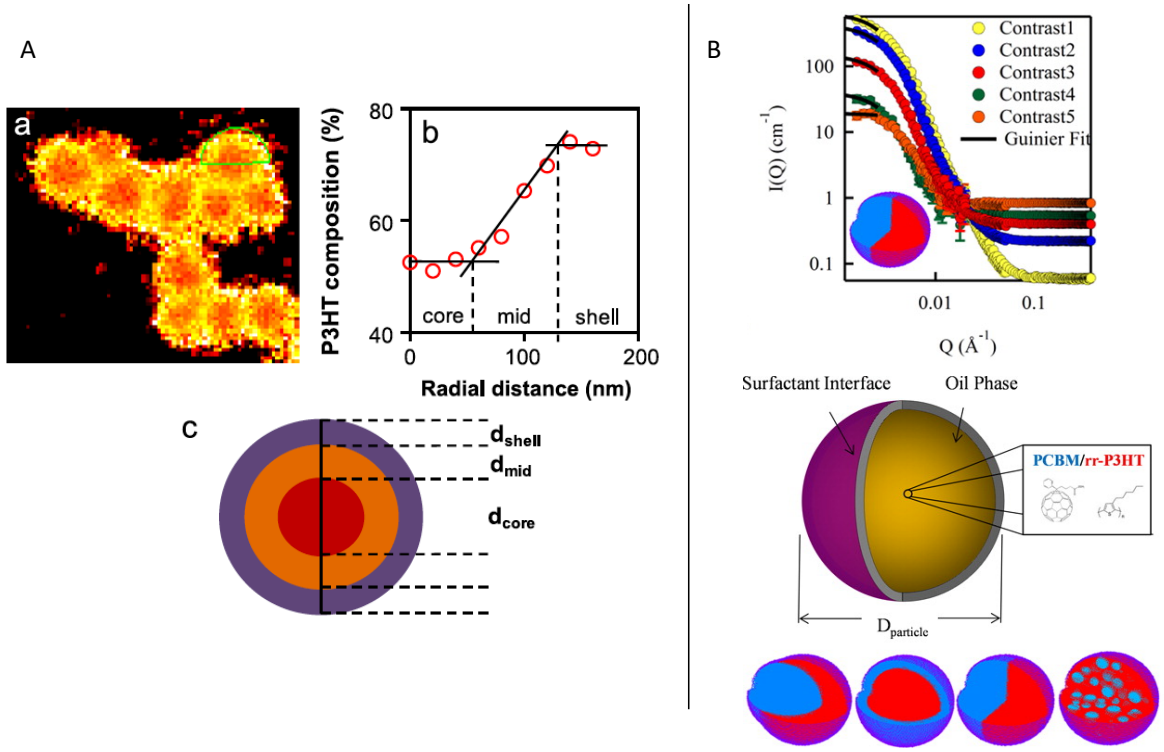

Figure 4: A) STXM observation of a P3HT:PCBM NP a) P3HT composition map, b) P3HT radial composition calculated from green area in STXM image, c) scheme of the core-shell NP. Adapted with permission from ref [19] (Copyright 2013 Elsevier B.V.), B) Scattering profile obtained by contrast variation SANS for a Janus P3HT:PCBM NP, and scheme of the different possible NP internal morphologies. Adapted with permission from ref [21] (Copyright 2014 American Chemical Society)

The internal structure of the NPs depends on the surface energy of the materials, but can also vary with the evaporation kinetics or other processing parameters. In general, the materials with higher surface energy are be found in the core of the NPs. Thus, when PCBM is used in combination with an electron donor polymer, the NPs obtained by miniemulsion have usually a core-shell morphology with the fullerene derivative in the core and the conjugated polymer in the shell. It is the case of PCDTBT: $PC_{71}BM$ NPs, $PC_{71}BM$ having a higher surface energy (48 mJ.m^{-2}) than PCDTBT (37 mJ.m^{-2})

[14] or of P3HT:$PC_{61}BM$ [19] with surface energies of 38.2 $mJ.m^{-2}$ [23] and 26.9 $mJ.m^{-2}$ [24] for $PC_{61}BM$ and P3HT, respectively (see structures in **Figure 5**). Moreover, the size and composition of the two segregated phases, usually not pure, depend on different parameters. The molar mass of the polymer has a limited impact on the composition of the two phases after elaboration. However, it changes the fullerene derivative diffusion during annealing as discussed later in **section III.2**. Indeed, for a P3HT:$PC_{61}BM$ NPs [19], variation of the molar mass of P3HT between 9 and 72 $kg.mol^{-1}$ did not change significantly the composition of the core and shell, as obtained just after the miniemulsion process. The P3HT-rich shell contained 72 ± 5% of P3HT and the $PC_{61}BM$-rich core contained 73 ± 12% $PC_{61}BM$. Only for the lowest studied P3HT molar mass of 5 $kg.mol^{-1}$, was the particle fully blended with a composition of 54 ± 6% of P3HT and 46 ± 6% of $PC_{61}BM$. The impact of the ratio of the two materials, on the morphology of the NPS was demonstrated by Holmes *et al.*[25] Indeed, an increase of the $PC_{61}BM$ content in the P3HT:$PC_{61}BM$ NPs from 1:0.5 to 1:2, slightly increased the radius of the PCBM-rich core, while maintaining its composition at around 70 % of $PC_{61}BM$. However, a favorable increase of the amount of $PC_{61}BM$ in the P3HT-rich shell from 18 to 33 % before annealing was obtained, reaching 46 % after annealing which is higher than the percolation thresholds in bulk films[26]. Moreover, the phase separation and composition of the core and shell depends also logically on the nature of the materials and their miscibility. By STXM, Dam *et al*.[27] have compared the structure and composition of P3HT:$PC_{71}BM$ and PSBTBT:$PC_{71}BM$ NPs prepared by miniemulsion, with the same 1:1 blend ratio and a similar NP radius. PSBTBT is a highly crystalline low band gap polymer (**Figure 5**). They showed that while the radius of the core and the composition of the polymer-rich shell were similar, the purity of the $PC_{71}BM$-rich core was very different with 80% $PC_{71}BM$ in the core of P3HT-$PC_{71}BM$ NPs and only 60% $PC_{71}BM$ in the core of PSBTBT:$PC_{71}BM$ NPs. Finally, in the case of 1:1 P3HT:ICBA NPs, ICBA being a C60-bis-adduct derivative (**Figure 5**) highly miscible in P3HT, a core-shell structure was still obtained, due to the difference of surface energy of the two materials, but with a large core containing 41 % ICBA and a thin shell region containing only 23% ICBA. However, after annealing and due to this higher miscibility, the core-shell structure was quickly lost, and NPs became homogeneously blended [28].

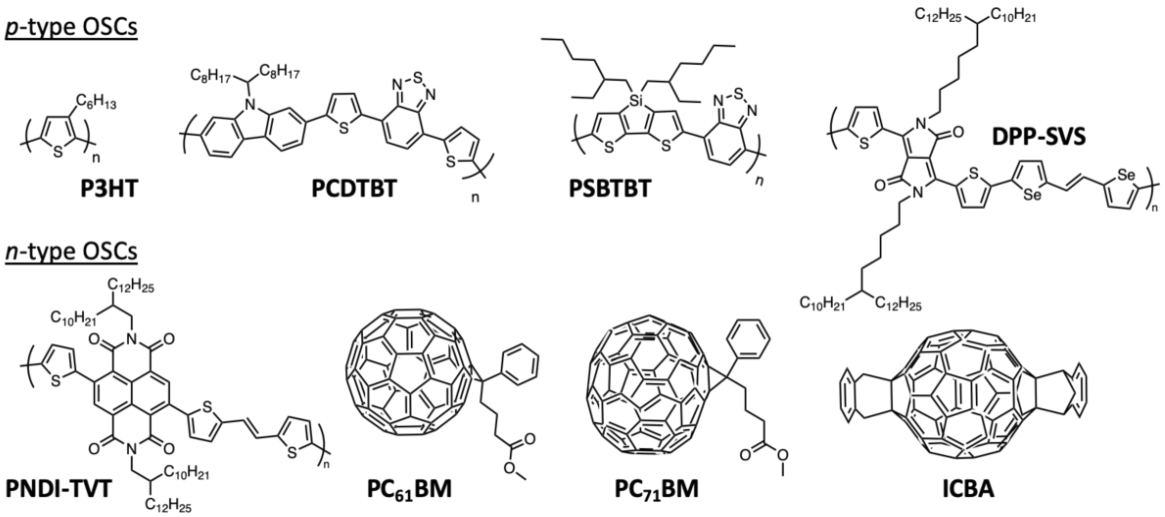

Figure 5: Chemical structures of P3HT, PCDTBT, PSBTBT, DPP-SVS, PNDI-TVT, $PC_{61}BM$, $PC_{71}BM$ and ICBA.

Influence of the solvent

Varying the quality and evaporation rate of the solvent used to prepare the NPs by miniemulsion also has an impact on the morphology of the NPs, both for the aggregation of polymer chains and for phase separation processes. As an example, Nagarjuna *et al.* [29] have prepared P3HT NPs by emulsification of P3HT solutions in chloroform, a good solvent for P3HT with a boiling point of 61°C, or toluene, a marginal solvent for P3HT with a boiling temperature of 110°C, or a mixture of both. Evaporation of the solvent was conducted at 80°C. They showed that the solvent did not change the amount of obtained aggregated phase (versus amorphous phase), but it affected its crystalline order *i.e.* the dispersity of crystals (size, shape, order …). Indeed, during the organic solvent evaporation process at 80°C, chloroform evaporated very fast and with no solvent annealing period leading to a higher degree of dispersity in the polymer aggregates. In the case of toluene, because of a higher boiling temperature and consequently a slower evaporation rate, the aggregates probably started to form before complete evaporation of the solvent and may subsequently be annealed in the presence of residual solvent, leading to tighter packing of the polymer chains. Finally, the NPs obtained from mixed solvents exhibited crystalline regions with higher degree of uniformity and structural order, thanks to the combination of slow evaporation and the presence of good solvent. Marks *et al.*[30] have prepared P3HT-$PC_{61}BM$ by miniemulsion, starting from chloroform solutions. They showed that a rapid evaporation under vacuum led to core-shell NPs with more mixed phases, the purity of the PCBM-rich core decreasing from 79% for a slow evaporation to 60% $PC_{61}BM$, and the purity of P3HT-rich shell decreasing from 70 % to 64%.

Moreover, the crystallinity of the P3HT was also slightly lower when the chloroform evaporation was rapid, due to a reduced time for the materials to self-organize in the NPs.

Choice of the surfactant

One of the drawbacks of the miniemulsion technique is the use of a surfactant. Most of the times, an anionic surfactant, sodium dodecyl sulfate (SDS, see structure in **Figure 6**) is used in order to decrease the interfacial tension between the organic phase and the water favoring emulsification, and to stabilize the NP dispersion over long period of times. However, in the active layer, this surfactant interferes with the charge transport (**see discussion in section IV.3**). Therefore it has to be removed before processing the film, by repeating numerous centrifugation dialyses or crossflow ultrafiltration steps [31]. Cho *et al.* [32] have tried to find general rules to choose the best surfactant for miniemulsion preparation. They studied 18 different surfactants, either anionic (with sulfate moieties), cationic (with ammonium groups) or non-ionic (with ethoxylated chains) (**Figure 6**). They prepared NPs of a naphthalene tetracarboxydiimide-base *n*-type polymer semiconductor (PNDI-TVT, **Figure 5**) and compared the NP sizes, the stability of the dispersions, the crystallinity of the polymer in the NPs and the efficiency of surfactant removal by washing the prepared film in ethanol. They found that surfactants with large aromatic tail did not interact efficiently with the polymer, compared to surfactants with linear alkyl chains that lead to strong van der Waals interactions with the pendant linear alkyl chains of the polymer. Moreover, nonionic surfactants were also less efficient to stabilize the NPs, resulting in larger particle sizes, even if in a previous paper, they had successfully prepared diketopyrrolopyrrole-based polymer (DPP-SVS, **Figure 5**) NPs of 200 nm diameter with a $C_{12}E_4$ (C_nE_m alkyl-ethoxyethyl, **Figure 6**) surfactant, producing films with high charge carrier mobility [33]. C_{12}-alkyl trimethyl ammonium bromide (C_{12}TAB, **Figure 6**) was found to be the surfactant that allowed the preparation of the smallest particles with a minimum excess of surfactant which was almost completely removed from the final film by ethanol washing. Finally, they also showed that an increasing alkyl tail length led to better packing of the polymer chains in the particles and thus a higher charge mobility in the final film. Tan *et al.* [34] also showed that the conjugation of an anionic surfactant similar to SDS, had an impact on the packing of P3HT in NP. An increase of the conjugation of the surfactant from SDS to dodecylbenzenesulfonate (SDBS, **Figure 6**) and disodium 4-dodecyl-2,4'-oxydibenzenesulfonate (DOBS, **Figure 6**) led to an increased chain order and conjugation-length of P3HT and a red-shifted absorbance spectrum. Fleischli *et al.* [35] have explored the use of two diblock copolymers made of poly(n-butylacrylate) or poly(2-(dimethylamino)ethylmethacrylate)) and poly(methyl(ethoxyethyl)$_n$ methacrylate) for the preparation of P3HT NPs. They have shown that by varying different parameters (*i.e*. the

macrosurfactant and the processing conditions, the organic solvent, the dissolution of the surfactant in the organic or aqueous phase, …), they were able to tune the optical properties of the NPs and the molecular arrangement of the P3HT chains in the NP from *H*- to *J*-like behavior.

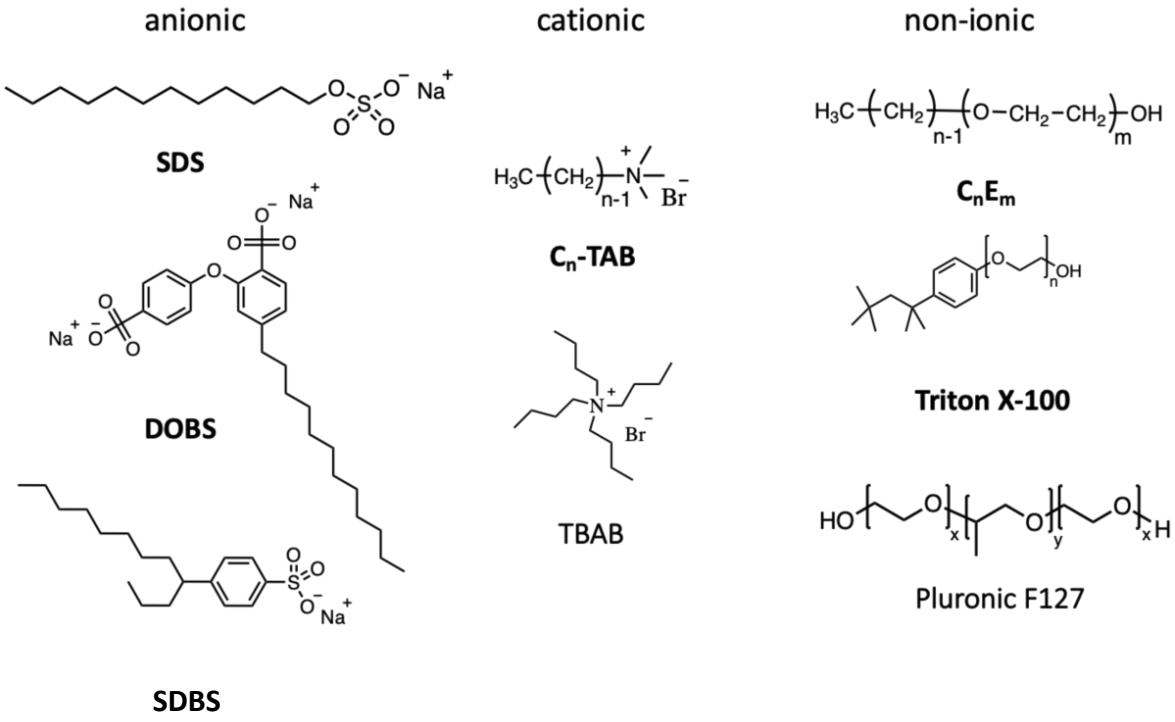

Figure 6: Chemical structures of surfactants used in the miniemulsion process.

Another strategy to prepare NPs, was to modify part of the donor or electron acceptor materials to make them amphiphilic and use them as a surfactant. Kim *et al.*[36] have grafted polyethylene glycol chains on fullerene to obtain a PEG-C_{60} surfactant (**Figure 7 A**). They have shown that this surfactant forms micelles of 2.6 nm radius in water under vigorous agitation, micelles which aggregate further to form 15 nm size clusters. By mixing this aqueous PEG-C_{60} solution with an organic phase of P3HT in chlorobenzene, and after homogenization and evaporation of the solvent, they obtained NPs with diameters of 30 to 72 nm, decreasing with increasing PEG-C_{60} concentration. The NPs were composed of a P3HT core surrounded by the PEG-C_{60} shell. Finally, OPV devices were prepared with these particles resulting in a PCE of 2.62%, higher than P3HT:$PC_{61}BM$ particles prepared with non-ionic $C_{16}E_{10}$ surfactant (1.68%), or with SDS (1.37%). In another paper [37], they proposed to increase the electronic charge density of the shell of the NP, in which the C_{60} groups are surrounded by PEG moieties, by adding $PC_{61}BM$ molecules in the shell of the particles. Two preparation protocols were discussed, leading to different particles with more or less $PC_{61}BM$ in the shell (**Figure 7 A**), thus successfully increasing the charge separation properties of the particle and the PCE to over 5%. On the contrary, Subianto *et al.*[38] chose to use a surfactant

close to the electron donor polymer, the 2-(3-thienyl)ethyloxybutylsulfonate sodium salt (TEBS, **Figure 7B**) to prepare P3HT-PCBM NPs by miniemulsion. The NPs were slightly larger than the ones stabilized by SDS, but UV-visible spectroscopy and SANS results revealed a different structure. While NPs stabilized with SDS had a core-shell structure, the ones stabilized with TEBS showed a more homogeneous structure with multiple domains of $PC_{61}BM$ and P3HT (**Figure 7B**), which should be favorable to increase the percolation of $PC_{61}BM$ and P3HT domains in the final OPV active layer.

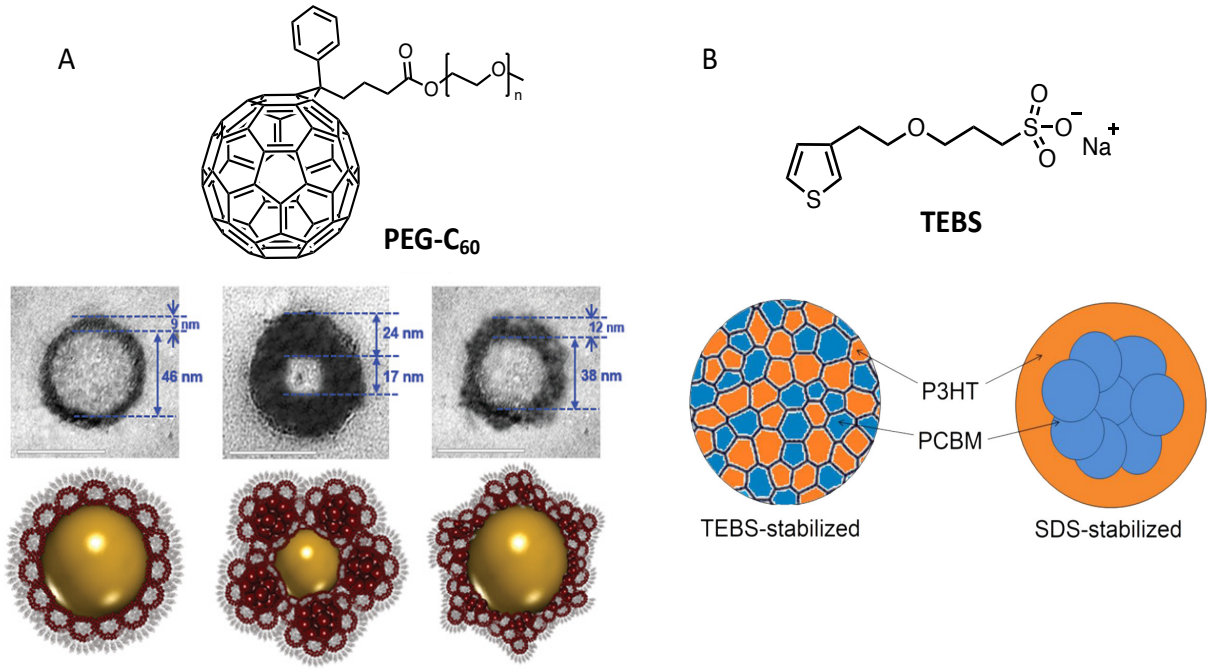

Figure 7: A) TEM image of core-shell NP stabilized by PEG-C60, the core is composed of P3HT and the shell of PEG-C60 micelles mixed with various amount of PC61BM. Adapted with permission from ref [37] (Copyright 2018 WILEY-VCH Verlag),
B) scheme of the structure of the P3HT: PC61BM stabilized by TEBS. Adapted with permission from ref [38]
(Copyright 2018 American Chemical Society).

II.2 Nanoprecipitation:

The nanoprecipitation technique is the second way to prepare OSCs NPs in an aqueous or alcohol based non-toxic solvent. A polymer solution in an organic solvent is injected into a non-solvent of the polymer, miscible with the initial solvent (**Figure 8 A**). The solubility of the polymer decreases, and the system becomes supersaturated. At low supersaturation, in the metastable region between the binodal and spinodal lines of the phase diagram, particle formation takes place through nucleation and growth, whereas for high supersaturation in the spinodal region, the systems demixes spontaneously [39] (**Figure 8 B**). The organic solvent is then evaporated. The advantage of this technique, as compared to the miniemulsion evaporation process, is that no surfactant is needed. However, the NP dispersions tend to aggregate during long-term storage and the formation of stable small NPs is usually obtained in the binodal region at very low polymer concentrations, leading to very dilute dispersions. Moreover, to obtain dispersions in water or in alcohol, the choice of suitable solvents is limited to miscible ones such as tetrahydrofuran (THF) or chloroform.

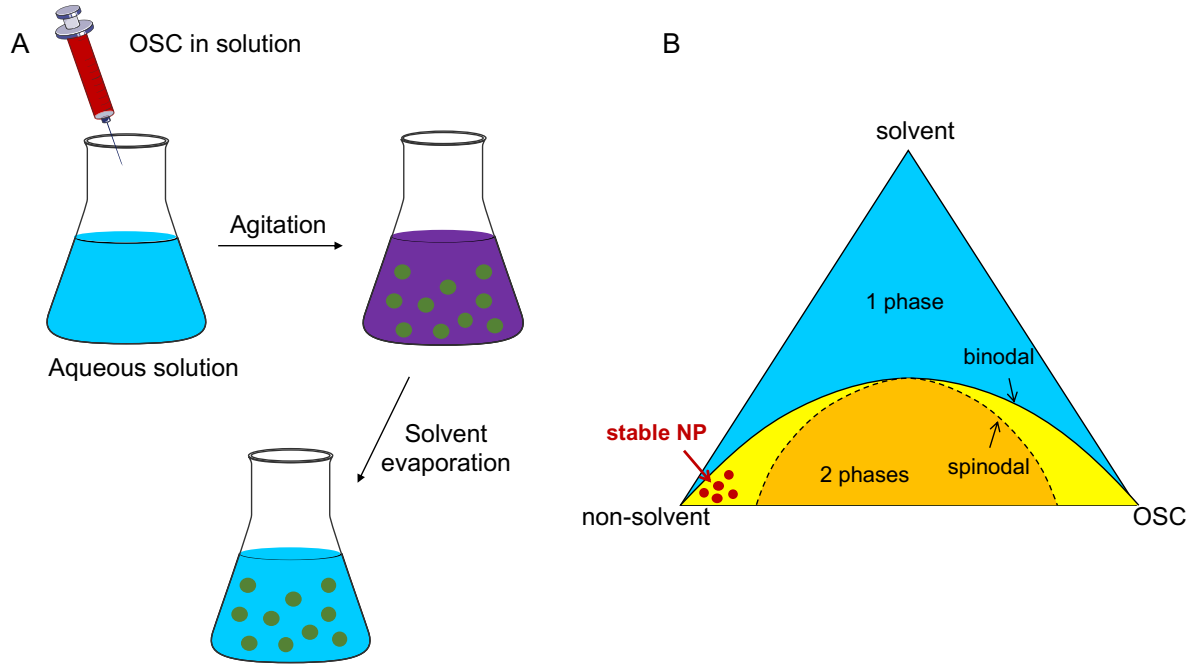

Figure 8: A) Scheme of the nanoprecipitation process, B) Phase diagram of a the OSC/solvent/non-solvent system showing the concentration zone in which stable NP are obtained.

Wang et *al.*[40] studied the aggregation-driven growth of the NPs in the first hours after their nucleation, as a function of the structure of the polymer. They compared the aggregation behavior

of poly(bithiophene-*alt*-azulene) bearing either alkyl (alkyl-PTA) or alkoxy side chains (alkoxy-PTA) during its nanoprecipitation from chloroform solution into methanol (**Figure 9 a**). The diameter of alkyl-PTA NPs increases from 60 nm, 1 min after vigorously mixing the 10^{-5} M polymer solution in chloroform with an equal volume of methanol, to 400 nm after 4h, after which the NPs became polydisperse. In the case of alkoxy-PTA, a smaller initial diameter of 30 nm was obtained. The NP diameter increased slightly up to 130 nm after 5h but kept a very low dispersity (**Figure 9 b**). To explain the difference between these two behaviors, the authors observed the evolution of the UV-visible absorption spectra with time and concluded that the electron donation to the conjugated polymer backbone is enhanced for alkoxy groups as compared to alkyl groups, resulting in stronger π-π stacking of the polymer backbone. Thus, alkoxy side chains favors the nucleation step leading to an increased number of smaller NP and faster consumption of the free macromolecules. This example illustrates the mechanism of nucleation and growth of the nanoprecipitation. Moreover, as in the case of miniemulsion, several processing parameters, such as the solvent or the relative concentration of species, may also influence the size of the NPs, as well as their crystallinity. Millstone et *al.*[41] have prepared P3HT NP by nanoprecipitation from chloroform polymer solutions into ethanol. They have shown that the final diameter of NPs increases from 30 to 83 nm with the initial concentration of P3HT in chloroform increasing from 0.005% to 0.5%. Moreover, when using monodisperse regioregular P3HT synthesized by Grignard metathesis, they obtained NPs with anisotropic shape due to their high crystallinity. As in the case of the miniemulsion technique, composite NPs can also be prepared by nanoprecipitation, starting from a solution containing both electron donor and acceptor materials further mixed with a non-solvent of the two materials. In this case also, the processing parameters allow to control the size and stability of the prepared NPs. Using a high-throughput engineering method with a robot, Xie *et al.*[42] investigated systematically the effect of the different processing parameters on the size and stability of P3HT:ICBA NPs precipitated from chloroform solutions into five different alcohols with increasing alkyl chain length from ethanol to cis-3-hexen-1-ol. They also showed that, whatever the used alcohol, increasing the materials concentration in chloroform, from 0.1 to 20 mg/mL, increased the NP diameters from around 20 nm to 100 nm. The nature of the alcohol had a smaller impact on the NP diameters, which decreased slightly with the length of the alkyl chain. However, it had an important impact on the surface charge density of the NPs and consequently, on the stability of the dispersion over time. Indeed, NPs produced in a more polar solvent, like ethanol, acquired a higher zeta potential resulting in more electrostatic repulsion and better stability, as compared to NPs dispersed in cis-3-hexen-1-ol which aggregated within less than 24 h. Finally, they observed a tendency of the diameter of the NP to decrease with an increasing content of ICBA in the NPs, which could be due

to a difference in solubility of the two components leading to a difference in the number of nuclei formed during the nucleation period.

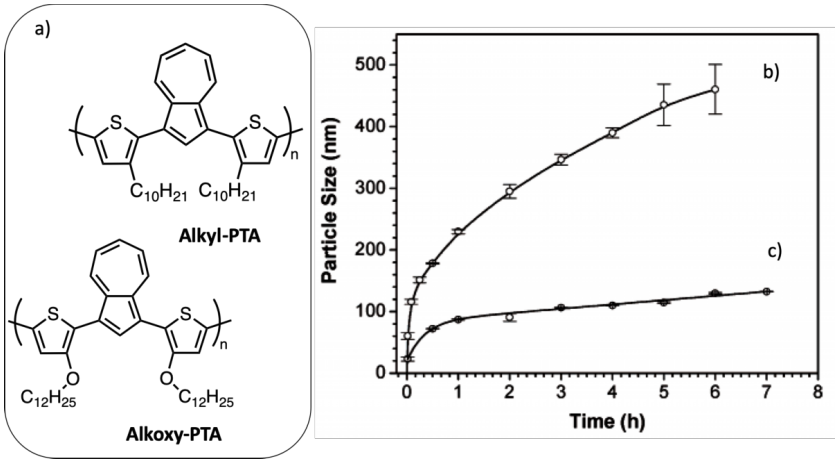

Figure 9: (a) Chemical structures of poly{1,3-bis[2-(3-n-decylthienyl)]azulene} ($C_{10}H_{21}$-PTA) and poly{1,3-bis[2-(3-n-dodecoxythienyl)]azulene} ($C_{12}H_{25}O$-PTA). Time-dependent size evolutions of conjugated polymer nanoparticles in the 1:1 mixed chloroform/methanol solutions containing (b) 10^{-5} M $C_{10}H_{21}$-PTA and (c) 10^{-5} M $C_{12}H_{25}O$-PTA, respectively. ***Adapted with permission from ref. [40] (Copyright 2005 WILEY-VCH Verlag).***

Phase separation

Composite NPs obtained from a low band gap donor (LBG) polymer with fullerene-derived acceptor PCDTBT:$PC_{71}BM$ NP have been prepared by nanoprecipitation from THF solutions into water (**Figure 5**) [(43)]. The presence of the two materials in the same particles could be demonstrated by the photoluminescence quenching of the composite NPs dispersion as compared to single PCDTBT NPs dispersion. Clafton *et al.*[(44)] have used steady-state absorption and fluorescence spectra combined with femtosecond transient absorption spectroscopy, to infer the internal morphology of regioregular P3HT:$PC_{61}BM$ NPs obtained by nanoprecipitation from THF solutions in water. By applying an exciton diffusion model to the transient absorption signal, they showed that rr-P3HT:$PC_{61}BM$ particles contained semi-crystalline P3HT domains of size of around 5 nm dispersed in the particles containing 5 to 50 wt% $PC_{61}BM$. Schwarz *et al.*[(45)] used the same technique to compare the structure of P3HT:$PC_{61}BM$ NPs obtained by nanoprecipitation or by miniemulsion. They showed that P3HT domains in composite NPs prepared by miniemulsion contained ca. 57% of aggregated P3HT domains with higher crystalline quality and larger conjugation lengths than NPs obtained from nanoprecipitation which contained only 45% of P3HT domains as aggregated material with poorer crystalline quality. The crystallinity of P3HT in nanoprecipitated NPs was similar to unannealed P3HT:$PC_{61}BM$ films cast from chloroform solutions, while the morphology of

the NPs obtained by miniemulsion could be compared to films cast from chloroform solutions and annealed at 160°C. In the case of the nanoprecipitation, the materials have less time to rearrange as compared to miniemulsion, in which a kind of solvent annealing occurs. The phase separation into NPs has been studied by SANS with contrast variation for composite P3HT:ICBA NPs prepared by nanoprecipitation from chloroform solution into methanol [46]. They confirmed that the two materials were homogeneously distributed in the NPs having a diameter of around 100 nm. By SANS, it was not possible to observe phase separation down to the 10 nm size observable by this technique. However, by transient absorption spectroscopy revealed long-lived (up to 20 ps) stimulated emission of P3HT singlets excitons being consistent with a degree of P3HT and ICBA phase separation in the NPs. The nanoprecipitated NPs thus contains uniformly dispersed domains smaller than 10 nm. In order to prepare core-shell NPs by nanoprecipitation, Chambon *et al.*[47,48] performed the sequential double nanoprecipitation of P3HT and $PC_{61}BM$. They first started from a solution of P3HT and $PC_{61}BM$ in THF and triggered the nanoprecipitation of the P3HT core in dimethyl sulfoxide (DMSO), in which $PC_{61}BM$ is soluble enough to remain in solution. In a second step, this dispersion was added to water inducing the precipitation of a $PC_{61}BM$ shell surrounding the P3HT core of NPs. They thus obtained P3HT:$PC_{61}BM$ core-shell NP of 80 to 100 nm in diameter, depending on the starting concentrations, which variation is however limited by the low solubility of $PC_{61}BM$ in DMSO.

Compared to the miniemulsion process, the simple nanoprecipitation normally allows the formation of more uniform phase separation inside the NPs without the use of a surfactant, which makes it very attractive for OPV applications. However, the production of small NPs with low dispersity in size and good stability over time is a real challenge. Moreover, its success depends on the material/solvent/non-solvent phase diagram which is different for each molecule, the stable dispersion being obtained in the binodal region at very low polymer concentration, yielding very dilute NP dispersions. Recently, Xie *et al.*[49] developed a surfactant assisted nanoprecipitation method which allows the synthesis of stable dispersions at higher concentrations in the spinodal region and is therefore more versatile regarding the nature of the materials. As surfactant, they cleverly chose Pluronic F127 (**Figure 6**), a thermosensitive block copolymer of ethylene glycol and propylene glycol. It has the advantage of being non-ionic. Moreover, its solubility in water increases at low temperature. F127 could therefore be easily stripped off from NPs at 4°C in a few centrifugation dialysis steps, much more efficiently than for SDS removal (**Figure 10**). With this technique, they prepared composite NPs of P3HT and a non-fullerene acceptor (NFA) *o*-IDTBR

(**Figure 10 a**), starting from a 5 mg.mL^{-1} materials solution in THF followed by precipitation into water with a high solvent: non-solvent ratio of 1:2, whereas it is usually in the range of 1:8 or lower in standard nanoprecipitation. Such strategy resulted in a dispersion having a higher final NP concentration than what it is usually achieved in classical nanoprecipitation. Moreover, after surfactant stripping, the NPs dispersions remained stable for more than 3 months. Finally, the authors demonstrated the versatility of this technique by preparing dispersions of composite NPs with two LBG polymers PCE10 or PBQ-QF, and two NFA, *o*-IDTBR or ITIC (**Figure 10a**), that have been used in OPV to reach a record efficiency for NP based systems of 7.5%.

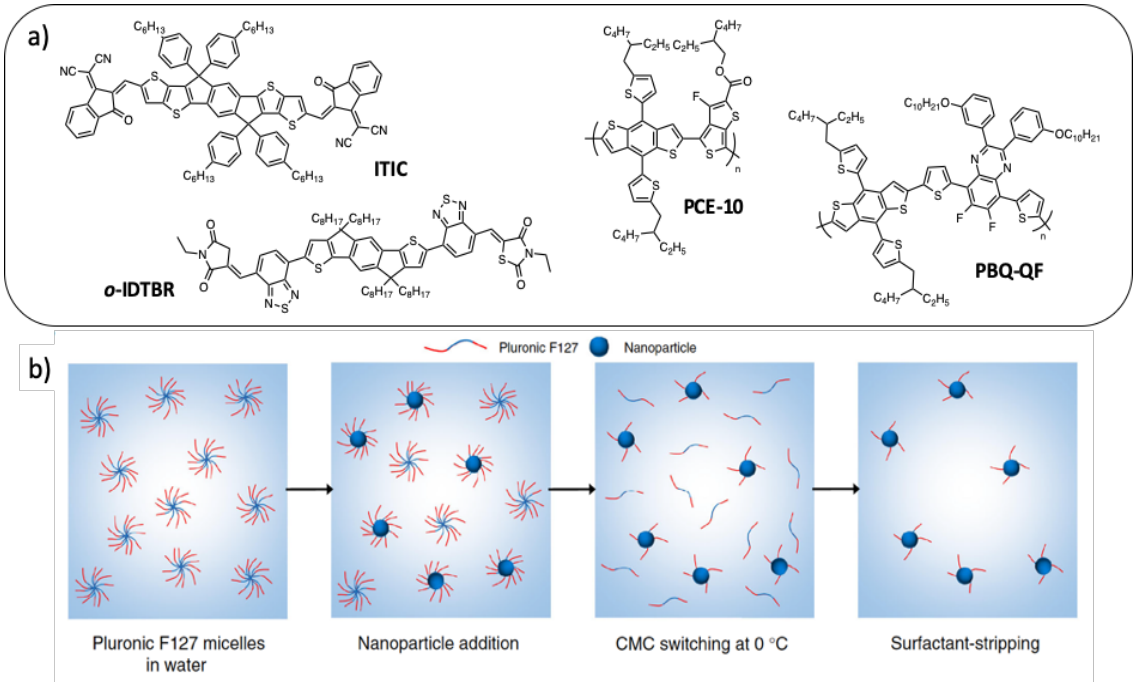

Figure 10: a) Chemical structures of ITIC, o-IDTBR, PCE-10 and PBQ-QF used to prepare NP by surfactant-assisted nanoprecipitation. b) Pluronic F127 is a copolymeric surfactant with temperature-depend critical micellar concentration (cmc). After elaboration of the NPs at room temperature, the dispersion is cooled down to 0°C. At this low temperature, the surfactant becomes more soluble in water, its cmc increases and it desorbs from the NP surface. It can then be easily removed by centrifugal dialysis in a few steps only. ***Adapted with permission from ref.[49] (Copyright 2018 Springer Nature)***

III. Building the active layer by NPs assembly, and its resulting morphology:

Once synthesized, the NPs have to be assembled into a functional active layer. As already described, the ideal morphology of the film is a two phases bicontinuous structure with percolating pathways allowing the efficient conduction of electrons and holes towards the electrodes (**Figure 1**).

The elaboration of an active layer from an NPs ink is performed in two steps: first, the deposition and assembly of the solid NPs during solvent evaporation and then, an annealing step allowing the diffusion of the materials in the interparticle voids, leading to more compact and smooth active layers. Rearrangement of the donor and acceptor phases can also occur during annealing. These two steps can then be repeated several times in order to obtain a thicker and/or a multilayered film.

III.1 Processes used to build an active layer from NP dispersions:

Different processes have been used to build a film from the NPs dispersions for the preparation of active layers from the laboratory scale to the industrial one. Several issues are encountered. Among them, one can cite the low solid contents of the prepared aqueous dispersions (**Table 1**) requiring additional concentration steps, and their low viscosity leading to low film thicknesses. It is then often necessary to repeat the deposition step in order to increase the active layer thickness. Another difficulty is the poor wettability of the aqueous dispersions on more or less hydrophobic substrates resulting in a non-homogeneous layer with large roughness, responsible of current leakages and failure of the device.

OSC system		Solution [] mg/mL	Dispersion, Solid content, mg/mL		Reference
			after elaboration	for the coating process	
P3HT/o-IDTBR	Solution	24 in CB			[50]
	Surfactant-assisted nanoprecipitation		2.5 in water	80 in water	[49]
P3HT/$PC_{61}BM$	Solution	~40 in oDCB			[50]
	Surfactant-assisted nanoprecipitation		2.5 in water	50 in water	[49]
	Miniemulsion		3.3 in water	10 in water	[51]
P3HT/ICBA or P3HT/ICxBA	Solution	40 in CB			[52]
	Nanoprecipitation		0.025 to 5 in ethanol	10 in ethanol	[42,53]
	Miniemulsion		10 in water	10 in water	[28,54]
PBDTTPD/$PC_{71}BM$	Solution	17.5-20 in CB			[55]
	Miniemulsion		9.5 to 28.5 in water	40 in water	[15]
PCE10(PTB7-Th)/ o-IDTBR	Solution	20-37.5 in *o*-DCB			[56]
	Surfactant-assisted nanoprecipitation		2.5 in water	50 in water	[49]
PBQ-QF/o-IDTBR or PBQ-QF/ITIC	Solution	12 in THF			[57]
	Surfactant-assisted nanoprecipitation		2.5 in water	50 in water	[49]

Table 1: Examples of solution/dispersions concentrations after preparation and before processing for various OSC systems

At the lab scale, the main used process is the spin-coating of the NP dispersions. Bag *et al.*[51] have optimized the spin-coating conditions of a P3HT:$PC_{61}BM$ blend in order to obtain a reproducible deposited active layer. Optimization was performed both for separate and composite NPs for a direct PV structure of glass/ITO/PEDOT:PSS/active layer/Ca/Al, the direct structure allowing illumination through a transparent hole-collecting electrode (ITO/PEDOT:PSS). Thus, a UV-O_3 treatment of the PEDOT-PSS layer allowed to decrease its water contact angle to less than 2°, leading to a rapid and uniform spreading of the NP dispersion and a low surface roughness. A better packing of the NPs in the layer was also obtained by spin-coating NPs in a solvent mixture of ethanol:water (20:80) rather than water alone, probably thanks to a decrease of electrostatic repulsion between the NPs, while increasing van der Waals attraction. Moreover, in order to prevent the PEDOT-PSS sublayer to re-dissolve when in contact with the aqueous dispersion, the evaporation of the solvent was sped up by preheating the substrate with an IR lamp. Ambient

atmosphere was also important as a relative humidity below 30% has also shown to increase the porosity and roughness of the deposited layer. Finally, the addition of a thin $PC_{61}BM$ buffer layer on top of the active layer, before Ca/Al electrode deposition, reduced the surface roughness to 10 nm and prevented leakage current to the electron-collecting electrode. OPV device characterization clearly highlights the positive effect of this buffer layer, especially on the Filling Factor (*FF*) which reached 65%. Although modest, the final PCE of 2.15% is clearly in the average for such P3HT-based blends [58].

By studying composite NPs made of two fluorene-based polymers, one electron donating derivative, called PFB, and one electron accepting derivative, called F8BT (**Figure 11 b**), Stapleton *et al.*[59] have shown that the successive deposition of NPs by spin-coating, with a rapid annealing at 70°C between each layer deposition for drying purpose, allowed to tune the thickness of the final film. In addition, they observed that the roughness of the film decreased with the number of deposited layers (**Figure 11 a**). The voids left in the underlying film were filled by the freshly deposited NPs, thus increasing the compactness and quality of the film. However, when the film became too thick, cracks appeared on its surface probably due to negative capillary pressure between NPs resulting from water removal. Hence, an optimum has to be found for the number of NP deposition layers and thickness of the film in order to achieve the best morphology.

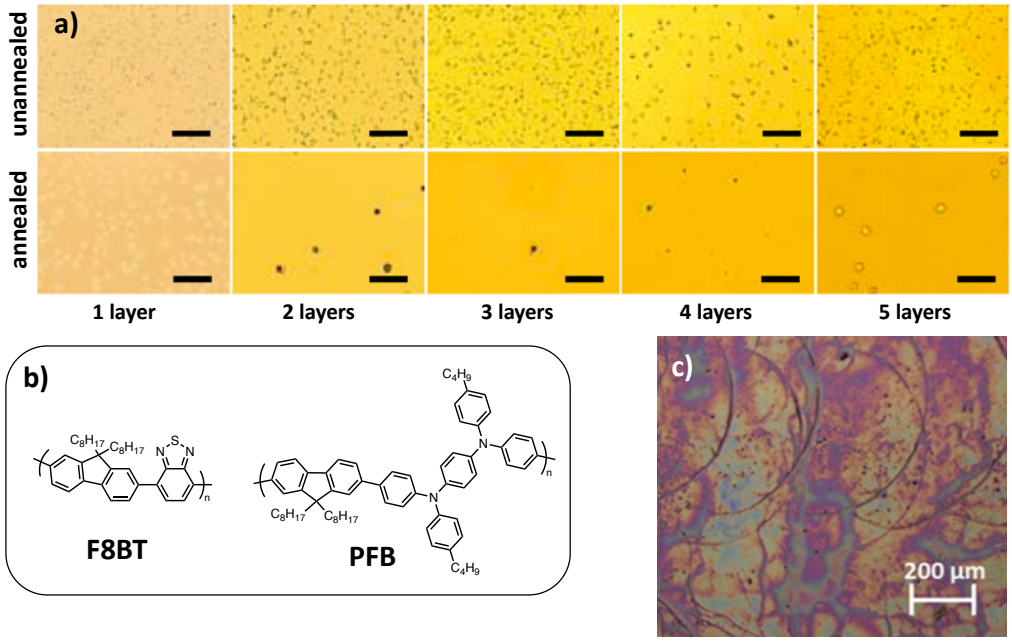

Figure 11: a) Optical micrographs for the unannealed (upper row) and annealed (lower row) for nanoparticulate films consisting of one to five layers. The scale bar is 5 mm in each micrograph. Adapted with permission from ref.[59] (Copyright 2012 Elsevier B.V.); b) Polymer chemical structures; c) Optical micrograph of an ink-jet printed P3HT:IC[60]BA nanoparticulate film after annealing, showing the typical signature of droplet edges, originating from the coffee stain effect. Adapted with permission from ref. [60] (Copyright 2015 Elsevier B.V.).

Preparation of large surface devices is not possible by using spin-coating, therefore other deposition techniques have been studied such as spray coating, ink-jet printing or doctor blading.

P3HT films were prepared by spray coating of aqueous dispersions of P3HT NPs in water leading to NPs assemblies with thicknesses up to 1.5 µm [61]. The cleaned ITO substrate was heated at 80-85°C and an UV-O_3 pretreatment improved the film quality. The presence of surfactant in the dispersion had an important influence on the packing of NPs in the films, leaving voids in the film due to electrostatic repulsion between the particles. Therefore, removal of the excess of surfactant, as discussed for the miniemulsion process (**section II.1**), was necessary to obtain closed-packed NPs assemblies.

Ink-jet printing is an interesting technique that allows the deposition of solar cells with customer-designed shapes, while doctor blading is limited to large surfaces homogeneously coated[62]. The formulation of the dispersion has to be adapted in order to avoid nozzle clogging for ink-jet printing. As an example, in the case of P3HT:ICBA NP dispersions in ethanol, a higher boiling point solvent butoxyethanol (boiling point 170°C), often used in paints, had to be added[60]. The temperature of the substrate can also be optimized to tune the spreading of the droplets and evaporation rate. If the deposited film is too thin, several layers can also be printed. However, one of the difficulties of this technique is to avoid the coffee stain effect, an accumulation of NPs at the edge of the deposited droplets. Indeed, it leads to the formation of ridges with increased thickness in the final film (**Figure 11 c**).

Doctor-blading is the deposition technique that closely resembles to slot-dye coating used in the roll-to-roll processes. Sankaran *et al.*[60] have prepared inverted OPV devices, with structure glass/ITO/ZnO/composite NPs/PEDOT:PSS/Ag, by doctor-blading active layers of surfactant-free P3HT:ICBA NP dispersions in ethanol onto ZnO. Two blading sublayers were applied before thermal annealing at 150°C leading to similar performances as for spin coated devices. They also demonstrated the possibility to prepare device active area of 1.1 cm^2 with minimal loss of performance from 3.9 % for 0.105 cm^2 to 3.4%. Xie *et al*.[42] have also prepared inverted OPV devices with structure glass/ITO/ZnO/composite NPs/MoO_x/Ag by doctor-blading P3HT-ICBA NPs in different alcohols on ZnO. The best device performance was obtained for ethanol with a PCE of 4.26 %. Indeed, NPs in alcohol with increasing alkyl chain up to hexanol, showed stronger aggregation and lower wetting on substrate. Four sequentially blade-coated layers were necessary to obtain an active layer thickness of 240 nm.

OPV active layers have also been deposited onto flexible PET foil from aqueous dispersions of composite conjugated polymer: fullerene derivatives NPs by roll-to-roll processing [54,63]. One of the important issues encountered in the case of slot-die coating of aqueous dispersion onto a ZnO

electron transporting layer (ETL) for inverted structures or a PEDOT-PSS hole transporting layer (HTL) for direct structures, is the dewetting of the NP ink before complete drying of the film. This phenomenon can be controlled by fine tuning of the ink formulation. In particular, it was shown that leaving an optimized concentration of SDS surfactant in the ink allowed to control dewetting, but was detrimental to the device performance. Andersen *et al.*[63,64] have added a non-ionic fluorosurfactant (FSO-100) to the ink formulation. However, in excess, this surfactant could be responsible for low film adhesion to the substrate. Another way to control the interfacial surface energy is to use ozone treatment to change the substrate chemistry. Applied to the PEDOT-PSS HTL, this treatment lowered the water contact angle by increasing the PSS fraction at the surface of the film, resulting in a good wetting of the NP ink slot-dyed coated onto it and thus increasing the homogeneity of the active layer film[54]. Simultaneous double slot-die coating of active layer and the PEDOT-PSS HTL onto ZnO was also demonstrated[65]. In this case, it was shown by film delamination in NaOH solution, and by Time of Flight - Secondary Ion Mass Spectrometry (TOF-SIMS) analysis, that a double layer had been obtained with only limited inter-diffusion between the active and the hole transporting layers, the diffusion of NPs being too slow for the two dispersions to mix before drying. Even if significant process optimization has still to be done in order to increase the device performances, the possibility to prepare NPs OPV flexible devices entirely elaborated by roll-to-roll processes has been demonstrated with a PCE up to 0.45 % [54]. Roll-to-roll processing of aqueous NP dispersion is thus the most promising route to large scale printing of OPV devices from aqueous solvents.

III.2 Morphology of the BHJ film at the mesoscale:

In this part, we discuss the morphology of the active layer composed of both electron donor and acceptor materials, formed by the assembly of the NPs, as building blocks. The phase separation of the two materials is discussed, keeping in mind that the ideal morphology is formed by two percolating materials networks allowing excitons dissociation at interfaces and charges transport to the electrodes[66]. In order to illustrate these features, a correlation with the OPV device performances is also made when it makes sense. In order to make this review as exhaustive and clear as possible, the reader will find in **Table 2**, the main features associated with the performance of organic photovoltaic devices reported in the literature.

In the following, we discriminate between active layers prepared from a dispersion of composite NP or from a dispersion of a binary mixture of electron donor NPs and electron acceptor NPs.

Films from binary mixture of NPs

Many studies have focused on the ordered assembly of a binary mixture of two kinds of NPs. Indeed, some of the ordered crystalline structures, such as the AlB_2 structure (**Figure 12a&b**), could be very interesting for photovoltaic applications because they allow the formation of continuous percolation paths in the vertical direction[67]. However, this kind of assembly necessitates the use of particles with very low dispersity in diameter and the fine tuning of their interactions: van der Waals attraction, electrostatic or steric repulsion. Moreover, the preparation of such ordered assembly also requires a slow sedimentation or particle concentration step in order to give enough time for the spheres to crystallize at volume fractions of 0.49 to 0.55[68].For semiconducting NPs usually deposited using rapid processes such as spin-coating, a metastable “disordered” assembly also called random close-packed (RCP) is obtained (**Figure 12c**). In this case, several parameters can be varied in order to optimize the assembly of the two types of particles and thus, the final morphology of the film. The main parameters are the proportions of each type of particles and their difference in diameter. Gehan *et al.*[69] have prepared films from a mixture of P3HT NPs and $PC_{61}BM$ NPs of equal diameter and in equal proportion. The morphology of the film was observed by SEM showing a disordered glassy state. Further selective dissolution of $PC_{61}BM$ in dichloromethane revealed a random mixture without segregation of the two types of particles. Moreover, they used conducting Atomic Force Microscopy (cAFM) to characterize the hole conduction pathways formed by the network of neighbouring P3HT particles percolating through the film. Time of Flight (TOF) mobility measurement in the P3HT phase were also performed showing a hole mobility of ~ 8×10^{-5} $cm^2/(V.s)$ for films processed from the mixture of P3HT NPs and $PC_{61}BM$ NPs as compared to a

hole mobility of ~ 2 x 10^{-4} $cm^2/(V.s)$ measured for films processed from pristine P3HT solutions or P3HT-only NPs dispersions. By using cAFM and TOF, the same group also estimated the percolation limit at ~30% in proportion of particles in a binary assembly of P3HT and polystyrene (PS) NPs[70]. They found an increase of conduction pathways and hole mobility, following a power scaling law, with the proportion of P3HT NPs (**Figure 12 d & g**). For donor:acceptor (D:A) active layers, they found that the optimum P3HT:PC_{61}BM NP ratio was 2:1, with a maximum PCE of 1.84 % measured on a direct-structure OPV device. Such a ratio is similar to the ones usually observed in solution processed P3HT:PC_{61}BM devices[58].

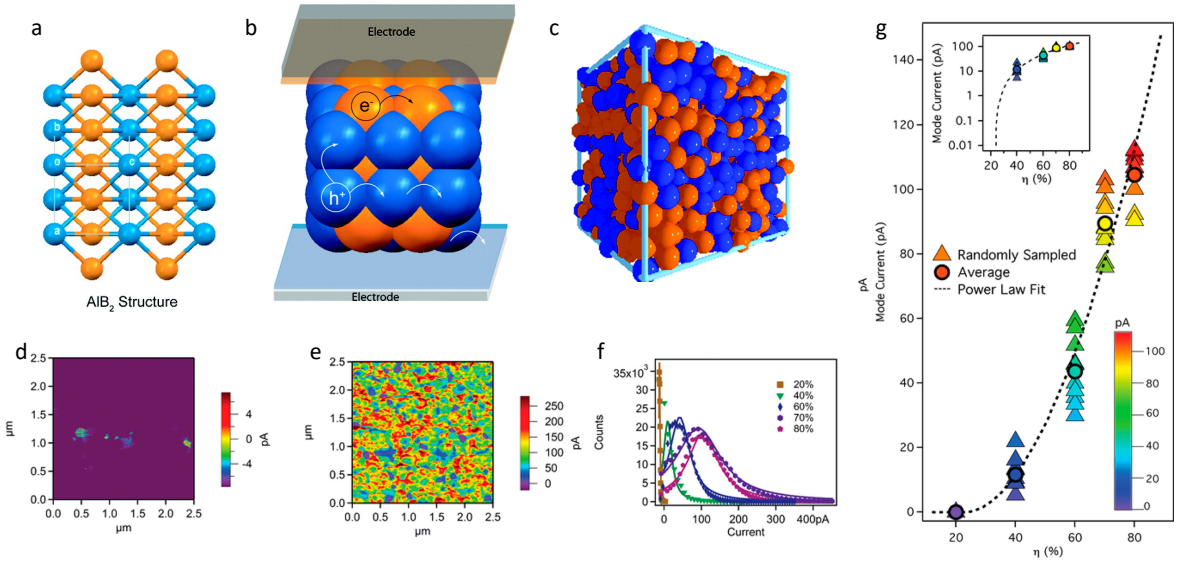

Figure 12: a-b) Expanded view of the AlB2 structure showing continuous pathways for electron/hole transport to the cathode/anode, respectively, c) Disordered assembly of NP (RCP). Adapted with permission from ref. [67] ***(Copyright 2020 American Chemical Society). d-g) Conductive AFM maps of binary P3HT/PS nanoparticle films at P3HT volume fractions (η) equal to (d) 20% and (e) 80%. (f) Pixel current histogram plots for five cAFM maps with varying η. (g) Mode current from current distributions as a function of η (dashed line) for ten randomly sampled subselections of each cAFM map, in closed triangle symbols, and the average in closed circle symbols. The semilog plot in the inset shows log mode current as a function of η. Adapted with permission from ref.*** [70] ***(Copyright 2016 American Chemical Society).***

After the deposition step, the random closed-packed assembly of NPs still contains voids between the NPs and an annealing step is required to obtain a continuous compact film, by joining the NPs, thus increasing the contact area between the two different phases were the exciton dissociation occurs and form the charge conduction pathways, leading to the final film morphology (**Figure 13 b**).

Kietzke *et al.*[18] have prepared films from a mixture of separate NPs of two fluorescent polymers, one poly(p-phenylene)-type ladder polymer (m-LPPP, **Figure 13 a**) which does not show softening before its high decomposition temperature and one derivative of polyfluorene with a T_g close to the room temperature. The two polymers were selected to study the morphology of the films by energy-transfer experiments. After deposition by spin-coating, RCP NPS assemblies were obtained with partial merging of the soft polymer particles. The film became smoother after annealing at 200°C, and optical excitation at the absorption wavelength of the polyfluorene resulted in a quenching of the polyfluorene emission and charge transfer to the m-LPPP polymer, which emission was increased by four, indicating an increase of the interfacial area between these two polymer phases during annealing. A similar phenomenon was observed for a binary mixture of PFB and F8BT NPs, showing an increased charge transfer after annealing of the film slightly above the T_g of the polymers[18]. Holmes *et al.*[71] have prepared binary mixtures of $PC_{61}BM$ and P3HT NPs. They have shown using STXM and photoluminescence experiments that careful thermal annealing above the T_g of P3HT, allowed the softening of the NPs increasing contact area between them and the diffusion of $PC_{61}BM$ into the amorphous parts of the P3HT phase, leading to a three-phase microstructure with P3HT crystalline domains, $PC_{61}BM$ domains and a mixed amorphous third phase containing more than 20% $PC_{61}BM$ (**Figure 13 b**). Diffusion of $PC_{61}BM$ into a P3HT phase had already been demonstrated in solvent-cast P3HT: $PC_{61}BM$ films [72,73]. This third mixed phase together with the high crystallinity of P3HT allowing a high diffusion length of excitons, resulted in an exciton dissociation efficiency as high as 60%, as compared to 37% before annealing.

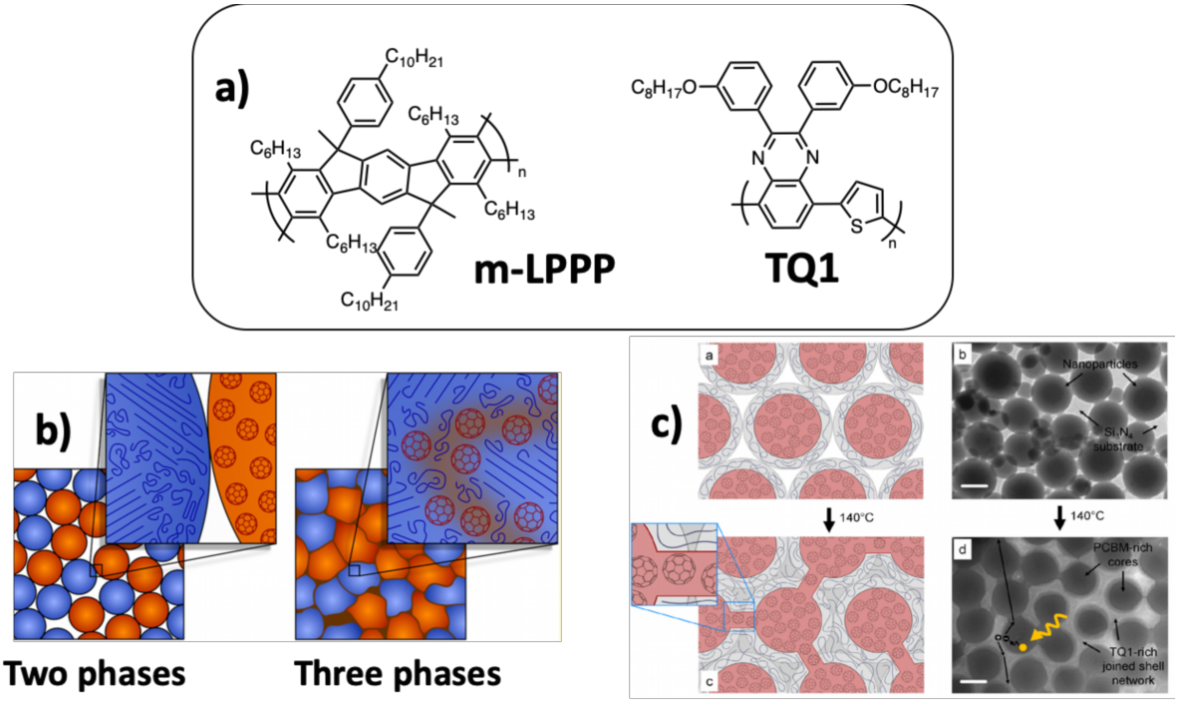

Figure 13: a) m-LPPP and TQ1 chemical structures; b) Schematic representation of the three phases film microstructure obtained by thermal annealing the assembly of PCBM NP and P3HT NP comprising crystalline P3HT and amorphous P3HT subdomains. A third mixed phase is obtained by sintering and diffusion of PCBM in the P3HT amorphous domains. Adapted with permission from ref. [71] ***(Copyright 2018 American Chemical Society). c) Schematic representation and TEM images of composite NPs made of a PCBM-rich core and an amorphous TQ1-rich shell. Mobility of the TQ1 polymer chains during thermal annealing slightly above its T_g allowed the movements of PCBM molecules and creation of bridging pathways between the PCBM-rich cores. Adapted with permission from ref.*** [74] ***(Copyright 2016 Elsevier B.V.)***

Films from composite NPs

In the case of composite particles containing at the same time the electron donor and acceptor materials, the morphology of the resulting films is different. The phase separation domains depends on the particles size [(20)] and on their internal morphology that can be Janus or core-shell. The most common case of core-shell NPs is not the ideal geometry as it might be difficult to obtain a percolation path of the core material in the film. However, Gehan *et al.*[(69)] found a higher PCE (2.15%) for composite nanoparticles of P3HT:$PC_{61}BM$ than for binary mixtures of the pristine NPs (1.84%). By AFM and TOF, they also demonstrated differences in the hole conducting pathways of P3HT, which is the shell material as demonstrated earlier by Holmes *et al.*[(19)] The composite NP films had a hole mobility in the same order of magnitude as P3HT-only NP films at low-field regime. In the case of core-shell composite particles, thermal annealing of the film plays a fundamental role in the possible connection of the core material domains and the final film morphology. As an

example, when using core-shell composite NPs with poly[2,3-bis-(3-octyloxyphenyl)quinoxaline-5,8-diyl-alt-thiophene-2,5-diyl] (TQ1, **Figure 13 a**), an amorphous electron donor polymer as the shell, in combination with $PC_{71}BM$ as the core, it was demonstrated that annealing at a moderate temperature of 140°C, slightly above the T_g of TQ1, led to the formation of nano-pathways between the PCBM core of neighboring particles (**Figure 13 c**), thus allowing the percolation of the core-material in the film[74]. However annealing at higher temperatures above 160°C, resulted in the loss of the NPs structure with gross phase separation and formation of large PCBM aggregates of a few hundreds of nm, which is detrimental to the OPV performance. Indeed, the correlation between phase segregation and solar cell PCE is particularly obvious in this case since PCE first increases with the temperature reaching 2.5 % at 160°C, before decreasing sharply at higher annealing temperatures.

In several cases, it was shown that the use of composite NPs, together with mild thermal annealing, is a good way to control the size of the phase-separated domains, even when it was not possible by solution casting. As an example, PDPP-TNT (**Figure 14 a**), a diketopyrrolopyrrole-based electron donor polymer, and $PC_{71}BM$, processed in chloroform solutions led to phase segregated morphology with domain sizes reaching the micron scale (**Figure 14 b**). In contrary, films prepared from composite NPs allowed to control the morphology of the active layer at the nanometer length scale (**Figure 14 c**) even if a mild annealing (at 130°C for 10 min) was necessary to join the NPs and obtain a working OPV device (1.99% at best)[75]. However, the control of the morphology of the film was lost at higher annealing temperature or longer annealing time resulting in a gross phase segregation of the fullerene outside the particles and a drop of the PCE.

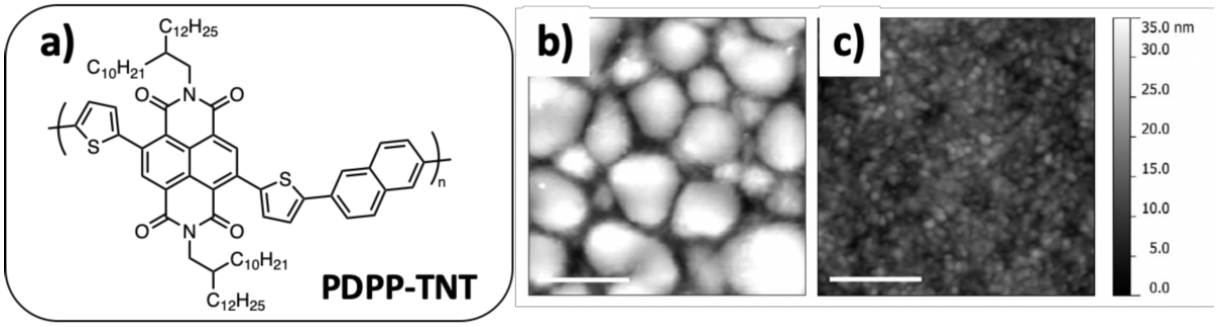

Figure 14: a) PDPP-TNT chemical structure. AFM images of b) an as-spun PDPP-TNT:$PC_{71}BM$ 1:2 blend film spincast from chloroform and c) an as-spun PDPP-TNT:$PC_{71}BM$ 1:2 nanoparticulate film. Scale bars are 500 nm. Adapted with permission from ref. [75] ***(Copyright 2014 The Royal Society of Chemistry)***

This effect of coarse phase separation was also observed for P3HT:$PC_{61}BM$ composite NP films, at a lower annealing temperature of 140°C for 4 min[76], probably due to the lower T_g of P3HT as compared to PDPP-TNT or TQ1. In addition, the authors demonstrated, by combining optical

spectroscopic and microscopic (STXM and TEM) analyses of the thin films, that before annealing, NP films already show evidence for greater phase segregation and interchain order within NPs than in an unannealed solution cast BHJ films. Consequently, the coarse phase segregation occurs very quickly in NP films upon thermal annealing as compared to BHJ films. This clearly suggests that the initial state of the film constituents plays a preponderant role in the thermal annealing effect and thus influences the temperatures and times to be applied. Subsequently, using similar analysis methods and still based on the P3HT:$PC_{61}BM$ binary system, the same team[77] showed the different impact of thermal annealing at 140°C for 30 min, as a function of the NPs preparation process, on the final film morphology. Indeed, while the composite P3HT:$PC_{61}BM$ NPs prepared by miniemulsion exhibit a core-shell structure, the NPs prepared by nanoprecipitation are fully blended. OPV performances measured on unannealed as-cast films are similar in both cases. However, upon thermal annealing the core-shell NPs undergo a significant phase segregation, leading to micron-sized domains of near-pure $PC_{61}BM$ and P3HT, while blended nanoprecipitated NPs melted together without any phase segregation allowing the conservation of an optimum blended morphology. Consequently, charge transport and device efficiency were improved upon annealing. A final PCE of 1.09 % for the nanoprecipitated NPs was reported by the authors. As compared to standard P3HT:$PC_{61}BM$ spin-coated films, the lower PCE could be mainly attributed to the lower short-circuit current density (J_{SC}) and Fill Factor (*FF*) . It can thus be assumed that blended NPs, as obtained by nanoprecipitation, are less subjected to coarse phase separation and consequently tolerate harder thermal annealing.

Gärtner *et al*.[78] have illustrated this point clearly. Indeed, as seen previously, they produced P3HT:ICBA blended surfactant-free NPs by nanoprecipitation in MeOH and elaborated multilayer homogeneous thin-films of approximately 250 nm thickness. Subsequent thermal annealing (up to 200°C) does not show any impact on P3HT crystallization as probed by UV-vis absorption spectroscopy. However, this thermal annealing is of crucial importance for the device efficiency that increases significantly up to such temperatures, well above the T_g of the organic materials (**Figure 15**). In order to better understand the thermal annealing - OPV device efficiency relationship, the authors investigated the limiting recombination processes by performing intensity dependent photo-current density measurements. Upon thermal annealing, the limiting recombination process changes from bimolecular to monomolecular. Associated with a simultaneous decrease in film roughness and a significant increase in open circuit voltage (V_{oc}) and *FF*, the authors suggested that thermal annealing increases the close packing of NPs and therefore facilitates the charge carrier transport and extraction. They thus reached PCE as high as 4.1 %, not

so far from the standards of the system having the same composition but deposited from toxic solvent solutions.

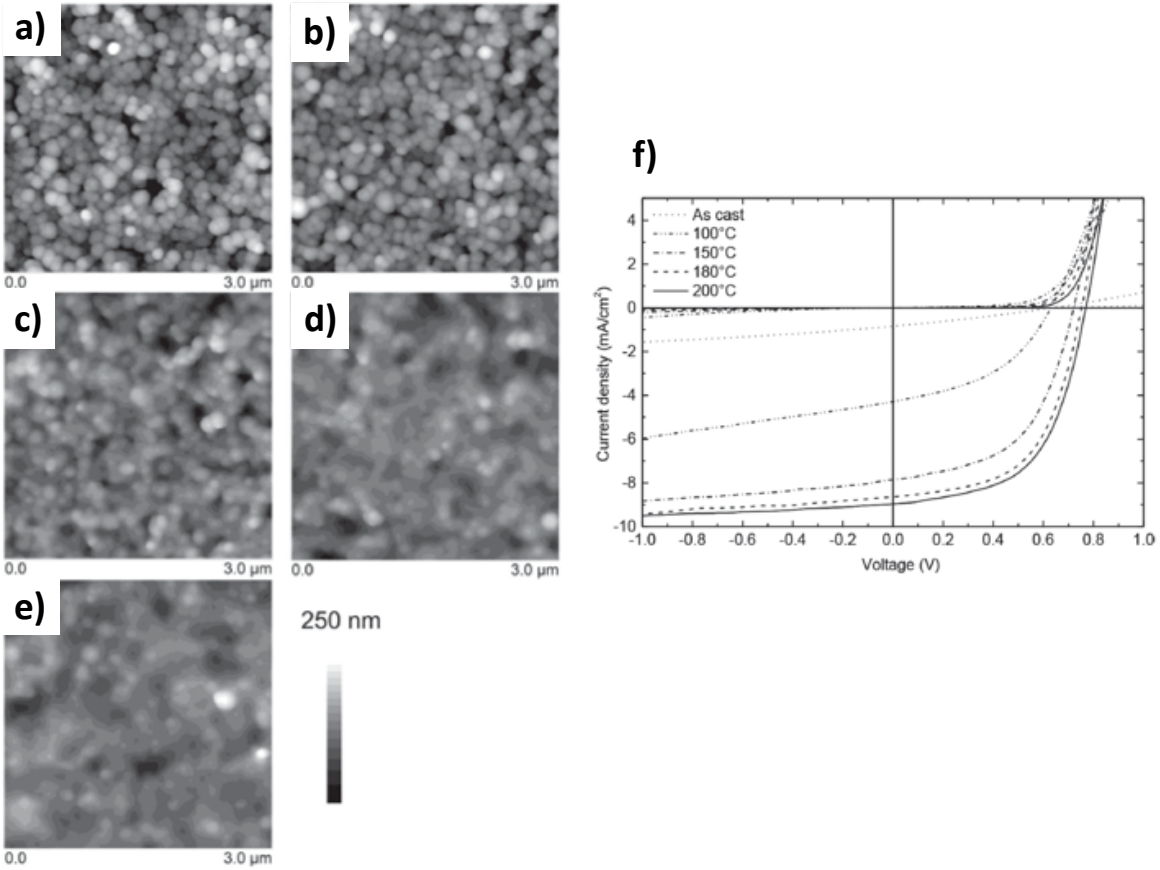

Figure 15: 3 x 3 µm² AFM images of the P3HT:ICBA nanoparticulate active layers spin coated from a 10 mg/mL dispersion in methanol: a) As-cast photo-active layer; b) Photo-active layer annealed for 10 min at 100 °C; c) 150 °C; d) 180 °C; and e) 200 °C. The corresponding root mean square roughness R q is (a) 43 nm, (b) 46 nm, (c) 30 nm, (d) 24 nm and (e) 23 nm, respectively. f) Typical J–V curves of nanoparticulate solar cells with inverted device architecture for different annealing temperatures. Adapted with permission from ref.[78] (Copyright 2018 WILEY-VCH Verlag).

IV. OPV cells:

The development of an effective OPV device is not limited to the processing of a suitable photoactive thin film. Indeed, many chemical and physical parameters have to be taken into consideration, as the donor: acceptor ratio, the interfacial layers, the type of electrodes or the nature of the optoelectronic components.

IV.1 Donor: Acceptor ratio:

A key parameter in OPV is the optimum donor: acceptor (D:A) ratio to achieve the most ideal morphology, the right balance between charge carriers mobilities and the best PCE. This ratio usually depends mainly on the nature of the donor and acceptor components and, to a lesser extent, on the deposition parameters such as the solvent, the deposition temperature or the presence of additives. But very often this ratio evolves within a very narrow range of values. For example, when considering the P3HT:$PC_{61}BM$ binary blend, it is well established that the suitable ratio is around 1:0.8 by weight [58]. Interestingly, a few articles show that this optimal ratio can be considerably modified when switching to active layers elaborated from NPs. This is particularly noticeable in the case of core-shell NPs, obtained by mini-emulsion.

Indeed, Holmes *et al.* [25] investigated the OPV performances of core-shell NP-based thin films with varied D:A ratio. In particular, they highlight a PCE evolution, as a function of the $PC_{61}BM$ content, that is very different from the trend generally observed in P3HT:$PC_{61}BM$ BHJs. Indeed, with high P3HT:$PC_{61}BM$ ratio ranging from 1:1 to 1:2, they observed a constant and relatively high PCE value while it quickly decreases for P3HT:$PC_{61}BM$ ratio below 1:1 and in particular for the observed 1:0.8 optimum ratio in standard BHJs solar cells. Using a combination of STXM and SEM microscopies, the authors observed that increasing the $PC_{61}BM$ proportion does not significantly affect the size of the $PC_{61}BM$-rich core, which is still smaller than the exciton diffusion length, but it has a strong impact on the composition of the initially P3HT-rich shell, after thermal annealing. For the annealed 1:0.5 ratio, the joined shell phase consists of less than 20 % $PC_{61}BM$, which is below the minimum concentration required to achieve continuous $PC_{61}BM$ percolation pathways (percolation threshold) in the bulk film. When increasing the initial NPs $PC_{61}BM$ content to ratio over 1:1, the $PC_{61}BM$ shell fraction increases to values above 33 %, approaching the optimum blend ratio required for balanced charge mobility. As such, they observed an uncommon increased $PC_{61}BM$ photocurrent contribution (up to 30 %) for P3HT:$PC_{61}BM$ blend ratio of 1:2.

By investigating two different binary systems, Dam *et al.*[27] have demonstrated that the deviation from the optimal D:A ratio observed in BHJ can be directly correlated with the miscibility between

the two components. Indeed, they investigated the morphology and device performance of NP-based OPV devices for two very different polymer:fullerene blends (*i.e.* P3HT:$PC_{71}BM$ and a more crystalline PSBTBT low bandgap (LBG) polymer blended with $P_{71}CBM$, **Figure 16**), the authors showed that the crystalline nature and the miscibility between (macro-)molecular components are key parameters to control the NPs core and shell composition, called mesomorphology in their article. If both blends show similar core-shell NPs of comparable sizes (diameter around 24 nm) and similar $PC_{71}BM$-rich core volume of 20% of the NP, STXM investigations allowed the authors to highlight the marked difference in core composition. Indeed, the core of the P3HT:$PC_{71}BM$ NPs is considerably richer in PCBM relative to that of the PSBTBT:$P_{71}CBM$ NPs (**Figure 16**). Moreover, if the shell compositions are really close in both cases with a polymer fraction of around 0.7, this value for PSBTBT:$PC_{71}BM$ NPs is very far from the ideal composition of PSBTBT:PCBM blends (reported to be 0.4 in BHJ), whereas it is only 20% higher than the ideal case for P3HT:PCBM (0.56 in BHJ). Consequently, the authors suggest that the region in which charge generation occurs will be different in both cases. Thus, in the P3HT:$PC_{71}BM$ NPs, the charge generation is expected to be dominated by the shell region, while the opposite is true with the PSBTBT:$PC_{71}BM$ NPs. However, taking into account the relative volume proportion of core and shell in these NPs (only 20% of core in NPs volume) a much lower performance in OPV device can be expected from the PSBTBT:$PC_{71}BM$ NPs. Indeed, if the two blends gave identical PCE values of 1.3%, the decrease in performance compared to the reference BHJ device is much greater in the PSBTBT:$PC_{71}BM$ NPs case. Especially a J_{SC} divided by 2.6 has been measured in PSBTBT:$PC_{71}BM$ NPs compared to the same blend in BHJ, while it is divided by only 1.6 in the P3HT:PCBM case. These studies show that the D:A ratio can be tuned in order to optimize the shell composition of NPs.

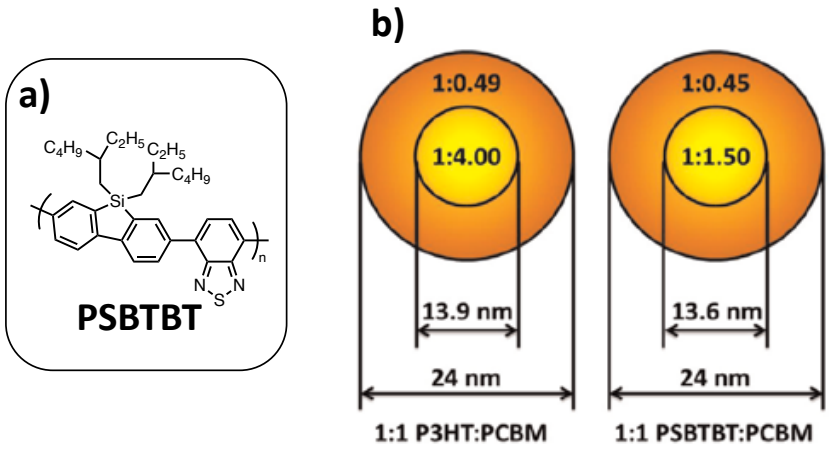

Figure 16: a) Chemical structure of PSBTBT; b) Schematic of small 1:1 P3HT:$PC_{71}BM$ and PSBTBT:$PC_{71}BM$ NPs showing core and shell diameters and the polymer:PCBM ratio in the core and shell regions. Adapted with permission from ref. [27] ***(Copyright 2015 Elsevier B.V.)***

IV.2 Vertical composition through the active layer:

Interestingly, in addition to the manipulation of the D:A ratio, usually performed to optimize the power conversion efficiency of OPV devices, the colloid approach also enables to finely tune the vertical composition of thin films, thanks to a multilayer deposition approach. It has been demonstrated for vapor deposited devices that a vertical gradient in donor concentration towards the anode and acceptor concentration towards the cathode was beneficial to limit the charge recombination while driving the charge to the corresponding electrodes [79,80]. However, the vertical morphology of a film processed from solutions is difficult to control and multilayer deposition is not possible without redissolving the previous layers. In the case of composite NPs of F8BT:PFB or P3HT:$PC_{61}BM$, multilayered films (up to five layers) have been prepared by varying the composition of donor: acceptor NPs for each layer to 1:0, 2:1, 1:1, 1.2 and 0:1, thus improving the V_{OC} in these devices[81]. This sequential deposition strategy was also used by Gärtner *et al*.[53] who prepared new device architectures, introducing variable vertical composition (**Figure 17**). Device A is a reference inverted device with ITO/ZnO used as a transparent electron-collecting electrode and PEDOT:PSS/Ag as a hole-collecting electrode. Device B includes a pristine P3HT NP layer on the top of the active layer (i.e. in contact with the hole-collecting electrode). Device C includes an additional ICBA layer below the active layer, (i.e. on top of the hole-collecting electrode). Finally, device D is built to bring a favorable gradient composition in P3HT and in ICBA in the active-layer and a P3HT NP layer on the top of the active layer. The gradient in the active layer has been introduced by synthesizing and depositing P3HT:ICBA NPs with different mixing ratios. Therefore, they sequentially applied P3HT:ICBA (1:3) NPs and P3HT:ICBA (1:1) NPs atop the ITO/ZnO cathode.

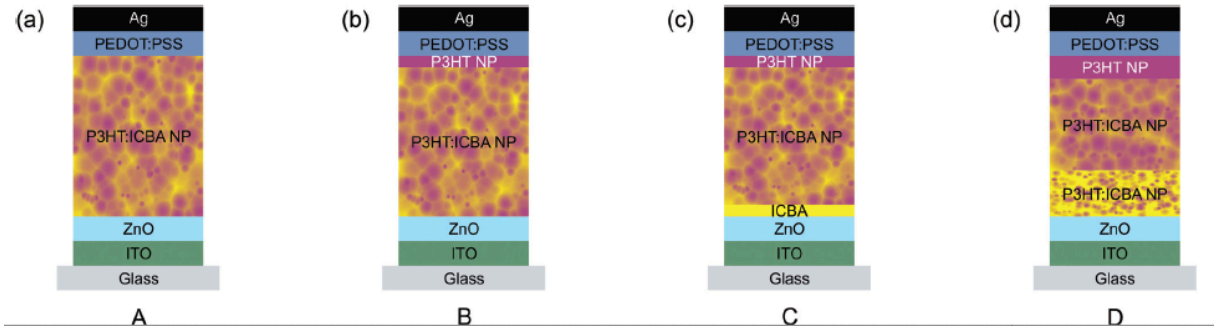

Figure 17: Device architectures: (a) Reference device comprising a ITO/ZnO bottom cathode and a PEDOT:PSS/Ag top anode as well as a nanoparticulate P3HT:ICBA absorber layer. (b) Neat P3HT nanoparticles were introduced between the absorber layer and the PEDOT:PSS layer. The nanoparticulate P3HT top layer is not closed with its thickness of 15 nm representing the average layer thickness. The thickness of the entire absorber layer was reduced to match the overall amount of P3HT in configuration A. (c) A 15 nm nanoparticulate P3HT and a 20 nm ICBA interlayer were introduced. The overall amount of P3HT and ICBA approximately matches the reference device. (d) The vertical composition of the P3HT:ICBA layer was varied by subsequent deposition of nanoparticles with different mixing ratios ((1:3), (1:1), neat P3HT). Adapted with permission from ref. [53] (Copyright 2016 The Royal Society of Chemistry).

In order to keep similar photon harvesting properties, and to compare only the impact of composition gradient on OPV device performance, they used the same amount (mass) of photo-active P3HT, neglecting ICBA absorption and thin-film interference. By combining the photovoltaic and light-intensity dependent photocurrent measurements, the authors concluded that the vertical composition gradient introduced in devices B and C provides enhanced percolation paths for photo-generated charge carriers to the respective electrodes. The increased *FF* and V_{OC} in these devices, as regards to the reference device A, combined with a *FF* that does not depend on the illumination intensity support this hypothesis (**see discussion on mechanisms in section IV.3**). The PCE reaches 4.2 % for both devices B and C, compared to a PCE of only 3.7 % in device A. Device D exhibits unfortunately a lower PCE of only 3.9 %, probably because of a thinner active layer, as confirmed by a significantly lower J_{SC}. However, no significant dependence of the *FF* versus the illumination intensity between I = 250 W.m^{-2} and I = 1000 W.m^{-2} has been observed, highlighting again the probable enhanced percolation pathways for photo-generated charge carriers.

Such a multilayer approach paves the way towards tandem device development, that already demonstrated to be a promising approach for effectively managing the absorption properties of such OPV devices [82].

IV.3 Limiting mechanisms in the particular case of OPV devices made from NP dispersions:

The most studied blend for OPV cells is based on an electron-donor polymer (P3HT) and an electron-acceptor small molecule ($PC_{61}BM$) [58]. This reference blend has been therefore widely studied for NPs solar cells, as we have seen throughout this manuscript. This blend is therefore a suitable reference for attempting to analyze the main factors limiting OPV device efficiencies made from dispersions, in comparison with devices made from the same materials in solution. Two major mechanisms can hinder the OPV cells PCE. The first one is the free charge-carrier generation that necessitates exciton dissociation and the second one is free charge extraction. For both mechanisms, the specificity of NP active layers can be questioned. Further, separate P3HT and $PC_{61}BM$ NPs that are blended to form the active layer and intimate blends of P3HT and $PC_{61}BM$ in the same NP forming the active layer (composite NPs) can intuitively have different behaviors in terms of charge generation and charge extraction.

In 2018, Al-Mudhaffer *et al.*[83] used core-shell P3HT:$PC_{61}BM$ composite (1:1) NPs, prepared by miniemulsion, as the active layer of a direct structure solar cell (ITO/PEDOT:PSS/active layer/Ca/Al) and studied in details the light-absorption and charge-extraction properties of their solar-cells. They compare their NP solar cells with conventional bulk heterojunction (BHJ) solar cells ((P3HT:$PC_{61}BM$) (1:0.8)) as a reference cell. On the one hand, a careful analysis of the optical properties of the cells led the authors to rule out plasmonic effects or light scattering by the nanoparticles as important mechanism to explain different light absorption behavior. On the other hand, the spectral response of the OPV cells together with an extraction of the different parameters to calculate the internal quantum efficiency led them to conclude that the main limiting parameter in their NP solar cells is the low exciton dissociation efficiency in that type of device, probably originating from the core-shell donor-acceptor morphologies in the active layer (**Figure 18**).

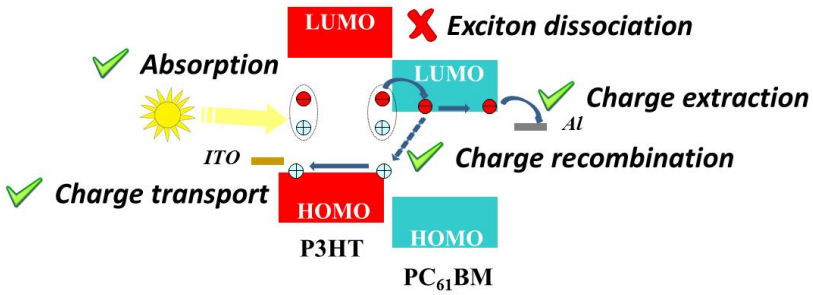

Figure 18: Schematic illustration of the different mechanism leading to power conversion in BHJ and NP P3HT:PCBM solar cells. The exciton dissociation is a marked difference between BHJ and NP devices. Adapted with permission from ref. [83] ***(Copyright 2018 Elsevier B.V.)***

This conclusion is in contradiction with other reports on different systems. For instance, Gärtner *et al.*[78] elaborated inverted solar cells (ITO/ZnO/active layer/MoO_3/Al) based on composite NPs of P3HT and ICBA made by nanoprecipitation. They carefully investigated the photovoltaic parameters and the film morphology evolution as a function of thermal annealing treatments. They obtained, after an optimal annealing step, an efficiency comparable to BHJ solar cells elaborated from solution with similar architecture devices with, in particular, a high short-circuit current density (J_{SC}) and a high open-circuit voltage (V_{OC}) but with negligible variations in the morphology of the film and on the crystallinity of the NPs during the thermal annealing. Their conclusion was that thermal annealing reduces the recombination of the free-charge carriers in NPs devices but did not impact the free-charge generation that was already efficient, even in non-annealed devices. Indeed, in the case of nanoprecipitation, composite NPs are uniform with segregated domains smaller than 10 nm. Consequently, as deposited NP films morphology already resembles the ideal BHJ morphology with nanophase separation. With the same electron-donor polymer but using a non-fullerene acceptor (NFA), namely *o*-IDTBR (**Figure 10**), Xie *et al.*[49] elaborated inverted solar-cells (ITO/ZnO/active layer/MoO_x/Ag) with a composite NPs active layer. Comparing NPs devices with BHJ devices made of the same system, they extracted explicitly the free-charge carrier generation rate that is equivalent in NPs and BHJ solar cells. It seems therefore that, using carefully elaborated NPs (and especially composite NPs) and optimized devices, the free-charge carrier generation via exciton dissociation is not the limiting factor in NPs solar cells.

Once the free-charges are generated, the charge extraction may be problematic in NPs solar-cells. Different methods can be used to anticipate or to directly measure the charge-extraction efficiency. One of them is to measure the charge-carrier mobility.

Charge transport properties are a key concern in organic semiconducting materials for electronic applications and in particular for OPV [84]. Hole and electron mobilities should be high enough to use thick active layers, but they should also be well balanced to avoid the internal electric field screening by space-charge zones. It is therefore crucial to check that charge transport occurs through a thin film obtained from NP dispersion deposition. Different devices can be used to probe the mobility either along the substrate plane or in the out-of-plane direction. For example, Organic Field Effect Transistor (OFET) devices provide mobility values in the substrate plane [85], while Time Of Flight (TOF) [86] devices or Space Charge Limited Current (SCLC) [87] diodes allow to estimate mobilities in a direction perpendicular to the electrodes (out-of-plane direction), which is the preferential direction of charge transport in multilayer OPV devices. However, one has to be careful when comparing mobility values extracted from different devices, using various architectures and elaborated in disparate conditions. For instance, OFET and TOF devices do not involve at all the

same charge carrier density, which is much higher in OFET devices nor the same active-layer thickness which is much higher in TOF experiments. Such a difference usually results in a significantly higher OFET mobility value, except in the case of a very pronounced charge-transport anisotropy with a highly favored out-of-plane mobility for structural solid-state reasons.

Bag et al.[61] estimated the hole transport mobilities in P3HT NPs films using TOF measurements. They found hole mobilities in the same order of magnitude as for P3HT pristine thin films but the TOF measurements showed very dispersive characteristics. Decreasing the surfactant concentration led to a less dispersive hole transport. A high surfactant concentration hindered the close packing of the NPs and increased the dispersive character of the hole transport in NPs films. This behavior was further observed and explained by Han *et al*.(88) who analyzed their TOF measurements in the frame of a conventional set of diffusion and drift equations. The authors showed that the presence of surfactants in NPs P3HT films increased the trap concentration as well as the trapping rate for charge carriers (in agreement with the observed dispersive hole transport). They get one step further in their analysis showing that the detrapping rate in the presence of surfactants was really high, meaning that the surfactant trap state is associated with shallow trapping energy levels and low activation energy barriers so that the trapped holes can be easily detrapped to contribute to the hole current. The hole current is therefore more dispersive in the presence of surfactants and one order of magnitude lower than for surfactant-free NPs films or drop-casted P3HT films, but the hole transport is not completely hindered in surfactant P3HT NPs films. Another important conclusion of this study was that for drop casted P3HT films or P3HT NPs where NPs contained or not a high concentration of surfactants, the energetic or positional disorder was in the same range. All the conclusions drawn here are for TOF studies in P3HT NPs films only and the situation can be very different in the active layer of solar cells.

A few publications are devoted to the comparison of charge carrier transport properties measured by TOF, into P3HT:$PC_{61}BM$ thin films made either from separate NPs or composite NPs [69,89]. Gehan *et al.* showed the existence of conductive pathways for holes through the bulk for separate as for composite NPs films but with clearly more short pathways with low resistance for separate NPs films. The TOF hole mobility was slightly lower in separate P3HT:$PC_{61}BM$ (1:1) NPs films ($8x10^{-5}$ $cm^2/(V.s)$) than in pure P3HT NPs films ($2x10^{-4}$ $cm^2/(V.s)$) with in both cases a weak dependence with the electric field. In composite NPs films, even though the hole mobility at low electric field was comparable to the P3HT NPs films one, a marked decrease of the hole mobility was observed at high electric field. Such a behavior is in agreement with an increase of the positional disorder in composite NPs films [90]. The very same conclusion was made by Han *et al*.(89). They get even one step further connecting the charge trap-sites density to the charge transport pathway lengths. In

composite NPs films, each NP contains electron-transporting and hole-transporting material leading to continuous charge transport pathways with shorter charge hopping distances. In separate NP films, longer and more tortuous pathways for charge transport are anticipated. The charge-carrier trap-sites density depends closely on the surfactant presence in the prepared NPs highlighting the importance of surfactant removing strategies to obtain good charge-transport properties in NPs films. In these two publications [69,89], a strong emphasis was put on device engineering for efficient photovoltaic devices based on NPs. In particular, the authors insisted on the influence of interfacial layers (electron transporting layers or ETL and/or hole transporting layers or HTL) to promote charge extraction. The authors highlighted the beneficial use of an ETL (a $PC_{61}BM$ layer) on top of the active layer and before the electron-collecting electrode deposition in a direct structure. This is also true for inverted structures and charge dynamics analysis on OPV cells are only valid if they are performed on optimized solar cells. A first rough estimate of the charge-carrier dynamics consists in studying the photovoltaic parameters variation as a function of light intensity. Gärtner *et al*.[78] showed that for P3HT:ICBA NPs solar cells in an inverted structure (ITO/ZnO/active layer/MoO_3/Al), the J_{SC} in thermally annealed optimized devices varied almost linearly with light-intensity. This behavior indicates the predominance of monomolecular charge-carrier recombination at high electric field (short-circuit conditions) as expected in efficient OPV systems where bimolecular recombination does not hinder charge-extraction [91]. On a very similar system, Gärtner *et al.*[53] observed a strong drop of the *FF* when the light-intensity increases showing that when the electric field decreases, the bimolecular recombination mechanism became more important. Further, Gärtner *et al.* changed the active-layer configuration to vary the percolation pathways toward the electrodes and favor the charge extraction. They indeed showed that this strategy lowered the bimolecular recombination at low electric-field and ultimately improved the power conversion efficiency. The only way to efficiently study the charge-carrier dynamics is nevertheless a combination of transient photovoltage (TPV) and charge extraction (CE) as performed by Xie et al [49]. on efficient OPV NPs blends. Optimizing the NPs elaboration as well as the device fabrication, they obtained a more than 5% efficiency with a composite NPs active layer with P3HT and *o*-IDTBR. The measured recombination order (*R*) in the optimized NPs system is higher than two (*R* = 2.89) indicating the remaining presence of charge-carrier trap sites. However, it approaches the R measured for optimized (P3HT:*o*-IDTBR) BHJ solar-cells (*R* = 2.1) showing that efficient organic photovoltaic cells that are not limited by charge transport and extraction can be processed from NPs. This conclusion is confirmed by the high PCEs measured by the same authors on different systems and described below.

Electron Donor/ Acceptor	NP synthesis technique	Good / Bad Solvent	Surfactant	AL Thermal Annealing T°C/ time (min)	Voc (mV)	Jsc (mA/cm²)	FF (%)	PCE (%)	Device architecture	Reference
PFB / F8BT	Miniemulsion	CF / water	SDS	n.d.	n.d.	n.d.	n.d.	n.d.	Standard ITO/PEDOT-PSS/AL/Ca/Al	92
PFB / F8BT	Miniemulsion	CF / water	SDS	140/2	770	1.81	28	0.39	Standard ITO/PEDOT-PSS/AL/Al	59
PFB / F8BT	Miniemulsion	CF / water	SDS	n.d.	n.d.	n.d.	n.d.	1.7	Standard ITO/AL/Ca/Al	18
P3HT / $PC_{61}BM$	Miniemulsion	CF / water	SDS	80/60 under vacuum	470	4.89	50.5	1.16	Inverted ITO/ZnO/AL/MoO_3/Ag	93
P3HT / $PC_{61}BM$	Miniemulsion	CF / 20% EtOH in water	SDS	RT under vaccum	509	6.38	66.2	2.15	Standard ITO/PEDOT-PSS/AL/Ca/Al	69
P3HT / $PC_{61}BM$	Miniemulsion	CF / water	SDS	None	360 ± 10 (380)	5.9 ± 0.5 (7.1)	52 ± 2 (54)	0.9 ± 0.1 (1.2)	Standard ITO/PEDOT:PSS/AL/ZnO/Al	30
P3HT / $PC_{61}BM$	Miniemulsion	CF / water	SDS	140/4	529 ± 4.7 (524)	4.18 ± 0.27 (4.6)	41 ± 1 (42)	0.91 ± 0.07 (1.00)	Standard ITO/PEDOT-PSS/AL/Ca/Al	25
P3HT / $PC_{61}BM$	Nanoprecipitation	CF / EtOH	-	130/4	634 ± 37	4.84 ± 0.78	36 ± 2	1.09 ± 0.16	Standard ITO/PEDOT-PSS/AL/Al	77
P3HT / $PC_{61}BM$	Miniemulsion	CF / water	SDS	150/n.d.	510 (520)	5.84 (6.38)	65.4 (67.9)	1.94 (2.15)	Standard ITO/PEDOT-PSS/AL/Al	51
P3HT / $PC_{61}BM$ + PEG-C_{60}	Miniemulsion	CF / water	PEG-C60	n.d.	540 ± 10	10.3 ± 0.03	55.3 ± 0.06	2.94 (3.08)	Inverted ITO/MoO_3/AL/LiF/Al	37
P3HT / PEG-C_{60}	Miniemulsion	CB / water	None	n.d.	540	9.11	53.4	2.62	Inverted ITO/MoO_3/AL/LiF/Al	36
TQ1 / $PC_{61}BM$ P3HT / $PC_{61}BM$	Miniemulsion	CF / water	SDS	80/-	910	0.37	28.2	0.1	Inverted Tandem PET/ZnO/AL1/V_2O_5/ZnO/ AL2/PEDOT-PSS/Ag (4 cm^2)	64
P3HT / ICBA	Miniemulsion	CF / water	SDS	150/10	763 ± 17	5.85 ± 0.20	55 ± 1	2.44 ± 0.04	Standard ITO/PEDOT-PSS/AL/Ca/Al	28
P3HT / ICBA	Nanoprecipitation	o-DCB / MeOH	-	200/10	781	9	58	4.1	Inverted ITO/ZnO/AL/MoOx/Ag	78
P3HT / ICBA	Nanoprecipitation	CF / water	-	150/10	834 ± 2	9.0 ± 0.1	55 ± 1	4.2 ± 0.1	Inverted ITO/ZnO/AL/PEDOT-PSS/Ag	53
P3HT / ICBA	Nanoprecipitation	CF / EtOH	-	150/10	797 ± 6	9.2 ± 0.2	53 ± 1	3.9 ± 0.1	Inverted PET/ITO/ZnO/AL/ PEDOT:PSS/Ag	46

P3HT / ICBA	Nanoprecipitation	*o*-DCB / EtOH	-	150/10	832 ±1	9.4 ± 0.1	55 ± 1	4.3 ± 0.1	Inverted ITO/ZnO/AL/PEDOT-PSS/Ag	60
P3HT / ICBA	Nanoprecipitation	CF / EtOH	-	160/10	810 ± 10	9.74 ± 0.27	56.5 ± 0.9	4.44 ± 0.15 (4.52)	Inverted ITO/ZnO/AL/MoOx/Ag	42
P3HT / ICxBA	Miniemulsion	CF / water	SDS	110/10	500 ± 10 (510)	3.64 ± 0.22 (3.95)	36 ± 1 (37)	0.67 (0.73)	Standard ITO/PEDOT-PSS/AL/Ca/Al	31
P3HT / ICxBA	Miniemulsion	CF / water	SDS	110/10	573 ± 17 (600)	4.18 ± 0.26 (4.73)	47 ± 1 (49)	1.14 ± 0.11 (1.39)	Standard ITO/PEDOT-PSS/AL/Ca/Al (1cm2)	54
P3HT / *o*-IDTBR	surfactant assisted nanoprecipitation	THF / water	F127	150/10	760 ± 10	10.36 ± 0.39	62.9 ± 2.0	4.95 ± 0.32 (5.23)	Inverted ITO/ZnO/AL/MoOx/Ag	49
PCDTBT / $PC_{71}BM$	Nanoprecipitation	THF / water	-	160/4	480	1.65	29	0.19	Inverted ITO/ZnO/AL/MoO_3/Ag	43
PSBTBT / $PC_{61}BM$	Miniemulsion	CF / water	SDS	80/-	470	3.99	29.3	0.55	Inverted PET/ITO/ZnO/AL/PEDOT:PSS/Ag-(printed) (4 cm2)	63
PSBTBT / $PC_{61}BM$	Miniemulsion	CF / water	SDS	140/2	620	6.2	33	1.3	Inverted ITO/ZnO/AL/PEDOT-PSS/Ag	27
PDPP-TNT / $PC_{71}BM$	Miniemulsion	CF / water	SDS	130/10	760	6.09	43	1.99	Standard ITO/PEDOT-PSS/AL/Ca/Al	75
PDPP5T / $PC_{71}BM$	Miniemulsion	CF / water	SDS	140/10	540	9.43	47	2.36	Inverted ITO/PEIE/AL/MoOx/Ag	94
PCDTBT / $PC_{71}BM$	Miniemulsion	CF / water	SDS	140/n.d.	605 ± 87	3.79 ± 0.7	30.7 ± 3	0.7 ± 0.24	Inverted ITO/ZnO/AL/MoO_3/Ag	14
PTNT / $PC_{71}BM$	Miniemulsion	o-Xylene / water	SDS	140/4	870 ± 20 (890)	4.58 ± 0.13 (4.73)	39 ± 1 (39)	1.56 ± 0.06 (1.65)	Inverted ITO/ZnO/AL/MoO_3/Ag	16
TQ1 / $PC_{71}BM$	Miniemulsion	CF / water	SDS	140/5	691 ± 39 (696)	8.26 ± 0.92 (10.06)	37.7 ± 2 (36)	2.11 ± 0.21 (2.54)	Standard ITO/PEDOT-PSS/AL/Ca/Al	74
P(TBT-DPP) / ICBA	Miniemulsion	CF / 20% EtOH in water	SDS	150/10	430 ± 10 (440)	10.49 ± 2.65 (12.73)	47 ± 5 (47)	2.16 ± 0.5 (2.63)	Standard PEN/PEDOT-PSS/AL/C60/Al	95
PDPP5T / $PC_{71}BM$	Miniemulsion	CF / water	SDS	150/10	540	11.59	49	3.07 (3.38)	Inverted ITO/ZnO/AL/MoOx/Ag	96
PBDTTPD / $PC_{71}BM$	Miniemulsion	CB / water	SDS	180/20	764 ± 136 (860)	10.45 ± 0.64 (9.99)	40 ± 6 (44)	3.2 ± 0.8 (3.8)	Inverted ITO/ZnO/AL/MoOx/Ag	15
PBDTT-FTTE / $PC_{61}BM$ + PEG-C_{60}	Miniemulsion	CF / water	PEG-C60	n.d.	720 ± 10	13.6 ± 0.06	55.1 ± 0.09	5.29 (5.39)	Inverted ITO/MoO_3/AL/LiF/Al	37

PCE10 / *o*-IDTBR	surfactant assisted nanoprecipitation	THF / water	F127	150/10	970 ± 30	12.01 ± 0.43	42.4 ± 2.0	4.94 ± 0.25 (5.19)	Inverted ITO/ZnO/AL/MoOx/Ag	[49]
PBQ-QF / *o*-IDTBR	surfactant assisted nanoprecipitation	THF / water	F127	150/10	950 ± 30	13.09 ± 0.41	47.9 ± 4.3	5.96 ± 0.58 (6.52)	Inverted ITO/ZnO/AL/MoOx/Ag	[49]
PBQ-QF / ITIC	surfactant assisted nanoprecipitation	THF / water	F127	150/10	850 ± 20	14.87 ± 0.30	52.7 ± 2.9	6.97 ± 0.53 (7.50)	Inverted ITO/ZnO/AL/MoOx/Ag	[49]

Table 2: OPV results for the different NP-based systems published in the literature (in brackets, the best values when available)

IV.4 Device optimization through chemical selection:

The recent progress observed in BHJ OPV is mainly due to the development of device architectures (interlayers, electrodes, coating process...) and photoactive materials. As seen in previous sections, due to their commercial availability and moderate costs, P3HT and $PC_{61}BM$ continue to be considered as reference systems for in-depth physico-chemical and physical studies on the structural and electrical properties of OPV active layers [58,97]. However, their intrinsic optical and electronic properties limit the performance of OPV solar cells. One easy and known strategy to achieve higher efficiencies is to replace $PC_{61}BM$ with a fullerene bisadduct called ICBA. ICBA derivative has indeed, a LUMO level about 0.1-0.2 eV higher than PCBM, which improves V_{oc}, and is also more soluble in organic solvents [98]. Using this P3HT:ICBA binary system, Ulum *et al*.[28] early described the elaboration of core-shell NPs with an ICBA-rich core and a P3HT-rich shell. Interestingly, as seen previously, ICBA being more miscible in P3HT than $PC_{61}BM$, at all weight fractions they showed that a standard thermal annealing step led to a more blended morphology. Indeed, upon thermal annealing, the core-shell structure is lost, the particles merge together and the ICBA migrates from core to shell (**Figure 19**). Further STXM observations support this scenario. This blended morphology provides enhanced charge carrier pathways and results in improved *FF* after thermal annealing (around 55% against 35% for unannealed thin films). They thus recorded a best PCE of approximately 2.5 % with an expected improved V_{oc} of almost 800 mV. Later, using the same blend and optimizing both the device structure and active layer deposition process, a few teams reported PCEs more in adequacy with the references obtained in BHJ, in the range of 4 to 4.5% [42,53,78] It could be noticed that in 2016, Sankaran *et al*.[60] reported a 1.1 cm^2 active area solar cells deposited by doctor blade from the P3HT:ICBA binary system with a PCE of 3.4%, thereby showing the benefits of this approach in terms of process (**see Table 2**).

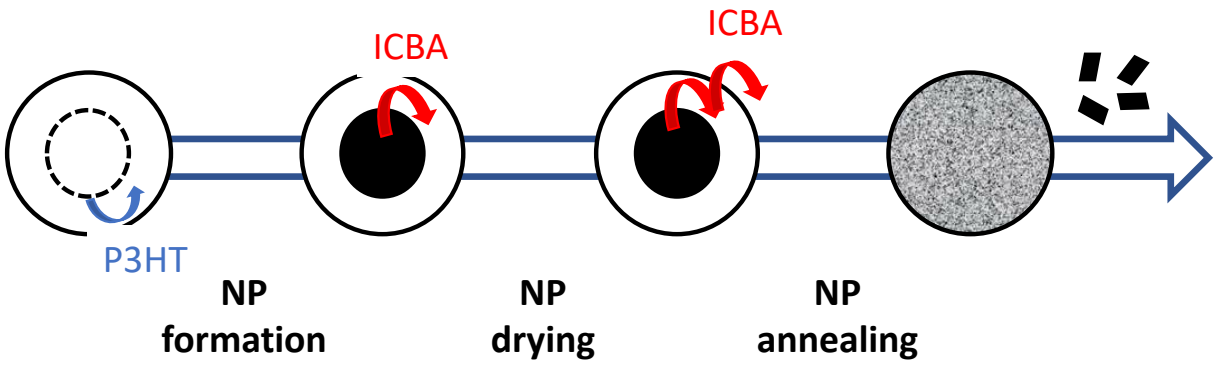

Figure 19: Schematic model of NP evolution during elaboration and thermal treatment. During NP formation, P3HT tends to migrate toward the shell due to its lower surface energy. A core-shell NP is obtained with a core containing 41% of ICBA and a shell containing only 23% of ICBA. After drying of the NPs (110 °C for 4 min), the ICBA shell composition increases to 34%, while the core composition remains the same. Finally, during thermal annealing at 150°C for 15 min, ICBA continues to migrate toward the surface of the particle resulting in homogeneous NPs with an average ICBA composition of 32%. Part of the ICBA is also lost from the NP during annealing and small crystallites can be observed outside the NP. Reprinted with permission from ref.[28]

Although progress has been made through the use of this ICBA fullerene derivative, PCEs remain far from the standards nowadays measured in conventional BHJs. Indeed, the OPV field experienced a very recent and rapid development of photoactive materials with properties increasingly more appropriate for photon harvesting and charge carrier transport, such as low bandgap (LBG) polymers [5,99] and non-fullerene acceptors (NFA) [100]. However, these materials, particularly the LBG polymers, generally have a much lower solubility than the reference P3HT [6,101]. Obviously, this makes their dissolution tricky in low-boiling organic solvents. Consequently, the NPs synthesis and stable dispersion elaboration are challenging. This probably explains why very few reports have been done on LBG polymers NPs.

However, although exhibiting very low PCEs, it could be noticed that very early on, many groups studied others conjugated polymers, such as the PFB fluorene derivative previously discussed [18,59,92].

Another extensively studied building-block for OPV application is the diketopyrrolopyrrole (DPP). It exhibits indeed extraordinary charge absorption and transport properties associated with good solubility due to the presence of two alkyl side chains.[102] In this regard, it appears to be a scaffold of choice for preparing NP dispersions. Therefore, several studies have used DPP in combination with different comonomers to prepare NP based OPV devices (see PDPP5T and PDPP-TNT structures in **Figure 20** and **Figure 14**, respectively)[75,94]. However, the best PCE reported recently par Xie *et al.*[96] is limited to 3.5%. Although promising, this work also highlights a limitation

commonly encountered in NP-based devices, the non-geminate recombination due to lower charge carrier mobilities and higher densities of traps (**see section IV.3 on limiting mechanisms**).

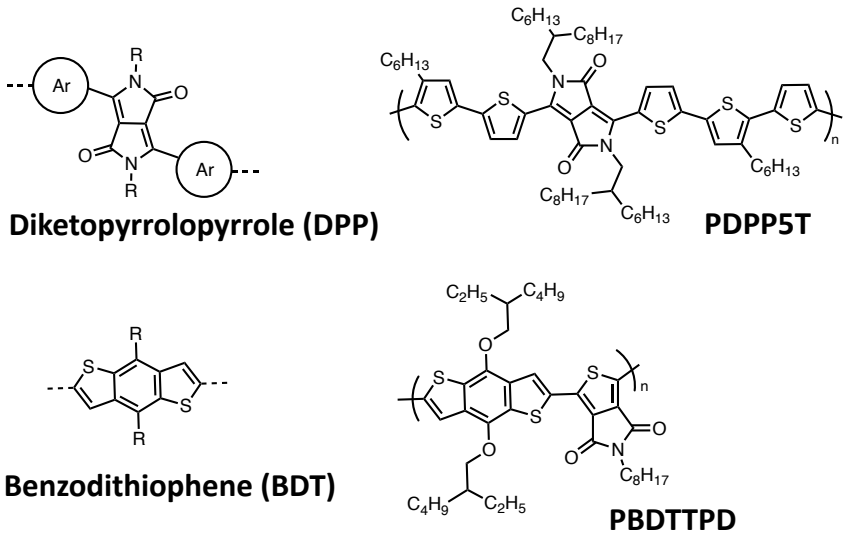

Figure 20: Chemical structures of diketyrrolopyrrole (DPP) and PDPP5T, and of Benzodithiophene (BDT) and PBDTTPD.

Recently, D'Olieslaeger *et al*.[15] used another well-known building-block in OPV, the benzodithiophene (BDT).[103] They described the fabrication of organic solar cells from mixed NPs elaborated by miniemulsion, using a mixture of PBDTTPD, a moderate band-gap BDT-based polymer (**Figure 20**) and $PC_{71}BM$, that reached best PCEs of 3.8% after a thermal annealing step. As already demonstrated on the reference P3HT:$PC_{61}BM$ system, this thermal annealing step, whose characteristics (time, temperature) must be adapted to each binary blend, has the effect of melting particles into a continuous interconnected film with enhanced continuous pathways for holes and electrons.

As seen in all the previously discussed examples, the NP-based BHJ approach is highly appealing but still suffers from a number of limitations: i) in the miniemulsion case, the presence of surfactant and the predominantly core-shell nature of the synthesized NPs limit the charge carrier transport and extraction; ii) in the nanoprecipitation case, the control of the NP size is difficult, and the resulting dispersions lack stability.

In this context, Xie *et al*.[49] recently reported a very promising and innovative NP synthesis approach called surfactant assisted nanoprecipitation technique as described in **section II.2**. This concept based on a non-ionic surfactant Pluronic F127 with temperature sensitive critical micellar concentration (cmc) was demonstrated to stabilize NPs. After preparation, surfactant stripping from the NPs was facilitated by its increased solubility at low temperature. This highly versatile approach enables the synthesis of high purity light-harvesting NPs by minimizing the amount of

residual surfactant in aqueous system. Consequently, in NP films with low surfactant amounts, electron donor polymers are able to reorganize and exhibit higher crystallinities and charge-carrier mobilities. In addition, the versatility of this approach is highlighted by the authors who successfully obtained several composite polymer:NFA NPs. Thus, a champion PCE of 5.23% with a high *FF* of 65% was achieved for P3HT:*o*-IDTBR NPs solar cells, being comparable to the devices processed from the halogenated solvents. Moreover, NPs-based devices using the low-bandgap polymer PBQ-QF (**Figure 10**), further boosted the record PCE of water/alcohol-processed OPV up to 7.5%. However, it is important to notice that this approach requires the use of organic semiconductor materials that are soluble in THF, which is not the case for most of them. Nevertheless, by overcoming the charge transport and recombination limits usually experienced in NP-based devices with traditional ionic surfactant, this approach paves the way towards a more systematic use of water-based dispersion in the OPV field.

V. Conclusion:

In this article, we reviewed the NP dispersion strategy to elaborate the photoactive layer of bulk heterojunction (BHJ) organic solar cells. The main aim of using NPs in that case is to avoid the use of toxic solvents while still controlling the morphology at a nanometer scale.

Miniemulsion and nanoprecipitation are the main strategies to produce single or composite organic semiconducting NPs (containing both the electron-donor and the electron-acceptor material). It has been shown that the internal morphology of the NPs depends greatly on the used technique. While the miniemulsion technique seems more versatile and produces stable NP dispersions, it leads more frequently to composite core-shell NPs. Moreover, removal of the surfactant is necessary to improve the active layer homogeneity and the OPV efficiency. In the case of the nanoprecipitation, the two semi-conducting materials are better mixed with smaller domains inside the NP, their morphology being closer to the one of the active layers obtained by solvent casting. However, the NP are less stable due to the absence of surfactant. To solve this problem, surfactant assisted nanoprecipitation was recently developed and appeared as a very promising route leading to records PCE of 7.3%[(49)]. Further, the morphology of the active layer obtained by the assembly of the synthesized NPs has also been discussed thoroughly as well as its influence onto the charge-carrier dynamics. Specifically, the exciton dissociation efficiency as well as the charge-carrier transport and collection properties have been described in light of the specific photoactive-layer morphologies obtained from NPs inks. Finally, the different photovoltaic parameters including the Power Conversion Efficiency (PCE) of NP devices have been analyzed.

Research on OPV device elaboration from NP dispersions has made significant progress in the last decade and PCE values reached by this approach are nowadays compatible with industrial criteria. Moreover, using NPs for the elaboration of the active layer of BHJ solar cells appeared to be an efficient way to finely tune the active-layer morphology. Further, it opens the way to interesting concepts like controlled vertical composition gradients in BJH solar cells that may lead to real breakthroughs in terms of efficiency. However, a lot of effort is still needed to get closer to the performance standards of solution processed organic solar cells. In particular, we believe that customized materials can be developed in order to better adapt the physico-chemical properties of organic semiconductor to the constraints of NP elaboration. In particular, the use of polar side chains would help to make such semiconducting materials more soluble and simultaneously organic semiconductor-based nanoparticles more stable in alcohol or water. Interestingly, driven by other applications like thermoelectricity, water photocatalysis, electrochemical energy storage or

bioelectronics[104], such conjugated materials are currently undergoing significant development [105–107].

We are therefore convinced that the NP approach is a major step not only toward the industrialization of organic photovoltaics, but also towards the use of these semiconducting polymer materials in many other applications, as illustrated recently by Kosco *et al*.[108] in photocatalytic hydrogen production.

VI. Thesis Project:

This bibliographic survey demonstrates that the use of organic semiconductor-based NP inks is a promising approach to elaborate efficient and greener OPV devices. Indeed, this technology is generally dominated by the use of toxic and environmentally harmful solvents such as chlorinated solvents. In addition, the NP approach is not necessarily accompanied by a systematic fall in performance in devices, since it allows, for example, to finely control the active layer morphology by adjusting the NPs diameter and their compositions (core shell, Janus, …).

The research work described in this thesis manuscript is part of this field. It consists in preparing colloidal inks made of organic semiconductor-based NPs that will be used as active layer for OPV devices. This thesis combines several competences present on the Cronenbourg campus, namely colloid science, organic semiconducting material synthesis and their characterization in solar cells.

Most of the studies carried out during this thesis were based on an electron donor polymer developed in the laboratory and very efficient in solar cells, PF2 [109].

Two NPs elaboration techniques will be investigated in this work, namely the miniemulsion approach (**chapter III**) and the nanoprecipitation approach (**chapter V).**

The core-shell structure of NPs obtained by miniemulsion has been deeply studied by a combination of characterization tools including UV-Visible and photoluminescence spectroscopies, TEM and STXM microscopy analyses (**chapter III**). This advanced NPs have been further used to elaborate OPV devices and space charge limited current (SCLC) devices, which provides information on perpendicular charger carrier mobilities (**chapter IV**). In addition, thin-films were characterized by AFM and GIWAXS.

Finally, in the first part of **chapter V** on nanoprecipitation, the reader will find a section dedicated to the synthesis of electron donor polymers modified to exhibit improved solubility in organic solvents and improve the stabilization the NPs dispersion in water.

VII. References:

1. V. Muteri, M. Cellura, D. Curto, V. Franzitta, S. Longo, M. Mistretta and M. L. Parisi, Review on life cycle assessment of solar photovoltaic panels, *Energies*, 2020, **13**, 252.
2. Q. Liu, Y. Jiang, K. Jin, J. Qin, J. Xu, W. Li, J. Xiong, J. Liu, Z. Xiao, K. Sun, S. Yang, X. Zhang and L. Ding, 18% Efficiency organic solar cells, *Science Bulletin*, 2020, **65**, 272–275.
3. C. L. Chochos, M. Spanos, A. Katsouras, E. Tatsi, S. Drakopoulou, V. G. Gregoriou and A. Avgeropoulos, Current status, challenges and future outlook of high-performance polymer semiconductors for organic photovoltaics modules, *Progress in Polymer Science*, 2019, **91**, 51–79.
4. R. Po, G. Bianchi, C. Carbonera and A. Pellegrino, "All That Glisters Is Not Gold": An Analysis of the Synthetic Complexity of Efficient Polymer Donors for Polymer Solar Cells, *Macromolecules*, 2015, **48**, 453–461.
5. N. Leclerc, P. Chávez, O. A. Ibraikulov, T. Heiser and P. Lévêque, Impact of Backbone Fluorination on π-Conjugated Polymers in Organic Photovoltaic Devices: A Review, *Polymers*, 2016, **8**, 11.
6. Y. Liu, J. Zhao, Z. Li, C. Mu, W. Ma, H. Hu, K. Jiang, H. Lin, H. Ade and H. Yan, Aggregation and morphology control enables multiple cases of high-efficiency polymer solar cells, *Nature Communications*, 2014, **5**, 5293.
7. S. Zhang, L. Ye, H. Zhang and J. Hou, Green-solvent-processable organic solar cells, *Materials Today*, 2016, **19**, 533–543.
8. C. Duan, K. Zhang, C. Zhong, F. Huang and Y. Cao, Recent advances in water/alcohol-soluble π-conjugated materials: new materials and growing applications in solar cells, *Chem. Soc. Rev.*, 2013, **42**, 9071–9104.
9. Z. Ma, B. Zhao, Y. Gong, J. Deng and Z. Tan, Green-solvent-processable strategies for achieving large-scale manufacture of organic photovoltaics, *J. Mater. Chem. A*, 2019, **7**, 22826–22847.
10. S. Subianto, N. Dutta, M. Andersson and N. R. Choudhury, Bulk heterojunction organic photovoltaics from water-processable nanomaterials and their facile fabrication approaches, *Advances in Colloid and Interface Science*, 2016, **235**, 56–69.
11. J. Pecher and S. Mecking, Nanoparticles of Conjugated Polymers, *Chemical Reviews*, 2010, **110**, 6260–6279.
12. Z. Tian, J. Yu, C. Wu, C. Szymanski and J. McNeill, Amplified energy transfer in conjugated polymer nanoparticle tags and sensors, *Nanoscale*, 2010, **2**, 1999.

13. K. Landfester, R. Montenegro, U. Scherf, R. Güntner, U. Asawapirom, S. Patil, D. Neher and T. Kietzke, Semiconducting Polymer Nanospheres in Aqueous Dispersion Prepared by a Miniemulsion Process, *Advanced Materials*, 2002, **14**, 651–655.
14. L. Parrenin, G. Laurans, E. Pavlopoulou, G. Fleury, G. Pecastaings, C. Brochon, L. Vignau, G. Hadziioannou and E. Cloutet, Photoactive Donor–Acceptor Composite Nanoparticles Dispersed in Water, *Langmuir*, 2017, **33**, 1507–1515.
15. L. D'Olieslaeger, M. Pfannmöller, E. Fron, I. Cardinaletti, M. Van Der Auweraer, G. Van Tendeloo, S. Bals, W. Maes, D. Vanderzande, J. Manca and A. Ethirajan, Tuning of PCDTBT:PC71BM blend nanoparticles for eco-friendly processing of polymer solar cells, *Solar Energy Materials and Solar Cells*, 2017, **159**, 179–188.
16. X. Pan, A. Sharma, D. Gedefaw, R. Kroon, A. Diaz de Zerio, N. P. Holmes, A. L. D. Kilcoyne, M. G. Barr, A. Fahy, M. Marks, X. Zhou, W. Belcher, P. C. Dastoor and M. R. Andersson, Environmentally friendly preparation of nanoparticles for organic photovoltaics, *Organic Electronics*, 2018, **59**, 432–440.
17. O. Ghazy, Preparation and Characterization of P3H:PCBM Blend Nanoparticles and Their Plasmonic Modification, *Macromol. Symp.*, 2015, **352**, 25–32.
18. T. Kietzke, D. Neher, K. Landfester, R. Montenegro, R. Güntner and U. Scherf, Novel approaches to polymer blends based on polymer nanoparticles, *Nat Mater*, 2003, **2**, 408–412.
19. N. P. Holmes, K. B. Burke, P. Sista, M. Barr, H. D. Magurudeniya, M. C. Stefan, A. L. D. Kilcoyne, X. Zhou, P. C. Dastoor and W. J. Belcher, Nano-domain behaviour in P3HT:PCBM nanoparticles, relating material properties to morphological changes, *Solar Energy Materials and Solar Cells*, 2013, **117**, 437–445.
20. T. Kietzke, D. Neher, M. Kumke, O. Ghazy, U. Ziener and K. Landfester, Phase Separation of Binary Blends in Polymer Nanoparticles, *Small*, 2007, **3**, 1041–1048.
21. J. J. Richards, C. L. Whittle, G. Shao and L. D. Pozzo, Correlating Structure and Photocurrent for Composite Semiconducting Nanoparticles with Contrast Variation Small-Angle Neutron Scattering and Photoconductive Atomic Force Microscopy, *ACS Nano*, 2014, **8**, 4313–4324.
22. K. B. Burke, A. J. Stapleton, B. Vaughan, X. Zhou, A. L. D. Kilcoyne, W. J. Belcher and P. C. Dastoor, Scanning transmission x-ray microscopy of polymer nanoparticles: probing morphology on sub-10 nm length scales, *Nanotechnology*, 2011, **22**, 265710.
23. C. M. Björström, A. Bernasik, J. Rysz, A. Budkowski, S. Nilsson, M. Svensson, M. R. Andersson, K. O. Magnusson and E. Moons, Multilayer formation in spin-coated thin films of low-bandgap polyfluorene:PCBM blends, *J. Phys.: Condens. Matter*, 2005, **17**, L529–L534.

24. X. Wang, T. Ederth and O. Inganäs, In Situ Wilhelmy Balance Surface Energy Determination of Poly(3-hexylthiophene) and Poly(3,4-ethylenedioxythiophene) during Electrochemical Doping−Dedoping, *Langmuir*, 2006, **22**, 9287–9294.
25. N. P. Holmes, N. Nicolaidis, K. Feron, M. Barr, K. B. Burke, M. Al-Mudhaffer, P. Sista, A. L. D. Kilcoyne, M. C. Stefan, X. Zhou, P. C. Dastoor and W. J. Belcher, Probing the origin of photocurrent in nanoparticulate organic photovoltaics, *Solar Energy Materials and Solar Cells*, 2015, **140**, 412–421.
26. K. Vakhshouri, D. R. Kozub, C. Wang, A. Salleo and E. D. Gomez, Effect of Miscibility and Percolation on Electron Transport in Amorphous Poly(3-Hexylthiophene)/Phenyl-C_{61}-Butyric Acid Methyl Ester Blends, *Phys. Rev. Lett.*, 2012, **108**, 026601.
27. H. F. Dam, N. P. Holmes, T. R. Andersen, T. T. Larsen-Olsen, M. Barr, A. L. D. Kilcoyne, X. Zhou, P. C. Dastoor, F. C. Krebs and W. J. Belcher, The effect of mesomorphology upon the performance of nanoparticulate organic photovoltaic devices, *Solar Energy Materials and Solar Cells*, 2015, **138**, 102–108.
28. S. Ulum, N. Holmes, M. Barr, A. L. D. Kilcoyne, B. B. Gong, X. Zhou, W. Belcher and P. Dastoor, The role of miscibility in polymer:fullerene nanoparticulate organic photovoltaic devices, *Nano Energy*, 2013, **2**, 897–905.
29. G. Nagarjuna, M. Baghgar, J. A. Labastide, D. D. Algaier, M. D. Barnes and D. Venkataraman, Tuning Aggregation of Poly(3-hexylthiophene) within Nanoparticles, *ACS Nano*, 2012, **6**, 10750–10758.
30. M. Marks, N. P. Holmes, A. Sharma, X. Pan, R. Chowdhury, M. G. Barr, C. Fenn, M. J. Griffith, K. Feron, A. L. D. Kilcoyne, D. A. Lewis, M. R. Andersson, W. J. Belcher and P. C. Dastoor, Building intermixed donor–acceptor architectures for water-processable organic photovoltaics, *Phys. Chem. Chem. Phys.*, 2019, **21**, 5705–5715.
31. F. Almyahi, T. R. Andersen, N. A. Cooling, N. P. Holmes, M. J. Griffith, K. Feron, X. Zhou, W. J. Belcher and P. C. Dastoor, Optimisation of purification techniques for the preparation of large-volume aqueous solar nanoparticle inks for organic photovoltaics, *Beilstein J. Nanotechnol.*, 2018, **9**, 649–659.
32. J. Cho, S. Yoon, K. M. Sim, Y. J. Jeong, C. E. Park, S.-K. Kwon, Y.-H. Kim and D. S. Chung, Universal selection rule for surfactants used in miniemulsion processes for eco-friendly and high performance polymer semiconductors, *Energy Environ. Sci.*, 2017, **10**, 2324–2333.
33. J. Cho, K. H. Cheon, H. Ahn, K. H. Park, S.-K. Kwon, Y.-H. Kim and D. S. Chung, High Charge-Carrier Mobility of 2.5 cm2 V−1 s−1 from a Water-Borne Colloid of a Polymeric Semiconductor via Smart Surfactant Engineering, *Advanced Materials*, 2015, **27**, 5587–5592.

34. B. Tan, Y. Li, M. F. Palacios, J. Therrien and M. J. Sobkowicz, Effect of surfactant conjugation on structure and properties of poly(3-hexylthiophene) colloids and field effect transistors, *Colloids and Surfaces A: Physicochemical and Engineering Aspects*, 2016, **488**, 7–14.
35. F. D. Fleischli, N. Ghasdian, T. K. Georgiou and N. Stingelin, Tailoring the optical properties of poly(3-hexylthiophene) by emulsion processing using polymeric macrosurfactants, *J. Mater. Chem. C*, 2015, **3**, 2065–2071.
36. Y. J. Kim and B. Lee, Unique p–n Heterostructured Water-Borne Nanoparticles Exhibiting Impressive Charge-Separation Ability, *ChemSusChem*, 2018, **11**, 1628–1638.
37. Y. J. Kim, R. D. Schaller and H. C. Fry, Control of Shell Morphology in p–n Heterostructured Water-Processable Semiconductor Colloids: Toward Extremely Efficient Charge Separation, *Small*, 2019, **15**, 1803563.
38. S. Subianto, R. Balu, L. de Campo, A. Sokolova, N. K. Dutta and N. R. Choudhury, Sulfonated Thiophene Derivative Stabilized Aqueous Poly(3-hexylthiophene):Phenyl-C61-butyric Acid Methyl Ester Nanoparticle Dispersion for Organic Solar Cell Applications, *ACS Appl. Mater. Interfaces*, 2018, **10**, 44116–44125.
39. D. Horn and J. Rieger, Organic nanoparticles in the aqueous phase—theory, experiment, and use, *Angewandte Chemie International Edition*, 2001, **40**, 4330–4361.
40. F. Wang, M.-Y. Han, K. Y. Mya, Y. Wang and Y.-H. Lai, Aggregation-Driven Growth of Size-Tunable Organic Nanoparticles Using Electronically Altered Conjugated Polymers, *J. Am. Chem. Soc.*, 2005, **127**, 10350–10355.
41. J. E. Millstone, D. F. J. Kavulak, C. H. Woo, T. W. Holcombe, E. J. Westling, A. L. Briseno, M. F. Toney and J. M. J. Fréchet, Synthesis, Properties, and Electronic Applications of Size-Controlled Poly(3-hexylthiophene) Nanoparticles, *Langmuir*, 2010, **26**, 13056–13061.
42. C. Xie, X. Tang, M. Berlinghof, S. Langner, S. Chen, A. Späth, N. Li, R. H. Fink, T. Unruh and C. J. Brabec, Robot-Based High-Throughput Engineering of Alcoholic Polymer: Fullerene Nanoparticle Inks for an Eco-Friendly Processing of Organic Solar Cells, *ACS Appl. Mater. Interfaces*, 2018, **10**, 23225–23234.
43. G. Prunet, L. Parrenin, E. Pavlopoulou, G. Pecastaings, C. Brochon, G. Hadziioannou and E. Cloutet, Aqueous PCDTBT:PC(71)BM Photovoltaic Inks Made by Nanoprecipitation, *Macromolecular Rapid Communications*, 2017, 1700504.
44. S. N. Clafton, D. M. Huang, W. R. Massey and T. W. Kee, Femtosecond Dynamics of Excitons and Hole-Polarons in Composite P3HT/PCBM Nanoparticles, *J. Phys. Chem. B*, 2013, **117**, 4626–4633.

45. K. N. Schwarz, S. B. Farley, T. A. Smith and K. P. Ghiggino, Charge generation and morphology in P3HT:PCBM nanoparticles prepared by mini-emulsion and reprecipitation methods, *Nanoscale*, 2015, **7**, 19899–19904.
46. S. Gärtner, A. J. Clulow, I. A. Howard, E. P. Gilbert, P. L. Burn, I. R. Gentle and A. Colsmann, Relating Structure to Efficiency in Surfactant-Free Polymer/Fullerene Nanoparticle-Based Organic Solar Cells, *ACS Appl. Mater. Interfaces*, 2017, **9**, 42986–42995.
47. S. Chambon, C. Schatz, V. Sébire, B. Pavageau, G. Wantz and L. Hirsch, Organic semiconductor core–shell nanoparticles designed through successive solvent displacements, *Materials Horizons*, 2014, **1**, 431–438.
48. A. Palacio Valera, C. Schatz, E. Ibarboure, T. Kubo, H. Segawa and S. Chambon, Elaboration of PCBM Coated P3HT Nanoparticles: Understanding the Shell Formation, *Front. Energy Res.*, 2019, **6**, 146.
49. C. Xie, T. Heumüller, W. Gruber, X. Tang, A. Classen, I. Schuldes, M. Bidwell, A. Späth, R. H. Fink, T. Unruh, I. McCulloch, N. Li and C. J. Brabec, Overcoming efficiency and stability limits in water-processing nanoparticular organic photovoltaics by minimizing microstructure defects, *Nature Communications*, 2018, **9**, 5335.
50. S. Holliday, R. S. Ashraf, A. Wadsworth, D. Baran, S. A. Yousaf, C. B. Nielsen, C.-H. Tan, S. D. Dimitrov, Z. Shang, N. Gasparini, M. Alamoudi, F. Laquai, C. J. Brabec, A. Salleo, J. R. Durrant and I. McCulloch, High-efficiency and air-stable P3HT-based polymer solar cells with a new non-fullerene acceptor, *Nat Commun*, 2016, **7**, 11585.
51. M. Bag, T. S. Gehan, L. A. Renna, D. D. Algaier, P. M. Lahti and D. Venkataraman, Fabrication conditions for efficient organic photovoltaic cells from aqueous dispersions of nanoparticles, *RSC Adv.*, 2014, **4**, 45325–45331.
52. Y. He, H.-Y. Chen, J. Hou and Y. Li, Indene−C60 Bisadduct: A New Acceptor for High-Performance Polymer Solar Cells, *J. Am. Chem. Soc.*, 2010, **132**, 1377–1382.
53. S. Gärtner, S. Reich, M. Bruns, J. Czolk and A. Colsmann, Organic solar cells with graded absorber layers processed from nanoparticle dispersions, *Nanoscale*, 2016, **8**, 6721–6727.
54. F. Almyahi, T. R. Andersen, A. Fahy, M. Dickinson, K. Feron, W. J. Belcher and P. C. Dastoor, The role of surface energy control in organic photovoltaics based on solar paints, *J. Mater. Chem. A*, 2019, **7**, 9202–9214.
55. J. A. Bartelt, J. D. Douglas, W. R. Mateker, A. E. Labban, C. J. Tassone, M. F. Toney, J. M. J. Fréchet, P. M. Beaujuge and M. D. McGehee, Controlling Solution-Phase Polymer Aggregation with Molecular Weight and Solvent Additives to Optimize Polymer-Fullerene Bulk Heterojunction Solar Cells, *Advanced Energy Materials*, 2014, **4**, 1301733.

56. S. F. Hoefler, T. Rath, N. Pastukhova, E. Pavlica, D. Scheunemann, S. Wilken, B. Kunert, R. Resel, M. Hobisch, S. Xiao, G. Bratina and G. Trimmel, The effect of polymer molecular weight on the performance of PTB7-Th:O-IDTBR non-fullerene organic solar cells, *J. Mater. Chem. A*, 2018, **6**, 9506–9516.
57. Z. Zheng, O. M. Awartani, B. Gautam, D. Liu, Y. Qin, W. Li, A. Bataller, K. Gundogdu, H. Ade and J. Hou, Efficient Charge Transfer and Fine-Tuned Energy Level Alignment in a THF-Processed Fullerene-Free Organic Solar Cell with 11.3% Efficiency, *Advanced Materials*, 2017, **29**, 1604241.
58. M. T. Dang, L. Hirsch and G. Wantz, P3HT:PCBM, Best Seller in Polymer Photovoltaic Research, *Advanced Materials*, 2011, **23**, 3597–3602.
59. A. Stapleton, B. Vaughan, B. Xue, E. Sesa, K. Burke, X. Zhou, G. Bryant, O. Werzer, A. Nelson, A. L. David Kilcoyne, L. Thomsen, E. Wanless, W. Belcher and P. Dastoor, A multilayered approach to polyfluorene water-based organic photovoltaics, *Solar Energy Materials and Solar Cells*, 2012, **102**, 114–124.
60. S. Sankaran, K. Glaser, S. Gärtner, T. Rödlmeier, K. Sudau, G. Hernandez-Sosa and A. Colsmann, Fabrication of polymer solar cells from organic nanoparticle dispersions by doctor blading or ink-jet printing, *Organic Electronics*, 2016, **28**, 118–122.
61. M. Bag, T. S. Gehan, D. D. Algaier, F. Liu, G. Nagarjuna, P. M. Lahti, T. P. Russell and D. Venkataraman, Efficient Charge Transport in Assemblies of Surfactant-Stabilized Semiconducting Nanoparticles, *Advanced Materials*, 2013, **25**, 6411–6415.
62. S. K. Karunakaran, G. M. Arumugam, W. Yang, S. Ge, S. N. Khan, X. Lin and G. Yang, Recent progress in inkjet-printed solar cells, *J. Mater. Chem. A*, 2019, **7**, 13873–13902.
63. T. R. Andersen, T. T. Larsen-Olsen, B. Andreasen, A. P. L. Böttiger, J. E. Carlé, M. Helgesen, E. Bundgaard, K. Norrman, J. W. Andreasen, M. Jørgensen and F. C. Krebs, Aqueous Processing of Low-Band-Gap Polymer Solar Cells Using Roll-to-Roll Methods, *ACS Nano*, 2011, **5**, 4188–4196.
64. T. T. Larsen-Olsen, T. R. Andersen, B. Andreasen, A. P. L. Böttiger, E. Bundgaard, K. Norrman, J. W. Andreasen, M. Jørgensen and F. C. Krebs, Roll-to-roll processed polymer tandem solar cells partially processed from water, *Solar Energy Materials and Solar Cells*, 2012, **97**, 43–49.
65. T.T. Larsen-Olsen, B. Andreasen, T.R. Andersen, A. P. L. Böttiger, E. Bundgaard, K. Norrman, J. W. Andreasen, M. Jørgensen and F. C. Krebs, Simultaneous multilayer formation of the polymer solar cell stack using roll-to-roll double slot-die coating from water. *Solar Energy Materials and Solar Cells*, 2012, **97**, 22–27.
66. F. Zhao, C. Wang and X. Zhan, Morphology Control in Organic Solar Cells, *Advanced Energy Materials*, 2018, **8**, 1703147.

67. J. A. Labastide, M. Baghgar, I. Dujovne, Y. Yang, A. D. Dinsmore, B. G. Sumpter, D. Venkataraman and M. D. Barnes, Polymer Nanoparticle Superlattices for Organic Photovoltaic Applications, *The Journal of Physical Chemistry Letters*, 2011, **2**, 3085–3091.
68. L. A. Renna, C. J. Boyle, T. S. Gehan and D. Venkataraman, Polymer Nanoparticle Assemblies: A Versatile Route to Functional Mesostructures, *Macromolecules*, 2015, **48**, 6353–6368.
69. T. S. Gehan, M. Bag, L. A. Renna, X. Shen, D. D. Algaier, P. M. Lahti, T. P. Russell and D. Venkataraman, Multiscale Active Layer Morphologies for Organic Photovoltaics Through Self-Assembly of Nanospheres, *Nano Lett.*, 2014, **14**, 5238–5243.
70. L. A. Renna, M. Bag, T. S. Gehan, X. Han, P. M. Lahti, D. Maroudas and D. Venkataraman, Tunable Percolation in Semiconducting Binary Polymer Nanoparticle Glasses, *J. Phys. Chem. B*, 2016, **120**, 2544–2556.
71. N. P. Holmes, M. Marks, J. M. Cave, K. Feron, M. G. Barr, A. Fahy, A. Sharma, X. Pan, D. A. L. Kilcoyne, X. Zhou, D. A. Lewis, M. R. Andersson, J. van Stam, A. B. Walker, E. Moons, W. J. Belcher and P. C. Dastoor, Engineering Two-Phase and Three-Phase Microstructures from Water-Based Dispersions of Nanoparticles for Eco-Friendly Polymer Solar Cell Applications, *Chem. Mater.*, 2018, **30**, 6521–6531.
72. D. Chen, F. Liu, C. Wang, A. Nakahara and T. P. Russell, Bulk Heterojunction Photovoltaic Active Layers via Bilayer Interdiffusion, *Nano Lett.*, 2011, **11**, 2071–2078.
73. N. D. Treat, M. A. Brady, G. Smith, M. F. Toney, E. J. Kramer, C. J. Hawker and M. L. Chabinyc, Interdiffusion of PCBM and P3HT Reveals Miscibility in a Photovoltaically Active Blend, *Advanced Energy Materials*, 2011, **1**, 82–89.
74. N. P. Holmes, M. Marks, P. Kumar, R. Kroon, M. G. Barr, N. Nicolaidis, K. Feron, A. Pivrikas, A. Fahy, A. D. de Z. Mendaza, A. L. D. Kilcoyne, C. Müller, X. Zhou, M. R. Andersson, P. C. Dastoor and W. J. Belcher, Nano-pathways: Bridging the divide between water-processable nanoparticulate and bulk heterojunction organic photovoltaics, *Nano Energy*, 2016, **19**, 495–510.
75. B. Vaughan, E. L. Williams, N. P. Holmes, P. Sonar, A. Dodabalapur, P. C. Dastoor and W. J. Belcher, Water-based nanoparticulate solar cells using a diketopyrrolopyrrole donor polymer, *Phys. Chem. Chem. Phys.*, 2014, **16**, 2647–2653.
76. S. Ulum, N. Holmes, D. Darwis, K. Burke, A. L. David Kilcoyne, X. Zhou, W. Belcher and P. Dastoor, Determining the structural motif of P3HT:PCBM nanoparticulate organic photovoltaic devices, *Solar Energy Materials and Solar Cells*, 2013, **110**, 43–48.

77. D. Darwis, N. Holmes, D. Elkington, A. L. David Kilcoyne, G. Bryant, X. Zhou, P. Dastoor and W. Belcher, Surfactant-free nanoparticulate organic photovoltaics, *Solar Energy Materials and Solar Cells*, 2014, **121**, 99–107.
78. S. Gärtner, M. Christmann, S. Sankaran, H. Röhm, E.-M. Prinz, F. Penth, A. Pütz, A. E. Türeli, B. Penth, B. Baumstümmler and A. Colsmann, Eco-Friendly Fabrication of 4% Efficient Organic Solar Cells from Surfactant-Free P3HT:ICBA Nanoparticle Dispersions, *Adv. Mater.*, 2014, **26**, 6653–6657.
79. S. Heutz, P. Sullivan, B. M. Sanderson, S. M. Schultes and T. S. Jones, Influence of molecular architecture and intermixing on the photovoltaic, morphological and spectroscopic properties of CuPc–C60 heterojunctions, *Solar Energy Materials and Solar Cells*, 2004, **83**, 229–245.
80. W. Tress, K. Leo and M. Riede, Effect of concentration gradients in ZnPc:C60 bulk heterojunction organic solar cells, *Solar Energy Materials and Solar Cells*, 2011, **95**, 2981–2986.
81. B. Vaughan, A. Stapleton, E. Sesa, N. P. Holmes, X. Zhou, P. C. Dastoor and W. J. Belcher, Engineering vertical morphology with nanoparticulate organic photovoltaic devices, *Organic Electronics*, 2016, **32**, 250–257.
82. L. Meng, Y. Zhang, X. Wan, C. Li, X. Zhang, Y. Wang, X. Ke, Z. Xiao, L. Ding, R. Xia, H.-L. Yip, Y. Cao and Y. Chen, Organic and solution-processed tandem solar cells with 17.3% efficiency, *Science*, 2018, **361**, 1094–1098.
83. M. F. Al-Mudhaffer, M. J. Griffith, K. Feron, N. C. Nicolaidis, N. A. Cooling, X. Zhou, J. Holdsworth, W. J. Belcher and P. C. Dastoor, The origin of performance limitations in miniemulsion nanoparticulate organic photovoltaic devices, *Solar Energy Materials and Solar Cells*, 2018, **175**, 77–88.
84. V. Coropceanu, J. Cornil, D. A. da Silva Filho, Y. Olivier, R. Silbey and J.-L. Brédas, Charge Transport in Organic Semiconductors, *Chem. Rev.*, 2007, **107**, 926–952.
85.. H. Sirringhaus, 25th Anniversary Article: Organic Field-Effect Transistors: The Path Beyond Amorphous Silicon, *Advanced Materials*, 2014, **26**, 1319–1335.
86 G. Bratina and E. Pavlica, Characterisation of charge carrier transport in thin organic semiconductor layers by time-of-flight photocurrent measurements, *Organic Electronics*, 2019, **64**, 117–130.
87. J. C. Blakesley, F. A. Castro, W. Kylberg, G. F. A. Dibb, C. Arantes, R. Valaski, M. Cremona, J. S. Kim and J.-S. Kim, Towards reliable charge-mobility benchmark measurements for organic semiconductors, *Organic Electronics*, 2014, **15**, 1263–1272.

88. X. Han, M. Bag, T. S. Gehan, D. Venkataraman and D. Maroudas, Analysis of hole transport in thin films and nanoparticle assemblies of poly(3-hexylthiophene), *Chemical Physics Letters*, 2014, **610–611**, 273–277.
89. X. Han, M. Bag, T. S. Gehan, D. Venkataraman and D. Maroudas, Analysis of Charge Transport and Device Performance in Organic Photovoltaic Devices with Active Layers of Self-Assembled Nanospheres, *J. Phys. Chem. C*, 2015, **119**, 25826–25839.
90. H. Bässler, Charge Transport in Disordered Organic Photoconductors a Monte Carlo Simulation Study, *physica status solidi (b)*, 1993, **175**, 15–56.
91. L. Liu and G. Li, Investigation of recombination loss in organic solar cells by simulating intensity-dependent current–voltage measurements, *Solar Energy Materials and Solar Cells*, 2011, **95**, 2557–2563.
92. T. Kietzke, D. Neher, M. Kumke, R. Montenegro, K. Landfester and U. Scherf, A Nanoparticle Approach To Control the Phase Separation in Polyfluorene Photovoltaic Devices, *Macromolecules*, 2004, **37**, 4882–4890.
93. E. B. L. Pedersen, M. C. Pedersen, S. B. Simonsen, R. G. Brandt, A. P. L. Böttiger, T. R. Andersen, W. Jiang, Z. Y. Xie, F. C. Krebs, L. Arleth and J. W. Andreasen, Structure and crystallinity of water dispersible photoactive nanoparticles for organic solar cells, *J. Mater. Chem. A*, 2015, **3**, 17022–17031.
94. F. J. M. Colberts, M. M. Wienk and R. A. J. Janssen, Aqueous Nanoparticle Polymer Solar Cells: Effects of Surfactant Concentration ²and Processing on Device Performance, *ACS Appl. Mater. Interfaces*, 2017, **9**, 13380–13389.
95. N. A. D. Yamamoto, M. E. Payne, M. Koehler, A. Facchetti, L. S. Roman and A. C. Arias, Charge transport model for photovoltaic devices based on printed polymer: Fullerene nanoparticles, *Solar Energy Materials and Solar Cells*, 2015, **141**, 171–177.
96. C. Xie, A. Classen, A. Späth, X. Tang, J. Min, M. Meyer, C. Zhang, N. Li, A. Osvet, R. H. Fink and C. J. Brabec, Overcoming Microstructural Limitations in Water Processed Organic Solar Cells by Engineering Customized Nanoparticulate Inks, *Advanced Energy Materials*, 2018, **8**, 1702857.
97. O. Cardozo, S. Farooq, A. Stingl and N. Fraidenraich, Investigation of performance of P3HT:PCBM organic photovoltaic module under real operating conditions, *Solar Energy*, 2019, **190**, 543–548.
98. M. Lenes, G.-J. A. H. Wetzelaer, F. B. Kooistra, S. C. Veenstra, J. C. Hummelen and P. W. M. Blom, Fullerene Bisadducts for Enhanced Open-Circuit Voltages and Efficiencies in Polymer Solar Cells, *Advanced Materials*, 2008, **20**, 2116–2119.

99. C. Liu, K. Wang, X. Gong and A. J. Heeger, Low bandgap semiconducting polymers for polymeric photovoltaics, *Chem. Soc. Rev.*, 2016, **45**, 4825–4846.

100. S. Dey, Recent Progress in Molecular Design of Fused Ring Electron Acceptors for Organic Solar Cells, *Small*, 2019, **15**, 1900134.

101. O. A. Ibraikulov, C. Ngov, P. Chávez, I. Bulut, B. Heinrich, O. Boyron, K. L. Gerasimov, D. A. Ivanov, S. Swaraj, S. Méry, N. Leclerc, P. Lévêque and T. Heiser, Face-on orientation of fluorinated polymers conveyed by long alkyl chains: a prerequisite for high photovoltaic performances, *Journal of Materials Chemistry A*, 2018, **6**, 12038–12045.

102. Q. Liu, S. E. Bottle and P. Sonar, Developments of Diketopyrrolopyrrole-Dye-Based Organic Semiconductors for a Wide Range of Applications in Electronics, *Advanced Materials*, 2020, **32**, 1903882.

103. H. Yao, L. Ye, H. Zhang, S. Li, S. Zhang and J. Hou, Molecular Design of Benzodithiophene-Based Organic Photovoltaic Materials, *Chem. Rev.*, 2016, **116**, 7397–7457.

104. S. Inal, J. Rivnay, A.-O. Suiu, G. G. Malliaras and I. McCulloch, Conjugated Polymers in Bioelectronics, *Acc. Chem. Res.*, 2018, **51**, 1368–1376.

105. Z. Hu, Z. Wang, X. Zhang, H. Tang, X. Liu, F. Huang and Y. Cao, Conjugated Polymers with Oligoethylene Glycol Side Chains for Improved Photocatalytic Hydrogen Evolution, *iScience*, 2019, **13**, 33–42.

106. D. Moia, A. Giovannitti, A. A. Szumska, I. P. Maria, E. Rezasoltani, M. Sachs, M. Schnurr, P. R. F. Barnes, I. McCulloch and J. Nelson, Design and evaluation of conjugated polymers with polar side chains as electrode materials for electrochemical energy storage in aqueous electrolytes, *Energy Environ. Sci.*, 2019, **12**, 1349–1357.

107. B. Xu, X. Yi, T.-Y. Huang, Z. Zheng, J. Zhang, A. Salehi, V. Coropceanu, C. H. Y. Ho, S. R. Marder, M. F. Toney, J.-L. Brédas, F. So and J. R. Reynolds, Donor Conjugated Polymers with Polar Side Chain Groups: The Role of Dielectric Constant and Energetic Disorder on Photovoltaic Performance, *Advanced Functional Materials*, 2018, **28**, 1803418.

108. J. Kosco, M. Bidwell, H. Cha, T. Martin, C. T. Howells, M. Sachs, D. H. Anjum, S. Gonzalez Lopez, L. Zou, A. Wadsworth, W. Zhang, L. Zhang, J. Tellam, R. Sougrat, F. Laquai, D. M. DeLongchamp, J. R. Durrant and I. McCulloch, Enhanced photocatalytic hydrogen evolution from organic semiconductor heterojunction nanoparticles, *Nature Materials*, 2020, **19**, 559–565.

109. N. Leclerc, P. Chávez, O. A. Ibraikulov, T. Heiser and P. Lévêque, Impact of Backbone Fluorination on π-Conjugated Polymers in Organic Photovoltaic Devices: A Review, *Polymers*, 2016, **8**, 11

CHAPTER II

MATERIALS & METHODS

I. Materials – polymers synthesis:

All reagents and chemicals were purchased from Aldrich or TCI except $PC_{71}BM$ from Ossila and EH-IDTBR from 1-material. THF and Toluene were distilled from Na/benzophenone at the ICPEES.

NMR analysis ^{1}H: spectra were recorded on a Bruker 400 UltrashieldTM 400 MHz NMR spectrometer, with an internal lock on the 2H-signal of the solvent ($CDCl_3$).

I.1. PBDTTPD monomer's:

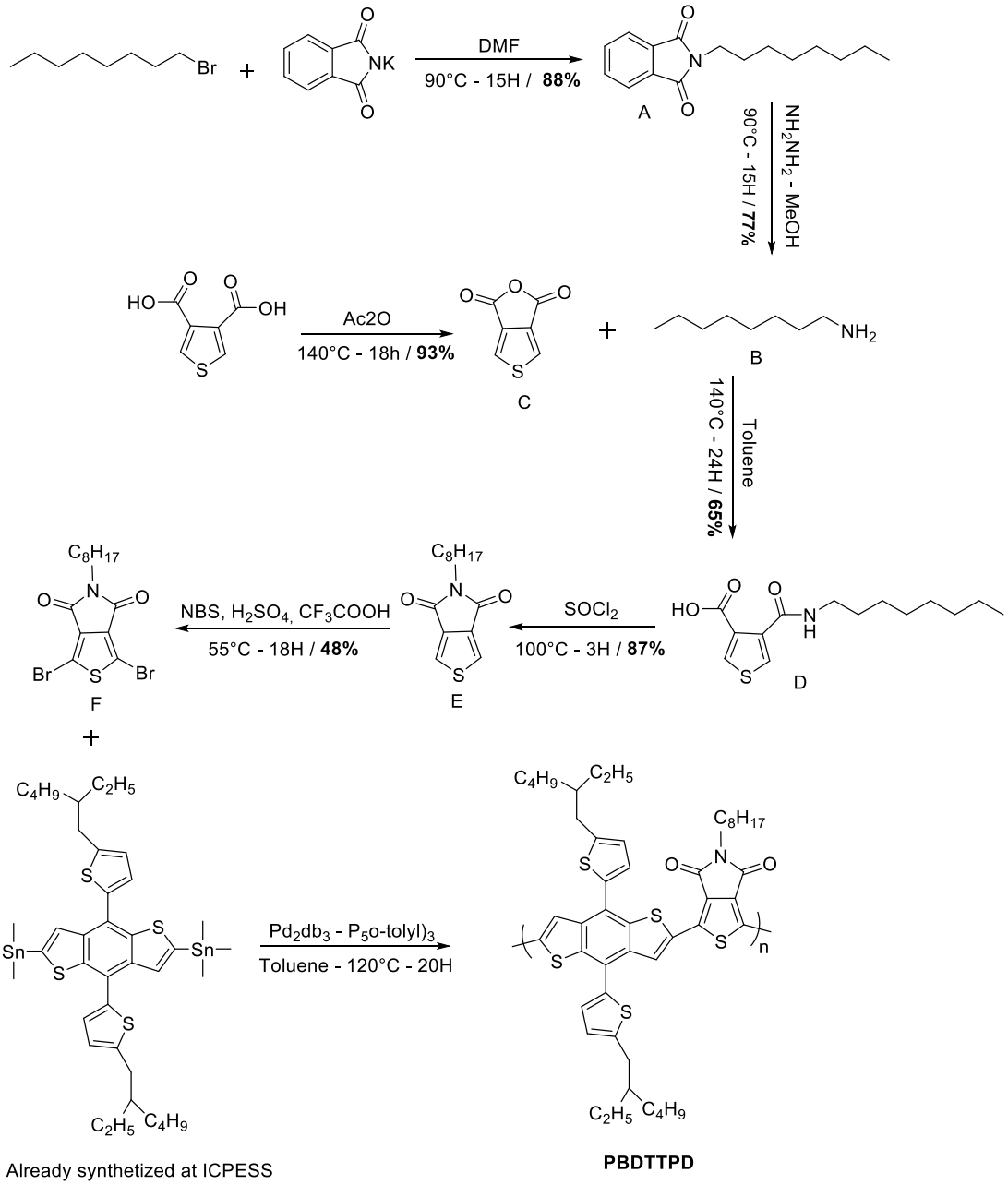

Scheme 1: PBDTTPD synthesis

Compound A: *2-octylisoindoline-1,3-dione*

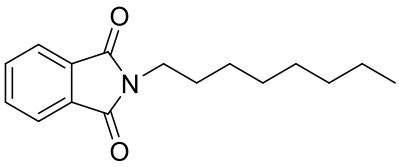

In a Schlenk, a solution of 1-bromooctane (5.27 g, 27.3 mmol, 1 eq), potassium phthalimide (5.86 g, 31.6 mmol, 1.16 eq) and DMF (550 mL) was stirred overnight at 90°C. After cooling to RT, the reaction was quenched with 300 mL of water. The reaction mixture was then extracted by dichloromethane, washed twice by KOH (10 %) and finally by NH_4Cl. The final product was dry over Na_2SO_4, and purified by recrystallization from heptane, to afford a white crystal (88 %, 6.21 g).

^1H NMR ($CDCl_3$, 400 MHz) δ: 7.75 (d, 2H), 7.85 (d, 2H), 3.6 (t, 2H), 1.7 (m, 2H), 1.4 (m, 10H), 0.85 (t, 3H).

Compound B: *octan-1-amine*

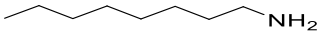

In a Schlenk of 250 mL, compound a (6 g, 23.13 mmol, 1 eq), hydrazine mon hydrate (4.63 g, 92.54 mmol, 4 eq) and methanol (140 mL) were added and stirred at 90°C for 17 hours. After cooling to RT, the initial solvent was then evaporated. The residue was dissolved in CH_2Cl_2 and washed with 10 wt% of KOH aqueous solution, then extracted again with CH_2Cl_2, then washed with NaCl solution. Finally, organic layer was dried over Na_sSO_4, filtered and concentrated. A yellow/gold oily compound was obtained (77 %, 2.3 g).

^1H NMR ($CDCl_3$, 400 MHz) δ : 2.65 (t, 2H), 1.42 (t, 2H), 1.28 (m, 10H), 0.85 (t, 3H).

Compound C: *Thiophene-3,4-dicarboxylic anhydride*

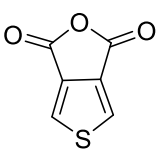

A solution of thiophene-3,4-dicarboxylic acid (4.56 g, 26.5 mmol) in acetic anhydride (125 mL) was stirred at 140 °C overnight. The reaction mixture was subsequently concentrated to afford a pale brown solid, which was recrystallized from toluene to afford a yellow compound (93 %, 3.72 g).

^1H NMR ($CDCl_3$, 400 MHz) δ: 8.2 (s, 2H).

Compound D : *4-(nonylcarbamoyl)thiophene-3-carboxylic acid*

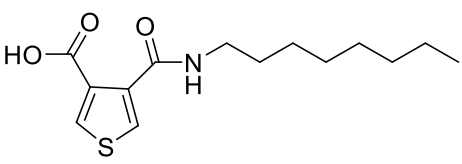

In a Schlenk of 500 mL, were added under argon flux, compound C (2.6 g, 16.2 mmol, 1 eq) and compound b (2.2 g, 17 mmol, 1.05 eq). The mixture was stirred for 24 hours at 140°C. After cooling to RT, the chemical mixture was washed with a 5 % HCl aqueous solution and extract with diethyl ether. The organic phase was dried over Na_2SO_4 and concentrated. A solid yellow product was obtained (65 %, 2.92 g).

^{1}H NMR ($CDCl_3$, 400 MHz) δ: 8.45 (d, 1H), 7.95 (d, 1H), 7.05 (m, 1H), 3.5 (m, 2H), 1.42 (t, 2H), 1.28 (m, 10H), 0.85 (t, 3H).

Compound E*: 5-octylthieno[3,4-c]pyrrole-4,6-dione*

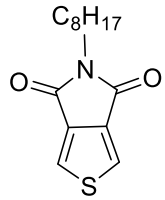

In a Schlenk of 500 mL, add under N2 flux, compound d (2.83 g, 10 mmol, 1 eq), and thionyl chloride (90g, 750 mmol, 75 eq). The mixture was stirred for 3 hours at 100 °C. After cooling to RT, the solution was neutralized with 2.5 M aqueous NaOH solution. The organic layer was then extracted by diethyl ether and washed with water. After drying over Na_2SO_4, the organic phase was filtered and concentrated to give a solid yellow compound (87 %, 2.35 g).

^{1}H NMR ($CDCl_3$, 400 MHz) δ : 7.90 (s, 2H), 3.59 (t, 2H), 1.63 (m, 2H), 1.28 (m, 10H), 0.87 (t, 3H).

Compound F: *1,3-dibromo-5-octylthieno[3,4-c] pyrrole-4,6-dione*

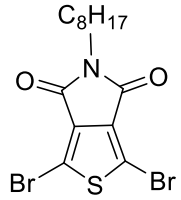

Compound e (2.25 g, 8.5 mmol, 1 eq) was dissolved in trifluoroacetic acid (46 mL) and sulfuric acid (14 mL). While stirring, NBS (6 g, 34 mmol, 4 eq) was added in small portions. The reaction mixture was stirred at 55°C for 36 hours. 200 mL of cold water were added for reaction quenching. The organic layer was extracted with $CHCl_3$, dried over Na_2SO_4 and concentrated. The crude product was purified by column chromatography on silica gel using CH_2Cl_2: petroleum ether 1:1 as the eluent, to give a white compound (48 %, 1.7 g).

^{1}H NMR ($CDCl_3$, 400 MHz) δ : 3.59 (t, 2H), 1.63 (m, 2H), 1.8 (m, 10H), 0.87 (t, 3H).

I.2 PF2-C_4- OEG monomer – strategy I:

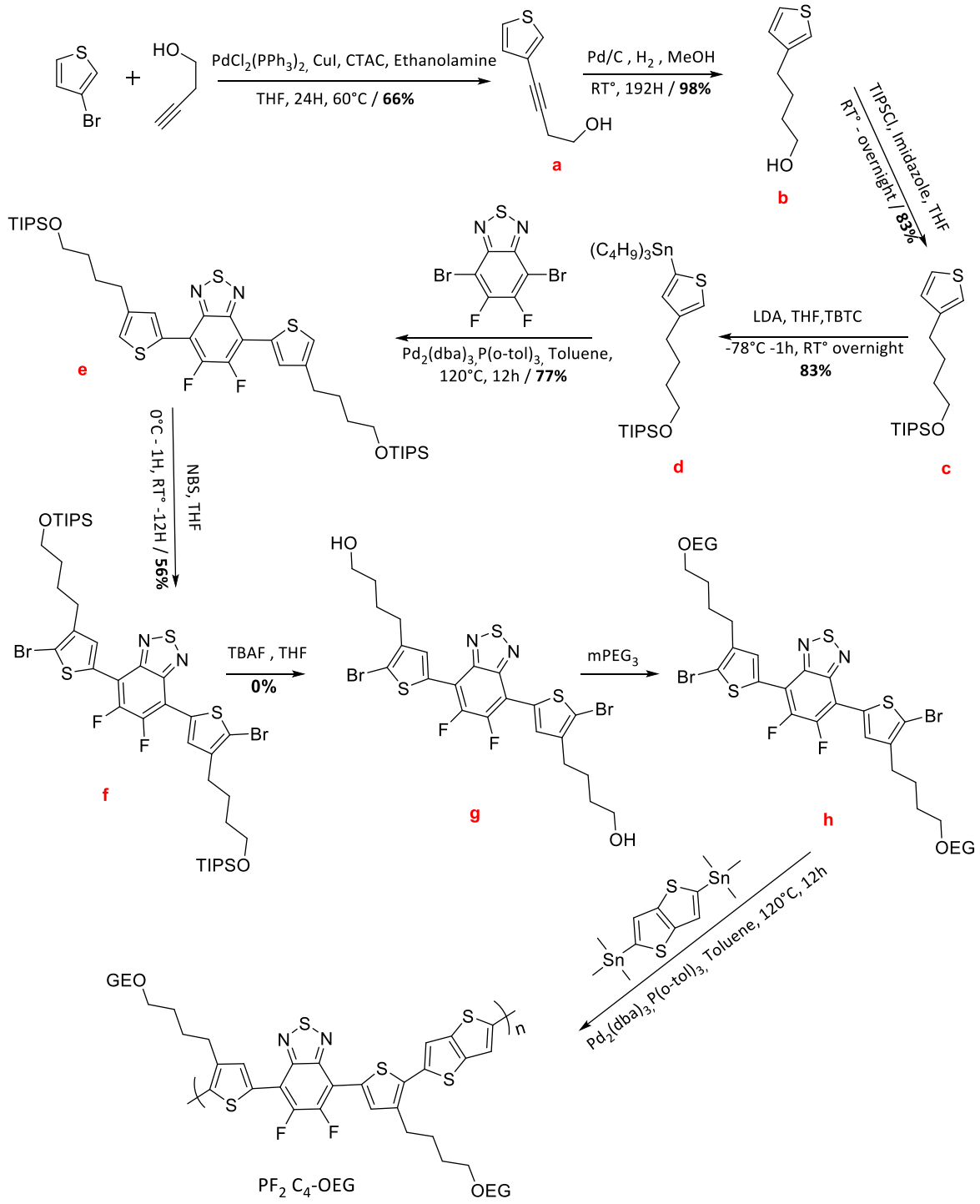

Scheme 2: schematic synthesis of PF2-C_4-OEG - strategy I

Compound a: *4-(3-thienyl)-3-butyn-1-ol*

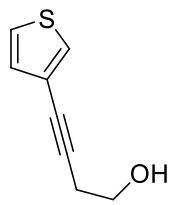

To a 250 mL Schlenk tube equipped with a magnetic stirring bar, were added 3-bromothiophene (2.82mL, 45mmol, 1.5 eq), $PdCl_2(PPh_3)_2$ (105mg, 0.15mmol, 0.05eq), CuI (57mg, 0.3 mmol, 0.1eq), Hexadecyltrimethylammonium chloride CTAC (96 mg, 0.1 mmol, 0.1 eq) and THF (150 mL) under N_2 flux. To the mixture, were added 3-butyn-1-ol (2.26mL, 30 mmol, 1 eq) and ethanolamine (6 mL). The resulting mixture was heated at 60°C for 24 hours. After cooling to room temperature, 100 mL of water was added, followed by an extraction using ethyl acetate. The organic layer was dried over Na_2SO_4 and concentrated. The brown product obtained was purified by column chromatography on silica gel using diethyl ether:petroleum ether 1:1 as the eluent, to give a colorless compound (66 %, 3 g).

^{1}H NMR ($CDCl_3$, 400 MHz) δ: 7.4 (dd, 1 H), 7.26 (dd, 1H), 7.10 (dd, 1 H), 3.81 (q, 2H), 2.67 (t, 2H) 1.64 (OH, 1H).

Compound b*:* *4-(3-thienyl)-3-butan-1-ol*

In a Schlenk, a solution of compound a (2 g, 13.14 mmol, 1 eq), Palladium on carbon (1.4 g, 1.314 mmol, 1eq of Pd/C) and methanol (110 mL) was added. A flux of hydrogen was introduced to the medium and kept for 1 week. Finally, the chemical mixture was filtered from Pd/C by using a filter paper. Yellow pure product was obtained after evaporating the initial solvent (98 %, 2g).

^{1}H NMR ($CDCl_3$, 400 MHz) δ : 7.24 (m, 1H), 6.94 (m, 2H), 3.67 (t, 2H), 2.67 (t, 2H), 1.56 (m, 4H), 1.24 (OH, 1H).

Compound c: *triisopropyl(4-(thiophen-3-yl)butoxy)silane*

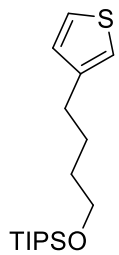

A mixture of compound b (1.6 g, 10.24 mmol, 1 eq), imidazole (0.91 g, 13.31 mmol, 1.3 eq) and TIPSCl (2.65 mL, 12.29 mmol, 1.2 eq) in anhydrous THF (30 mL) was stirred at room temperature overnight. The solvent was removed under reduced pressure and the residue was diluted with water and extracted three times with dichloromethane. The organic layers were combined, washed with brine, dried, and evaporated to obtain compound c (83 %, 2.66 g).

^{1}H NMR ($CDCl_3$, 400 MHz) δ : 7.23 (q, 1H), 6.93 (m, 2H), 3.70 (t, 2H), 2.67 (t, 2H), 1.70 (m, 2H), 1.60 (m, 3H), 1.08(m, 20H).

Compound d: *triisopropyl(4-(5-(tributylstannyl)thiophen-3-yl)butoxy)silane*

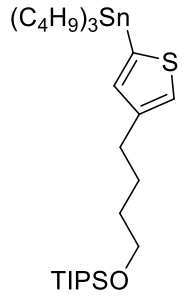

In a Schlenk, under N_2 flux, diisopropylamine (0.73mL, 5.2mmol, 1.3eq) was added to 20 mL of dry THF. After cooling to -40°C using a bath of ethanol-dry ice, *n*-BuLi 2.5M is added dropwise (1.92mL, 4.8mmol, 1.2eq), the mixture was then kept under agitation for 30 minutes. After cooling to -78°C, compound c was added quickly (1.25g, 4 mmol. 1 eq). The resulting mixture was kept under reaction for 1 hour at -78°C, then tributyltin chloride was added quickly (1.42 mL, 5.2 mmol, 1.3 eq). After reacting for 10 min at -78°C, then cooling to RT, the resulting mixture was kept under stirring overnight. Finally, the reaction was quenched by adding (15 mL) of water. The organic layer was then extracted by diethyl ether, dried over Na_2SO_4 then concentrated. Yellow oily compound is obtained (83 %, 2 g).

^{1}H NMR ($CDCl_3$, 400 MHz) δ : 7.20 (s, 1H), 6.96 (s, 1H), 3.70 (t, 2H), 2.68 (t, 2H), 1.7-0.9(m, 52H).

Compound e: *5,6-difluoro-4,7-bis(4-(4-((triisopropylsilyl)oxy)butyl)thiophen-2-yl)benzo[c] [1,2,5] -thiadiazole*

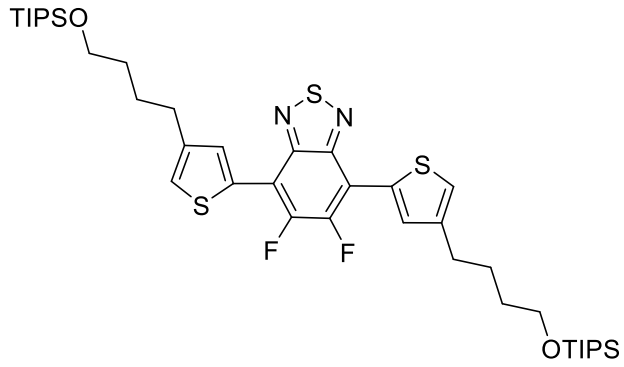

Compound d (1.82 g, 3.03 mmol, 2 eq), 4,7 Dibromo-5,6-difluoro-2,1,3 benzothiadiazole (500 mg, 1.515 mmol, 1 eq), $Pd_2(dba)_3$ (28 mg, 0.03 mmol, 0.02 eq) and $P(o\text{-}tol)_3$ (37 mg, 0.121 mmol, 0.08 eq) were dissolved in 150 mL of dry Toluene. The mixture was stirred for 24 hours at 120 °C. After cooling to RT°, 50 mL of ethyl acetate is added. Finally, the organic layer was extracted with diethyl ether then concentrated. Orange impur product was obtained, purified by column chromatography on silica gel using toluene:petroleum ether 1:1 as the eluent, to give a yellow, fluorescent compound (77 %, 930 mg).

^{1}H NMR ($CDCl_3$, 400 MHz) δ : 8.07 (s, 1H), 7.16 (s, 1H), 3.70 (t, 2H), 2.68 (t, 2H), 1.7-0.9(m, 25H)

Compound f: *4,7-bis(5-bromo-4-(4-((triisopropylsilyl)oxy)butyl)thiophen-2-yl) 5,6difluorobenzo -[c][1,2,5]thiadiazole*

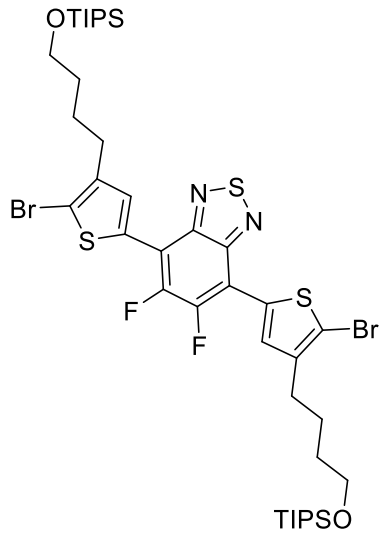

Compound e (750 mg, 0.945 mmol, 1 eq) was dissolved in THF (15 mL). While stirring at 0°C, NBS (337 mg, 1.9 mmol, 2 eq) was added in small portions. The reaction mixture was stirred at 0°C. After 2 hours, water/ice bath was removed, and the reaction was left overnight under stirring at RT. Finally, the organic layer was extracted with diethyl ether then concentrated. Orange impur product was obtained, purified by column chromatography on silica gel using petroleum ether /toluene 7/3 as the eluent, to give also a yellow, fluorescent compound (56 %, 600 mg).

^{1}H NMR ($CDCl_3$, 400 MHz) δ: 8.07 (s, 1H), 3.70 (t, 2H), 2.68 (t, 2H), 1.7-0.9(m, 25H).

Compound g: *4,4'-((5,6-difluorobenzo[c][1,2,5]thiadiazole-4,7-diyl)bis(2-bromothiophene-5,3-diyl))bis(butan-1-ol)*

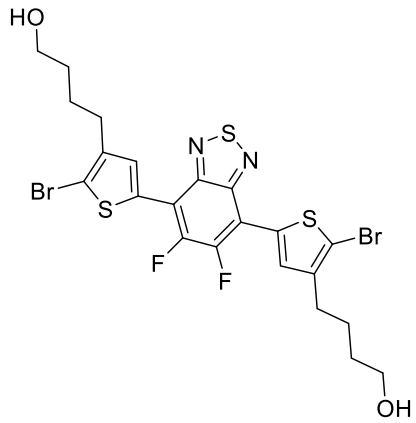

To a solution of the compound f (50 mg, 0.0525 mmol, 1 eq) in 5 mL THF was added TBAF (1.0 M in THF, 0.22 mL, 0.21 mmol, 4 eq) at 0°C, and the resulting mixture was allowed to warm to RT° overnight. The reaction was quenched by adding a solution of $NaHCO_3$. The chemical mixture was then extracted by ethyl acetate, dried over Na_2SO_4 and concentrated.

The reaction failed.

I.3 PF2-C_4- OEG monomer – strategy II:

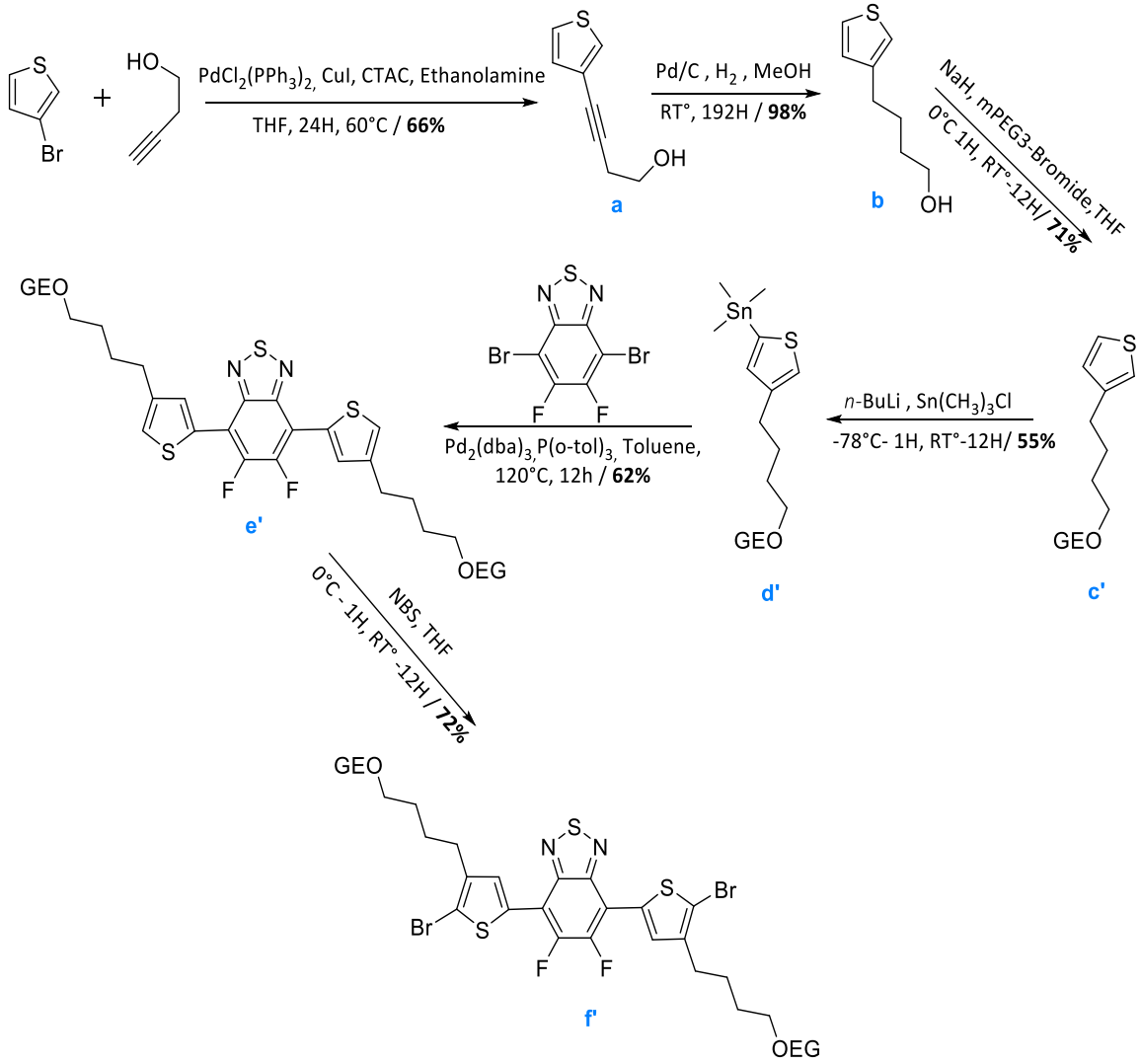

Scheme 3: schematic synthesis of PF2-C_4-OEG monomer - strategy II

Compound a &b: check **section I.2** (compounds a & b).

Compound c': *15-(thiophen-3-yl)-2,5,8,11-tetraoxapentadecane*

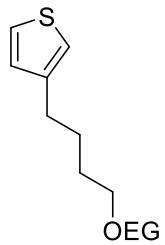

To a solution of the compound b (2.5 g, 16 mmol, 1 eq), NaH (2.3 g, 96 mmol, 6 eq) in 170 mL THF was added mPEG3-Bromide (5 mL, 32 mmol, 2 eq) at 0 °C using ice-water bath, and the resulting mixture was allowed to warm to RT° for 12 hours. The reaction was quenched by adding 100 mL of water. The organic layer was extracted by diethyl ether, washed with brine, dried over Na_2SO_4, concentrated. the crude product was then purified by column chromatography on silica gel using ethyl acetate:petroleum ether 3:7 as the eluent, to give also a yellow, fluorescent compound (71 %, 3.4 g).

^{1}H NMR ($CDCl_3$, 400 MHz) δ : 7.2(q, 1H), 6.9(m, 2H), 3.6(m, 8H), 3.54(m, 4H), 3.45(t, 2H), 3.3 (s, 3H), 2.63(t, 2H), 1.64 (m, 4H).

Compound d': *(4-(2,5,8,11-tetraoxapentadecan-15-yl)thiophen-2-yl)trimethylstannane*

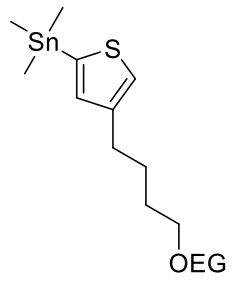

In a Schlenk, add under N_2 flux, 10 mL of dry THF and compound c' (300 mg, 1 mmol, 1 eq). After cooling to -78°C using a bath of ethanol-dry ice, *n*-BuLi 1.6M is added dropwise (0.63 mL, 1.2 mmol, 1.2 eq). The mixture was then kept under agitation for 1 hour. After that, trimethyltin chloride was added quickly (1.25 g, 1.3 mmol, 1.3 eq). After reacting for 1 hour at -78°C, followed by a cooling to RT°, the resulting mixture was kept under stirring overnight. Finally, water (15 mL) was added to quench the reaction. Organic layer was then extracted by diethyl ether, dried over Na_2SO_4 then concentrated. A colorless compound was obtained (55 %, 255 mg).
^{1}H NMR ($CDCl_3$, 400 MHz) δ : 7.2(s, 1H), 7.0(s, 1H), 3.6(m, 8H), 3.54(m, 4H), 3.45(t, 2H), 3.3 (s, 3H), 2.63(t, 2H), 1.64 (m, 4H), 0.34(s, 9H).

Compound e': *4,7-bis(4-(2,5,8,11-tetraoxapentadecan-15-yl)thiophen-2-yl)-5,6-difluorobenzo[c] -[1,2,5]thiadiazole*

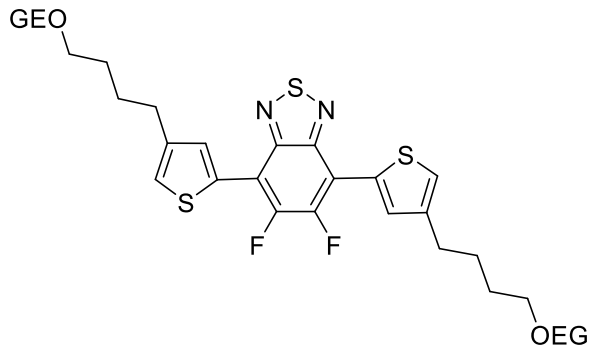

Compound d' (1.18 g, 2.5 mmol, 2 eq), 4,7-Dibromo-5,6-difluoro-2,1,3-benzothiadiazole (370 mg, 1.25 mmol, 1 eq), $Pd_2(dba)_3$ (22 mg, 0.025 mmol, 0.02 eq) and $P(o\text{-}tol)_3$ (27 mg, 0.1 mmol, 0.08 eq) were dissolved in 150 mL of dry Toluene. The mixture was stirred for 24 hours at 120 °C. After cooling to RT°, 50 mL of ethyl acetate was added. Finally, the organic layer was extracted with diethyl ether then concentrated. A Orange product was obtained and purified by column chromatography on silica gel using 100% ethyl acetate as the eluent, to give a red, fluorescent compound (62 %, 820 mg). ^{1}H NMR ($CDCl_3$, 400 MHz) δ : 8.07 (s, 1H), 7.17 (s, 1H), 3.64 (m, 12H), 3.55 (t, 2H), 3.3 (s, 3H), 2.71 (t, 2H), 1.74 (m, 4H).

Compound f': *4,7-bis(5-bromo-4-(2,5,8,11-tetraoxapentadecan-15-yl)thiophen-2-yl)-5,6-difluoro -benzo[c][1,2,5]thiadiazole*

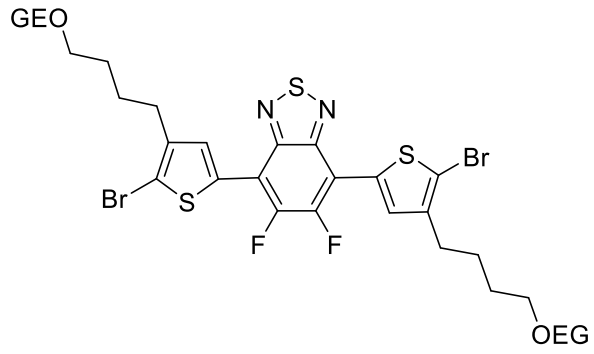

Compound e' (1 g, 1.3 mmol. 1 eq) was dissolved in THF (50 mL). While stirring at 0°C, NBS (460 mg, 2.6 mmol, 2 eq) was added in small portions. The reaction mixture was stirred at 0°C. After 2 hours, water/ice bath was removed, and the reaction was left overnight under stirring at RT. Finally, the organic layer was extracted with ethyl acetate then concentrated. A red/black product was obtained and purified by column chromatography on silica gel using 95:5 ethyl acetate:ethanol, given a red compound (72 %, 890 mg).

^{1}H NMR ($CDCl_3$, 400 MHz) δ : 7.95(s, 1H), 3.64(m, 12H), 3.55(t, 2H), 3.36 (s, 3H), 2.68(t, 2H), 1.74 (m, 4H).

I.4 General Stille polymerization procedure:

A flame dried Schlenk was charged with monomer A and monomer B (Equimolar), 2 mol % $Pd_2(dba)_3$ and 8 mol % $P(o\text{-}tol)_3$ were dissolved in 20 equivalents of dry Toluene. The mixture was stirred for 24 hours at 120 °C. The reaction was quenched with 2-(trimethylstannyl)-thiophene (0.6 eq) then followed by 2-bromothiophene (0.6 eq). After cooling down to room temperature, the polymer crude was purified by precipitation in ethanol, filtered and separated by Soxhlet extraction with ethanol, acetone, cyclohexane and chlorobenzene. Then, the sodium diethyldithiocarbamate solution was added in the cyclohexane fraction and the mixture was stirred at 60°C for 1 hour. The organic phase was washed with water and dried over Na_2SO_4. Finally, the polymer was precipitated in methanol, filtered and dried under reduced pressure at 40-50°C overnight.

I.5 polymer's characterization:

- **Size exclusion chromatography (SEC):** measurements were performed with a Waters Alliance GPCV 2000 instrument (Milford/MA) equipped with a differential refractive index detector and a viscosimeter. 1,2,4-Trichlorobenzene was used as the mobile phase at a flow rate of 1 mL/min at 150°C. It was stabilized with 2,6-di(*tert*-butyl)-4-methylphenol. The polymer was injected at a concentration of 1 $mg.mL^{-1}$. The separation was carried out on three Agilent columns (PL gel Olexis 7*300 mm) protected by a guard column (PL gel 5 µm). Columns and detectors were maintained at 150°C. The Empower software was used for data acquisition and analysis. The molar mass distributions were calculated with a calibration curve based on narrow polystyrene standards (Polymer Standard Service, Mainz).

- **Differential Scanning Calorimetry (DSC):** measurements were performed with TA Instruments Q1000 instrument, operated at scan rate of 5°C/min on heating and on cooling.

- **Thermogravimetric analysis (ATG):** Thermogravimetric analyses were performed on the composite PF2:$PC_{71}BM$ NPs prepared by miniemulsion, and compared to the bulk PF2, PCBM and SDS materials, in order to determine the amount of SDS remaining in the particles after dialysis. For these analyses, a Q5000 analyzer (TA Instruments). The sample (1 to 3 mg) was deposited in a platinum pan previously cleaned with a flame and weighed. The pan and its contents were introduced into an oven, placed under a nitrogen flow at 25 mL/min and heated to 450°C at a rate of 50°C/min. The evolution of mass was followed with a high sensitivity thermobalance, itself stabilized by a nitrogen flow of 10 mL/min. As shown in **Figure 1**, the degradation of SDS happens at 200°C while the degradation of PF2 and PCBM starts only at more than 380°C. The thermogram of the dialysed NPs, with a measured conductivity of less than 10 µS/c, shows a mass loss of around 20% between 200°C and 380°C, that could be attributed to remaining SDS in the particles. A rapid calculation of the quantity of SDS adsorbed at the surface of NP of 60 nm diameter, for a dense monolayer (with A_{dense}=0.4 nm^2, the area occupied by 1 SDS molecules [(1)]) gives 12 wt%, slightly lower than the measured mass loss.

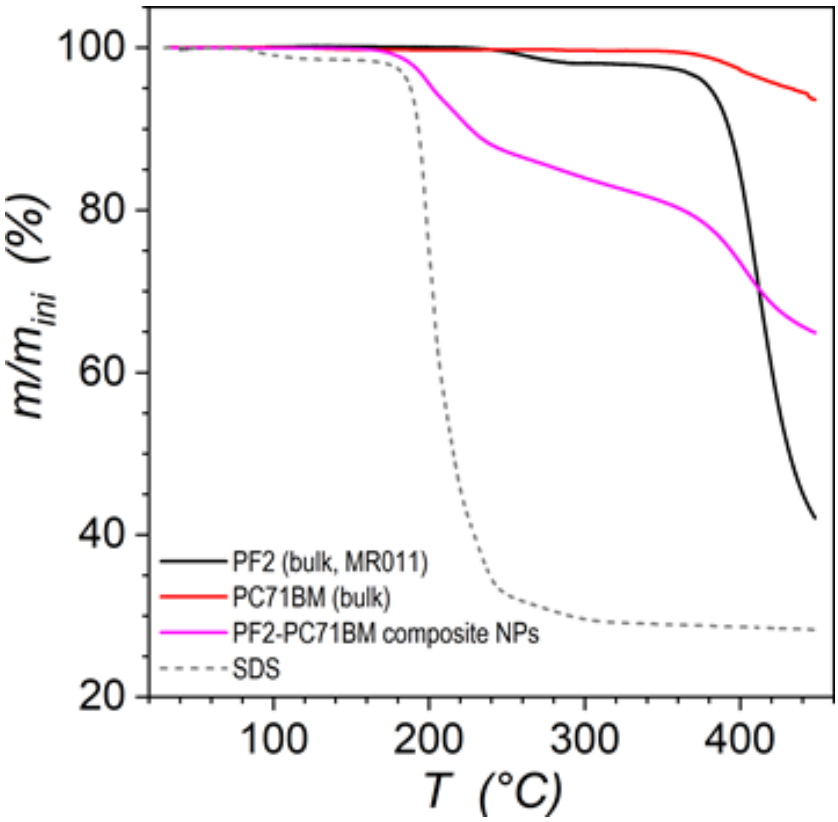

Figure 1: ATG measurements of different polymers / molecules used in this manuscript

- **Cyclic voltammetry (CV):** Oxidation and reduction potentials were determined by cyclic voltammetry with a conventional 3-electrodes system using a Biologic potentiostat equipped with a platinum micro disk (2 mm^2) working electrode and a platinum wire counter electrode. Potentials were calibrated versus the saturated calomel electrode (SCE) at a conventional scan rate of 100 mV/s. Recrystallized tetrabutylammonium hexafluorophosphate (Bu_4NPF_6) was used as the supporting electrolyte (0.1 M) in distilled and anhydrous acetonitrile. Acetonitrile was distilled from CaH_2 under a nitrogen atmosphere. The ferrocene/ferricenium couple was used as an internal reference.

II. Nanoparticle elaboration:

II.1 Miniemulsion:

Typical procedure for PF2, $PC_{71}BM$ and EH-IDTBR separate nanoparticles by post-polymerization miniemulsion (for 1 $mg.mL^{-1}$ material concentration and 4 $mg.mL^{-1}$ SDS concentration) :

The NPs were prepared using a miniemulsion evaporation method. 1 mg of π-conjugated polymer or small molecule acceptor was solubilized in 1 mL of $CHCl_3$ (1.49 g). The $CHCl_3$ solution was then introduced into an SDS aqueous solution (7 mg of SDS in 1.75 mL of MQ−water filtered with 0.22 µm cellulose acetate filter) followed by agitation for 1 hour at 500 rpm to obtain a coarse macroemulsion. Miniemulsion was then formed after sonication for 3 min at 40% (Branson Sonifier 400 W). The miniemulsion was then heated at 60 °C in a sand bath for around 180 min, under magnetic stirring at 500 rpm, to insure a complete $CHCl_3$ evaporation. During the evaporation, the flask was covered by anti-dust paper.

Typical Procedure for PF2:$PC_{71}BM$ and PF2:EH-IDTBR composite nanoparticles by post-polymerization miniemulsion (for 1 $mg.mL^{-1}$ total materials concentration and 4 $mg.mL^{-1}$ SDS concentration):

Composite NPs were prepared using the same procedure as for separate nanoparticles keeping the total amount of semiconducting materials, donor and acceptor to 1 mg, with varying donor/acceptor ratios.

II.2 Nanoprecipitation:

Typical procedure for PF2, $PC_{71}BM$, PBDTTPD, PF2-C_4-OEG separate NPs or PF2-C_4-OEG:$PC_{71}BM$ composite NPs by nanoprecipitation:

The materials solution (donor, acceptor or both in the case of composite NPs) in THF or $CHCl_3$ was prepared with desired concentration. Using the micropipette, 1 mL of this solution was then added rapidly into the non-solvent that could be an alcohol (ethanol, isopropanol, butan-3-ol), pure MQ-water or MQ-water/PF127 (20 $mg.mL^{-1}$) followed by ultrasonication for 3 min at 40 % (Branson Sonifier 400 W).

The solvent was then removed by evaporation in a sand bath without any agitation at 60 °C for 3 hours.

II.3 Nanoparticle's characterizations:

- **Dynamic light scattering (DLS):** The size and distribution measurements of NPs were performed with a CGS-3 goniometer (ALV) equipped with a monochromatic helium-neon laser with a wavelength of 633 nm. The diluted suspension having a concentration of 0.001 to 0.002 $mg.mL^{-1}$ was placed in 10 × 75 mm glass tubes in a thermostated toluene bath (20°C). An angle θ = 90° was imposed between the incident beam and the detector.

- **Removal of excess surfactant:** The excess of surfactant can be almost removed by dialysis using centrifugation dialysis tubes purchased from Sartorius (Vivaspin 30 kDa MWCO – 20mL). The suspension was placed into the dialysis tube and centrifuged at 5000 rpm for 5 min (Eppendorf centrifuge 5804). The filtrate containing water and SDS was then removed, and the remaining suspension was diluted with 16 mL of MQ–water. Around 16 centrifugation dialysis steps were performed until the conductivity of the filtrate was less than 10 µS/cm. In addition, the ATG measurements of lyophilized dialysed NPs suspension showed the around 20% wt of SDS remains in the NPs, corresponding approximately to a dense SDS monolayer at the surface of the NPs. The dialyses steps only allows to remove the SDS from the aqueous phase, without desorbing it from the NPs surface.

- **Suspension conductivity measurements:** Suspension or filtrate conductivities were measured using an electrical conductivity meter (Mettler Toledo). Two standard solutions (purchased from InLab) of 84 µS/cm and 1413 µS/cm were used as reference for the calibration.

- **UV-visible spectroscopy:** The UV-visible spectroscopy analyses were performed with a UV-2600 spectrometer (Shimadzu). *Solutions*: materials were solubilized in $CHCl_3$ at a concentration of 1 $mg.mL^{-1}$ and heated in at 45 °C for 18 h to give the mother solutions. Their dilution by a factor of 50 resulted in daughter solutions at concentrations of approximately 0.02 $mg.mL^{-1}$, which were analysed in 10.00 mm wide quartz cells. *Films:* Few drops of the mother solution were deposited onto a 24 × 24 mm quartz substrate and dried at room temperature and atmospheric pressure for 24 h. Solid films were then analyzed by UV-visible spectroscopy. *NPs suspensions*: elaborated NPs suspensions were diluted to 0.02 $mg.mL^{-1}$ and analysed in 10.00 mm wide quartz cells.

  The optical blank was performed with a quartz cell containing pure $CHCl_3$ for solutions, MQ-water for suspension and quartz slide for solid state analysis.

- **Fluorescence spectroscopy:** Florescence spectroscopy analyses were performed with a FluoroMax-4 spectrometer (Horiba Scientific) in 10.00 mm wide quartz cells. A suspension concentration of approximately 0.002 $mg.mL^{-1}$ was needed. The optical blank was performed with a quartz cell containing pure water-MQ. Fluorescence spectra were obtained by selecting an excitation wavelength of 630 nm and scanning the emission wavelengths from 650 to 800 nm.
- **Scanning electron microscopy (SEM):** Morphological aspects of NPs were analyzed by SEM (Vega 3 TESCAN) in high vacuum mode with a voltage of 5 kV. Few drops of the dialysed NPs suspension were drop casted on aluminum paper. After water evaporation for 18 hours, they were then coated by a thin layer of gold with a sputter coater (Q150RS, Quorum).

- **Photoluminescence PL spectroscopy:** The samples of 0.1 $mg.mL^{-1}$ were excited using 90 ps light pulses of 0.05 nJ energy at 515 nm and 20 MHz repetition rate from a Spectra-Physics Mai Tai laser. Time resolved-PL was measured using a Hamamatsu C6860 streak camera with a S-20 photocathode in synchro scan mode. The instrument response function (IRF) of the setup was 10 ps at full width half maximum (FWHM). Laser pulse duration being much greater than the response time of the system, the temporal resolution is of the order of a hundred ps.

- **Transmission Electron Microscopy (TEM):** Morphological and structural aspects of NPs were analyzed by Dris Ihiawakrim on the IPCMS electron microscopy platform using JEOL 2100 F LaB6 200Kv with a resolution of 0.21 nm, equipped with a STEM detector. Samples of NPs suspension with a concentration of 0.57 $mg.mL^{-1}$ were deposited on copper TEM grids and dried at room temperature for a few hours.

- **Scanning Transmission X-ray Microscopy** (**STXM):** Scanning Transmission X-ray Microscopy was performed at the STXM instrument (RI GmbH) at HERMES beamline at synchrotron SOLEIL. Thin films (200-300 nm) of PF2, PC71BM and eh-IDTBR were prepared and floated onto TEM grids for measurement of NEXAFS (Near edge x-ray absorption fine structure) of the pure materials. Horizontally polarized X-rays were incident normal to the sample surface. Energy stacks were obtained at the Carbon K-edge for all the samples. Diluted dialysed NPs suspensions were then drop-casted onto silicon nitride membrane windows (Norcada Inc.) for STXM measurements. The STXM analysis software aXis2000 (ref: aXis2000 source http://unicorn.mcmaster.ca/aXis2000.html), was used for the singular

value decomposition (SVD) of the NPs stacks using the NEXAFS spectra of the material resulting in thickness maps with pixel resolution of 19 nm.

The first step of the analysis of the STXM images was to convert thickness maps into composition maps (**Figure 2**), using the density of PF2 (d_{PF2}=1.15) and of PCBM (d_{PCBM}=1.47).

For each pixel:

$$\%PF2 = \frac{th_{PF2} \times d_{PF2}}{th_{PF2} \times d_{PF2} + th_{PCBM} \times d_{PCBM}} \quad ; \quad \%PCBM = \frac{th_{PCBM} \times d_{PCBM}}{th_{PF2} \times d_{PF2} + th_{PCBM} \times d_{PCBM}}$$

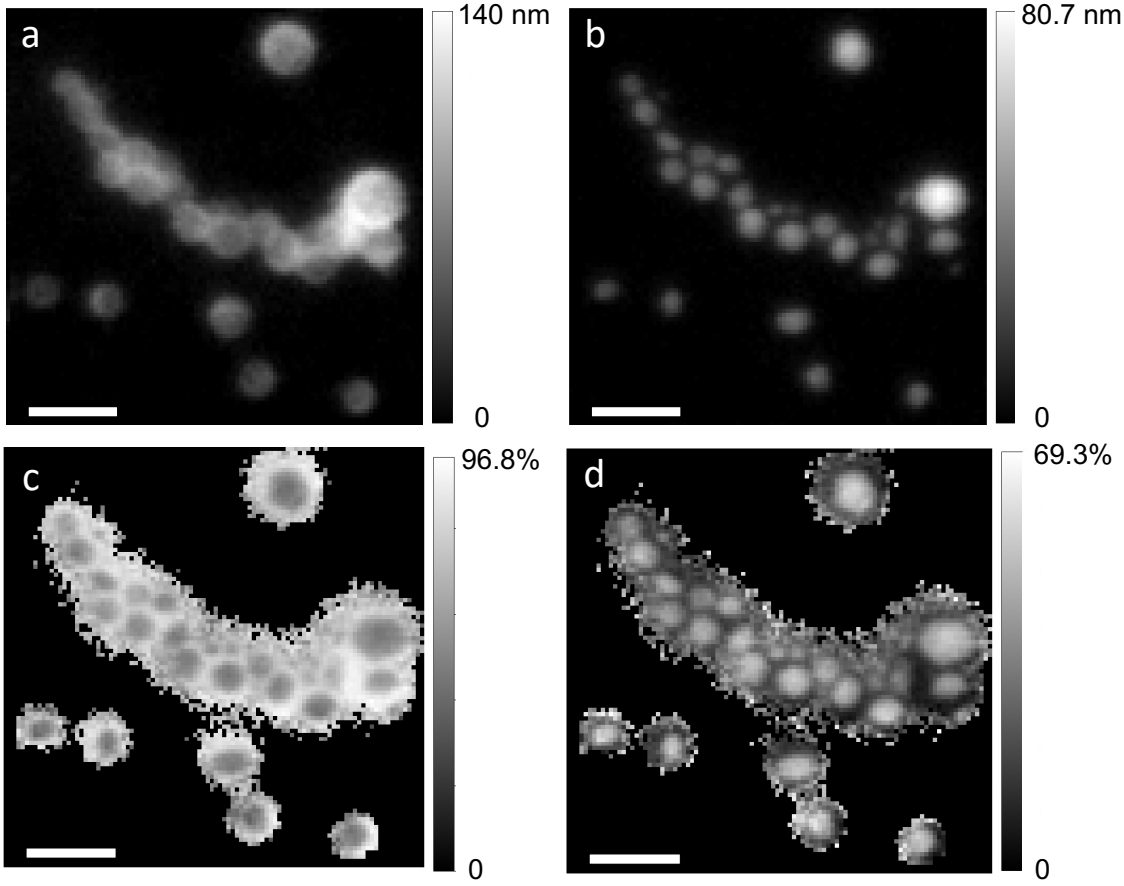

Figure 2: STXM images of dialysed PF2:PCBM 1:1 composite NPs. Thickness maps (a, b) and composition maps (c, d) of PF2 (a, c) and PCBM (b, d). Scale bar represent 400 nm.

Radial composition profiles of 5 to 10 NPs were then measured. STXM being a transmission microscopy technique, the radial profiles represent the composition through the whole NP thickness, *ie* through the core and the shell. A model has to be used in order to find the composition inside the core and inside the shell.

We tried to use two different fitting models of the particle (**Figure 3**).

The first model, close to the one described in the literature [2], describes a particle with a core of radius r_c and composition f_{PF2}^c, an intermediate domain with a radial gradient in composition

between r_c and r_s, and a shell of fixed composition f_{PF2}^s between r_s and r_p (**Figure 3 a-c**). The radial symmetry of the particles allows to consider only h(x) as the height through which the beam passes, $h(x)= h_{shell}(x) +h_{interm}(x)+h_{core}(x)$. Calculation of the composition of PF2 through the intermediate part with radial gradient was performed numerically, taking 100 successive shells with increasing composition. The Python script used to fit the experimental data is given in **Figure 4**. The second model describes a simplier core-shell NP with a core of radius r_c and fixed composition f_{PF2}^c and a shell of fixed composition f_{PF2}^s (**Figure 3 d-f**).

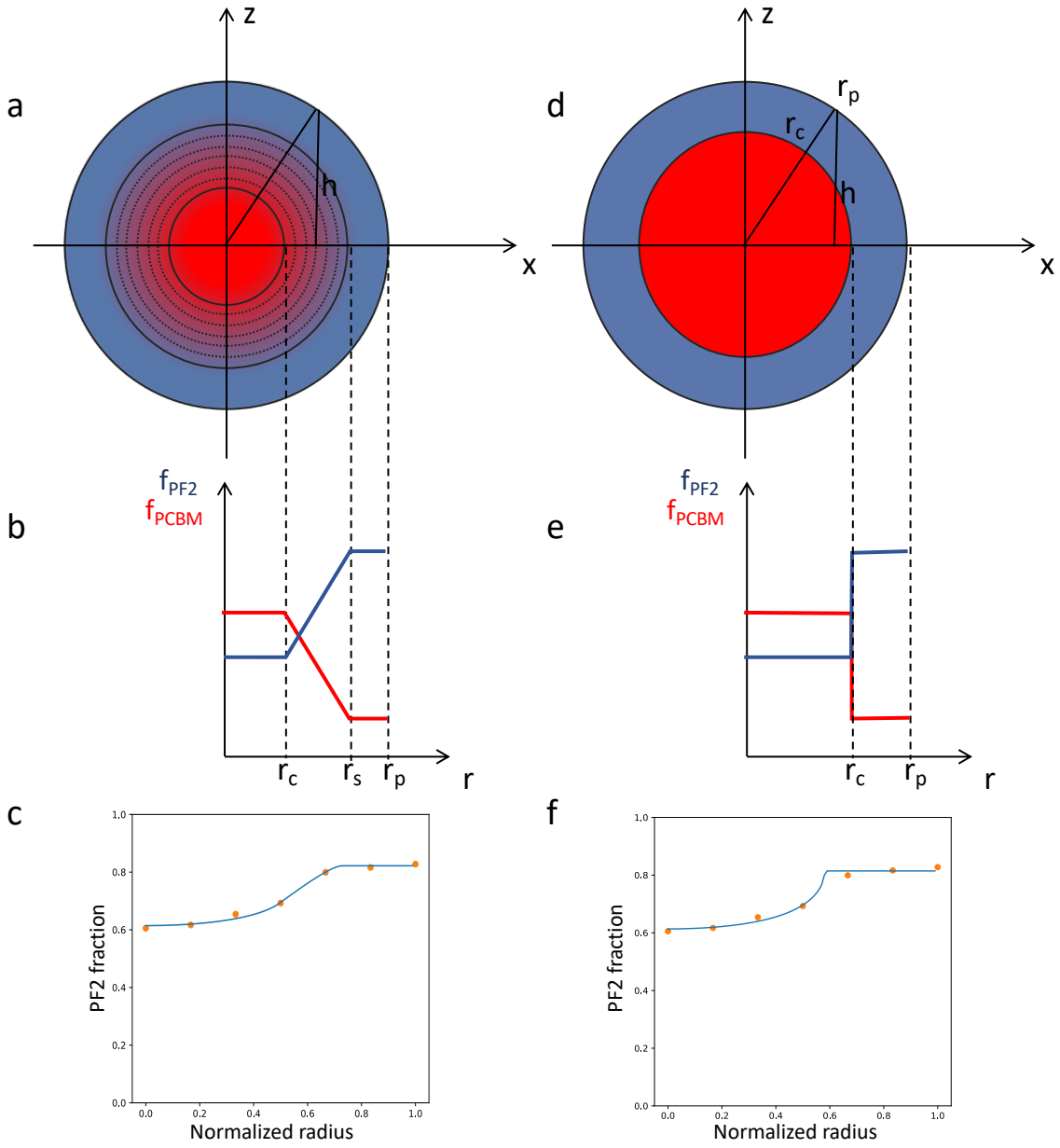

Figure 3: a) model of the core-shell gradient particle used for the fit of the STXM composition profiles. b) radial composition of the particle with a core of radius r_c and materials fraction f_{PF2}^c and f_{PCBM}^c, a shell comprised between r_s and r_p with materials fraction f_{PF2}^s and f_{PCBM}^s, and an intermediate region between r_c and r_s with linear radial composition gradient. c) Example of a fitted STXM composition profile: r_c=0.21, r_s=0.80, f_{PF2}^c = 0.30, f_{PF2}^s = 0.82. d) model of the simple core-shell particle used for the fit of the STXM composition profiles. e) radial composition of the particle with a core of radius r_c and materials fraction f_{PF2}^c and f_{PCBM}^c, and a shell of materials fraction f_{PF2}^s and f_{PCBM}^s. f) Example of the same fitted STXM composition profile: r_c=0.54, f_{PF2}^c = 0.36, f_{PF2}^s = 0.8

```
def hsphere(x, r):
     h = np.where((x<r), np.sqrt(abs(r**2-x**2)), 0)
     return h

def hshell(x,r1,r2):
     h = hparticle(x,r2)-hparticle(x,r1)
     return(h)

def Fgrad(r,r1,f1,r2,f2):
     f=r*(f2-f1)/(r2-r1)+f1-r1*(f2-f1)/(r2-r1)
     return(f)

def fPF2_fit(x, rc, rs, fPF2c, fPF2s):
    r = np.linspace(rc,rs,101)
    PF2 = fPF2c*hparticle(x,rc) + fPF2s*hshell(x,rs,rp)
    PCBM = (1-fPF2c)*hparticle(x,rc) + (1-fPF2s)*hshell(x,rs,rp)

    for loop in range(1,100):
        PF2 += Fgrad(r[loop],rc,fPF2c,rs,fPF2s)*hshell(x,r[loop-1],r[loop])
        PCBM += Fgrad(r[loop],rc,1-fPF2c,rs,1-fPF2s)*hshell(x,r[loop-1],r[loop])

    fPF2 = PF2/(PF2+PCBM)

    return fPF2
```

Figure 4: Python script for the fit of the radial composition of core-shell gradient particle. hsphere returns the height of a sphere of radius r in x, hshell returns the height of the shell comprised between r1 and r2 in x. Fgrad returns the material fraction as a function of r for a linear gradient between a core of radius r1 and fraction f1 and a shell of radius r2 and fraction f2, fPF2_fit is the function used for the fit of the PF2 radial composition. It returns the PF2 fraction in x as a function of four adjustable parameters: r_c, r_s, $fPF2_c$ and $fPF2_s$.

The core-shell gradient model is probably more realistic. However, fitting the compositions profiles with 4 adjustable parameters is certainly questionable regarding the number of experimental points of the profiles. Finally, when comparing both fits, the calculated material fractions in the core and shell of the NP found comparable. The STXM images thus allow us to confirm the core-shell structures and to show tendencies in the compositions of the core and shell as will be discussed in **chapter III** (with results from the simple core-shell model).

III. Thin film fabrication:

III.1 Film deposition:

Films of NPs were spin coated on glass ITO substrate covered by either ZnO or PEDOT-PSS interfacial layers, using the following program: spinning speed of 1000 rpm and acceleration 100 rpm/s during 60 s. 1, 2 or 3 layers were deposited, with drying under vacuum at 20°C during 3 hours between each layer.

III.2 Film characterization:

- **Contact angle measurement:** Contact angles of 17.5 wt% NPs suspensions on PEDOT:PSS, ZnO or a dried previously deposited layer of NPs were measured using a tensiometer (DSA25S) from Krüss.

- **Surface Free Energy measurement:** Contact angles of different liquids onto solution spin-coated films of the materials were first measured. Surface free energy was calculated using OWRK method [3,4,5]. The Owens, Wendt, Rabel and Kaelble (OWRK) method is a reference method for calculating the surface energy of a solid from the contact angle using at least two liquids. The polar and dispersive components of the surface energy are distinguished. Diiodomethane (CH_2I_2, Sigma-Aldrich) and freshly prepared MQ-water (resistivity > 18.4 MΩ.cm) were used for these measurements, because their surface tension as well as polar and dispersive components are known. Moreover, the surface tension of diiodomethane is purely dispersive, while the polar component of the surface tension of water is important. According to Young's equation, the free surface energy of a solid σ_s is given by $\sigma_s = \gamma_{sl} + \sigma_l \cdot \cos\theta$, where θ is the liquid solid contact angle, σ_l is the surface tension of the liquid and γ_{sl} is the solid liquid interfacial tension (**Figure 5**).

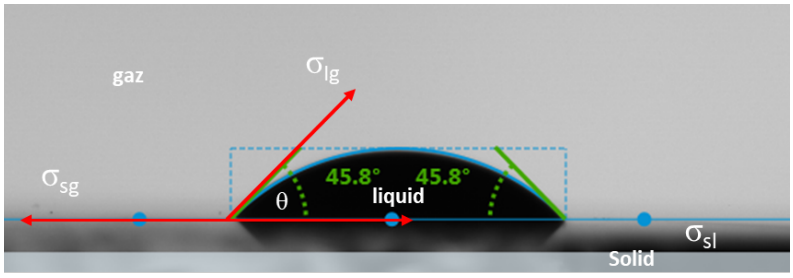

Figure 5: contact angle measurement of a composites PF2:PC$_{71}$BM NPs 1:2 dialyzed suspension (1.75 wt%) on ZnO

In order to calculate the surface energy from the contact angles, the second unknown variable γ_{sl} must be searched for. Based on the FOWKES[6] method, the calculation of the interfacial tension γ_{sl} is based on the two surface tensions σ_s and σ_l as well as similar interactions between the phases. These interactions are reflected in the geometric mean of the dispersive σ^D and polar σ^P components of the surface tension or surface energy:

$$\gamma_{sl} = \sigma_s + \sigma_l - 2\left(\sqrt{\sigma_s^D \, \sigma_l^D} + \sqrt{\sigma_s^P \, \sigma_l^P}\right)$$

Combining this equation with the Young's equation, results in the following linear equation:

$$\frac{\sigma_l(1+\cos\theta)}{2\sqrt{\sigma_l^D}} = \sqrt{\sigma_s^P} \cdot \sqrt{\frac{\sigma_l^P}{\sigma_l^D}} + \sqrt{\sigma_s^D}$$

At least two liquids whose polar and dispersive components of the surface tension are known are thus required to calculate the surface energy of a solid, and at least one of them must have a polar component > 0.

The results of the surface energy calculations for PF2 and $PC_{71}BM$ are given in **Table 1**. While the value obtained for $PC_{71}BM$ is close to the literature, the one obtained for eh-IDTBR was quite different when diiodomethane is used. In fact, we found that eh-IDTBR is partially soluble in this solvent, leading to the dissolving of the film during measurement, making the measurement wrong. For that reason and to complete the calculation, the contact angles of liquids, ethylene glycol and n-heptane, were measured for eh-IDTBR (**figure 6**). PF2-C_4-OEG showed the same issue with diiodomethane. **Table 2** represent the surface energy for eh-IDBTR and PF2-C_4-OEG using water, ethylene glycol and n-heptane as solvents.

Material	Contact angle water θ_{H2O} (°)	Contact angle Diiodomethane θ_{DIM} (°)	Disperse [mN/m]	Polar [mN/m]	Surface free energy [mN/m]
PF2	104	57	30.30	0.07	30.37
$PC_{71}BM$	91	22	47.17	0.23	47.40

Table 1 : contact angles of water and diiodomethane values and surface free energies calculation of Pf2 and $PC_{71}BM$

Material	Contact angle water θ_{H2O} (°)	Contact angle ethylene glycol θ_{EG} (°)	Contact angle n-heptane $\theta_{n\text{-heptane}}$ (°)	Disperse [mN/m]	Polar [mN/m]	Surface free energy [mN/m]
PF2-C_4-OEG	67	53	3	20.08	13.29	33.37
eh-IDBTR	92	65	2	20	4.80	24.80 (18.3 [7,8])

Table 2 : contact angles of water, ethylene glycol and n-heptane values and surface free energies calculation of PF2-C_4-OEG and eh-IDBTR.

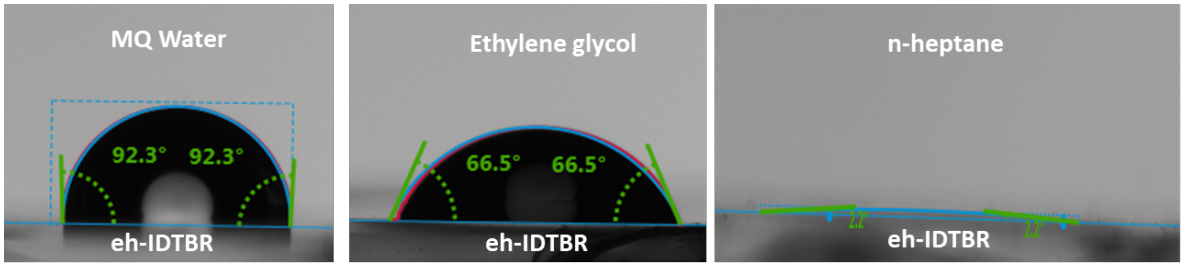

Figure 6: Contact angle of water, ethylene glycol and n-heptane on eh-IDBTR film deposit by spin coating on glass (15 mg.mL^{-1} solution in $CHCl_3$)

- **Atomic Force Microscopy AFM:** films prepared by spin coating for SCLC measurements were also analyzed by AFM using a Multimode 8 with Nanoscope V - 64bit controller – BRUKER AFM in Tapping mode.

  Tip: Budget Sensors, Type BS-Tap 300 Al, Resonant frequency 300 KHz, Spring Constant 40Nm.

- **Film thickness measurement by profilometry:** using Dektak 150 stylus surface profiler. Films were scratched manually using a clamp. The difference between covered surface and the scratched one, allows the calculation of film thickness.

- **Grazing-Incidence Wide-Angle X-ray Scattering (GIWAXS):**

  GIWAXS in Korea: GIWAXS measurements were conducted at PLS-II 9A U-SAXS beamline of Pohang Accelerator Laboratory (PAL) in Korea, by Dr. Benoit Heinrich (from IPCMS, Strasbourg). Samples consisted in thin-films deposited on silicon wafer (thickness was less than 50 nm). The X-rays coming from the vacuum undulator (IVU) were monochromated

using Si(111) double crystals and focused on the detector using K-B type mirrors. Patterns were recorded with a Rayonix 2D SX 165 CCD detector. The sample-to-detector distance was about 225 mm for energy of 11.015 keV (1.1256 Å) in a first session of 2019 and about 222 mm for energy of 11.07 keV (1.120 Å) in a second session of 2020.

GIWAXS at Synchrotron SOLEIL : GIWAXS measurements were conducted at SIRIUS beamline of SOLEIL synchrotron (Saclay, France), by Dr. Benoit Heinrich (from IPCMS, Strasbourg). Samples consisted in Si wafer pieces covered with thin nanoparticles film between 25 and 50 nm. Sample environment was flushed with helium to avoid air scattering. The X-rays generated in top-up mode and coming from undulator were monochromated using thick diamond optics. Patterns were recorded with a Pilatus detector in three vertically rotated detector positions, combined to suppress traces of blind detector zones. Residual background scattering was subtracted using bare Si wafers. The sample-to-detector distance was 350 mm for energy of 10 keV (1.24 Å).

IV. Optoelectronic characterization:

IV.1 Space-charge-limited currents (SCLC):

The SCLC device elaboration procedures are as follows:

1. Substrates cleaning: to remove the dusts and contaminants on the surface, the glass-ITO substrates were cleaned in deionized water, acetone and isopropyl alcohol at 45°C for 15 minutes each.
2. UV-Ozone treatment: the substrates were treated under an ultra-violet ozone system for 30 minutes to eliminate the organic residues on the surface;
3. Deposition of PEDOT:PSS layer (holes only devices): PEDOT:PSS (suspensions in water, purchased from Heraeus Clevios PH) was spin-coated onto the ITO layer using the following program: spinning speed of 5000 rpm with an acceleration of 1000 rpm/s during 60 s. Then, they were dried at 100°C for 30 minutes.

   Deposition of the ZnO layer (electrons only devices): A solution of ZnO (purchased from Avantama – 2.5 wt% in isopropanol) was spin-coated onto the ITO layer using the following program (dynamic deposition): spinning speed of 5000 rpm with an acceleration of 1000 rpm/s during 60 s. Then, they were dried at 100°C for 10 minutes.

4. Deposition of the active layer: 17.5 mg.mL^{-1} of NPs suspension was spin-coated on top of PEDOT:PSS or ZnO using the following program: spinning speed of 1000 rpm with an acceleration of 100 rpm/s during 60 s. 1, 2 or 3 layers were deposited, with drying under vacuum at 20°C during minimum 3 hours between each layer.
5. Top electrode evaporation: MoO_3/Ag (PEDOT:PSS) or Ca/Al (ZnO) were thermally evaporated on the top of the active layer under secondary vacuum (< 10^{-6} mbar). The top electrode has three surface sizes: 0.01 cm^2, 0.0064 cm^2, 0.0025 cm^2.
6. Electrical characterization: Devices were then measured on a probe station equipped with an optical microscope in a glovebox. The current-voltage responses were recorded by a Keithley 4200 semiconductor characterization system.

IV.2 Organic field-effect transistor (OFET):

Bottom contact bottom gate organic field-effect transistors (OFETs) were elaborated on commercially available pre-patterned test structures whose source and drain contacts were composed of a 30 nm thick gold layer on top of a 10 nm thick Indium Tin Oxide (ITO) layer. A 230 nm thick silicon oxide was used as gate dielectric and n-doped ($3x10^{17}.cm^{3}$) silicon crystal as gate electrode. The channel length and channel width were 20 µm and 10 mm, respectively. The test structures were cleaned in soapy water, acetone and isopropanol and subsequently for 30 minutes in an ultra-violet ozone system.

One layer of dialysed NPs suspensions at 17.5 $mg.mL^{-1}$ was then deposited by spin coating (spinning speed of 1000 rpm with an acceleration of 100 rpm/s during 60 s) on the devices.

The OFETs devices were then dried for 18 h under ultrahigh vacuum (< 10^{-6} mbar).

The transistor output and transfer characteristics were recorded using a Keithley 4200 semiconductor characterization system. The charge carrier mobility was extracted in the saturation regime using the usual formalism on FET devices annealed at different temperatures.

IV.3 Organic photovoltaic cells (OPV):

The OPV devices elaboration procedure is identical to SCLC devices, it includes:

1. Substrates cleaning;
2. UV-Ozone treatment;
3. Deposition of ZnO;
4. Deposition of the active layer;
5. Deposition of the top electrode MoO_3/Ag;
6. Electrical characterization: Photovoltaic characterizations were carried out under nitrogen atmosphere, respectively in darkness and under AM1.5g illumination at 100 $mW.cm^{-1}$ produced by a Sun 3000 solar simulator (LOT-Oriel)

V. References:

1. Landfester, K., Bechthold, N., Tiarks, F. & Antonietti, M. Formulation and Stability Mechanisms of Polymerizable Miniemulsions. **32**, 7 (1999).
2. Holmes, N. P. et al. Nano-domain behaviour in P3HT:PCBM nanoparticles, relating material properties to morphological changes. Solar Energy Materials and Solar Cells 117, 437–445 (2013).
3. D. H. Kaelble, Dispersion-Polar Surface Tension Properties of Organic Solids. In: J. Adhesion 2 (1970), P. 66-81.
4. D. Owens; R. Wendt, Estimation of the Surface Free Energy of Polymers. In: J. Appl. Polym. Sci 13 (1969), P. 1741-1747.
5. W. Rabel, Einige Aspekte der Benetzungstheorie und ihre Anwendung auf die Untersuchung und Veränderung der Oberflächeneigenschaften von Polymeren. In: Farbe und Lack 77,10 (1971), P. 997-1005.
6. F. M. Fowkes, Attractive Forces at Interfaces. In: Industrial and Engineering Chemistry 56,12 (1964), P. 40-52.
7. Barr, M. G. et al. Nanomorphology of eco-friendly colloidal inks, relating non-fullerene acceptor surface energy to structure formation. Mater. Chem. Front. 5, 2218–2233 (2021).
8. L. Krishnan Jagadamma, R. G. D. Taylor, A. L. Kanibolotsky, M. T. Sajjad, I. A. Wright, P. N. Horton, S. J. Coles, I. D. W. Samuel and P. J. Skabara, Sustain, Energy Fuels, 2019, 3(8), 2087–2099.

CHAPTER III

NPs ELABORATION VIA MINIEMULSION & CHARACTERISATION

I. Introduction:

The performances of organic solar cells have increased continuously over the last decade. The development of highly efficient photovoltaic materials based on fluorinated polymers has contributed significantly to this remarkable progress. Among them, PF2 (**Figure 1**) is a fluorinated electron donor low bandgap polymer developed at ICPEES. It is composed of difluorinated benzo[2,1,3]thiadiazole groups sandwiched between two thiophene units bearing long alkyl chains and thieno[3,2-b]thiophene (TT) group. It has been chosen in our studies, due to its interesting electronic and optoelectronic properties [(1)]. In fact, compared to its non-fluorinated counterpart PF0, the presence of two fluorine atoms in its chemical structure enhances the polymer face-to-face stacking cohesion and domain purity, as also p-stacking interactions between its patterns. For these reasons, PF2 shows exceptional performance when it is combined with [6,6]-Phenyl-C_{71}-butyric acid methyl ester ($PC_{71}BM$) during the fabrication of organic bulk heterojunction (BHJ) solar cells. A power conversion efficiency (PCE) around 10% was obtained in this case [(1)]. However, its increased stacking cohesion also results in a poor solubility in most solvents. Indeed, PF2 with high molar mass, is only soluble in hot *o*-dichlorobenzene (*o*-DCB) at a temperature above 90°C.

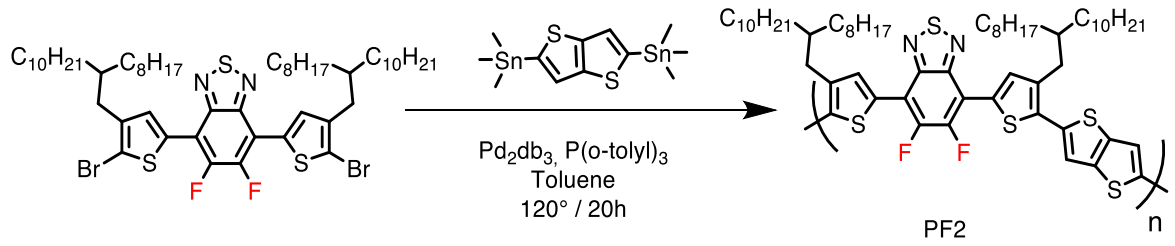

Figure 1: PF2 synthesis

One of the challenges for the OPV cells industry is related to processing of toxic chlorinated solvent such as *o*-DCB. In fact, heating *o*-DCB/PF2 solution to 90°C is required before spin coating of the active layer. It would therefore be highly desirable to process materials active layers from aqueous suspension, containing donor and acceptor nanoparticles (NPs).

For this purpose, several PF2 batches have been prepared by polycondensation mechanism between benzothiadiazole and thieno-thiophene monomers using Palladium (Pd) as catalyzer (Stille reaction – **Figure 1**).

The polycondensation reaction time has been varied from 20 hours to 20 minutes leading to a decrease of PF2 molar mass. Moreover, the obtained PF2 was purified by using a Soxhlet with different solvents. For this work, we used the polymer obtained from chloroform fraction. The molar masses measured by SEC in hot *o*-DCB were between 17 and 54 $kg.mol^{-1}$ with a dispersity of 2.2 to 2.8 depending on the batch used. No significant difference between the different batches

was observed on the NPs preparation and characterizations shown in this chapter. For the optoelectronic devices (**chapter IV**), the batch with 54 kg.mol^{-1} was used.

In this chapter we will discuss the elaboration of separate or composite nanoparticles (NPs) made by the miniemulsion technique using three main materials, PF2 as electron donor and $PC_{71}BM$ or eh-IDTBR **(Figure 2)** as electron acceptor. Then, the prepared particles will be characterized by photoluminescence spectroscopy as well as TEM and STXM in order to determine their morphology and their optical properties.

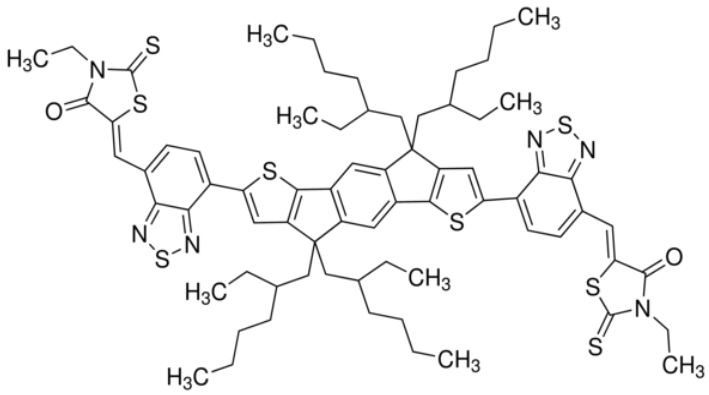

Figure 2: eh-IDTBR structure

II. Elaboration of separate PF2, $PC_{71}BM$ and eh-IDTBR NPs via miniemulsion:

Here, we first discuss the elaboration of separate NPs by miniemulsion, containing either PF2, $PC_{71}BM$ or eh-IDTBR . First, the material was solubilized in an organic solvent, for example chloroform ($CHCl_3$) or *o*-DCB. This solution was then introduced into an aqueous solution containing sodium dodecyl sulfate (SDS) as surfactant. After emulsification, the organic solvent was evaporated resulting in solid NPs. This last step depends strictly on the chosen solvent. In fact, when *o*-DCB, with 180°C as boiling point, is used, the evaporation procedure takes 3 days, during which the suspension is heated at 80°C and evaporated water must be regularly replaced by fresh water while evaporation takes less than 3 hours at 60°C when chloroform solutions are used (Bp = 64°C).

II.1 Small molecules acceptor NPs:

First $PC_{71}BM$ particles with a tunable diameter were produced from chloroform solutions according to the procedure described in the Experimental Part (**chapter II**). The miniemulsion major parameters were then studied.

Influence of different parameters on acceptor materials NPs diameter:

- **Variation of $PC_{71}BM$ concentration:**

The fullerene acceptor molecule, $PC_{71}BM$, is perfectly soluble in organic solvent, such as chloroform or *o*-DCB. Our work has begun by studying the effect of $PC_{71}BM$ concentration when it is solubilized in $CHCl_3$. **Figure 3** shows that increasing the initial $PC_{71}BM$ concentration in chloroform, has no impact on NPs diameter. In fact, it fluctuates around 60 ± 20 nm, regardless the $PC_{71}BM$ concentration.

- **Variation of SDS concentration:**

As discussed previously, NPs diameter can be modified by changing one of the miniemulsion process parameters. Here, we studied the effect of the SDS surfactant concentration during $PC_{71}BM$ NPs elaboration process. As shown in **Figure 3**, increasing the SDS concentration leads to smaller particles. However, above 4 $mg.mL^{-1}$ the average diameter of $PC_{71}BM$ reaches a plateau around 50 ± 15 nm even if the SDS concentration exceeds 16 $mg.mL^{-1}$. Therefore, the SDS concentration that will be used for the next studies will be fixed at 4 $mg.mL^{-1}$. This concentration will allow us to elaborate $PC_{71}BM$ NPs with the smallest size using a minimum amount of surfactant.

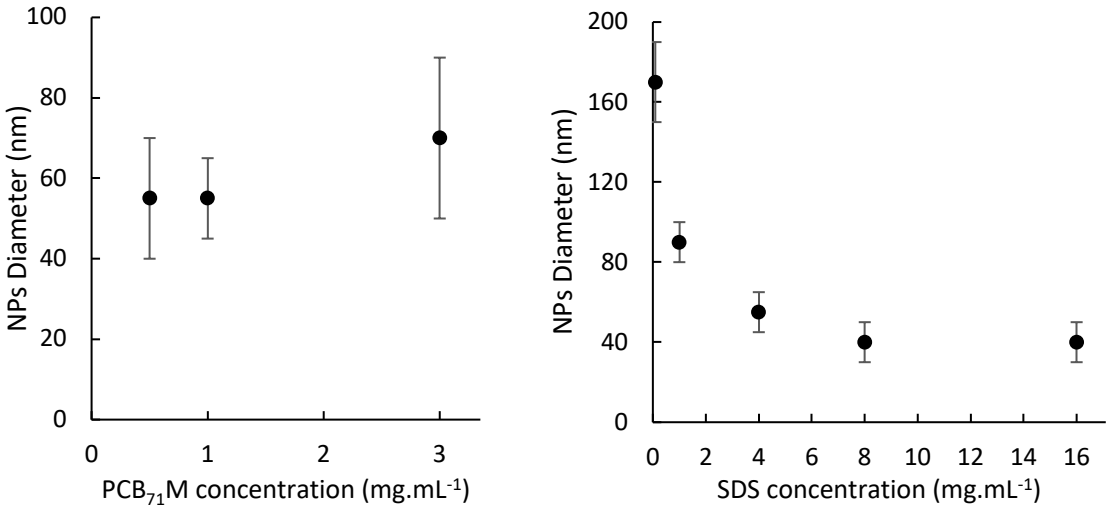

Figure 3: Effect of the concentration of $PC_{71}BM$ solubilized in $CHCl_3$ on the NPs diameter. $\phi_{organic}$ = 36%, [SDS] = 4 $mg.mL^{-1}$(left) . Effect of SDS concentration on $PC_{71}BM$ NPs, $PC_{71}BM$ initial concentration = 1$mg.mL^{-1}$ - $Ø_{organic}$ = 36% (right). Sonication 3min(3on-2off) - Hydrodynamic radius was measured by dynamic light scattering (DLS).

In a second step, eh-IDTBR NPs have also been prepared following the same elaboration procedure as for $PC_{71}BM$ NPs, with an initial concentration of 1 $mg.mL^{-1}$ of eh-IDTBR in chloroform and an SDS concentration of 4 $mg.mL^{-1}$. NPs of diameter 50 ± 15 nm were then obtained, in the same range as the $PC_{71}BM$ NPs. The same trend in the size of the eh-IDTBR NPs as a function of surfactant concentration as for $PC_{71}BM$ NPs is expected.

These NPs were then analyzed by UV-Visible spectroscopy. **Figure 4** presents the UV visible spectra of small molecule acceptors NPs dispersed in water compared to their solutions in $CHCl_3$ and solid films. In the case of eh-IDTBR, spectrum of the solid film presents two peaks due to the crystallization of the part of the molecules in the film. It is also red shifted compared to the one of the chloroform solution. The spectrum of the NPs suspension also presents two peaks however, it is surprisingly blue shifted compared to the solution in chloroform, while aggregation of the molecules in the NPs should lead to a red shift as compared to the solution. In order to better understand this phenomenon, we have prepared a solution of eh-IDTBR in *o*-DCB and measured its UV-vis spectrum at RT and after heating (**Figure 5**). The spectrum of the *o*-DCB solution at RT is similar to the one of the chloroform solution. However, when the *o*-DCB solution is heated, the spectrum is blue shifted indicating that eh-IDTBR is not completely soluble at RT in *o*-DCB or in chloroform. We thus deduce that eh-IDTBR is probably partly amorphous in the NPs and partly aggregated, but not really crystallized as in the solid film.

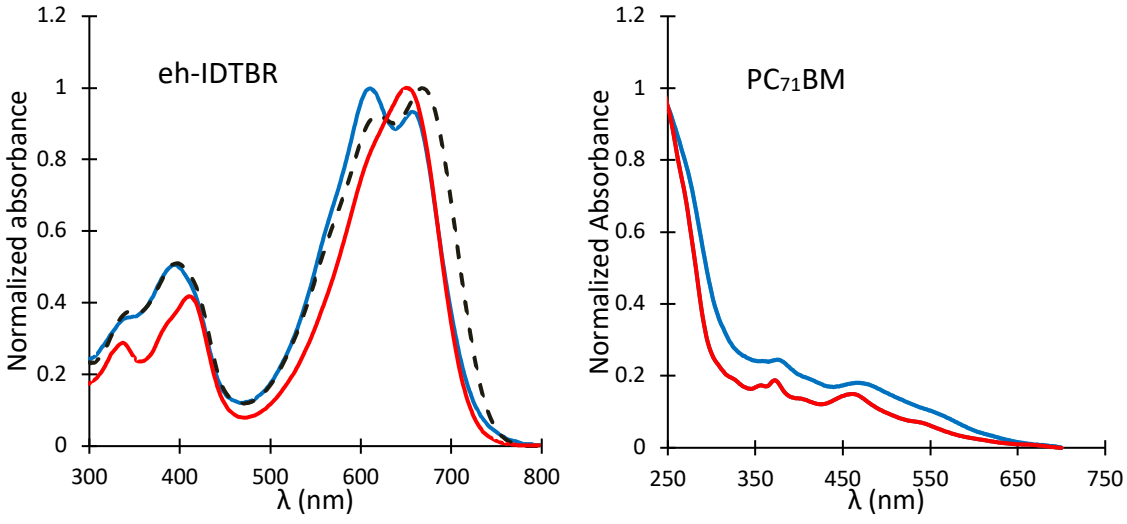

Figure 4: A & B) UV-Visible of solution in $CHCl_3$ (0.02 $mg.mL^{-1}$, red line), NPs in water (0.02 $mg.mL^{-1}$, blue line) and material film (dashed black line).
The absorbance of glass interferes with $PC_{71}BM$ absorbance (between 200 and 300 nm) making $PC_{71}BM$ UV-Visible spectra of film unmeasurable.

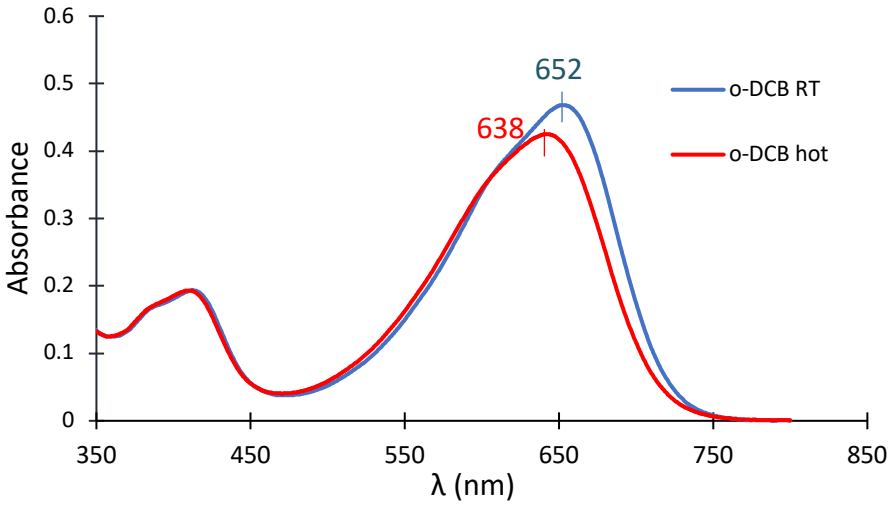

Figure 5: UV-Visible of eh -IDBTR solution in hot o-DCB or o-DCB at RT (0.02 mg.mL^{-1}).

II.2 PF2 NPs:

PF2 NPs were difficult to obtain since PF2 showed lower and incomplete solubility in organic solvents at room temperature. Attempts to elaborate separate PF2 NPs were performed using *o*-DCB and $CHCl_3$ as initial solvent.

According to the procedure described in the experimental section, PF2 particles with adjustable diameters were obtained by miniemulsion.

II.2.A PF2 in *o*-DCB:

It has been shown by D'Olieslaeger [(2)] that PCDTBT:$PC_{71}BM$ NPs elaboration by the miniemulsion process can be achieved using *o*-DCB (Bp=180°C), an organic solvent with higher boiling temperature then water. At the beginning, the same solvent was first used to prepare separate PF2 NPs having 160 ± 50 nm as average diameter. However, the suspensions have been heated at 80°C for three working days to totally evaporate *o*-DCB. During this time, fresh water has been regularly added to compensate its evaporation. Long *o*-DCB evaporation process at 80°C resulted in an increased droplets coalescence and/or NPs aggregation regardless the presence of surfactant. It is also necessary to mention a loss of a part of polymer as larger aggregates.

II.2.B PF2 in $CHCl_3$:

PF2 NPs were elaborated using the same procedure as for $PC_{71}BM$ NPs, starting from chloroform solutions. As PF2 showed low solubility in chloroform, we first tried to optimize its concentration in chloroform for NPs preparation. Then, the SDS amount in the aqueous solution was also varied in order to find the optimal SDS concentration leading to smallest NPs with minimum SDS use.

Influence of different parameters on PF2 NPs diameter:

- **PF2 concentration in chloroform solution:**

In this work, the highest initial concentration of PF2 was set at 1 mg.mL^{-1} due to its incomplete solubility in $CHCl_3$ above this concentration. Indeed, large aggregates could be seen when the concentration exceeded this amount. This study shows that the concentration of PF2 below 1 mg.mL^{-1} does not have any impact on the NPs diameter. For this study, the initial concentration of SDS in water was fixed to 4 mg.mL^{-1}. As shown in **Figure 6**, PF2 NPs diameter remains around 60 ± 30 nm even if the concentration reaches low concentration values (0.05 mg.mL^{-1}).

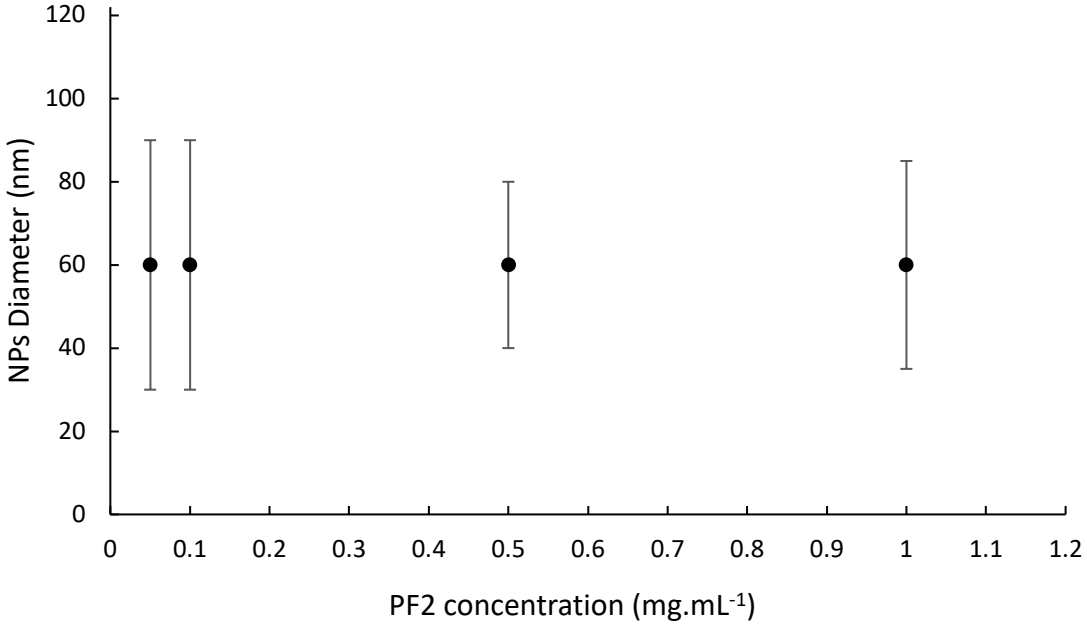

Figure 6: Effect of the concentration of PF2 solubilized in $CHCl_3$ on the NPs diameter. Sonication amplitude 40%, $\phi_{organic}$ = 36%, [SDS] = 4 mg.mL^{-1}.

These results seem incoherent with others reported in the literature[3-4]. Normally, for a stable miniemulsion, the droplet number should stay the same during evaporation. Consequently, for higher polymer concentration in the droplets, the final NP should be larger. In the case of PF2, the diameter of NPs remains unchanged even if the initial concentration was divided by 10. The explanation of this phenomenon can be deduced from the comparison of the UV-visible spectra of PF2 solution in chloroform at 0.02 mg.mL^{-1} with solid films (**Figure 7**). Both spectra are similar presenting vibronic bands $\lambda_{0\text{-}0}$ and $\lambda_{0\text{-}1}$ at 698 and 640 nm respectively, characteristic of the polymer aggregation[(5,6)]. Moreover, aggregates with sizes around 100 nm were measured by DLS analysis of a diluted solution of PF2 in chloroform (0.02 mg.mL^{-1}). It can then be concluded that PF2 is already partially aggregated in chloroform and these aggregates are probably difficult to break, even during

ultrasonication. This aggregation behavior on PF2 could explain why PF2 NPs diameter could not reach below 60 nm.

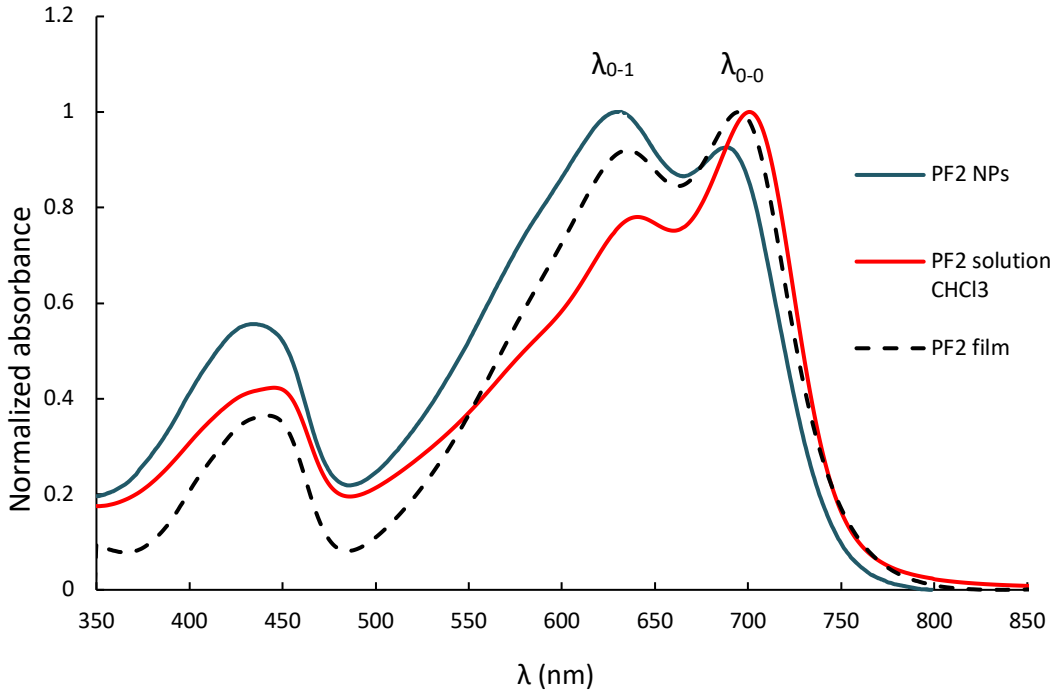

Figure 7: UV-Visible of PF2 solution in $CHCl_3$ (0.02 mg.mL^{-1}) , as solid film spin-coated on glass and PF2 NPs in water (0.02 mg.mL^{-1})

- **Surfactant concentration:**

The effect of surfactant concentration on NPs diameter was then studied, knowing that increasing the amount of SDS allows for a higher surface coverage and thus, smallest particles will be formed. Results presented in the **Table 1** showed that increasing the amount of SDS from 0.1 mg.mL^{-1} to 4 mg.mL^{-1} leads to smaller NPs, their diameter decreases from 180 nm to 60 nm respectively. However, average NPs diameter does not decrease further when doubling the amount of SDS to 8 mg.mL^{-1}. Two possible reasons could be discussed to understand this fact: either PF2 pre-aggregation in $CHCl_3$ as mentioned previously, or the reason that above 4 mg.mL^{-1}, a plateau with a minimum droplet size is reached.

Based on the NPs diameters and the SDS concentration in the aqueous phase, it is possible to calculate A_{surf}, the area occupied by one SDS molecule at the liquid droplet interface after sonication step, before solvent evaporation (**Table 1**). This area can be compared with the area in a dense SDS monolayer (A_{dense}≈0.4 nm^2), found in the literature [7]. At a concentration of 8 mg.mL^{-1}, $A_{surf} < A_{dense}$ which means that an excess of surfactant is present, probably as free surfactant micelles. Moreover, ultrasonication seems not strong enough to break the macroemulsion in smaller droplets. Therefore, the excess of unused SDS molecules forms micelles. Studies about excess surfactant removal will be briefly discussed in the next chapter.

SDS concentration in aqueous phase (mg/mL)	NPs diameter measured by DLS (nm)	Initial droplets diameter (nm)	A_{surf} (nm^2)
8	60 ± 30	600	0.34
4	60 ± 20	600	0.68
2	90 ± 40	900	0.91
0.1	180 ± 30	1800	9.11

Table 1: Effect of SDS concentration on PF2 NPs diameter. Initial PF2 concentration 1 mg.mL^{-1}, 3 min sonication, $\phi_{organic}$ = 36%.

These PF2 NPs were then observed by Scanning Electron Microscopy (SEM), showing particles with irregular spherical shapes (**Figure 8**).

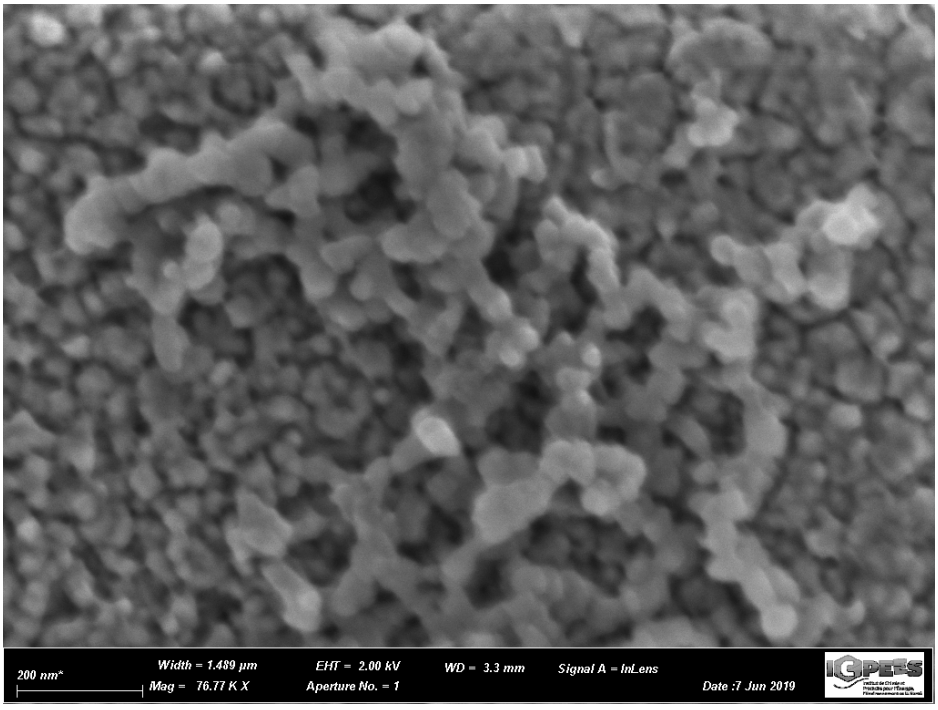

Figure 8 : SEM image of PF2 NPs suspension drop casted on aluminum paper. NPs hydrodynamic radius measured by DLS was around 60 ± 20 nm.

III. Elaboration of composite PF2:$PC_{71}BM$ or PF2:eh-IDTBR NPs:

Composites NPs containing both materials, the electron donor PF2 and the electron acceptor $PC_{71}BM$ or eh-IDTBR, were then prepared. The composite NP were prepared by miniemulsion, using the same protocol as for separate NP, except that in this case an organic solution containing both materials was prepared with total concentration of 1 $mg.mL^{-1}$ and variable D:A ratios.

III.1 PF2:$PC_{71}BM$:

Influence of the different parameters on the diameter of composites PF2:$PC_{71}BM$:

- **Variation of PF2:$PC_{71}BM$ ratio:**

It is important to be able to tune the PF2: $PC_{71}BM$ ratio in the NPs because it can be an optimization parameter for the OPV devices. As shown in **Table 2**, the variation of this ratio did not have an influence on the composite NPs average diameter.

Ratio PF2: $PC_{71}BM$	NPs diameter (nm) measured by DLS
8 : 2	60 ± 40
6 : 4	60 ± 30
5 : 5	60 ± 20
4 : 6	60 ± 40
2 : 8	60 ± 30

Table 2 : Effect of PF2: $PC_{71}BM$ ratio on composites NPs diameters. Sonication 3min(3on-2off) - $Ø_{organic}$ = 36%, [SDS] = 4 $mg.mL^{-1}$

- **Variation surfactant amount:**

As in the case of separate NPs, the amount of SDS surfactant was then modulated to find out the smallest composites NPs with minimum SDS concentration. In fact, as seen in the **Figure 9,** the particle diameter decreases as the surfactant concentration increases.

PF2: $PC_{71}BM$ composite particles with diameters ranging from 200 ± 70 nm (**Figure 10 – SEM image**) to 60 ± 20 nm were thus obtained when the concentration of SDS increases from 0.1 $mg.mL^{-1}$ to 4 $mg.mL^{-1}$, respectively. Above 4 $mg.mL^{-1}$, the diameter of PF2: $PC_{71}BM$ remains unchangeable even by attending excessive SDS concentration values (32 $mg.mL^{-1}$). We can explain these results by referring to our same demonstration described during separate PF2 NPs synthesis.

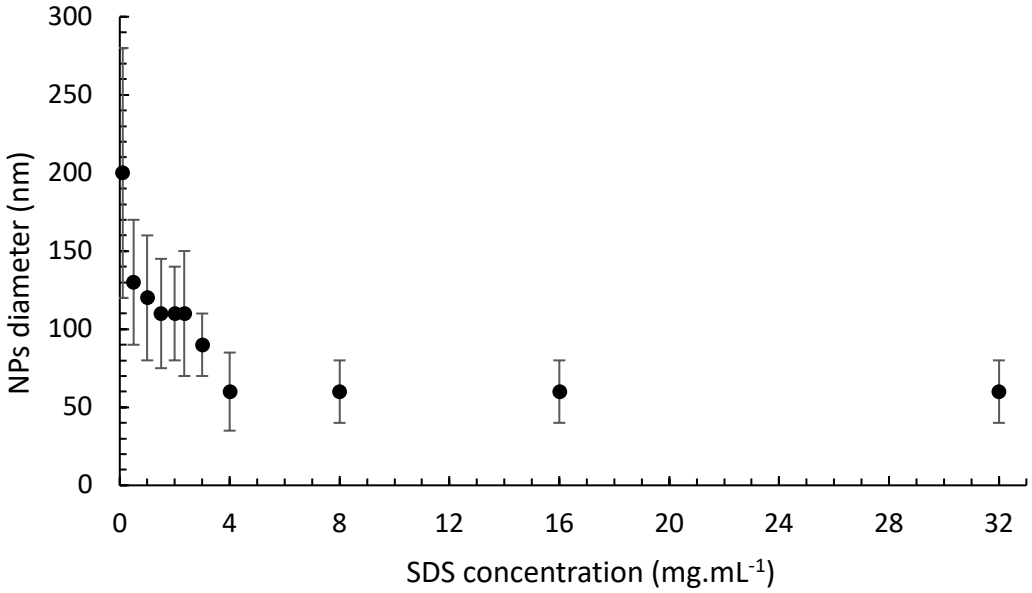

Figure 9 : Effect of SDS concentration on NPs composites PF2: $PC_{71}BM$ 1:1.5 . Sonication 3min (3on-2off) - $Ø_{organic}$ = 36%.

Finally, we were able to tune the NPs diameter from 200 nm to 60 nm. The smallest NPs will be used for the optoelectronic devices because thin films are needed. However, the largest NPs will be interesting for the morphological characterization by STXM as the resolution of such technique is of 19 nm.

These large NPs were then observed by SEM and show a spherical shape with smooth surface which can be surprising regarding the presence of PF2 aggregates in the initial chloroform solution.

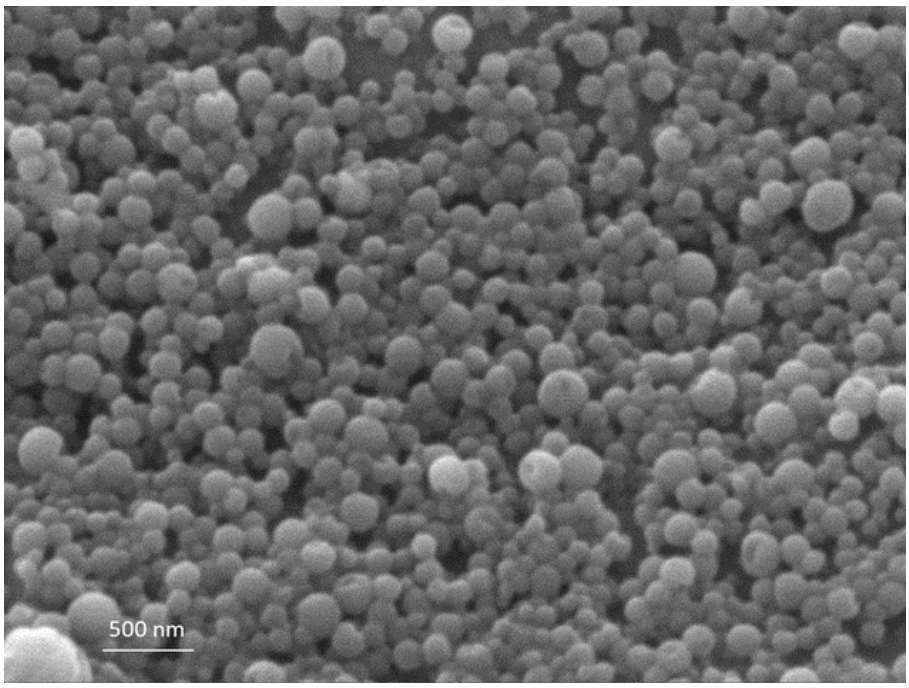

Figure 10: SEM image of PF2:$PC_{71}BM$ composites NPs suspension drop casted on aluminum paper. NPs hydrodynamic radius measured by DLS was around 200 ± 70 nm.

III.2 PF2:eh-IDTBR:

PF2:eh-IDTBR were than elaborated following the same procedure as for PF2: NPs. Replacing $PC_{71}BM$ by eh-IDTBR has no influence on the average diameter of the NPs. As expected, the ratio between PF2 and eh-IDTBR has no impact on particle diameter, it remains constant at 60 ± 20 nm whatever the ratio. Similarly to PF2:$PC_{71}BM$ composite NPs, the diameter of PF2:eh-IDTBR 1:1 decreases from 180 ± 60 nm to 60 ± 20 nm when increasing the amount of SDS in the aqueous solution from 0.1 $mg.mL^{-1}$ to 4 $mg.mL^{-1}$.

IV. Characterization of composites NPs:

PF2:$PC_{71}BM$ as well as PF2:eh-IDTBR composite NPs have been prepared with spherical morphology and tunable diameters between 60 and 200 nm. However, a deeper morphological characterization will be performed in order to confirm the presence of the donor and acceptor in the same particles, and determine their localization in the NPs. Indeed, as shown in **chapter I**, phase separation occurring in composite NPs could result in either a Janus or core-shell morphology.

IV.1. UV-visible spectroscopy:

UV-visible absorption of the composites PF2:$PC_{71}BM$ NPs was performed and compared to the theoretical UV-visible absorption of calculated using the absorption spectrum of separate NPs. In this case, as reported in **Figure 11 A**, the UV-vis spectrum of a 1:1 composite NPs and the theoretical spectrum using the same ratio almost overlap, confirming that both materials are present in the composites NPs suspension and conserving their initial ratio, with no material loss during the process. In the case of PF2:ehIDTBR, the same observation could be made. Moreover, it is interesting to note that both materials have similar UV-visible spectra, PF2 spectrum being slightly shifted to higher wavelengths. The composite PF2:ehIDTBR 1:1 NPs show as expected intermediate absorbance between the two spectra (**Figure 11 B**).

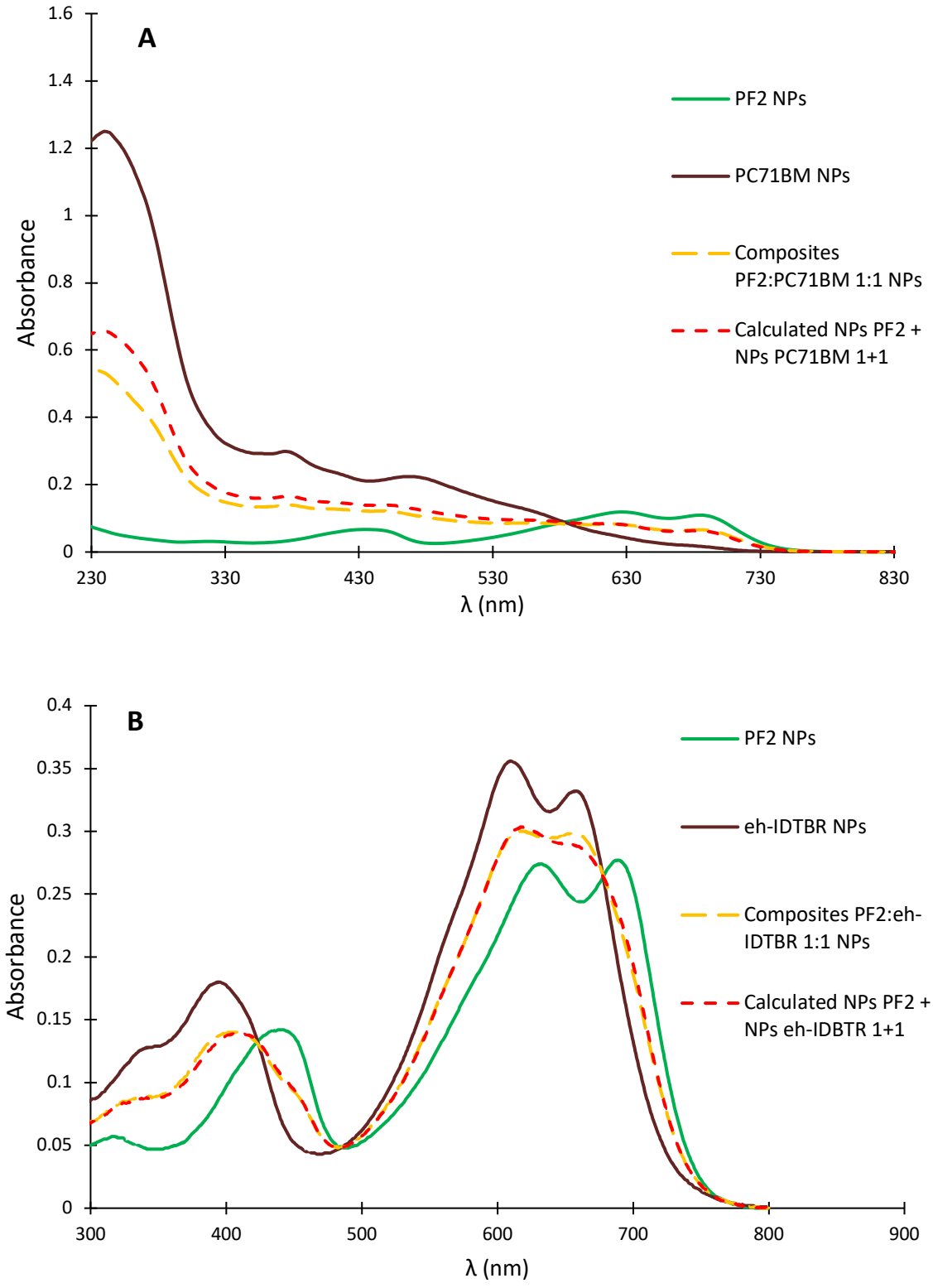

Figure 11 : UV-Visible spectra of different NPs Suspensions. Suspension concentration was set at 0.02 mg.mL^{-1}

IV.2 Fluorescence spectroscopy:

Steady state fluorescence spectroscopy was used as first option for composites NPs to confirm the presence of the donor and acceptor close to each other in the same particles. **Figure 12 A** shows the fluorescence spectra obtained by excitation at 630 nm, for PF2:$PC_{71}BM$ composite NPs dispersions with different ratio from 10/0 to 0/10. Only PF2 absorbs the light at 630 nm and fluoresces. It is clear that PF2 and $PC_{71}BM$ are located in the same particle, since PF2 fluorescence is almost quenched. In this case, charge transfer takes place between donor and acceptor.
To further support this statement, when PF2 and $PC_{71}BM$ are not enclosed in the same particles, as is the case when the separate PF2 and $PC_{71}BM$ NPs are mixed, the fluorescence decreases proportionally to PF2 NPs concentration (**Figure 12 B**), the total concentration remaining constant. PF2 NPs are thus replaced by an equivalent amount of $PC_{71}BM$ NPs. Hence, in mixed NPs case, charge transfer does not happen as the two materials are too far away in distinct NPs.

In the case of PF2:eh-IDTBR, the same experiments were performed but the interpretation is complicated by the fact that PF2 and eh-IDTBR have similar UV-vis absorption spectra. Both materials fluoresce when excited at 630 nm, but not with the same intensity. However, the two series of fluorescence emission spectra obtained for composites PF2:eh-IDTBR NPs(**Figure 12 C**) and the mixture of separate NPs (**Figure 12 D**) still show significant differences. The emission spectra of the mixture of separate NPs are all comprised between the emission spectra of eh-IDTBR and PF2. On the contrary, the intensity of emission spectra of the composite NPs, are all lower than the two spectra of the pure NPs. Adding at least 20 % of eh-IDTBR in the NPs seems to partly quench the fluorescence of PF2 but the emission spectra of the composites NPs are probably an addition of quenching and emission of the two materials. However, we can still conclude from the differences between both series of spectra that some charge transfer arises in the composite NPs due to the vicinity of the two materials in the same particles.

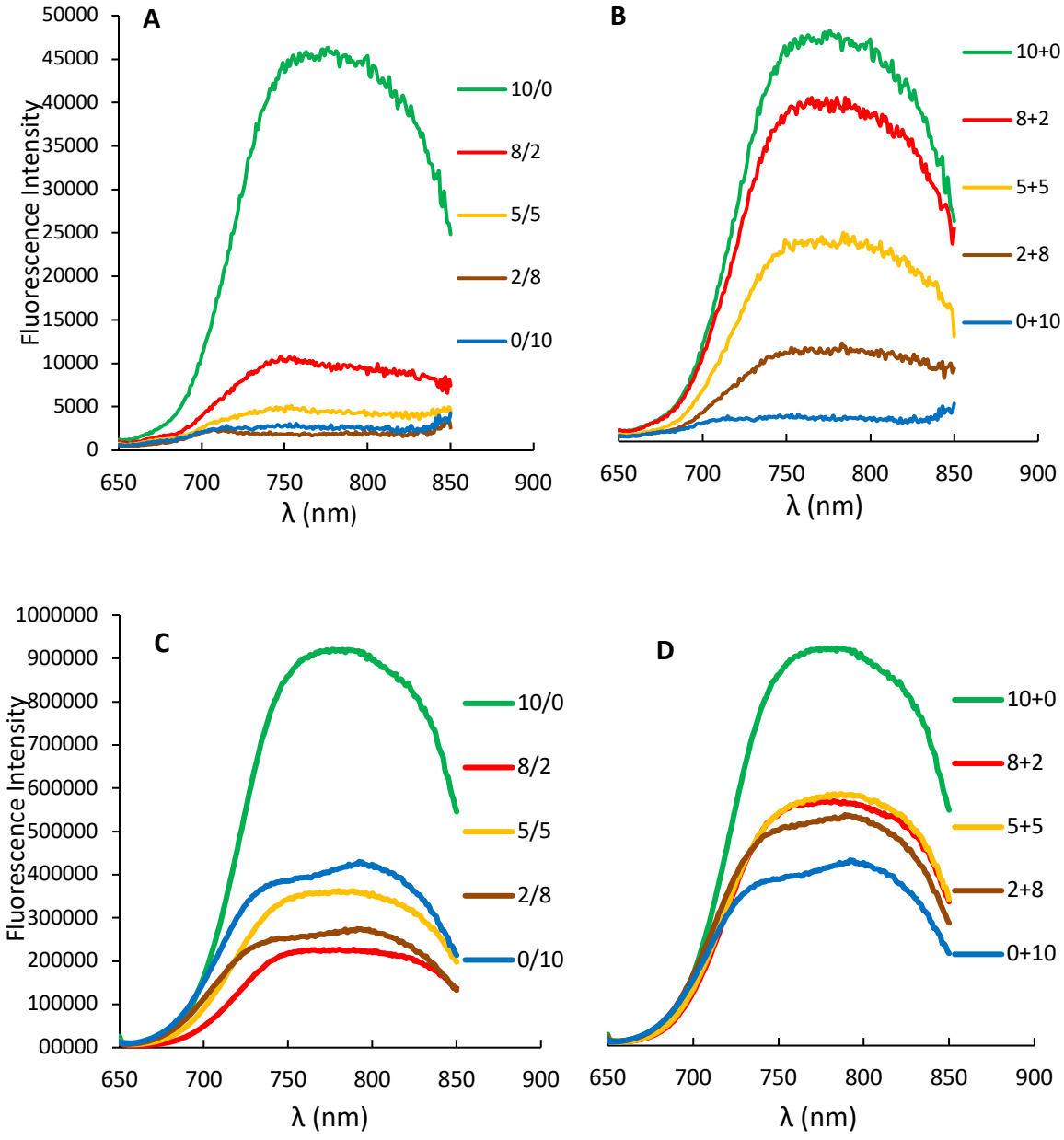

Figure 12: Fluorescence spectrum of different composites with different ratio: A)PF2:$PC_{71}BM$ or C) PF2:eh-IDTBR. Fluorescence spectrum of a mixture of separate NPs of PF2 and separate NPs of B) $PC_{71}BM$ or D) eh-IDTBR with different ratios. Excitation at 630 nm. Suspension concentration used = 0.002 $mg.mL^{-1}$

IV.3 Photoluminescence spectroscopy (PL):

Photoluminescence spectroscopy is a timed-resolved fluorescence technique that allows to estimate exciton lifetimes and show its decrease when a charge transfer occurs from the donor to the acceptor material.

Time-resolved PL of pure PF2 NPs and composite PF2: $PC_{71}BM$ NPs were studied for large particles of diameter 200 ± 70 nm and small particles of diameter 60 ± 20 nm.

Composite NPs with $PC_{71}BM$ content higher than 20 wt% were first tested. However, the intensity of PL was not high enough due to the important quenching and exciton lifetime was not measurable. Therefore, for PL measurements, new composites NPs containing less than 2 wt% of $PC_{71}BM$ were elaborated (**Figure 13**).

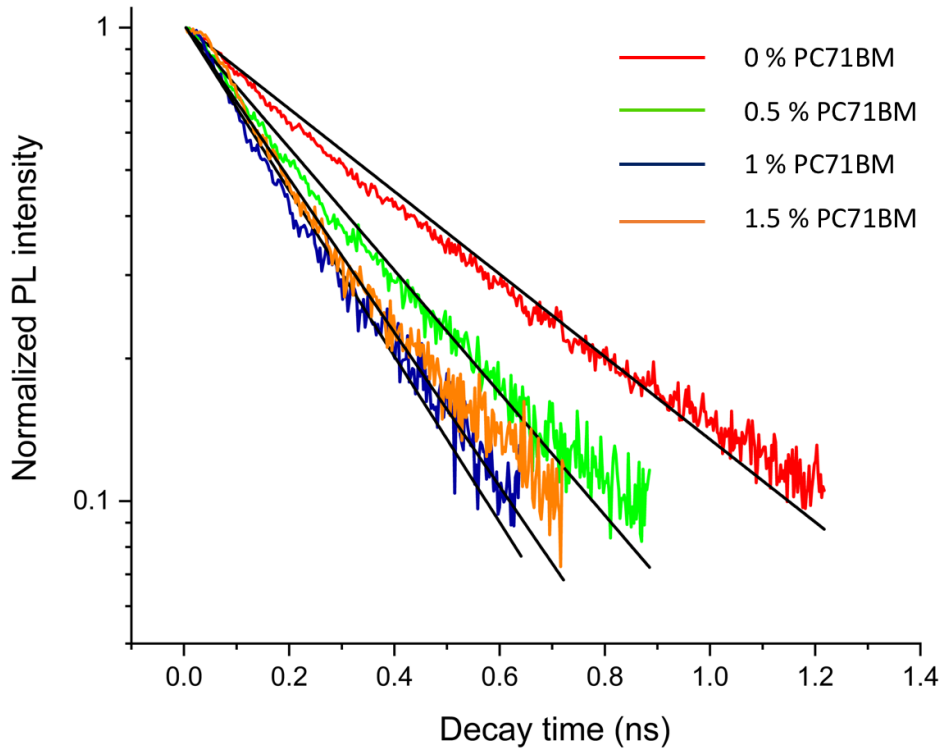

Figure 13: Normalized PL curve of pure PF2 separate NPs or PF2:$PC_{71}BM$ composites NPs with different ratio.
NPs diameter was measured by DLS 60 ± 20 nm. Excitation using a wavelength of 515 nm – pulse duration 90 ps.

The exciton lifetimes were obtained after data curve fitting using a simple exponential represented in the **equation 1**:

$$Y(fit) = Ae^{-Bt} \quad \text{(equation 1)}$$

where Y(fit) refers to the PL intensity, t refers to the time (ns) , A as a variable number and B (ns^{-1}) equivalent to 1/ τ.

SMALL NPs	$Y_{(fit)}$ = A*exp(-Bt)			LARGE NPs	$Y_{(fit)}$ = A*exp(-Bt)		
% PCBM	A	B	τ = 1/B	% PCBM	A	B	τ = 1/B
0	0,97	2,01	**0,5**	**0**	1,00	1,67	**0,60**
0,5	0,98	2,97	**0,33**	**0,5**	0,99	2,43	**0,41**
1	1,01	4,03	**0,25**	**1**	1,01	3,58	**0,28**
1,5	1,05	3,74	**0,26**	**1,5**	1,01	3,86	**0,26**

Table 3: Calculated lifetime (τ) for small or large – separated and composite PF2:$PC_{71}BM$ NPs

Theoretically, and according to equation 2, the inverse of tau (τ) represents the probability of de-excitation. The probability of radiative recombination $1/\tau_{rad}$ is intrinsic to the PF2 molecule, so it does not vary with the amount of $PC_{71}BM$. It is therefore the non-radiative ($\tau_{non\text{-}rad}$) recombination probability that increases with the quantity of $PC_{71}BM$ (quenching by dissociation of excitons at the Donor/Acceptor interface is more important). It means that when enough $PC_{71}BM$ molecules are added, non-radiative recombination by charge transfer to the $PC_{71}BM$ becomes predominant.

$$\frac{1}{\tau} = \frac{1}{\tau_{rad}} + \frac{1}{\tau_{non\,rad}} \qquad \textbf{(equation 2)}$$

Comparing the PL of pure PF2 NPs as a function of their diameter, it can be observed on **Figure 14** that the PL decreases more rapidly for smaller particles (τ = 0.6 ± 0.05 ns) than for larger particles (τ = 0.5 ± 0.05 ns). This could be explained by a lower surface-to-volume ratio for large particles, the proportion of non-radiative recombination at the surface is probably lower.

However, when $PC_{71}BM$ is added to the NP, whatever the diameter of the NPs, the measured τ decreases with the increase of the quantity of $PC_{71}BM$ to reach a value of 0.26 ± 0.05 ns in the case of PF2 composite NPs: $PC_{71}BM$ 98.5/1.5 (**Table 3**), dissociation of excitons at the donor/acceptor interface becoming preponderant.

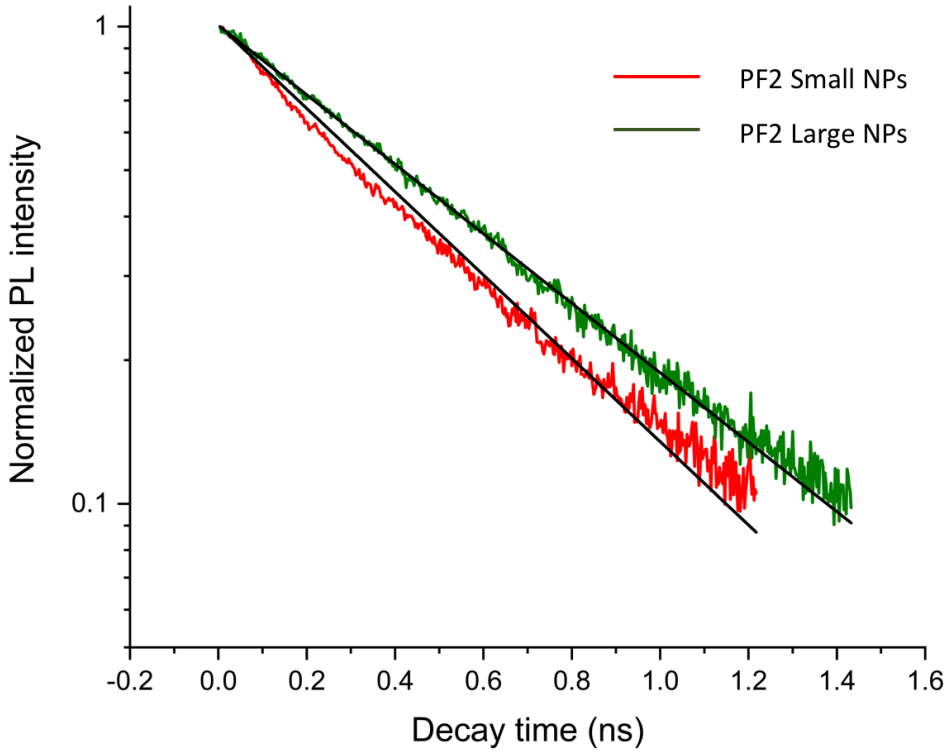

Figure 14: Normalized PL curve of larges pure PF2 NPs (green - NPs size 200 ± 70 nm) – Small pure PF2 NPs (red – NPs diameter 60 ± 20 nm). Excitation using a wavelength of 515 nm – pulse duration 90 ps.

IV.4 Transmission Electron Microscopy (TEM):

Above characterization methods confirm that both materials are localized in the same particle. TEM microscopy came to highlight the core shell structure of composite NPs made by PF2 and $PC_{71}BM$, as shown in **Figure 15 (a & b)** for large composite PF2: $PC_{71}BM$ 1:1.5 NPs, and on **Figure 15 (c & d)** for smaller composite NPs using the same composition. In fact, the contrast between PF2 and $PC_{71}BM$ was sufficiently high to observe a phase separation in the NPs and thus to prove the core-shell structure.

As opposed, in PF2:eh-IDTBR 1:1 large NPs composite case, structure identification by TEM studies seems challenging since no difference in contrast was found between both material (**Figure 15 e**).

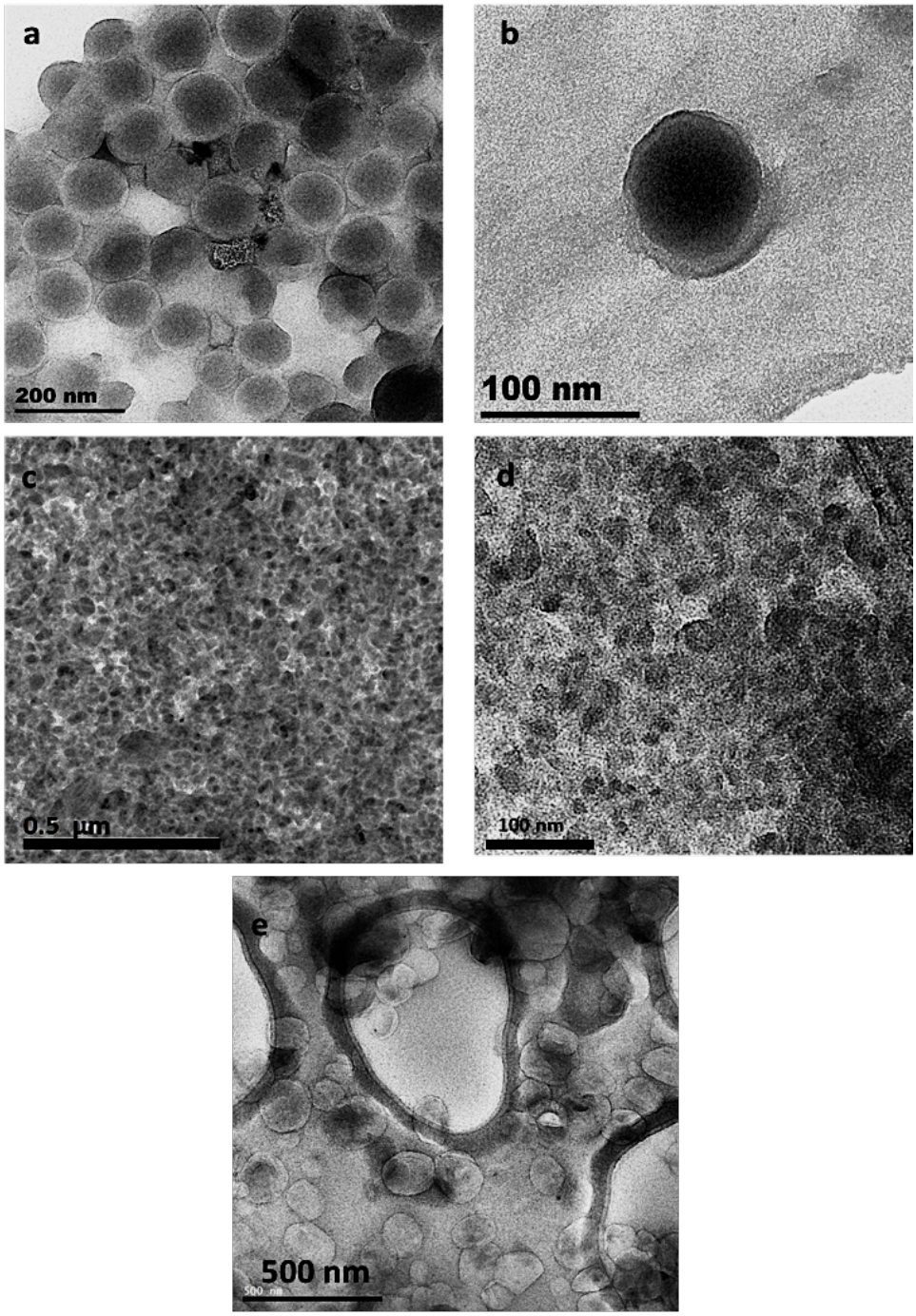

Figure 15: TEM image of a) an assembly of large composite PF2:$PC_{71}BM$ 1:1.5 NPs, b) one isolated composite PF2:$PC_{71}BM$ NP, c and d) an assembly of small composite PF2:$PC_{71}BM$ 1:1.5 NPs, e) assembly of large PF2:eh-IDTBR composites NPs.

However, it was not possible to identify from these images which compound is predominant in the core or in the shell of the nanoparticle. Barr *et al*[8], showed in a recent work that the internal structure of organic nanoparticles was controlled by the difference in surface energy of the electron donor polymer and the NFA material. The material having the lowest surface energy being located in the shell. In PF2 and $PC_{71}BM$ case, the measurement of their surface energy by tensiometry (see

chapter II), was respectively 30 $mN.m^{-1}$ and 47 $mN.m^{-1}$, with both materials having a very small (<1 $mN.m^{-1}$) polar component. Therefore, the fluorinated polymer should be preferentially located in the shell while fullerene acceptor occupies the core.

In the case of eh-IDTBR, the surface energy measured of 24 $mN.m^{-1}$ was slightly smaller to the one of the PF2, with a slightly higher polar component of 4 $mN.m^{-1}$, which would mean that either a Janus or a core-shell structure should be obtained with eh-IDTBR preferentially located in the shell.

In order to confirm these hypotheses and measure the purity of the two phase separated domains, scanning transmission X-ray microscopy (STXM) was performed on the composite NPs at the HERMES beamline of Synchrotron SOLEIL.

IV.5 Scanning transmission X-ray Microscopy (STXM):

STXM is a Spectro-microscopic scanning technique, using the focalization of an X-ray beam from synchrotron radiation sources. This technique allows to map the chemical composition of thin materials, the chemical contrast been obtained thanks to differences in the Near Edge X-ray Absorption Fine Structure (NEXAFS) of the materials.

The NEXAFS spectra of different materials used at the C K-edge are given in F**igure 16.**

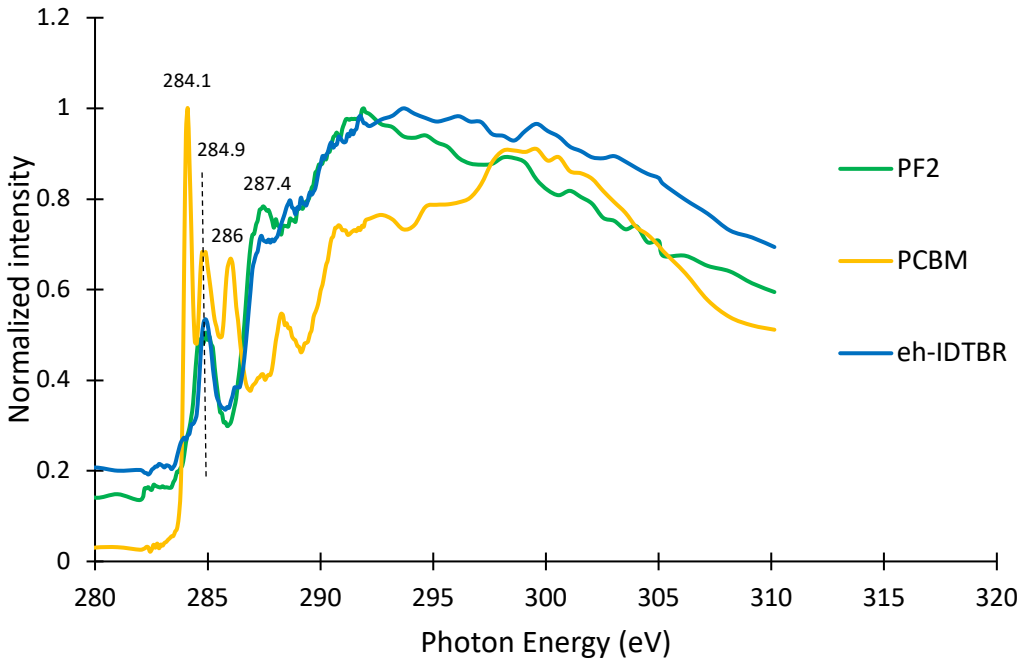

Figure 16: C K-edge - near edge x-ray absorption fine structure (NEXAFS) spectra of reference films spin coated on a glass substrate, yellow line: $PC_{71}BM$, blue line: eh-IDTBR, green line: PF2.

As observed in **Figure 16**, sufficient absorption contrast between NEXAFS spectra of PF2 and $PC_{71}BM$ are obtained with important absorption peaks at 284.1 and 286.0 eV for $PC_{71}BM$, while PF2 absorbs at 284.9 and 287.4 eV. On the contrary, NEXAFS spectra of PF2 and eh-IDBTR almost overlap, with only small difference of absorption at 287.4 eV. This poor contrast between the two components makes it difficult to identify them on the STXM images as shown below.

Finally, one should also note that the spatial resolution of the STXM used is of 19 nm. Therefore, in order to get sufficient insight on the internal morphology of the NPs, only large composite NPs could be observed by this technique. We have thus prepared large composite NPs with an average diameter of 200 nm.

IV.5.A Composition maps of composite PF2:$PC_{71}BM$ NPs:

In the case of PF2: $PC_{71}BM$ NPs, SVD analysis of the energy stacks, taking into account the reference NEXAFS spectra of the pure components, resulted the two thickness maps with a very small residual. They can then be further analyzed as described in **Chapter II**. leading to composition maps (**Figure 17**). As for TEM images, the STXM composition maps show the core-shell structure of the particles. From these maps, it is this time easy to deduce which component is present in the core and in the shell. Indeed, these particles are made of a $PC_{71}BM$ -rich core and a PF2-rich shell as could be predicted from the measured surface energies of the $PC_{71}BM$ (47 $mN.m^{-1}$) and PF2 (30 $mN.m^{-1}$).

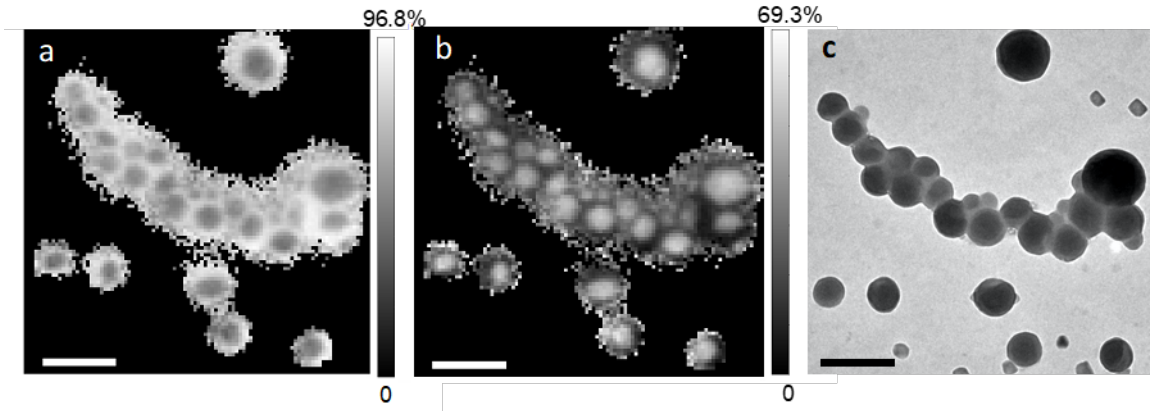

Figure 17: PF2: $PC_{71}BM$ 1:1 nanoparticle without annealing. a) STXM PF2 composition map, b) STXM $PC_{71}BM$ composition mat, c) TEM images of the same group of particles. Scale bar: 400 nm.

STXM being a transmission method, the composition maps give the composition of the two components for each pixel through the entire particle. The composition profiles of the particles were then measured for each particle and fitted with a core-shell model in order to calculate the relative radius, and the real composition of the $PC_{71}BM$ -rich core and the PF2-rich shell. The analysis

is described in **chapter II**, and results obtained from analysis of around 10 particles per sample are given in **Table 4**. The measurements were performed for dialyzed suspension of PF2:$PC_{71}BM$ 1:1 composite nanoparticle without annealing (**Figure 17**) or after annealing for 10 min at 150°C (**Figure 18 a & b**) and of PF2: $PC_{71}BM$ 1:2 composite nanoparticles without annealing.

	Thermal annealing	Relative core radius	PF2 in core (wt%)	PF2 shell (wt%)
PF2:$PC_{71}BM$ 1:1	no	0.59 ± 0.07	33 ± 11	75 ± 7
PF2:$PC_{71}BM$ 1:1	150°C / 10 min	0.54 ± 0.17	35 ± 11	58 ± 8
PF2:$PC_{71}BM$ 1:2	no	0.63 ± 0.11	29 ± 10	76 ± 4

Table 4: Results obtained from the fit of the particles profile using a core-shell particle model.

The fitting of the compositions profiles of the particle was rather difficult as the particles we used add diameters of around 200 nm and the resolution of the STXM was about 19 nm, which explains the errors obtained. Finally, no significant difference was obtained between the PF2: $PC_{71}BM$ 1:1 and 1:2 NPs. Both particles have a $PC_{71}BM$ -rich core containing around 70 wt% of $PC_{71}BM$ and 30 wt% of PF2, and a PF2-rich shell with 25 wt% $PC_{71}BM$. However, a significant difference was observed for the composition of the PF2-shell after annealing at 150°C during 10 min. In this case, $PC_{71}BM$ seems to migrate into the PF2-shell, its content increasing to 42 % $PC_{71}BM$. We can thus conclude that during annealing, the $PC_{71}BM$ is able to diffuse through the shell, which should allow an increase of the percolations path for the electrons transport towards the electrodes.

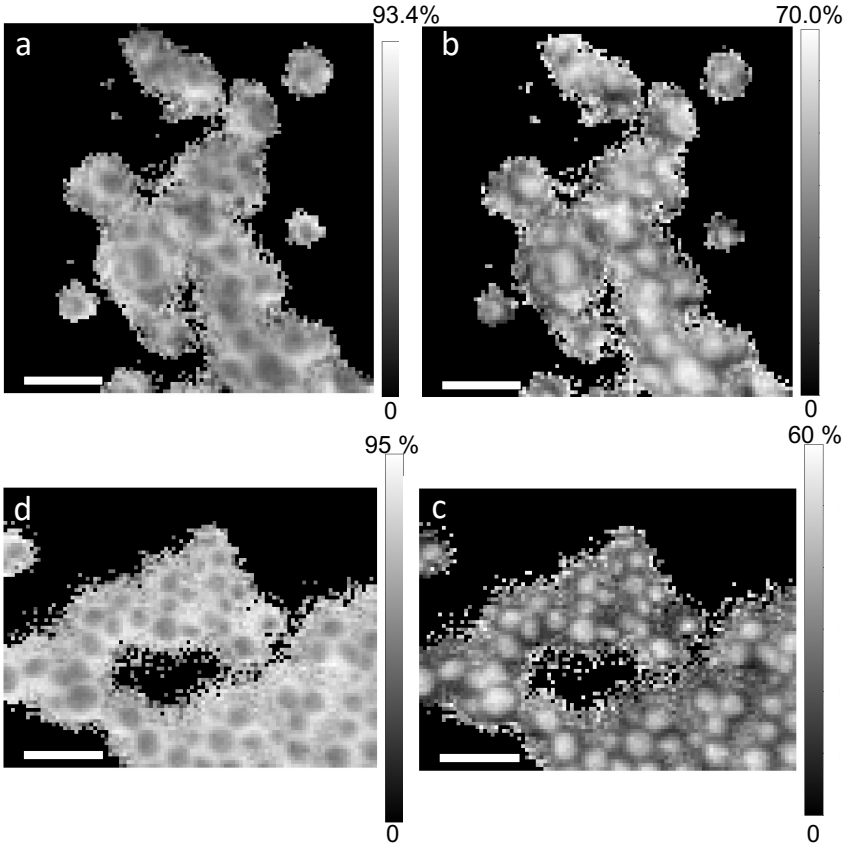

Figure 18 : STXM analyses. a) PF2 and b) $PC_{71}BM$ composition maps of PF2: $PC_{71}BM$ 1:1 NPs after annealing 10 min at 150°C; c) PF2 and d) $PC_{71}BM$ composition maps of PF2: $PC_{71}BM$ 1:2 NPs without annealing. Scale bar: 400 nm

IV.5.B Composition maps of composite PF2: eh-IDTBR NPs:

In the case of PF2:eh-IDTBR NPs, the poor absorption contrast between the two components makes the SVD analysis of the STXM energy stacks difficult, resulting in poorly defined thickness maps as shown in **Figure 19**. Therefore, it was not possible to analyze these experiments in order to obtain reliable composition maps.

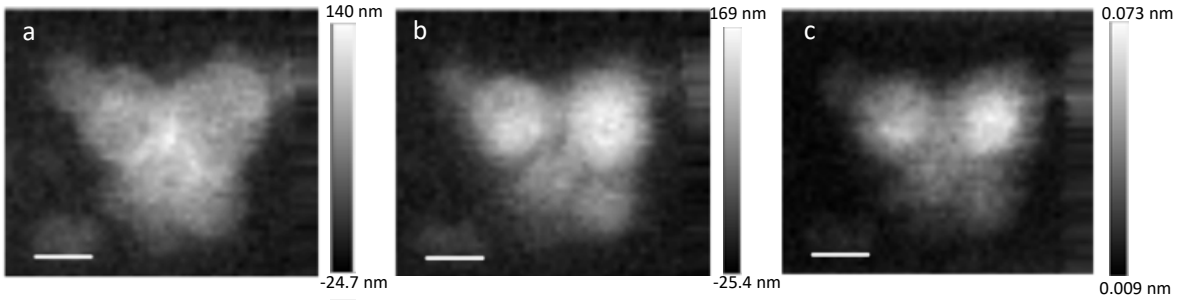

Figure 19: STXM images of a)PF2 regions and b) eh-IDBTR regions, c) residual, taken from composites larges PF2:eh-IDTBR composites 1:1 NPs – scale 200nm.

V. Conclusion:

Finally, in this Chapter, we have shown and optimized the elaboration of different types of NP using the miniemulsion evaporation technique.

Separate NPs of PF2, $PC_{71}BM$ and eh-IDTBR as well as the composite PF2:$PC_{71}BM$ and PF2:eh-IDTBR were prepared. We were able to tune the diameter of the NPs from 60 ± 20 nm to 180 ± 50 nm and the donor: acceptor ratios in composite NPs.

The composite NPs were then characterized showing their core-shell morphology with $PC_{71}BM$-rich domains in the core and PF2-rich domains in the shell of the NPs. Regarding the OPV application, this core-shell structure is not the more favorable, as percolation path of the two components should be present in the active layer film from one electrode to the other. However, STXM measurements showed that the core and shell domains are not pure in the NPs. Indeed, the core of the NPs contains around 70% of $PC_{71}BM$ and 30% of PF2, while the shell contains around 25% of $PC_{71}BM$ and 75% of PF2. The amount of $PC_{71}BM$ in the shell should be high enough to ensure the transport of electron towards the electrodes. We also observed the diffusion of the $PC_{71}BM$ into the shell of the NP upon thermal annealing.

In the case of PF2:eh-IDTBR NPs, the morphology of the NPs is more difficult to determine as there is only a poor contrast between the two materials in TEM or STXM. However, we also expect a core-shell morphology of the NPs with phase separation domains that are probably not pure either.

In the following chapter, thin films will be elaborated from the composite NPs and used as active layers in optoelectronic devices. The charge mobilities (hole and electron) will thus be measured in the plane (OFET) and out of plane (SCLC) as a function of thermal annealing. Finally, OPV devices will be prepared with the PF2:$PC_{71}BM$ NPs suspensions.

VI. References:

1. Ibraikulov, O. A. *et al.* Face-on orientation of fluorinated polymers conveyed by long alkyl chains: a prerequisite for high photovoltaic performances. *J. Mater. Chem. A* **6**, 12038–12045 (2018).
2. D'Olieslaeger, L. *et al.* Tuning of PCDTBT:PC71BM blend nanoparticles for eco-friendly processing of polymer solar cells. *Sol. Energy Mater. Sol. Cells* **159**, 179–188 (2017).
3. Prunet, G. *et al.* Aqueous PCDTBT:PC_{71}BM Photovoltaic Inks Made by Nanoprecipitation. *Macromol. Rapid Commun.* 1700504 (2017) doi:10.1002/marc.201700504.
4. Pras, O. *et al.* Photoluminescence of 2,7-Poly(9,9-dialkylfluorene- *co* -fluorenone) Nanoparticles: Effect of Particle Size and Inert Polymer Addition. *Langmuir* **26**, 14437–14442 (2010).
5. Zhong, Y., Biniek, L., Leclerc, N., Ferry, S. & Brinkmann, M. Segregated versus Disordered Stacking in Two Low Bandgap Alternated Copolymers for Photovoltaic Applications: Impact of Polymorphism on Optical Properties. *Macromolecules* **51**, 4238–4249 (2018).
6. Olla, T. *et al.* Benzothiadiazole Halogenation Impact in Conjugated Polymers, a Comprehensive Study. *Macromolecules* **52**, 8006–8016 (2019).
7. Landfester, K., Bechthold, N., Tiarks, F. & Antonietti, M. Formulation and Stability Mechanisms of Polymerizable Miniemulsions. **32**, 7 (1999).
8. Barr, M. G. *et al.* Nanomorphology of eco-friendly colloidal inks, relating non-fullerene acceptor surface energy to structure formation. *Mater. Chem. Front.* **5**, 2218–2233 (2021).

CHAPTER IV
FROM FILMS TOWARDS OPTOELECTRONIC DEVICES

I. Introduction :

As we mentioned previously, the final objective of this thesis work is to elaborate optoelectronic devices based on semiconducting NPs. In the third chapter, we have established an optimal amount of SDS in the aqueous solution allowing the synthesis of the smallest NPs using minimum quantity of surfactant (concentration set at 4 $mg.mL^{-1}$). In the meantime, accurate characterizations of NPs structure and morphology highlighted the core shell structure of composites NPs made up of PF2 and $PC_{71}BM$, with a 75 %wt PCBM-rich core and a 70 %wt PF2-rich shell.

This chapter presents the different steps to achieve in order to obtains photovoltaic devices from the NP suspensions. First the ionic surfactant needs to be removed by dialysis. Then, the current advances in the deposition of thin films from suspensions will be presented. Several parameters need to be screened in order to obtain the best possible thin films, such as the suspension concentration, the volume of deposited ink, the process parameters (acceleration, speed …), the drying parameters and so on.

The hole and electron mobility will then be measured in the film as a function of the film structure, modified by thermal annealing. Indeed, the photovoltaic device working principle requires to get within the film a bicontinuous network for holes and electrons diffusion towards the electrodes, with domains sizes of approximately twice the exciton diffusion length (15 – 25 nm). As discussed in **chapter I**, in the case of films obtained from NPs, especially of core-shell type, this morphology can be obtained by applying post-deposition thermal annealing. In addition, thermal annealing could help to make the film more homogeneous by merging the neighboring NPs.

Finally, the first results for the development of photovoltaics devices will be described at the end of this chapter.

II. Active layer deposition using NPs made by miniemulsion:

II.1 SDS elimination by centrifugal dialysis:

As discussed in the introduction, the amount of surfactant must be optimized for photovoltaic applications. Indeed, the surfactant insulating nature could negatively impact the photovoltaic performance if it is present in too large a quantity. Moreover, SDS being an ionic surfactant, it could impede the charge transport by acting as charge trap [(1)]. For these reasons, the excess of SDS surfactant molecules, present either in the suspension as micelles or single molecule or in excess at the NPs surface should be removed before active layer deposition [(2)].

To achieve this goal, we used centrifugal dialysis. In brief, the suspension containing NPs was washed many times with MQ water. It is a long process. The SDS quantity which remains in suspension was evaluated by conductimetry after each step. The initial SDS concentration used is well above its critical micellar concentration (2.35 $mg.mL^{-1}$)[3]. Consequently, the presence of SDS micelles with diameter below 10 nm in these suspensions is expected.

Figure 1 presents the size distribution of PF2 simple NPs non-dialyzed (solid line) in water. We can see a peak around 4 nm. As it clearly disappears after 16 washing steps using centrifugal dialysis (dashed line), we can suggest that this small diameter distribution is relative to SDS micelles in water. Also, it may be concluded from these spectra that NPs are stable all along the dialysis, as their average diameter remains around 70 ± 30 nm after dialysis.

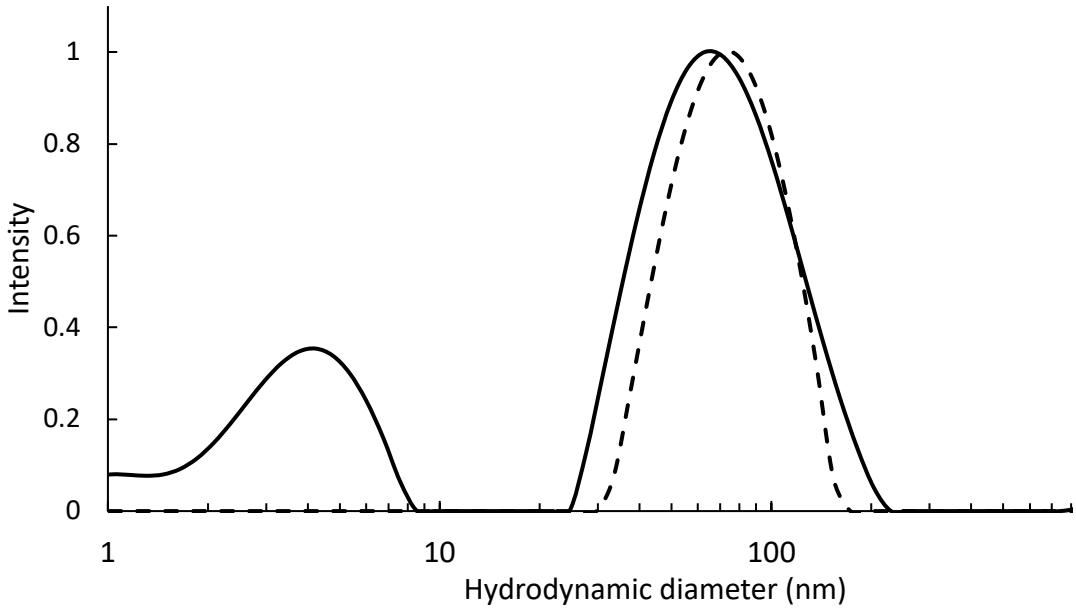

Figure 1: Simple NPs of PF2 – before (solid line) and after dialysis (dashed line)
$\phi_{organic}$ = 36%, [SDS] = 4 $mg.mL^{-1}$

II.2 SDS amount estimation via conductimetry measurements:

Conductimetry enables to estimate approximately the remaining SDS amount into the suspension after centrifugal dialysis. A calibration curve was first obtained by measuring the conductivity of SDS aqueous solution as a function of its concentration, as shown in the **Figure 2**.

In addition, **Figure 3** presents the conductivity values of the suspension measured as a function of the number of dialysis steps. In fact, we can clearly see that the conductivity decreases significantly during the first 10 washes and decreases more slowly for the last centrifugal dialysis steps. These

measurements have been carried out on a suspension of simple PF2 NPs including an initial concentration of SDS in water of 4mg.mL^{-1}.

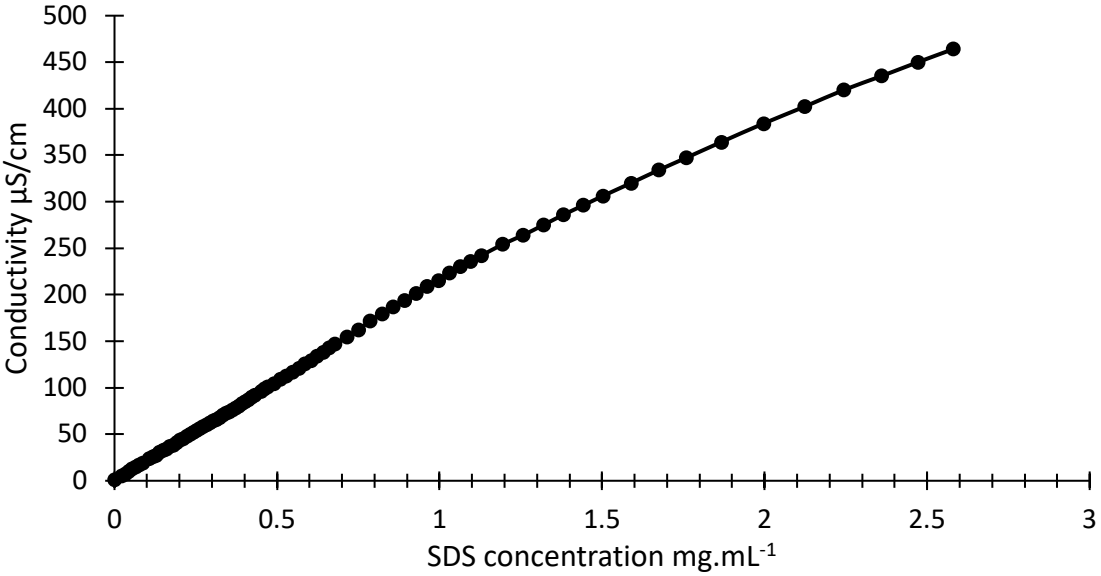

Figure 2: conductivity of MQ-Water after SDS/water solution addition

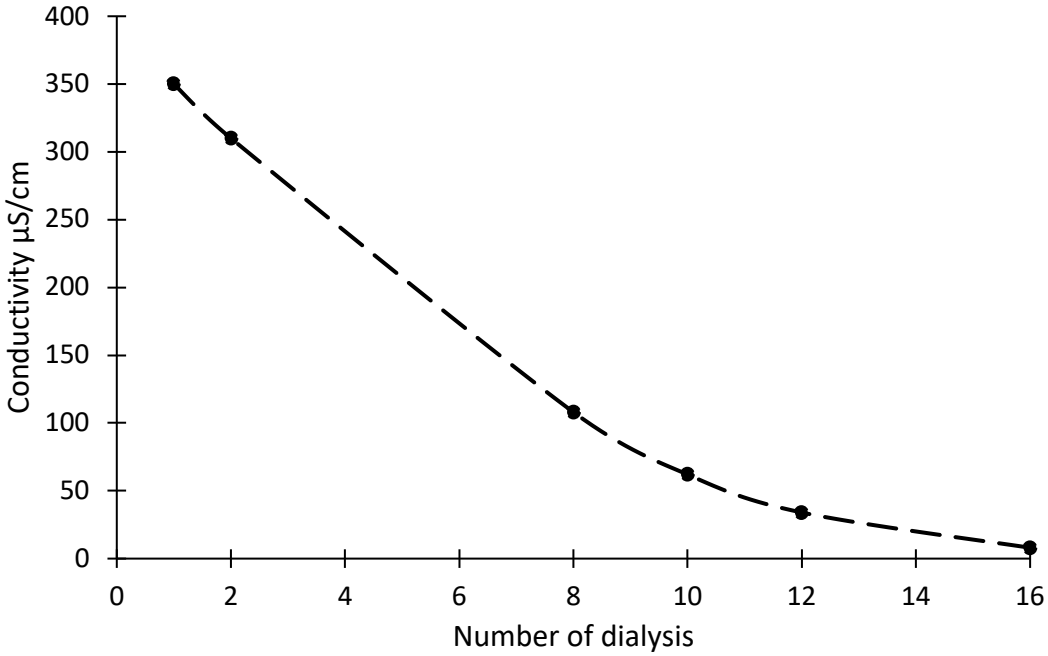

Figure 3: Suspension conductimetry values after several centrifugal dialysis

Referring to **Figure 2**, we estimated the concentration of SDS remaining in the suspension after sixteenth dialysis (0.032 mg.mL^{-1}). Combined with the disappearance of the peak seen in **Figure 1** at 4 nm of diameter, we can conclude on the efficiency of this multi-steps dialysis process for SDS

to remove excess surfactant from the suspension. However, ATG measurements of lyophilized dialyzed NPs suspensions showed the around 20% wt of SDS still remains in the NPs, corresponding approximately to a dense SDS monolayer at the surface of the NPs. The dialyses steps only allows to remove the SDS from the aqueous phase, without desorbing it from the NPs surface as had been observed by Bag *et al.* by measuring the zeta potential of the NPs before and after dialysis [(1)].

II.3 Active layer (film) deposition via spin coating:

Two main methods, spin coating and doctor blading, were then employed to deposit the active layer from the NPs suspension. The low viscosity of the suspensions combined with the variable hydrophilicity of interfacial layers used (PEDOT-PSS or ZnO), make the deposition of homogeneous active layers complex. In addition, because of relatively low solid content of our suspensions, it is required to deposit two or three times the same suspension on the top of each other in order to reach thick enough active layers. The **Figure 4** illustrates the different contact angles measured for the same suspension deposited on different sub-layers.

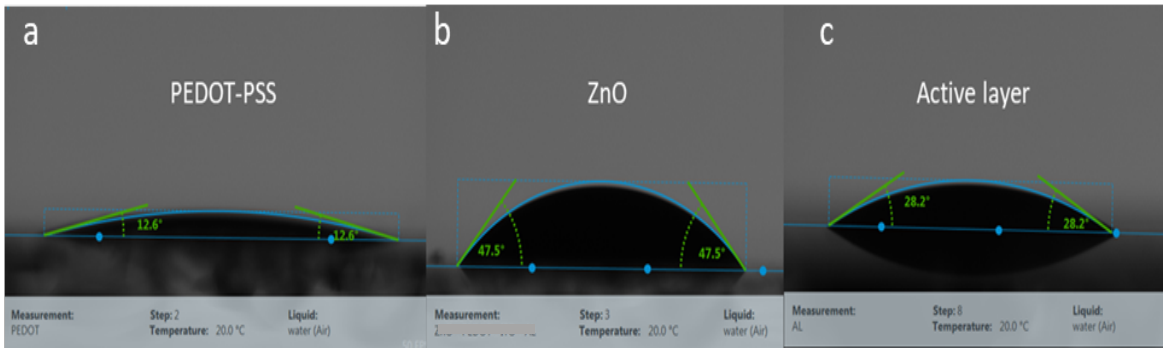

Figure 4: contact angle measured for a drop of 1.75 wt% dialyzed composites PF2:$PC_{71}BM$ NPs-based suspension deposited on a a) PEDOT-PSS interfacial layer (12°), b) Zno interfacial layer (47°), c) first layer of active materials (28°).

Therefore, a large number of attempts were done to improve the homogeneity of the active layer, made by PF2:$PC_{71}BM$ NPs, and to tune its thickness.

We started by using the doctor blade method to deposit the water suspension. The doctor blade method consists in a blade that moves relatively to a substrate. This movement spreads on the substrate the liquid initially deposited in front of the blade. The thickness is adjusted by adjusting several parameters, such as the deposition temperature, the ink concentration, the gap between the blade and the substrate, the solvent boiling point… As expected, the low evaporation rate of water implies a very different behavior than the one usually observed with highly volatile organic solvent-based solutions, such as $CHCl_3$ or THF. Slow volatilization of water, even upon substrate

heating, results in a not fully covered substrate. In addition, the deposited film presents strong ripples synonymous with a non-homogeneous thickness (**Figure 5**).

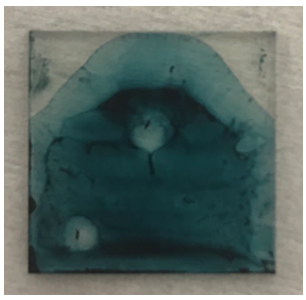

Figure 5: example of doctor blade deposition. Drop of 60 µL of a suspension of pure PF2 NPs with a concentration of 17.5 mg.mL^{-1}. Blade speed of 10 mm/s

Different parameters where modified in order to increase the film quality, such as:

- modulating the blade speed from 6 mm/s to 49 mm/s to enhance the suspension spreading,
- heating the suspension in order to increase the water evaporation rate,
- adding volatile solvent to the suspension (ethanol or isopropanol) to increase the solvent evaporation,
- increasing the drop volume from 20µL to 100 µL to fully cover the substrate,
- varying the suspension concentration from 5 mg.mL^{-1} to 20 mg.mL^{-1}.

In fact, none of these modifications has led to a significant and satisfying improvement of thin-film homogeneity.

We thus switched on to the spin coating method. It consists in depositing uniform thin films onto substrates by spreading a material in solution upon a centrifugal force at high spinning speed. The applied solvent is usually volatile and evaporates simultaneously to the spinning process. The thin-film thickness is adjusted by modulating several parameters, such as the spinning speed, the ink concentration, the deposition temperature, the solvent boiling point, the spinning acceleration…

In our case, many parameters have been varied to reach thick enough and homogeneous films (see illustration in **Figure 6-right**):

- Spinning speed: the rotation speed is usually ranging between 500 rpm and 5000 rpm. We observed that a high speed leads to a better surface coverage, but also to a thinner film. While a low speed (below 750 rpm) results in a bad suspension spreading. We found the speed of 1000 rpm combined with a low acceleration of 100 rpm/s to be a good compromise allowing the elaboration of homogeneous films of satisfying thickness.
- Suspension concentration/viscosity: high concentration (above 20 mg.mL^{-1}) required extra preparation time and do not lead to significant film thickness variations. In contrast low concentration (below 5 mg.mL^{-1}) make the suspension viscosity too low, increasing its

ejection from the substrate. Finally, an optimal concentration has been established to 17.5 mg.mL^{-1}.

- Drop volume using a suspension of 17.5 mg.mL^{-1}: the drop volume is usually ranging between 50 µL and 200 µL. We found that above 100 µL, the thickness is independent of the volume. In our case, 80 µL was adequate to cover the whole substrate. Below this optimal volume, there is a risk of not covering the entire surface.

The spin-coating deposition is also strongly depending on some parameters that could be difficult to quantify. For instance, in our case, we observed on some samples, a kind of coffee stain effect *i.e.* a pattern left by the water evaporation. In order to avoid this effect, we found that a very quick handling of the spin-coater was necessary after the suspension drop was deposited on the surface.

Figure 6 illustrates the improvement of the active layer quality deposition.

Figure 6: left: first attempts for film elaboration using spin coating, right: best homogeneous and thick film achieved after many tries – thickness of 70 nm was obtained.

Finally, we were able, using optimal parameters (suspension concentration of 1.75wt %, drop volume of 80 µL and spinning speed of 1000 rpm), to obtain homogenous films by spin coating, with a thickness around 70 nm for one deposited layer (a profilometer was used for thickness measurements). In addition, by applying a multi-steps deposition approach (keeping the same process parameters), thicknesses of 140 nm and 200 nm have been reached for 2 and 3 successive deposited layers, respectively **(Table 1- Figure 7 films**).

Number of depositions (layers)	Thickness (nm)
1	70 ± 10
2	140 ± 10
3	200 ± 15

Table 1: thickness of films based on PF2:$PC_{71}BM$ NPs inks. Films were obtained by spin coating at 1000 rpm using 80 µL of a 1.75 wt% suspension

III. Film characterization:

Although the eye can be a good detector to quickly have an opinion on the thin-film homogeneity, a further deep characterization is mandatory. For instance, Atomic Force Microscopy (AFM) allows to obtain information at the scale of the NPs, regarding the interactions between neighboring NPs, the homogeneity and film roughness, which is a key parameter. Indeed, high roughness generally results in poor contact between the active layer and the top electrode, decreasing significantly the device efficiency and reproducibility. Further, a roughness of the same order of magnitude as the active-layer device thickness will lead to short-circuited devices. Another useful technique is Grazing Incidence Wide Angle X-ray Scattering (GIWAXS), which gives information at the molecular scale, on the aggregation and orientation of the molecules in the film. These parameters are key parameters to understand the charge mobility inside the film.

III.1 Atomic force microscopy (AFM):

AFM was used to map the topography of the thin-film surface. By mapping a small area of the film, the shape, size and structure of the NPs as well as the film roughness can be easily determined.

❖ Multilayer deposition:

Figure 7 represents the AFM images recorded for a substrate on which we have deposited up to 3 successive layers of PF2:$PC_{71}BM$ (ratio of 1:2) NPs, using the conditions discussed above. Regardless of the number of spin-coated layers, one can clearly see closely packed NPs. In addition, the films topology seems very flat since the average film roughness was found to be around 20 nm for all samples. This low roughness value was probably favored by the polydispersity of NPs diameter, as seen previously by DLS. Indeed, DLS measurements showed an average hydrodynamic diameter of 60 nm with 20 nm of standard deviation.

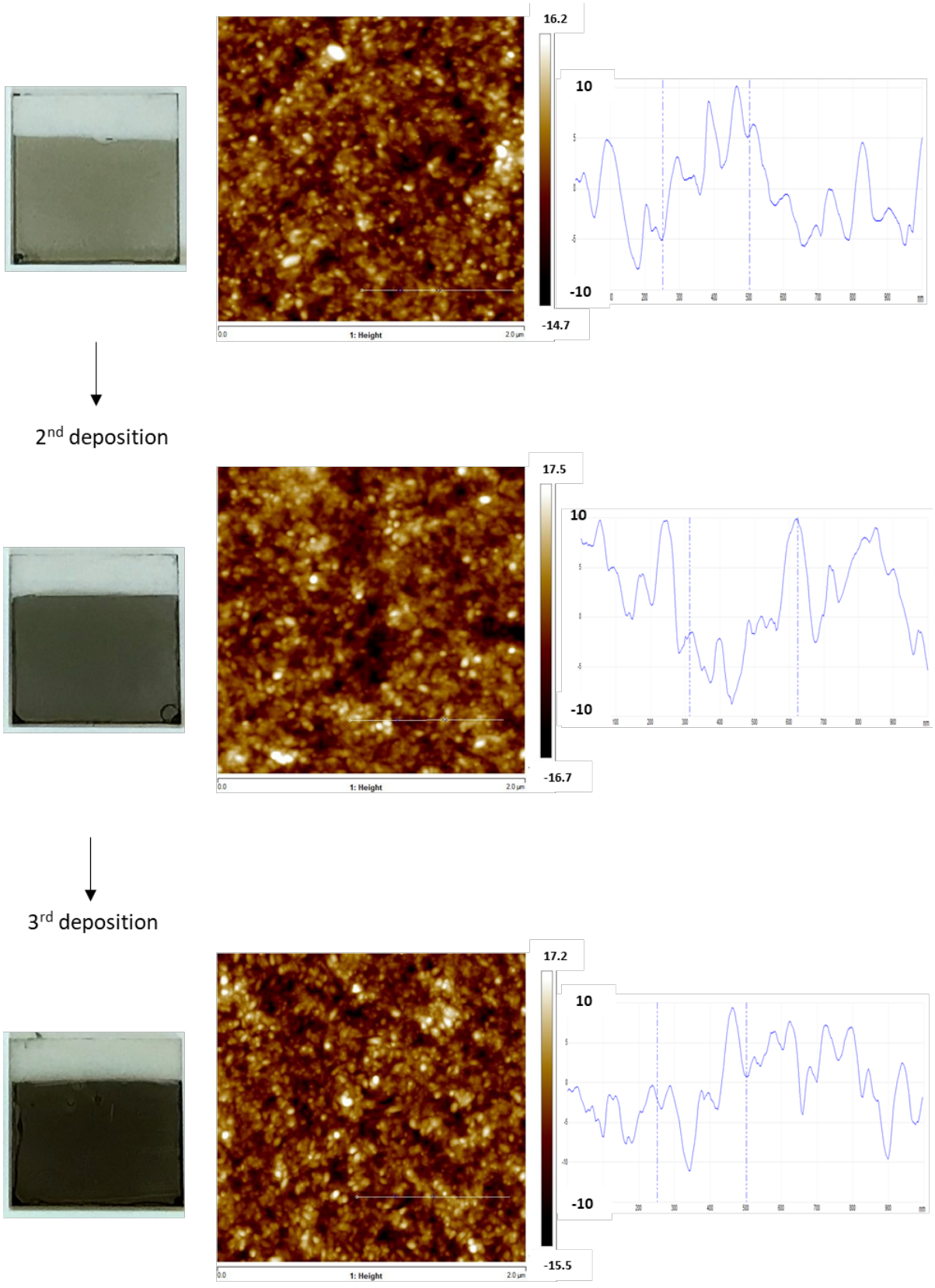

Figure 7: images of thin films after one, two and three deposited layers made by spin coating, with average film thickness 70, 140 and 200 nm, respectively. AFM height images (2µm x 2µm) with their roughnesses.

❖ Thermal annealing:

Referring to **chapter I** and **III**, annealing is a key step that could:

- improve the contact between the particles by creating more interfaces.
- increase the interface surface between both materials (PF2 and $PC_{71}BM$) within the same particle by interdiffusion of the two components.
- modify the film roughness.

AFM images (**Figure 8**) of a film elaborated from PF2:$PC_{71}BM$ 1:2 NPs confirm the above hypothesis. Indeed, the surface roughness of the non-annealed film (20 nm) decreases down to 10 nm after thermal annealing at 120°C for 10 minutes. Additionally, a slight coalescence of neighboring NPs is noticed. In contrast, further isochronal annealing at 160°C for 10 minutes also makes the film very rough (roughness of 100-150 nm). This behavior could be related to structural phase changes that may be due to co-crystallization of both materials as discussed in the next part.

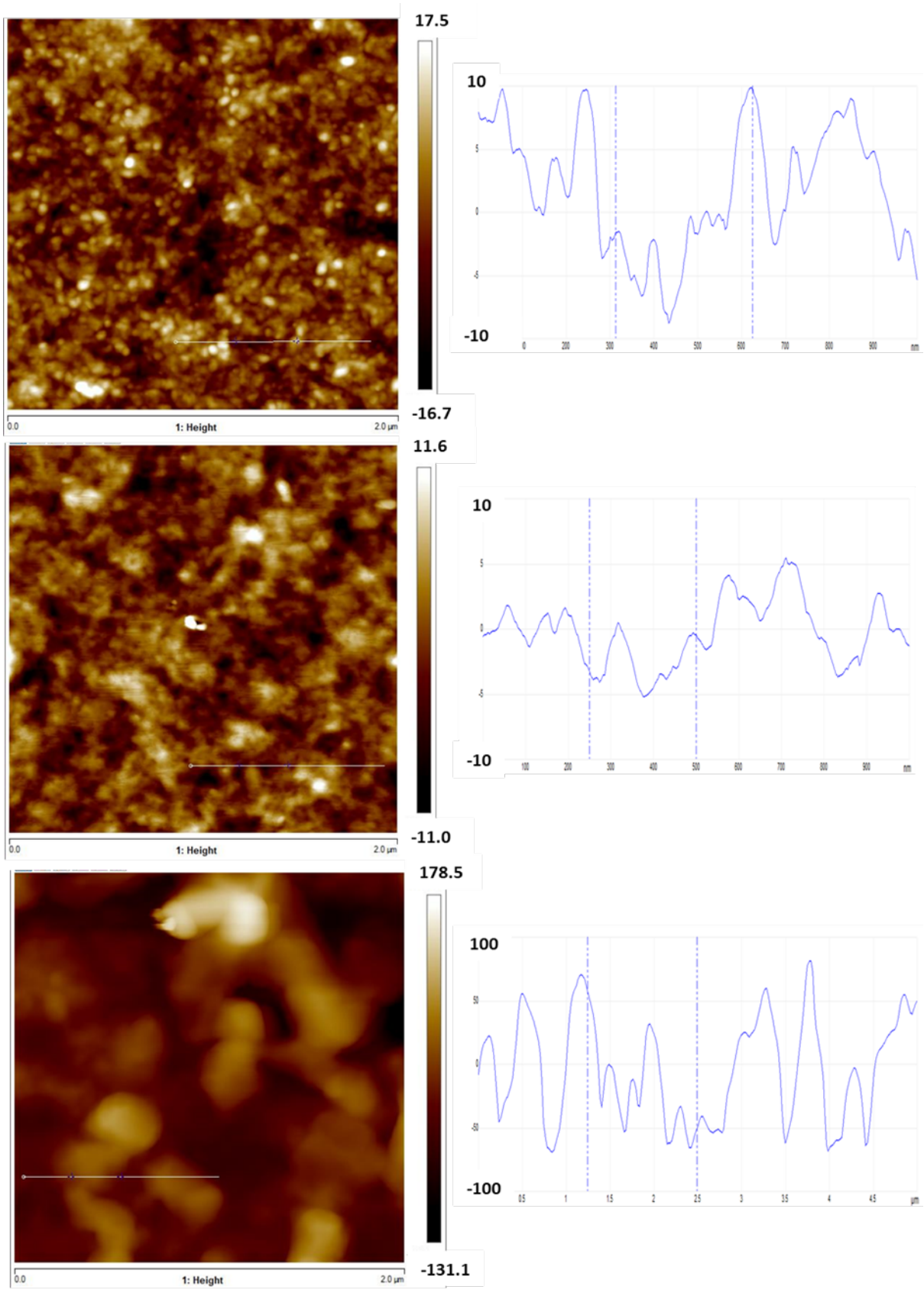

Figure 8: AFM height images of thin-films with or without thermal annealing - film thickness of 140 nm (top not annealed – middle 120°C - bottom 160°C°) scale: 2µm x 2µm

III.2 Grazing incidence wide angle X-ray scattering (GIWAXS):

Grazing incidence wide angle X-ray scattering (GIWAXS) was used to characterize the structure and morphology of the donor PF2 and the acceptor $PC_{71}BM$ materials within the thin films. First, thin films made of bulk materials or NP suspensions have been elaborated and characterized in order to be compared. Secondly, thermal annealing effect on NP-based films was applied and studied by GIWAXS.

Figure 9 presents the GIWAXS patterns of pure PF2-based films elaborated from standard organic solutions. **Figure 9-left** is relative to pristine films while **Figure 9-right** is relative to the film after a thermal annealing at 150°C. In both cases, we can notice the co-existence of two populations of PF2 lamellas, oriented with respect to the substrate, either edge-on (blue label) or face-on (red label) (see **Figure 10** for an orientation illustration). However, an increase of edge-on proportion is clearly noticed after annealing at 150°C (**Figure 9-right**).

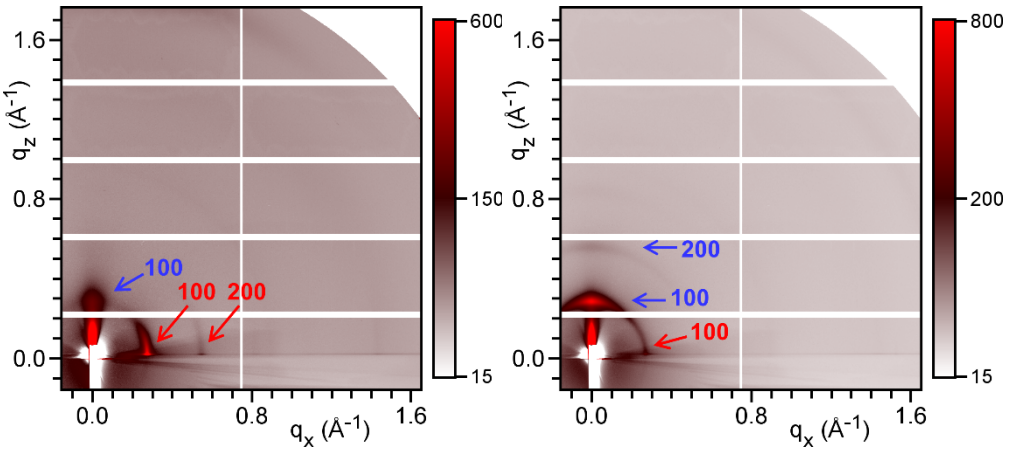

Figure 9: GIWAXS patterns of pristine PF2 (left) and PF2 annealed at 150 °C (right) - reference films.

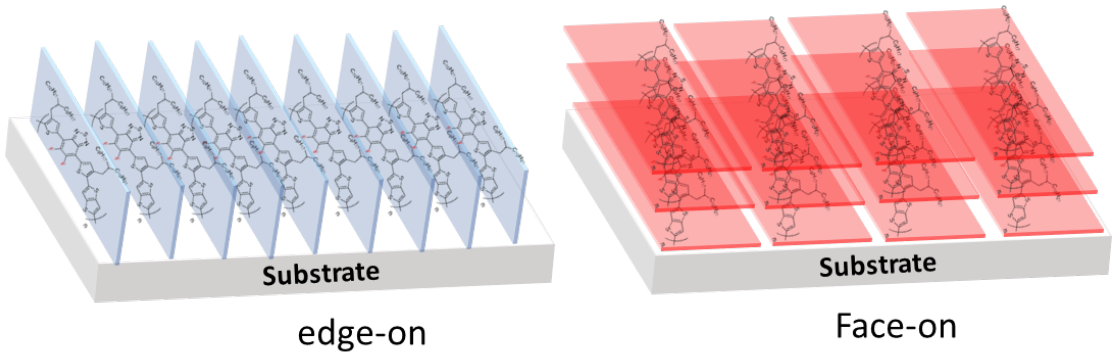

Figure 10: face-on and edge-on orientation of polymer lamellas

Indeed, PF2 bulk polymer and thin films self-assemble in a mesomorphous solid state M_{Lam} (intermediate between the amorphous (isotropic) and crystalline state) with a lamellar structure formed by the alternation of layers of stacked backbones and of molten alkyl chains. The GIWAXS pattern therefore displays series of lamellar reflections (h00), broad scattering ring of molten chains h_{ch}, semi-broad scattering signal from stacking distance h_p and reflection (004) from periodicity along backbones.

Separate Nanoparticles:

Compared to reference bulk PF2, films made from separate PF2-NPs exhibit two phases (**Figure 11**): (i) the frozen mesophase with lamellar periodicity d_{lam}≈ 23 Å (blue and red labels for both orientations respectively) and (ii) an original crystal polymorph Cr_{Lam} with a lamellar periodicity d_{lam}≈ 43 Å (green and magenta labels) corresponding to two molecular layers.

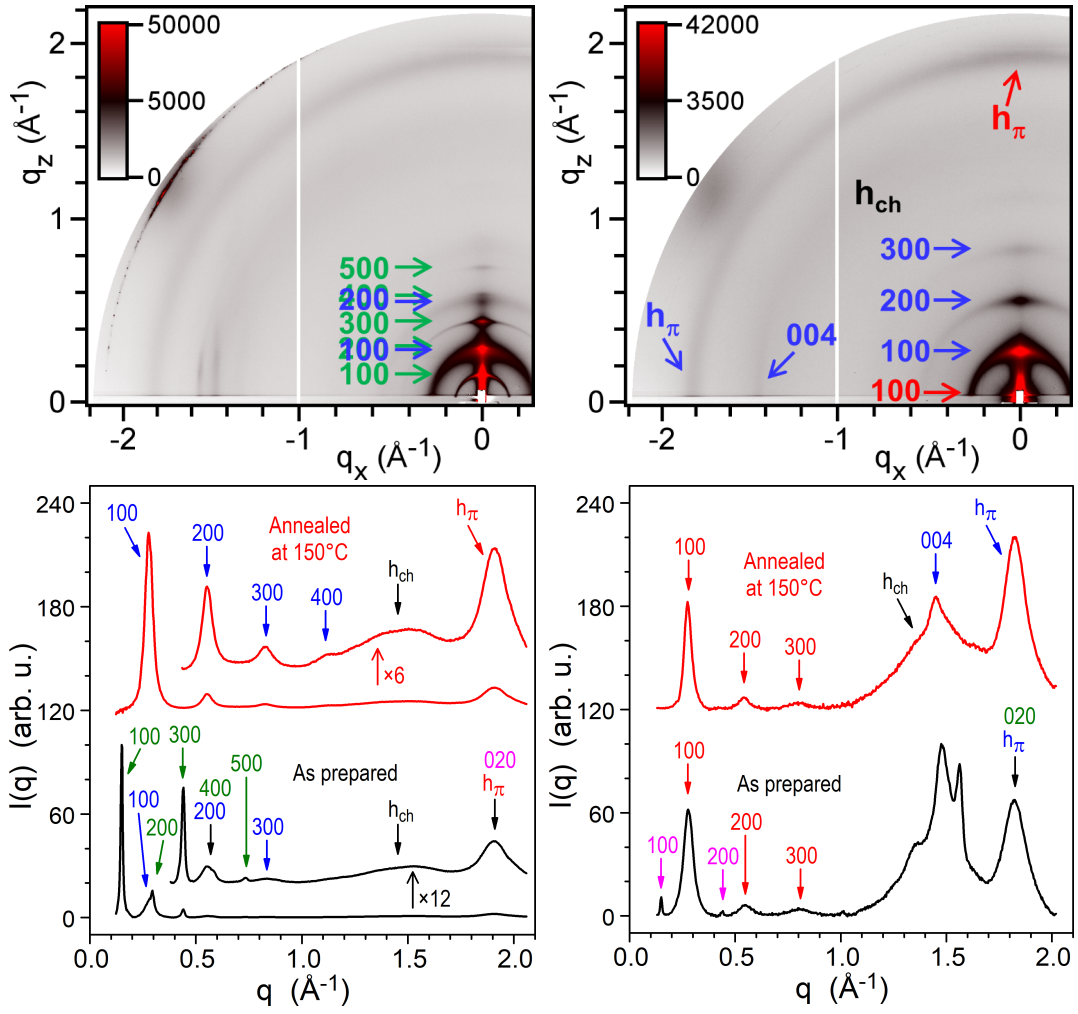

Figure 11: GIWAXS patterns of PF2 NPs in pristine state (top-left) and after annealing at 150°C (top-right). Radial profiles I(q) integrated from azimuthal angle y = -20° to 0° (meridian profile, left bottom) and y = -90° to -70° (equator profile, right bottom).

In fact, on annealing at 150°C, The Cr_{Lam} phase melts to M_{Lam}, which explains that the annealed solid state is purely M_{Lam}. The classification of M_{Lam} as a mesophase and of Cr_{Lam} as a crystal primarily relates to the conformation of the alkyl chains in the structures: in the mesophase, chains are in a molten conformation and give the characteristic scattering ring h_{ch}, whereas in the Cr_{Lam} phase, the lateral arrangement of the crystallized chains gives rise to sharp wide-angle reflections. Then, the study of the bulk material confirms the absence of phase transition (except a glass-like transition) between mesomorphous solid state and fluid mesophase, implying that they are two states of the same mesophase.

The domain orientation is different for both phases: M_{Lam} leads to mixed face-on/edge-on morphologies, which follows the intrinsic orientation tendency in thin films and the curvature coming from the globular shape of NPs. In Cr_{Lam} phase, the flat layers of crystallized chains favor the edge-on orientation, as confirmed by the intensity ratios in radial profiles.

Figure 12 shows the same film annealed at 100°C. Any significant difference is noticed with the pristine PF2 NPs film, since 100°C is below the melting temperature of Cr_{Lam} phase and insufficiently softens the M_{Lam} phase.

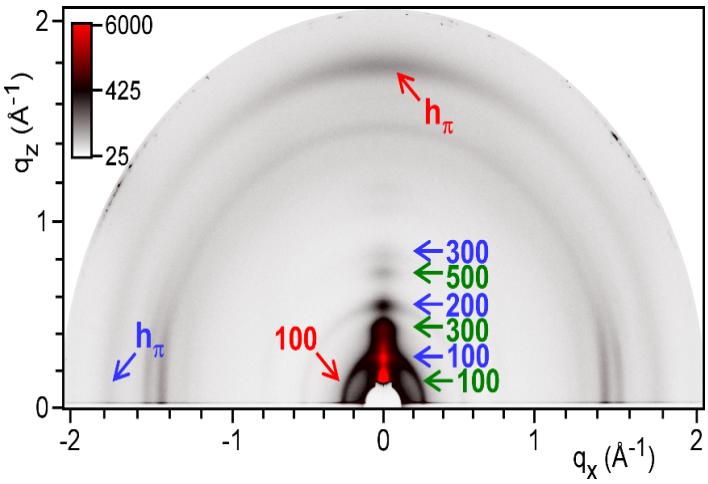

Figure 12: GIWAXS patterns of PF2 NPs annealed at 100°C

Then, pure $PC_{71}BM$-based NP films have been studied (**Figure 13**). An annealing step at 150°C is sufficient to trigger the crystallization of the NPs, as demonstrated by the appearance of sharp reflection rings (orange arrows). It should however be mentioned that the crystallization process of the NPs is incomplete as it leaves residual scattering rings of the amorphous phase.

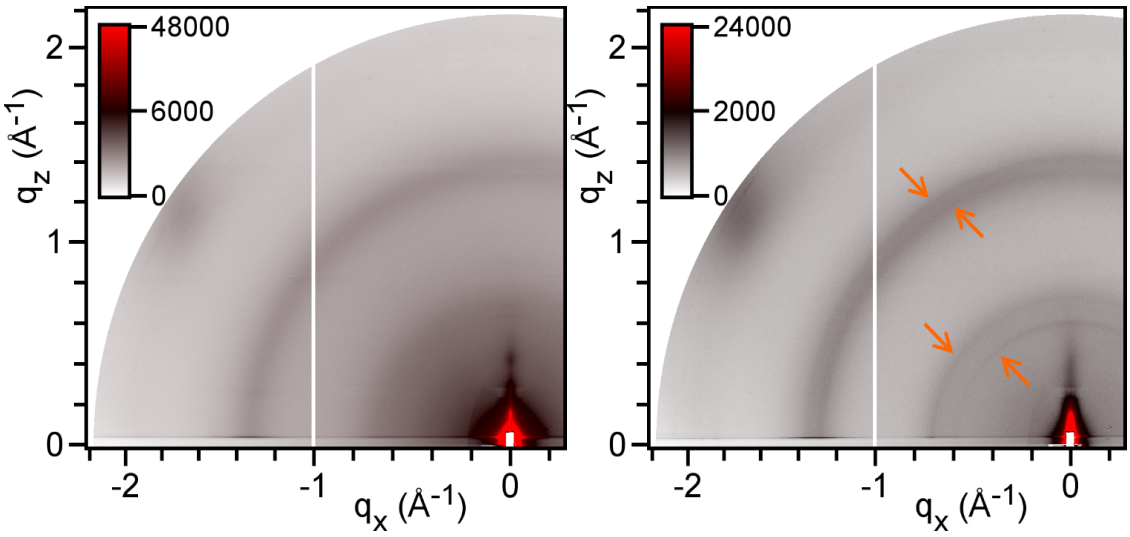

Figure 13: GIWAXS patterns of $PC_{71}BM$ NPs in pristine state (left) and after annealing at 150°C (right)

Composites and mixed NPs:

As shown in **Figure 14**, in the absence of annealing or for annealing below 150°C, patterns are undistinguishable from juxtaposition of neat PF2 and $PC_{71}BM$ domains. The film annealed at 150°C maintains an equivalent lamellar periodicity but the appearance of numerous reflections reveals the crossing of a phase transformation. Besides the (*h*00) spots that acquire a dot-like shape, other (*hkl*) spot series extending to high *h* are now visible (green arrows), which indicates well-defined crystalline lamellae that are well-oriented parallel to substrate. The small-angle region contains new reflections (green stars), which implies a large lattice structure or possibly phase coexistence. Otherwise, scattering rings of amorphous $PC_{71}BM$ have vanished and are not replaced by the reflections of crystalline $PC_{71}BM$. This suggests that a mixed structure incorporating $PC_{71}BM$ in PF2 lamellae has been formed.

As a conclusion, a phase changing that could related to a co-crystallization of both materials has been seen starting from 140°C confirming our AFM studies.

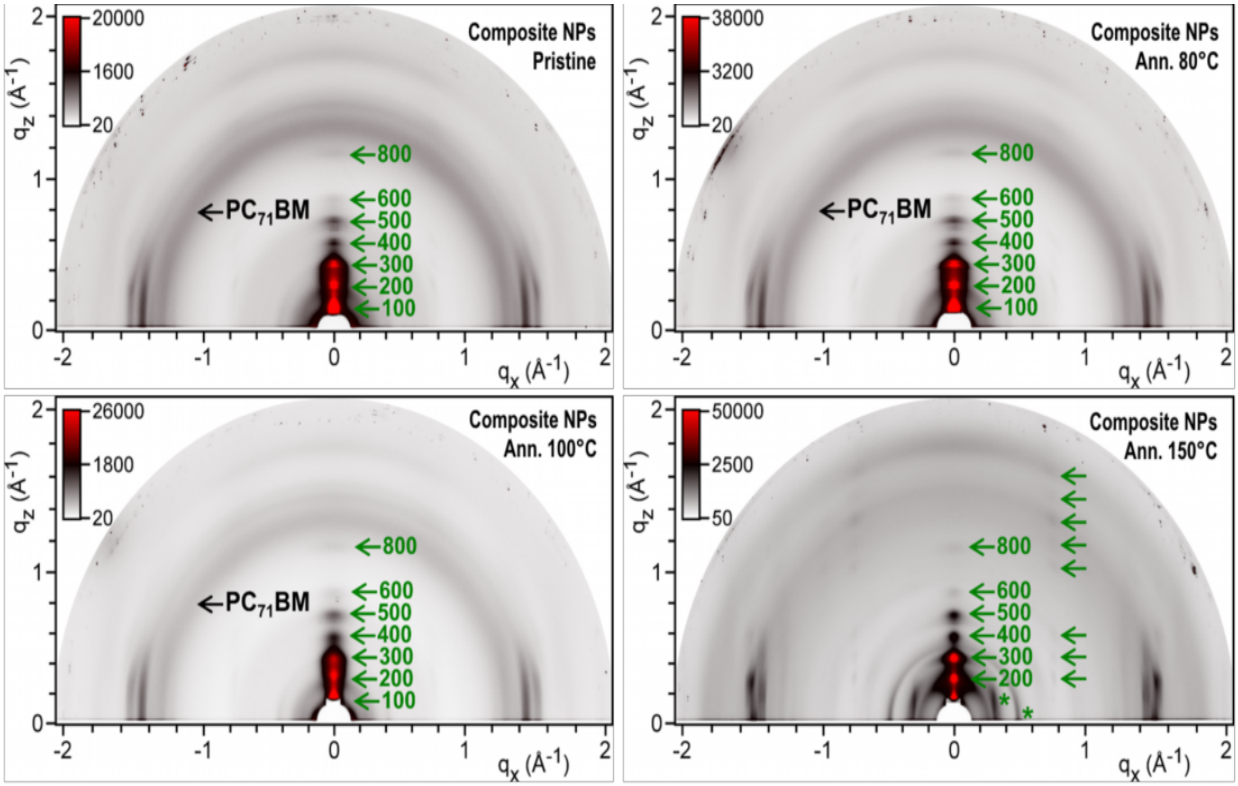

Figure 14: GIWAXS patterns of the PF2:$PC_{71}BM$ composite NPs, as prepared and after annealing at different temperatures.

III.3 Differential scanning calorimetry (DSC):

To further support our judgment concerning a phase changing around 140°C, DSC measurements were then performed. Separate $PC_{71}BM$ NPs and composites PF2:$PC_{71}BM$ NPs composites were tested. As presented in **Figure 15**, an endotherm peak appears at 100°C is attributed to the crystal-to-crystal liquid phase transition of SDS. Furthermore, the endotherm peak at higher temperature might come from melting of materials mixtures with SDS. The first heating curves of both NPs, separate $PC_{71}BM$ NPs and composites PF2:$PC_{71}BM$ 1:2 NPs composites, seem to exhibit an exotherm at 130-140°C, which could possibly correspond to the cold crystallization of the $PC_{71}BM$-rich phase.

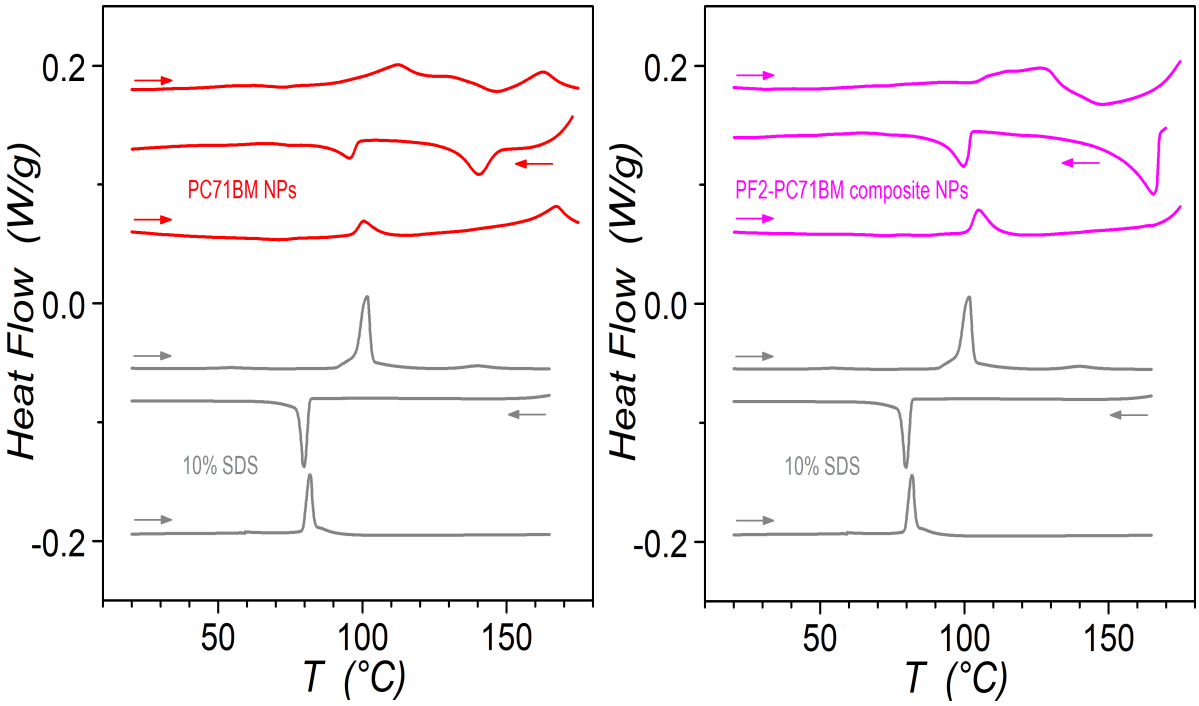

Figure 15: DSC first heating (top), cooling (middle) and second heating curves (bottom) of $PC_{71}BM$ NPs (left, red lines) and composite PF2:$PC_{71}BM$ 1:2 NPs (right, magenta lines), as compared to SDS pure molecule (grey lines - SDS curves were reduced by factor 10) (DSC Q1000 from TA Instruments; conditions: 5°C/min, endotherm up, N2).

IV. Device elaboration:

In order to estimate the potential use of NPs as active layer of an OPV device, we first measured the charge mobilities within the NPs active layer. In OPV devices, the photo-generated charges should be able to reach their respective electrodes, in a perpendicular direction with respect to the substrate. Consequently, we used space charge limited current (SCLC) devices that give access to charge-carrier mobility in the direction perpendicular to the substrate. In other side, a simple way to measure the charge-carrier mobility is to use organic filed-effect transistors (O-FETs), simple devices giving access to charge mobility in the substrate plane.

For all the optoelectronic devices prepared, composite PF2: PCBM 1:2 NPs with diameters of 60 ± 20 nm were used. Additionally, the same PF2 batch was used with a molar mass of 54 kg.mol^{-1} (Đ=2.8) measured by SEC.

IV.1 Space-charge-limited-current (SCLC):

This technique was first proposed in 1940 by the British physicists Mott and Gurney [4] and then improved in 1970 by Lampert and Mark [5]. In SCLC devices, the active layer is placed between two parallel electrodes. These electrodes are chosen to inject only one type of charge-carriers (holes or electrons). A voltage *U* is set between the two electrodes and the current-density *J* across the device is measured (**Figure 16**).

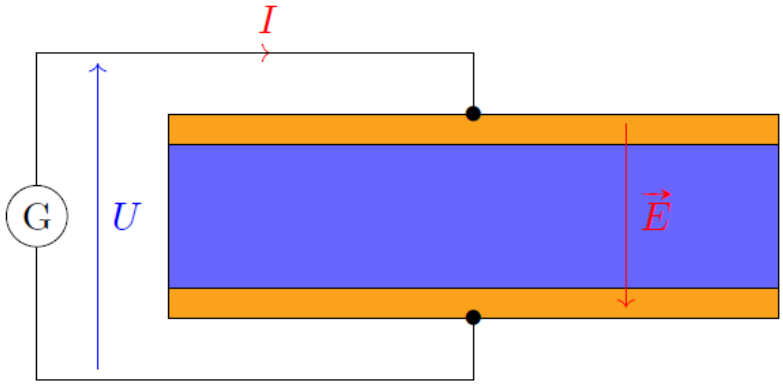

Figure 16: SCLC device architecture

Experimentally, two main regions on the curve J = f(U) are distinguished (**Figure 17**):

- Ohmic region ($J \propto U$) for low values of U.
- SCLC region ($J \propto U^2$) when U is sufficiently large.

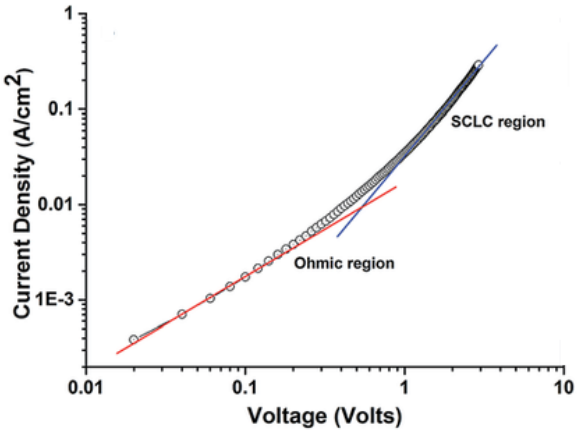

Figure 17: J-V curve of an SCLC measurement in log-log scale

In the SCLC zone, the current density *J* can be approximated by Mott-Gurney's law represented in **equation 1**:

$$J = \frac{9}{8}\frac{\varepsilon\ \mu\ U^2}{L^3} \qquad \textbf{(equation 1)}$$

Where ε is the dielectric permittivity, μ is the charge mobility, *U* is the applied voltage and *L* is the thickness of the active layer.

However, it should be noted that this equation is only valid if the following assumptions are satisfied:

- the SCLC mobility of charges μ is constant and independent of the electric field and charge carrier density
- the semiconductor layer contains no traps
- the observed dependence of *J* as a function of U^2 is due to SCLC and not to charge-injection limitations.

This last point is tested by the elaboration of SCLC devices of different thickness *L* and checking the validity of **equation 1** for every thickness. A disadvantage of the SCLC method is that a given device only provides access to the mobility of a single type of charge carrier. It is in fact the choice of electrodes that determines the type of charge carrier whose mobility is being evaluated (**Figure 18**).

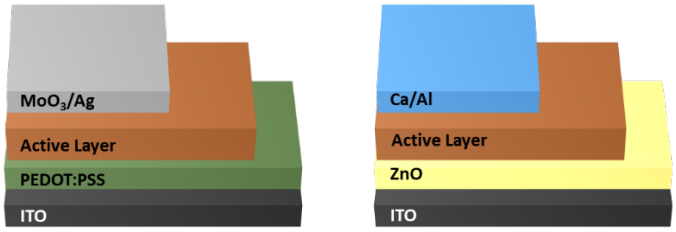

Figure 18: compositions of SCLC for holes (left) and electrons (right) mobilities studies.

IV.2 Organic field-effect transistor (OFET):

To measure the charge transport properties of an organic semiconductor, the simplest way to proceed is to use this material as the semiconducting channel of an organic field effect transistor. A transistor is an electronic component with three terminals called "gate", "source" and "drain".

The simplest OFET structure for organic semiconductor characterization is called bottom gate/bottom contact, which can be described as a stack of several layers **(Figure 19)**:

- a semiconductor layer made of doped silicon, which acts as a gate.
- an insulating layer usually made of silicon oxide (SiO_2) or silicon nitride (Si_3N_4).
- electrodes made of tin-doped indium oxide (ITO) topped by gold contact pins.
- a channel composed by the organic semiconductor.

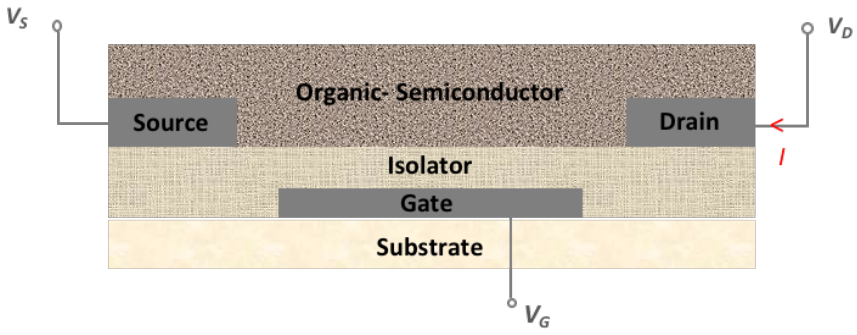

Figure 19: OFET device architecture (bottom gate/bottom contact)

We can then measure the current I through the transistor between the source and drain, depending on the potentials V_D and V_G applied respectively on the drain and the gate. When a voltage is applied between the source and the gate an electric field E appears orthogonally to the device. The insulating layer then behaves like a capacitor, with accumulation of charge carriers (electrons or holes) on both sides; thus, a conductive "channel" is formed in the active layer connecting the allowing the circulation of between the source and the drain:

- if $V_G < 0$, the conductive channel will be composed of holes.
- if $V_G > 0$, the conductive channel will be composed of electrons.

Charge transport investigations:

Charge transport studies have been carried out in horizontal (by OFET) and vertical directions (by SCLC). Holes mobilities have been measured by both approaches, but in contrast, electrons mobilities were only studied by SCLC, due to the presence of hydroxyl groups on the surface of the SiO_2 that could act as electron trap and thus making the measurement impossible. None of the usual surface treatments (HMDS, OTS…) performed to fill the hydroxyl groups were compatible

with the NPs deposition. Indeed, these surface treatments rendered the substrate highly hydrophobic leading to dewetting of the aqueous NPs suspensions.

➢ Electron mobility:

In the case of core-shell NPs, the $PC_{71}BM$ constitutes the core and electron mobility in as-cast devices may be impossible to measure. However, one should remember that the NPs shell contains approximately 30 wt% of PCBM (**Chapter III**). To study electron-mobility for core-shell NPs, SCLC substrates were prepared using PF2:$PC_{71}BM$ (ratio of 1:2) composites NPs as active layer. The device architecture was the following: Glass/ITO/ZnO/AL-NPs/Ca/Al. The number of deposited layers has been varied in order to reach different active layer thicknesses.

Thickness effect:

Table 2 summarizes the electron mobility μ_{e-} values for different active layer thicknesses. In addition, **Figure 20** reports their thickness normalized J-V curves. It shows that curves of non-annealed 2 and 3 layers samples are almost overlapping indicating that their electron mobilities are similar ($6x10^{-3}$ $cm^2/V.s$ compared to $3.2x10^{-3}$ $cm^2/V.s$ measured for PF2:$PC_{71}BM$ BHJ deposited from organic solution). However, mobility for very thin film (70 nm) was significantly lower. Although the reason for this low mobility is not really understood, it can be assumed that this film made from a single deposit (1 layer) has a lower thickness homogeneity.

Conditions	Thickness average (nm)	μ_e-($cm^2/V.s$)
1 layer	70	**$(1.0 \pm 0.5)x10^{-4}$**
2 layers	140	**$(5 \pm 2)x10^{-3}$**
3 layers	215	**$(6 \pm 2)x10^{-3}$**

Table 2: Electron mobility values for different active layer thickness (non-annealed samples)

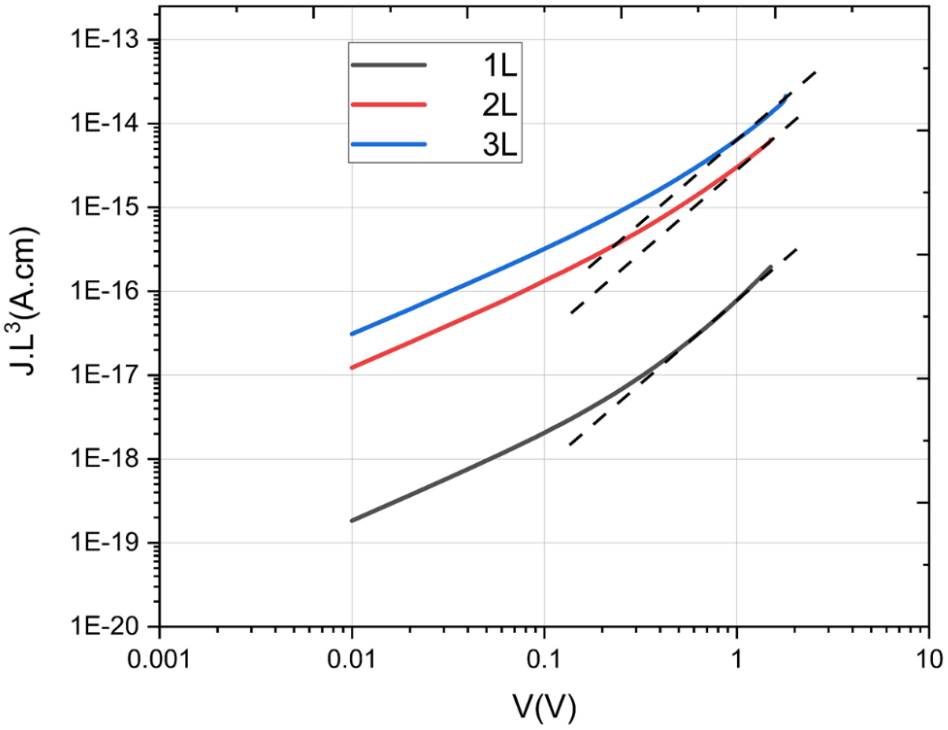

Figure 20: Thickness-scaled J-V characteristics of non-annealed electron-only SCLC devices based on composites PF2:$PC_{71}BM$ 1:2 NPs – diameter 60 ± 20 nm

Annealing effect:

As shown in **chapter I**, the annealing is a key step for OPV PCE enhancement. It is even more true in films elaborated from core-shell NPs as the percolation of electrons is only possible if the electron acceptor core, $PC_{71}BM$ in our case, migrates into the donor phase. Therefore, we studied the thermal annealing effect on electron mobility. As seen in AFM and GIWAXS measurements a significant effect of the thermal annealing is expected.

For this purpose, films of 140 nm have been prepared and thermally annealed before Ca/Al deposition. **Figure 21** and **22** report the results. As shown, the electron mobility increases slightly by annealing at 100°C, compared to unannealed samples. The electron mobility values were found to be around $6x10^{-3}$ $cm^2/V.s$. A slightly higher annealing temperature of 120°C leads to a further increase of the electron mobility, measured at $7.5x10^{-3}$ $cm^2/V.s$. This mobility enhancement agrees with a possible core-shell NPs melting, allowing a slight $PC_{71}BM$ diffusion and may also be related to a NPs coalescence. At higher annealing temperature, 140°C and 160°C, a drop of the electron mobility (μ = $2x10^{-3}$ $cm^2/V.s$) occurred. Although the high-temperature morphology is not fully understood, electron mobility measurements, combined with AFM and GIWAXS measurements, confirm the idea of phase change around 140-150°C, with possible crystallization or co-crystallization of the materials.

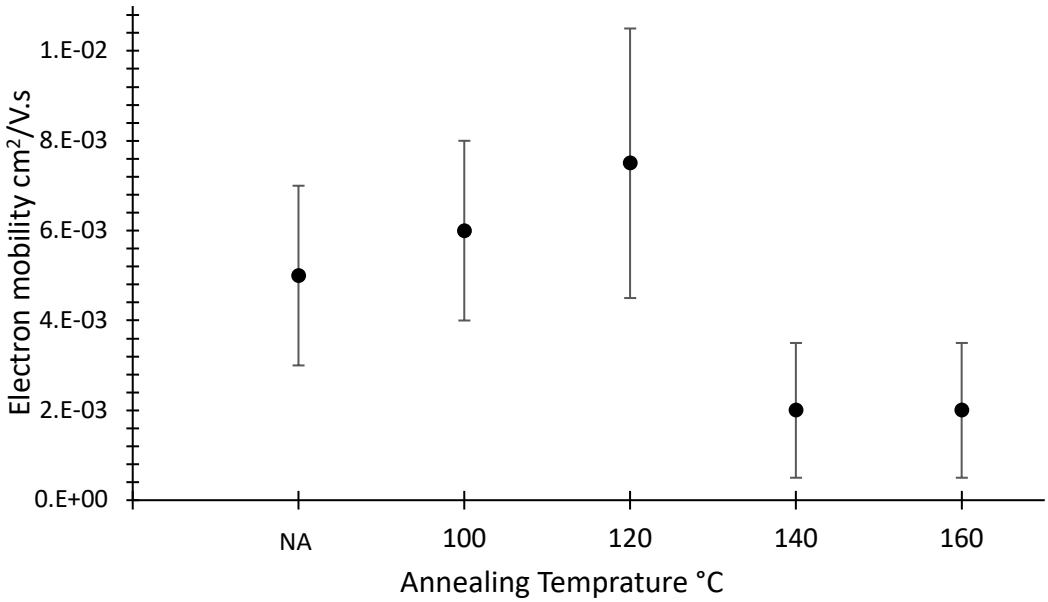

Figure 21: Electron mobility values for different annealing temperatures measured by SCLC devices whose active layer consists of composites PF2:$PC_{71}BM$ 1:2 NPs – diameter 60 ± 20 nm – film thickness ≈ 140 nm.

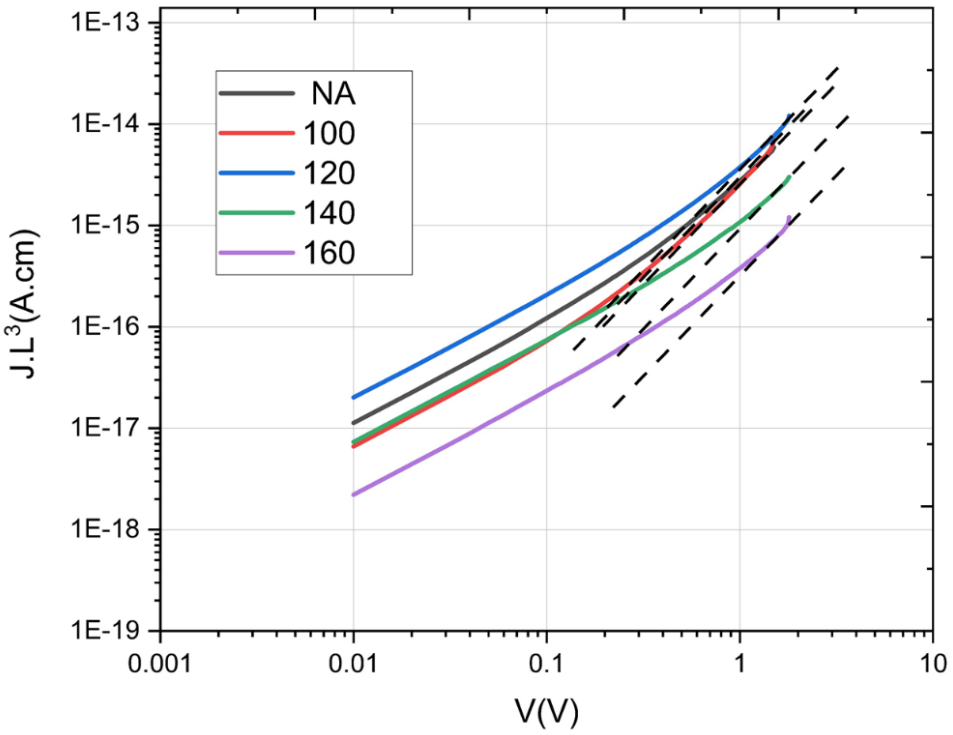

Figure 22: J-V characteristics of electron SCLC devices based on composites NPs for different annealing temperatures.

➢ Hole mobility:

For this study, SCLC substrates were prepared using PF2:$PC_{71}BM$ (ratio of 1:2) composites NPs as active layer. The device architecture is the following: Glass/ITO/PEDOT:PSS/AL-NPs/MoO_3/Ag. The number of deposited layers has been varied in order to reach different active layer thicknesses.
OFET substrates were prepared using the same NPs suspension. AL was deposited by spin coating on pre-patterned substrates directly after UV-O_3 cleaning (the interfacial layer such as HMDS or OTS has not been used in our case).

Thickness effect:

Table 3 summarizes the holes mobility μ_{h+} values measured by SCLC for different active layer thicknesses. In addition, **Figure 23** reports their thickness normalized J-V curves. It shows that curves of non-annealed 2 and 3 layers samples are overlapping indicating that their holes mobilities are similar (around $1x10^{-3}$ $cm^2/V.s$) and the SCLC study is approved.

Conditions	Thickness average (nm)	μ_{h+} ($cm^2/V.s$) average
2 layers	140	$(1.3 \pm 0.4)x10^{-3}$
3 layers	210	$(0.9 \pm 0.3)x10^{-3}$

Table 3: holes mobility values for different active layer thickness (non-annealed samples)

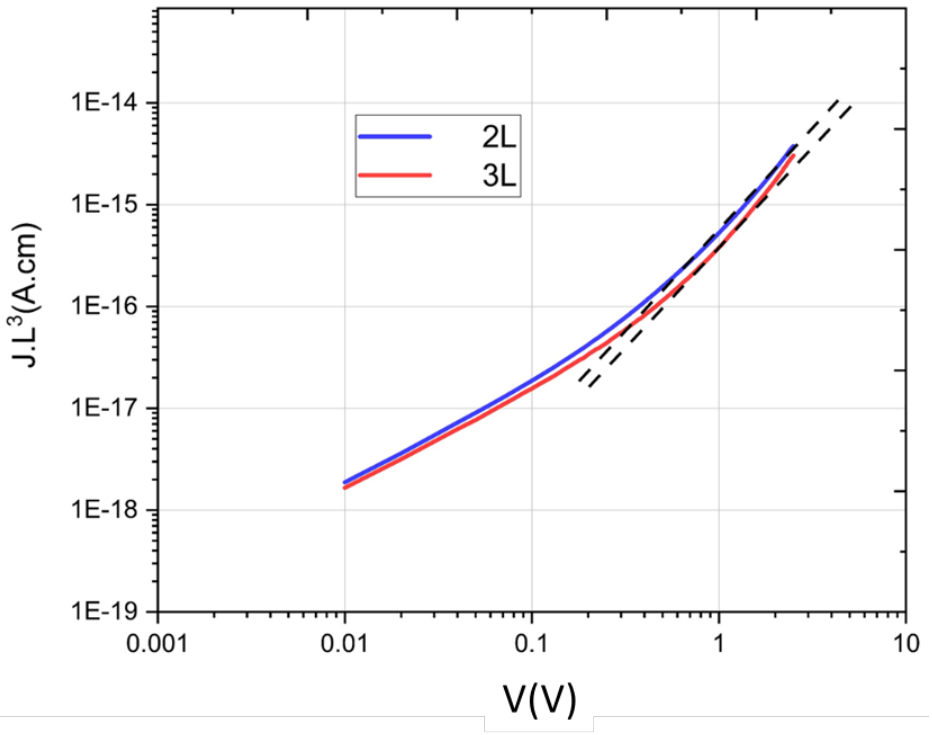

Figure 23: Thickness-scaled J-V characteristics of non-annealed holes-only SCLC devices based on composites PF2:PC71BM 1:2 NPs

Annealing effect:

Similar to μ_{e-} mobility, annealing has a huge impact on the μ_{h+} related to the donor material PF2. The μ_{h+} collected from SCLC devices, decreases when applying a thermal annealing to the substrate. In fact, hole mobility decreases from $(1.3 \pm 0.4)\times10^{-3}$ $cm^2/V.s$ for non-annealed substrate to $(0.5 \pm 0.4)\times10^{-3}$ $cm^2/V.s$, when the SCLC substrate has undergone a thermal annealing at 140°C for 10 minutes. Inversely, the μ_{h+} measured by OFET increased when the substrates were thermally annealed. The mobility increases proportionally to the annealing temperature to achieve a value of $(2.6 \pm 0.4)\times10^{-4}$ $cm^2/V.s$ at 160°C compared to a weak μ_{h+} $(6.7 \pm 0.8)\times10^{-7}$ for non-annealed substrates (**Figure 24**).

This contradictory behavior of annealing effect on positive charges can certainly be related to the orientation of the PF2 molecules after thermal annealing as reported above in the GIWAXS analyses. Before thermal annealing, PF2 molecules are mainly in a face-on orientation. This orientation favors charge-transport in the direction perpendicular to the substrate. This is consistent with the much higher hole mobility measured by SCLC (around 1×10^{-3} $cm^2/V.s$) compared to the one measured by OFET (around 7×10^{-7} $cm^2/V.s$) in as-cast devices. It should be noticed that a SCLC charge-carrier mobility higher than a OFET one is not an exception, but it indicates a strongly anisotropic charge-carrier mobility. After annealing at 150°C, the proportion of PF2 edge-on

orientation increases. Consistently, the SCLC hole-mobility is divided by two after annealing at 140°C (around $5x10^{-4}$ $cm^2/V.s$) while the OFET hole mobility is multiplied by almost 150 (around $1x10^{-4}$ $cm^2/V.s$).

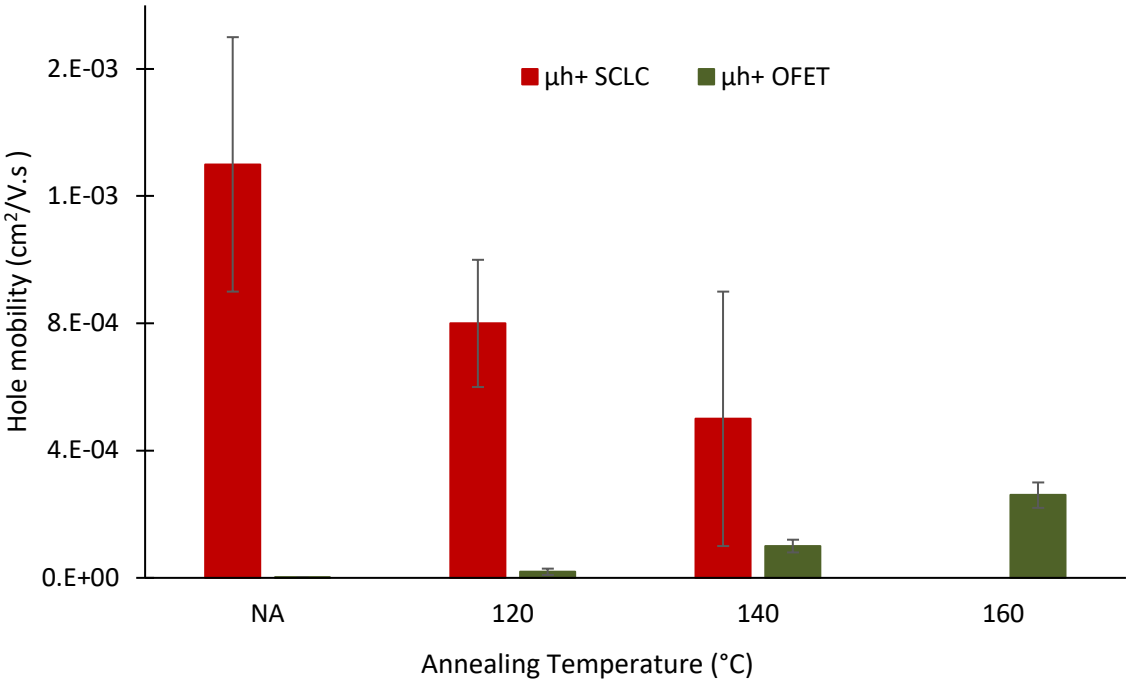

Figure 24 : hole mobility values for different annealing temperatures measured -by SCLC devices whose active layer consists of composites PF2:PC_{71}BM 1:2 NPs – diameter 60 ± 20 nm – film thickness ≈ 140 nm - by OFET transistor using composites PF2:PC71BM 1:2 NPs – diameter 60 ± 20 nm.

IV.3 Organic photovoltaic cell (OPV):

The above charge-carrier mobility measurements have shown promising electron and hole mobilities for the NPs-based thin films. Therefore, NPs-based inks made-up of a PF2:$PC_{71}BM$ blend in a ratio of 1:2 have been used to elaborate the OPV devices active layers (AL). Cells were composed of Glass/ITO/ZnO/NPs AL/MoO_3/Ag (inverted architecture – **Figure 25**).

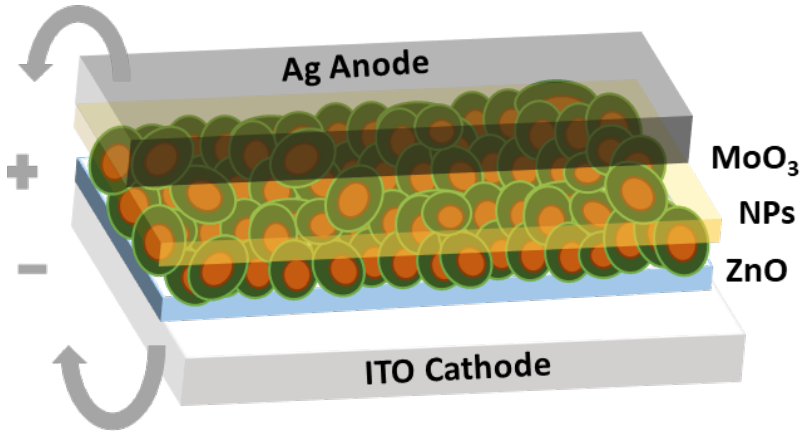

Figure 25: OPV cell inverted architecture where AL is composed from composite PF2:$PC_{71}BM$ 1:2 NPs.

BHJ and NPs inks comparison:

The work on OPV device elaboration and characterization is still in progress, and the results presented below are only preliminary results obtained on a very thin active layer (single layer deposition). In addition, as the standard evaporator was out of order for several weeks at the beginning of this OPV study, these solar cells have been elaborated using an old metallic evaporator that makes difficult the evaporation of multi-layer electrodes and involved a transfer of the device in ambient atmosphere.

Thus, compared to a BHJ devices using standard PF2:$PC_{71}BM$ blends prepared with the new standard metallic evaporator inside the glovebox, the NPs-based devices showed low efficiencies (see **Table 4**). Nevertheless, for the reasons listed above, these first results are promising.

As shown in **Figure 26**, as deposited NPs devices exhibit a reasonable diode-like behavior with a strong rectifying character. The current-density under illumination increases substantially when increasing the reverse bias. This is a strong indication of charge-extraction limitations even in very thin samples.

Compared to standard BHJ solar cells, the V_{OC} was surprisingly similar in NPs-based devices.

In contrast, the J_{SC} is dramatically reduced in the NPs-based OPV devices. Indeed, it decreased from 17.8 $mA.cm^{-2}$ for the standard BHJ to 2.16 $mA.cm^{-2}$ for NPs-based thin-film. Actually, The J_{SC} is

related to the number of charge-carriers extracted at the electrodes and is thus directly proportional to the quantity of photons absorbed by the active layer, to the numbers of free charges generated at the D/A interface and to the ability of the D/A blend to transport efficiently these free charges towards electrodes. Thus, considering the large difference in thickness measured between the BHJ [4] and the film made from NPs, it is likely that part of this J_{SC} decrease comes from the low absorption of NPs-based devices. But probably the most important losses come from a poorly adapted morphology with perhaps a D/A interface too limited in size and distribution within the bulk.

Furthermore, one can notice the FF decrease (from 66% to 34 %) indicating charge-extraction problems in NPs-based devices.

Conditions	V_{OC} (mV)	J_{SC} (mA.cm^{-2})	FF %	Thickness (nm)	PCE %
BHJ solution	760	17.8	66	235	9
NPs	760	2.16	34	70	0.6

Table 4: features of unannealed OPV devices made by organic solution (named BHJ solution using MMw PF2 as donor material) or by NPs-based ink deposition (named NPs).

Annealing effect:

Our previous studies showed that annealing is a key step optimizing the morphology and electron mobility as well. We therefore applied thermal annealing before MoO_3/Ag deposition, on the OPV devices. Results of this study are summarized in **Table 5** and **Figure 26**.

Annealing temperature °C – 10 minutes	V_{OC} (mV)	J_{SC}(mA.cm^{-2})	FF %	PCE %
No-Annealing	760	2.16	34	0.6
100	780	3.00	39	0.9
120	790	3.00	40	1
160	750	1.83	47	0.6

Table 5: features of OPV devices made by composites PF2:$PC_{71}BM$ 1:2 NPs diameter 60 ± 20 nm - films thickness 70 nm

Following the same trend already observed in the electron mobility study, the best PCE value of 1% was recorded for a device annealed for 10 min at 120°C. Thus, this increased PCE compared to other temperature is likely related to the better NPs interaction, to the higher electron mobility and to the higher D/A interface at 120°C, as reported previously.

It is worth noting that the V_{OC} value, around 770 mV, is independent of the annealing temperature. In contrast, the J_{SC} values seems to vary with the electron mobility values reported previously. Thus, increased J_{SC} of 0.36 mA.cm^{-2} have been measured for devices annealed at 100°C or 120°C, while a thermal annealing at 160 °C leads to a J_{SC} decrease. Here again, the morphology evolution highlighted previously, probably related to the $PC_{71}BM$-phase cold-(co)crystallization, seems to be detrimental for the device efficiency.

Finally, another point has to be raised. The presence of approximately 20 %wt of the ionic SDS surfactant in these NPs. It has been extensively demonstrated in the literature that the presence of a surfactant has a negative effect on cell performance, probably due to the appearance of traps for free charges. It is generally translating in FF and Jsc decrease.

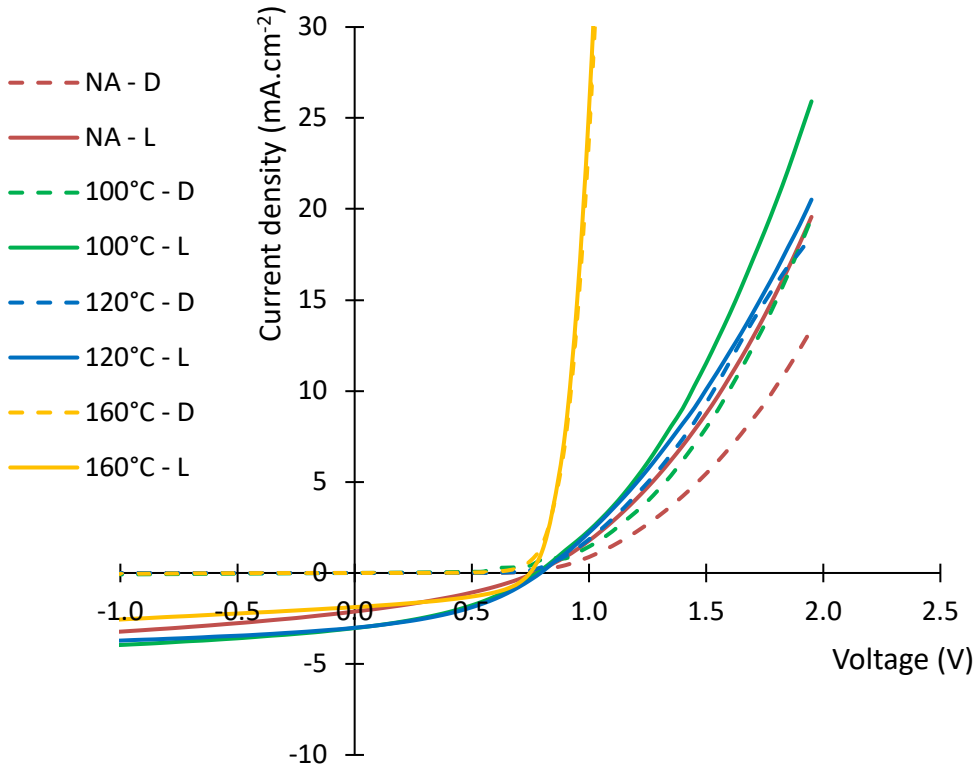

Figure 26: J-V curve of OPV cells devices made by NPs reported in table 5. (D = under Dark / L = under light)

V. Conclusion:

After dialysis of the prepared suspensions and careful optimization of the film deposition process, we succeeded in elaborating homogeneous thin films of variable thickness by spin-coating. These films were characterized by AFM showing the effect of thermal treatment first leading to a coalescence of the NPs and decrease of the film roughness around 120°C, followed by an important change in morphology above 140°C. This morphological change has been identified by GIWAXS analysis combined with DSC analysis, as a kind of co-crystallization of PCBM with PF2. Charge mobility measurements showed an increase of the electron mobility in the perpendicular direction at 100 and 120°C probably due to the diffusion of PCBM towards the shell of the NPs and/or the coalescence of the particles. In the same time, hole mobility decreases in the perpendicular direction to the electrodes and increases in the parallel direction. This could be assigned to a change in the orientation of PF2 molecules from a mixed edge-on/face-on orientation to predominant edge-on orientation.

The many issues that had to be addressed (including the COVID pandemic) slowed down the development of organic solar cell devices. Nevertheless, the preliminary results, obtained on devices including very thin films and developed under non-optimal conditions, are particularly promising. Indeed, a PCE of 1% has been obtained after annealing at 120°C. It is likely that working on the thickness of the active layer and on the optimization of the key step of post-deposition thermal annealing should allow us to significantly increase the conversion efficiency in solar cells. However, there is still the problem of the use of the ionic surfactant, SDS, in the miniemulsion process, which cannot be totally eliminated without destabilizing the NP suspensions. This surfactant can act as a charge trap during device operation. Therefore, in order to avoid this surfactant, we considered using the nanoprecipitation approach, which is the subject of the following chapter.

VI. Reference:

1. Bag, M. *et al.* Efficient Charge Transport in Assemblies of Surfactant-Stabilized Semiconducting Nanoparticles. *Adv. Mater.* **25**, 6411–6415 (2013).
2. Colberts, F. J. M., Wienk, M. M. & Janssen, R. A. J. Aqueous Nanoparticle Polymer Solar Cells: Effects of Surfactant Concentration and Processing on Device Performance. *ACS Appl. Mater. Interfaces* **9**, 13380–13389 (2017).
3. Aniansson, E. A. G. *et al.* Theory of the kinetics of micellar equilibria and quantitative interpretation of chemical relaxation studies of micellar solutions of ionic surfactants. *J. Phys. Chem.* **80**, 905–922 (1976).
4. Olzhas Ibraikulov, bulk heterojunction solar cells based on low bad-gap copolymers and soluble fullerene derivative, *PhD thesis*, University of Strasbourg 2016.

CHAPTER V

POLYMER DESIGN &

NANOPRECIPITATION

I. Introduction:

As discussed in previous chapters, the main objective of this PhD project, is to produce organic semiconducting donor and/or acceptor nanoparticle (NP) suspensions, used as inks for the preparation of organic photovoltaic device active layers. The miniemulsion, presented in **chapter III**, leads to stable NPs. However, despite interesting properties and features, this approach exhibits few drawbacks. Indeed, as shown in **chapter IV**, relatively low OPV performances have been obtained until now, probably due to the presence of the ionic surfactant (SDS), required for miniemulsion-based suspension stability. As shown in literature, this ionic surfactant may be at the origin of charge carrier traps within the OPV active layer[(1)]. Therefore, the nanoprecipitation approach, avoiding the use of ionic stabilizer is a promising approach and will be develop in this chapter. This process has been briefly described in **chapter I**. It consists in elaborating NPs from a polymer solution, which is precipitated into a non-solvent of the polymer, however miscible with the good initial solvent. Usually this non-solvent is an alcohol solution or water, while the good solvent is an organic compound. The strength of this process is its universality and versatility since any material can be processed as NPs, as long as it is soluble into water- or alcohol-miscible solvents. Actually, this last feature appears to be the key parameter to take into account for this nanoprecipitation process. Indeed, most water-miscible solvents are not very good solvents for the state-of-the-art organic semiconducting polymers, the best solvent being probably tetrahydrofuran (THF).

As we have seen in previous chapters, the best polymer from ICPEES for OPV device elaboration is the PF2. The electron donor polymer is particularly efficient due to the presence of weak halogenated bonds that planarize the conjugated backbone and increase strongly the π-stacking [(2)]. This leads to high hole mobilities but also to low organic solvent solubilities. Even low molar mass PF2 batches exhibit a low solubility, especially in THF. This solubility issue has turned the elaboration of PF2 NPs, by nanoprecipitation, a difficult challenge (results of PF2 nanoprecipitation will be reported below in this chapter). Therefore, we decided to design and synthesized new dedicated conjugated polymers, based on the laboratory's knowledge obtained from PF2. Consequently, the first part of this chapter will be devoted to the synthetic task description.

Our aim is to increase the PF2 solubility in low boiling point (BP) solvent such as chloroform or tetrahydrofuran. Two different approaches could be considered (**Figure 1**):

- *The conjugated backbone modification:* It is the simplest approach, but it usually translates in strongly different optoelectronic properties. This approach consists in increasing the number of side chains by changing the aromatic building blocks or decreasing the backbone planarity by for instance removing the halogen atoms (Route a).

- *The side chain modification:* Here, the idea is to change as little as possible the polymer architectural features. The best way is to use non-crystalline and polar side chains such as oligoethylene oxide segments (Route b). In addition, such polar side chains are expected to enhance the suspension stabilization when dispersed in polar solvents such as water or alcohols.

A second part of this chapter will be then devoted to the study of NPs suspension from PF2 and newly synthesized polymers by nanoprecipitation approach.

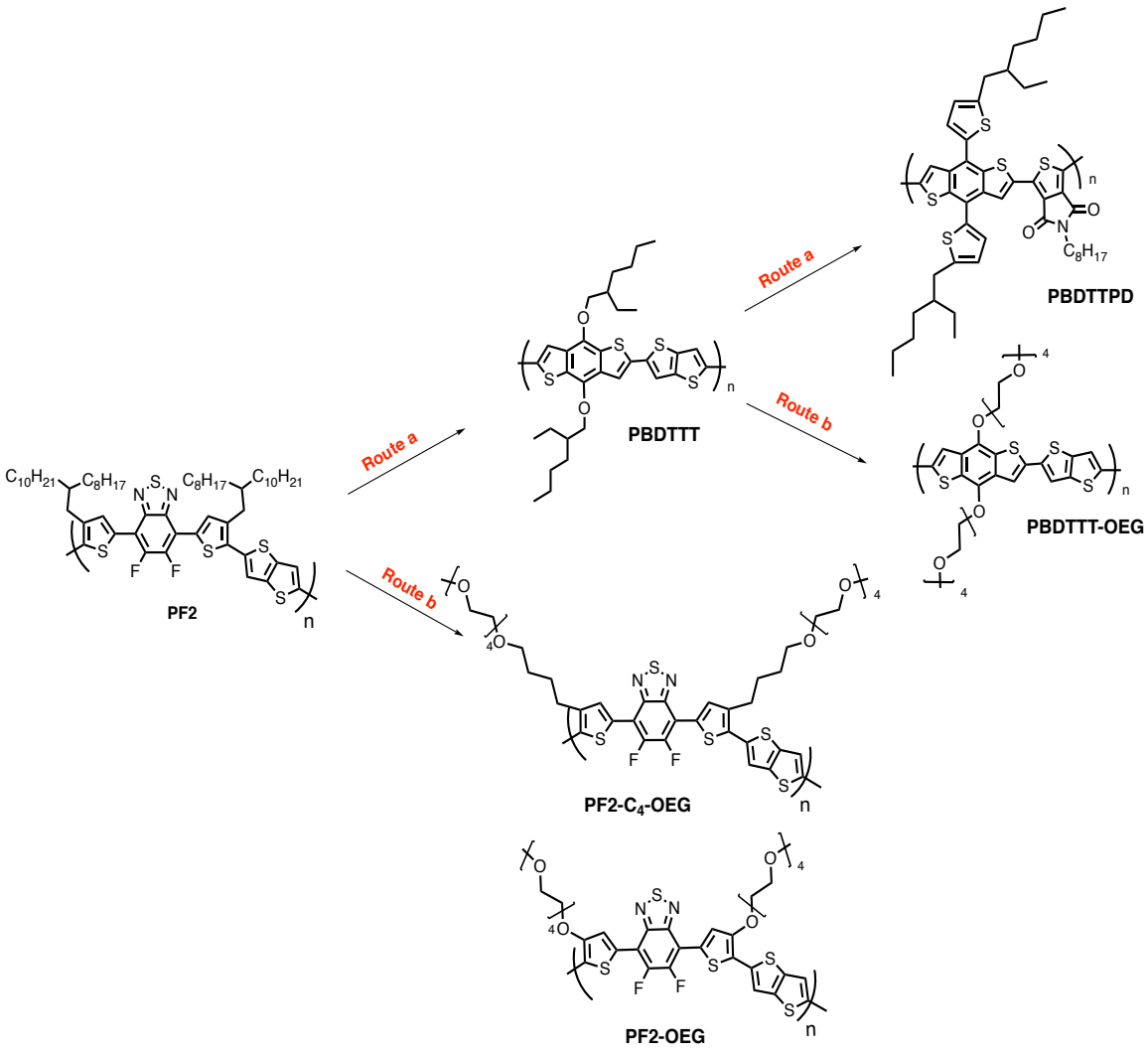

Figure 1: approaches of semi-conductor polymers engineering.

II. Molecular engineering and design:

- **Route a: Conjugated backbone modification:**

In order to increase the PF2 solubility, we first decided to investigate the difluorobenzothiadiazole (DFD) replacement. Indeed, due to fluorine atoms, this electron deficient unit limits strongly the solubility. Of course, by replacing it with another conjugated building-block, we are willing to drastically change the final properties of the copolymer. We used a planar benzodithiophene bringing two side chains (**PBDTTT in Figure 1**). By using two ramified ethyl-hexyl side chains in addition to the fluorine removal, we expected a significant solubility increase. The two monomers were already available in the laboratory (they have been previously synthesized by Stéphanie Ferry). We thus just have to perform the cross-coupling polymerization. The Stille cross-coupling reaction is probably one of the most performing and versatile palladium-catalyzed cross-coupling for conjugated material synthesis. It involves a cross-coupling between a bis-tin monomer and a di-halogenated monomer. In our case, it involves the bis-trimethyltin thieno[3,2-*b*]thiophene (TT) and the dibromo benzodithiophene unit, respectively (**Figure 2**)**.**

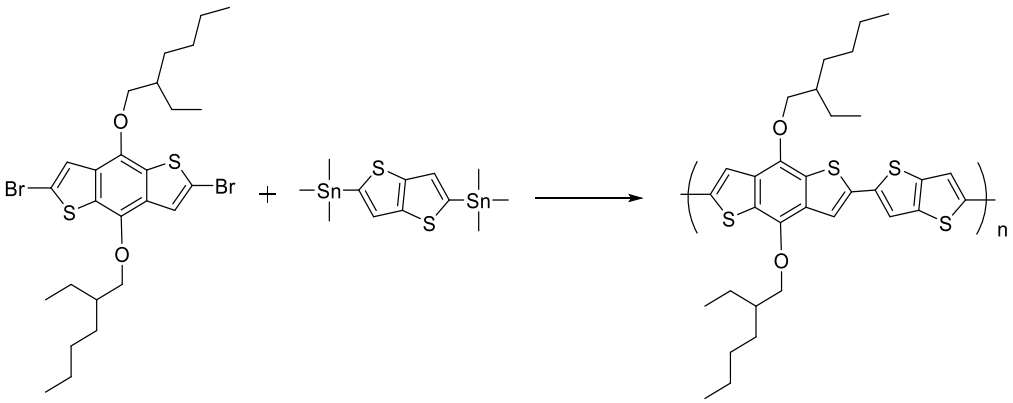

Figure 2: Stille cross-coupling polymerization of PBDTTT

Despite an increase solubility, as regards to standard PF2, this PBDTTT polymer did not exhibit the expected solubility in THF and $CHCl_3$. In fact, this polymer was totally insoluble in those solvents. Consequently, even the measurement of its molar mass in *o*-DCB at 150°C could not be performed accurately.

Furthermore, most semiconducting polymers have a color that changes when they are in aggregated or diluted form. The color change in solution upon heating is therefore a good indicator of polymer solubilization as long as the polymer is not completely soluble at room temperature. In this case, any color change has been observed during the solubility tests. In addition, some aggregates visible to the eye can be observed at room temperature even at high dilution. In order

to probe the solubility limit, we performed the UV-vis spectroscopy at high temperature in a high boiling point solvent, namely the *o*-DCB (we used a heat gun to reach the boiling point, so that the temperature is not controlled but we can estimate it during the measurement between 160 and 180°C). In solution (0.02 $mg.mL^{-1}$) at room temperature, the spectra exhibit a main two-peaks band centered around 490 nm (**Figure 3**). On the highest energy, one can see a small shoulder at 400 nm, probably relative to disordered chains. And on the highest wavelength a shoulder around 560 nm. This shoulder decreases in intensity with solution temperature increase. This shoulder is probably relative to a very ordered solid-state stacking. Its attenuation at high temperature confirms this hypothesis. However, the main band at 490 nm hardly changes at the relative intensity of the two peaks. The comparison with the thin-film spectrum supports our observations. Indeed, despite different intensities of different bands, the two shoulders, at high and low wavelengths, are more pronounced, the very great similarity in shape and measured wavelengths confirms that the polymer in solution, even at high temperature, never reaches complete solubility. From the solid-state spectrum, an optical bandgap of 1.87 eV has been calculated.

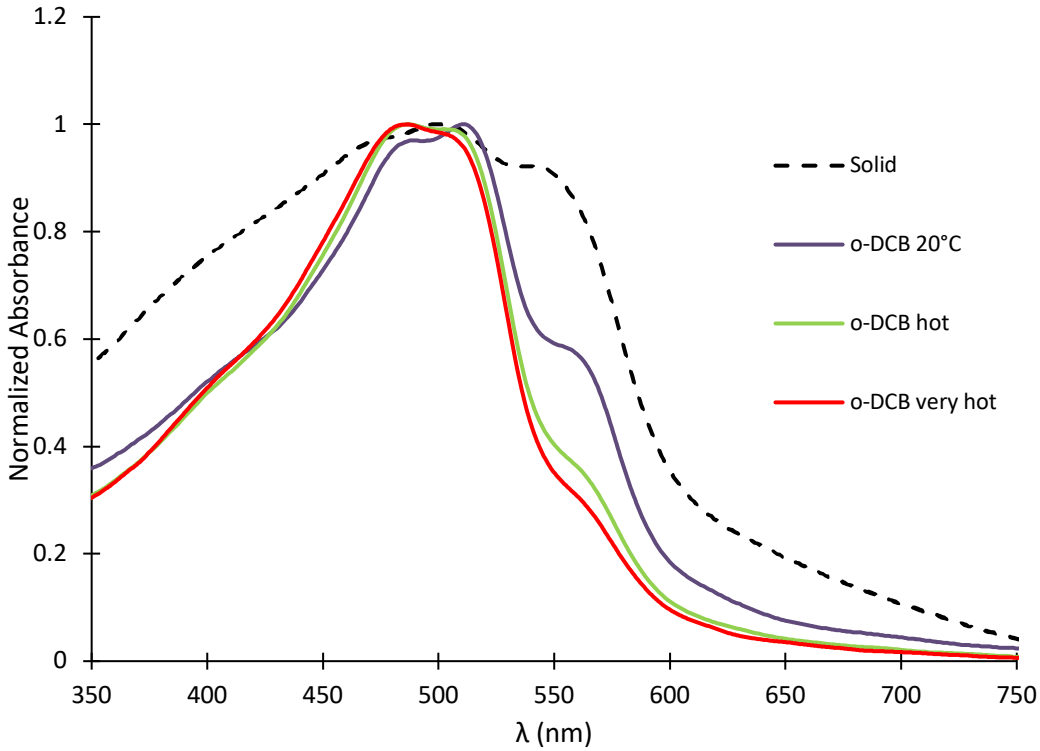

Figure 3: UV-visible spectra of PBDTTT in o-DCB solution and thin-film

Following our strategy, we targeted two new derivatives, called PBDTTPD and PBDTTT-OEG, respectively (**Figure 1**).

The first PBDTTPD uses a thienopyrroledione (TPD) as weak electron withdrawing unit instead of the thienothiophene. This new polymer does not look anymore to the PF2 at all. But the TPD brings a third side chain and a D/A alternating nature, which could strengthen the absorption properties

and the charge mobility. Actually, this polymer has been already described in a publication and the authors claimed a good solubility in THF [3]. Its synthesis is described in **Scheme 1** below.

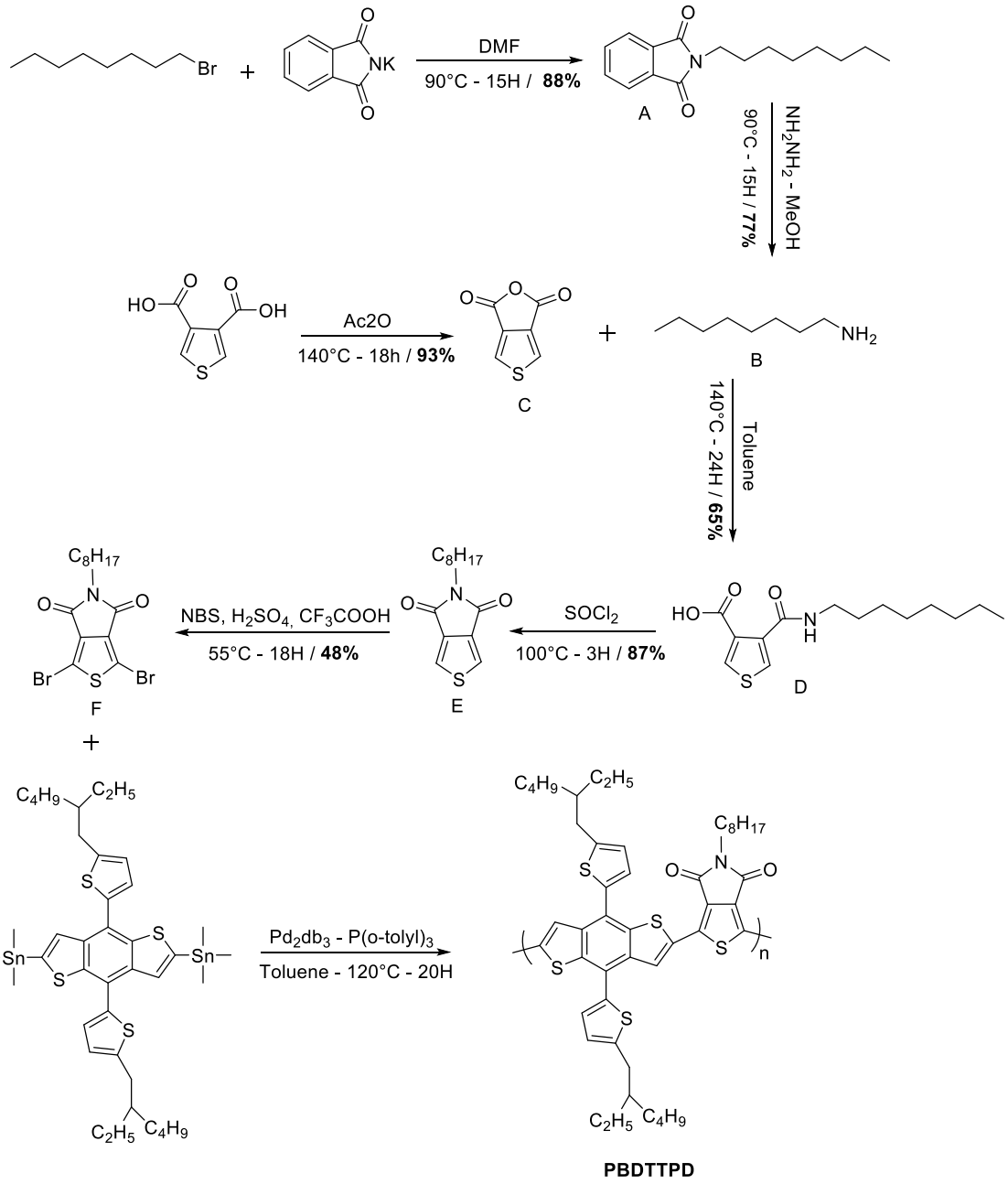

Scheme 1: PBDTTPD synthesis

The polymerization has been also performed by Stille cross-coupling. The PBDTPD molar mass has been measured by SEC in hot *o*DCB; M_n of 23 Kg.mol^{-1} with Đ of 1.5.

In UV- visible spectroscopy, the polymer exhibits a standard two-main bands absorption shape. The first band around 450 nm is attributed to a π-π* transition, while the lower energy band, split into two different peaks, is relative to the internal charge transfer (ICT) occurring from the electron-rich BDT unit to the electron-deficient TPD moiety. The two peaks are likely due to two different stacking

mode as already observed in numerous conjugated copolymers [4]. It is worth noting that despite few differences in peak intensities and in wavelength shifts, the spectra in solution at room temperature, whatever the solvent used, exhibit the same shape that the one measured in thin film (**Figure 5 top**). This is usually, a signature of a low solubility. Indeed, the polymer is probably already aggregated at room temperature in the three selected solvent, in contrast to what has been claimed in the reference publication.

In order to have more evidence, we used the *o*-DCB at high temperature, as previously shown for PBDTTT. Hot and a very hot solutions (close to the *o*-DCB boiling point) allows to conclude about the very low solubility of this PBDTTPD polymer. Indeed, at such a high temperature, if the solution color change (**Figure 4**), the UV-vis absorption spectra (**Figure 5 bottom)** change only partially. Actually, we can see a decrease in intensity of the band at highest wavelength with temperature increase. However, the first band at 550 nm remains, while a slight increase in intensity of the shoulder around 510 nm can be noticed. This shoulder is probably due to solubilized chains (corresponding to the amorphous zone in the thin-film spectrum). However, its low intensity together with the absence of band disappearance at 550 nm suggest that the polymer is still in aggregated form, even at high temperature in the *o*-DCB. Consequently, one can conclude that this PBDTTPD is not enough soluble at room temperature in low boiling point solvents. From the solid-state spectrum, an optical band-gap of 1.87 eV has been calculated.

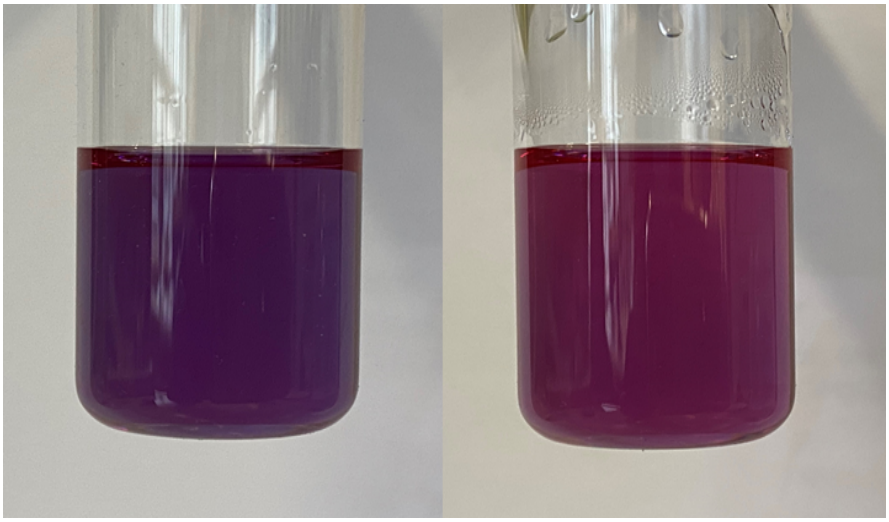

Figure 4: PBDTTPD in o-DCB, at room temperature (left), heated (right) – solution of 0.1mg.mL^{-1}

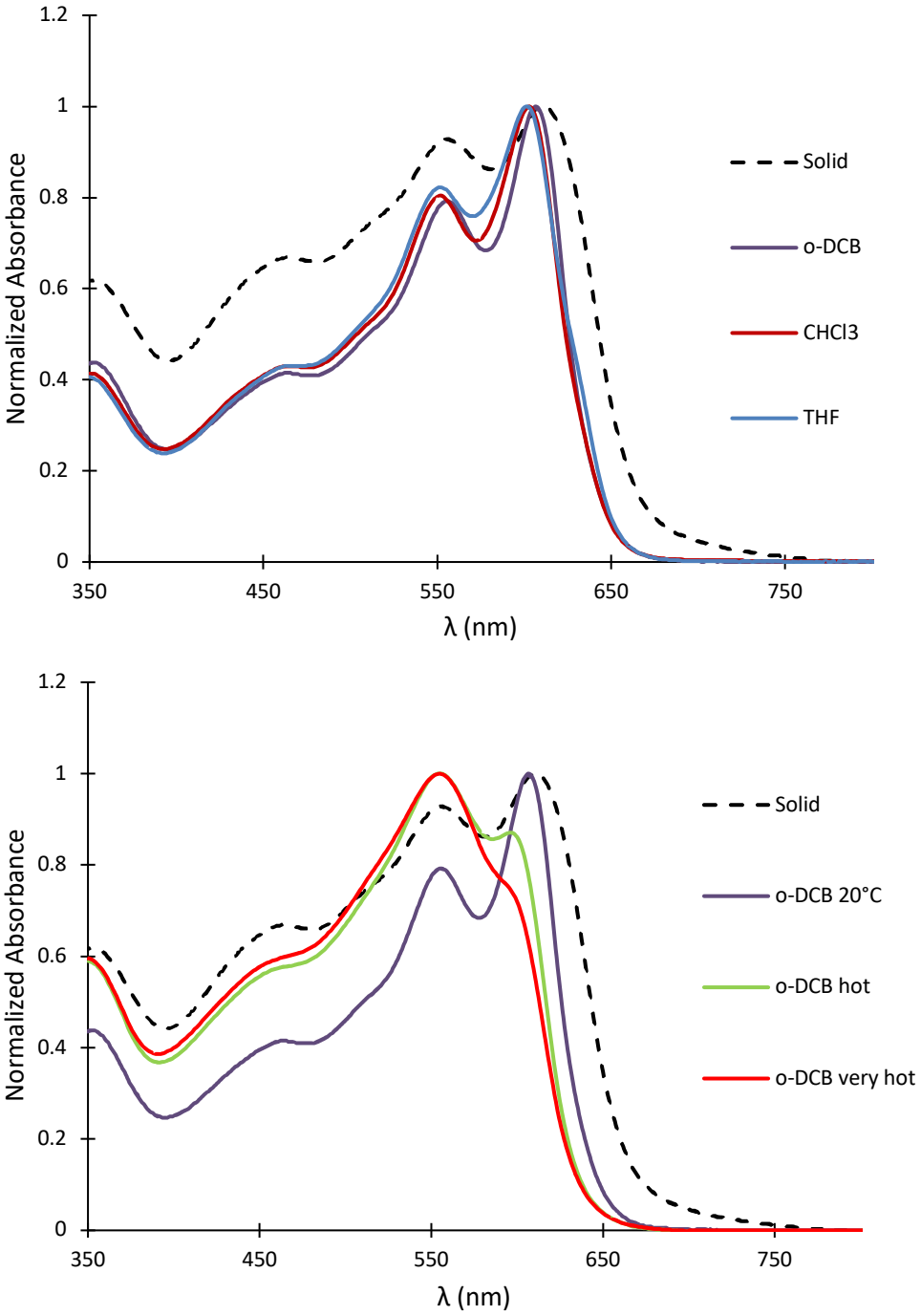

Figure 5: (top) UV-Visible spectra of PBDTTPD in solution in $CHCl_3$, THF and o-DCB – Solution of 0.02mg.mL^{-1} ; (bottom) UV-Visible spectra of PBDTTPD in solution in o-DCB at different temperatures as compared to thin-film

Therefore, from the previously synthesized PBDTTT polymer, we decided to apply the route b, which consists in replacing the alkyl ethylhexyl side chains with tetraethyleneglycol segments (**see PBDTTT-OEG in Figure 1**).

- **Route b: The side chain modification:**

Oligoethylene side-chains (OEG) are expected to enhance the polymer solubility. In this first attempt, we decided to graft directly, without carbon atom spacer, the oligoethylene side chain on the aromatic unit. It is not insignificant as the oxygen atom bonded to the aromatic unit will increase the electron density by mesomeric effect. This usually results in an upward shifted HOMO level.

Unfortunately, the synthesis is not as trivial as expected. In particular, the OEG side chains make the conjugated unit highly polar. As a consequence, the separation of byproducts by standard column chromatography becomes very challenging. In our case, if the side chain grafting has been performed with high yields, it has been impossible to accurately separate the bis-brominated and the mono-brominated species after bromination. Unfortunately, in order to obtain polymer with high molar masses by polycondensation, one need to carefully respect the stoichiometric ratio between the two monomers. We thus decided to not perform the polymerization of the PBDTTT-OEG polymer.

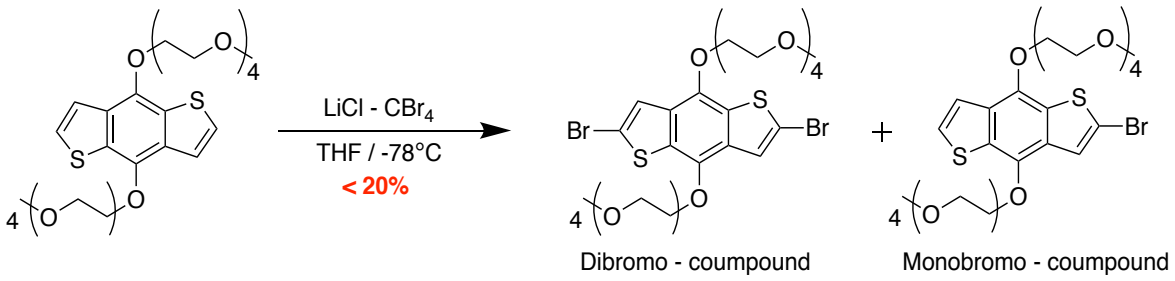

Figure 6: route for PBDTTT-OEG monomers

However, we attempted to apply this chemical strategy to the reference PF2. Indeed, this polymer has really accurate optoelectronic properties for photovoltaic applications. Two different OEG linkages were investigated. The direct linkage (**PF2-OEG in Figure 1**), as shown on the BDT unit previously, and the linkage through an alkylated spacer (linear butyl segment, see **PF2-C_4-OEG in Figure 1**). This strategy allowing to avoid the HOMO level up-shifting.

For PF2-C_4-OEG, we used two different chemical routes. The first one was designed in order to avoid the presence of the oligoethylene segment up to the last synthetic step in order not to face the same polarity issues as previously met. As shown in **Scheme 2**, it requires to protect the hydroxyl group, later used to graft the oligoethylene segment.

Unfortunately, if the first six first steps work well, the hydroxyl deprotection has been unsuccessful, despite the many tested conditions. Indeed, the NMR analysis showed us that the product probably degrades under deprotection conditions.

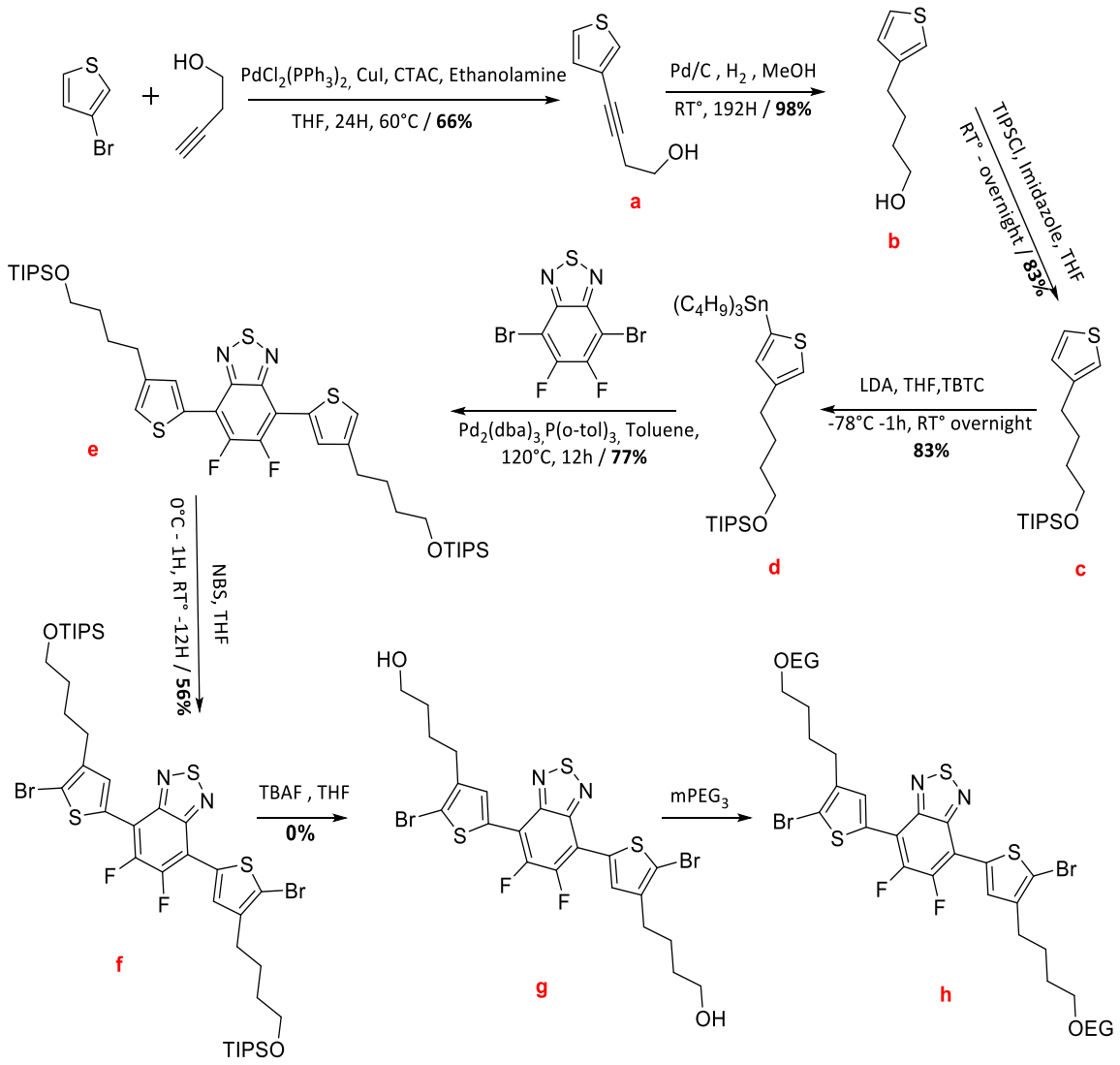

Scheme 2: schematic synthesis of PF2-C$_4$-OEG - strategy I

We consequently attempted to avoid the protection/deprotection steps by directly grafting the oligoethyelene glycol segment on the thiophene in first steps, taking the risk to be challenged by the polarity issue (**Scheme 3**). As expected, the compounds polarities were extremely high, involving the use of high polar solvents, such as ethyl acetate mixed with ethanol, for product purifications.

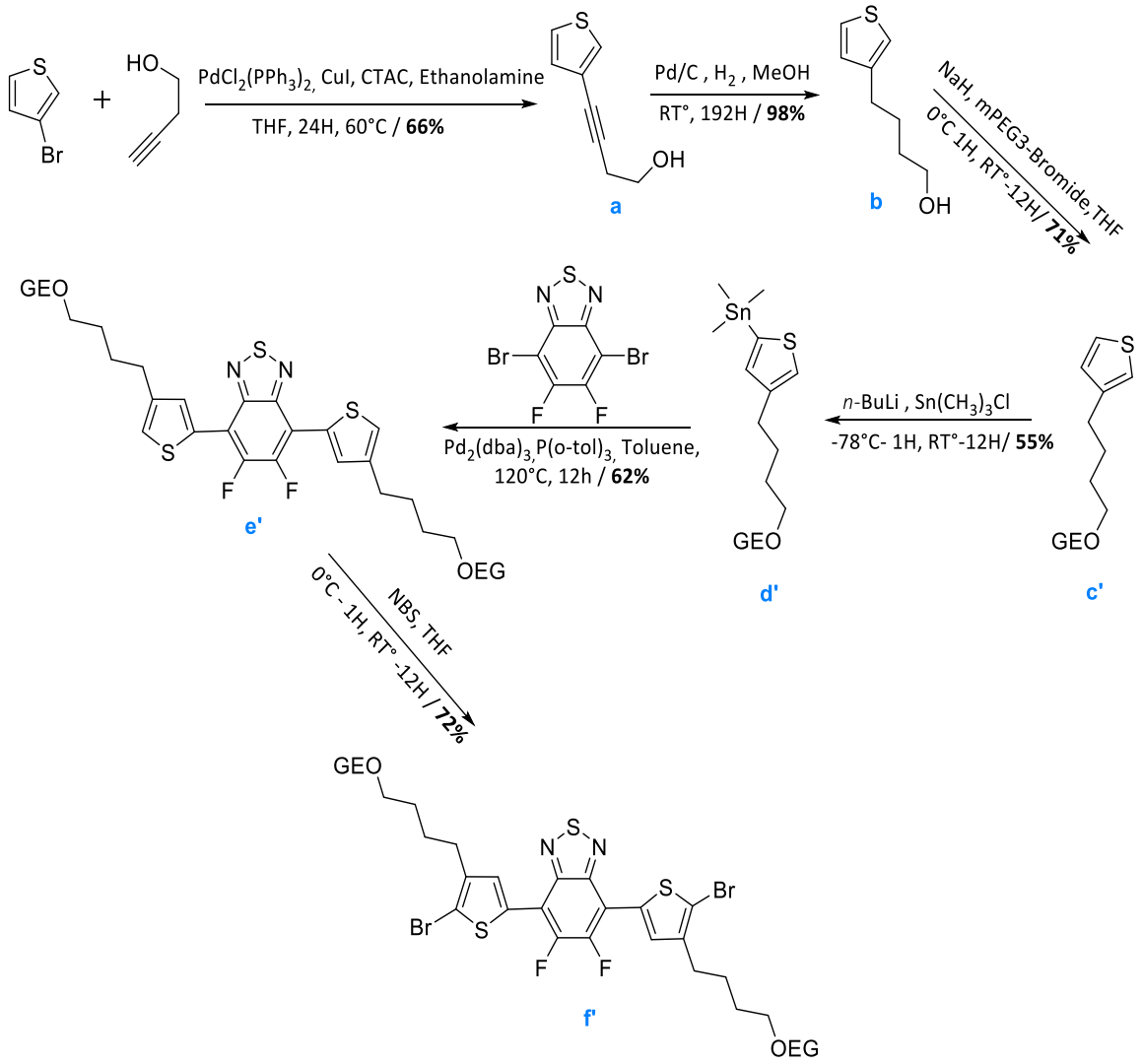

Scheme 3: schematic synthesis of PF2-C_4-OEG

Surprisingly, we succeeded to perform all the chemical steps, including the debromination and its purification. Additionally, the chemical yields of each step are reasonably high. Combined with the two steps saved by the absence of a protection/deprotection sequence, this chemical pathway is promising. However, it is not perfect either. Indeed, the thiophene stannylation step to obtain the compound **d'** is unfortunately not fully selective as it is in standard 3-alkyl-thiophene. Indeed, NMR analysis showed us that two α-positions (2 and 5) on the thiophene ring can be activated during the deprotonation step giving respectively the 2-trimethyltin-4-(C_4-OEG)-thiophene and 2-trimethyltin-3-(C_4-OEG)-thiophene (**Figure 7**), in a molar ratio of approximately 9:1.

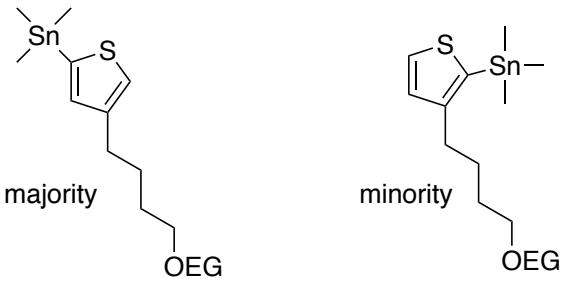

Figure 7: 2-trimethyltin-4-(C_4-OEG)-thiophene compounds (majority) and 2-trimethyltin-3-(C_4-OEG)-thiophene(minority)

Unfortunately, because of the polarity issue, but also of poor stability of the 3-methyltin derivatives on silica gel used in column chromatography, the separation of both compounds could not be performed. The further cross-coupling of these two regioisomers on the DFD unit led to possibly three different regioisomers (**Figure 8**), named, $\alpha\alpha$, $\alpha\beta$ and $\beta\beta$.

However, because of the low amount of the 2-trimethyltin-3-(C_4-OEG)-thiophene, one can suggest that the third $\beta\beta$ regiosiomer is probably really low in quantity. Although the presence of these regioisomers is critical for the optoelectronic properties as well as for the future reproducibility of this chemistry, we decided to continue with this route, considering that the polymer thus synthesized would nevertheless be a good model for the development of the nanoprecipitation process.

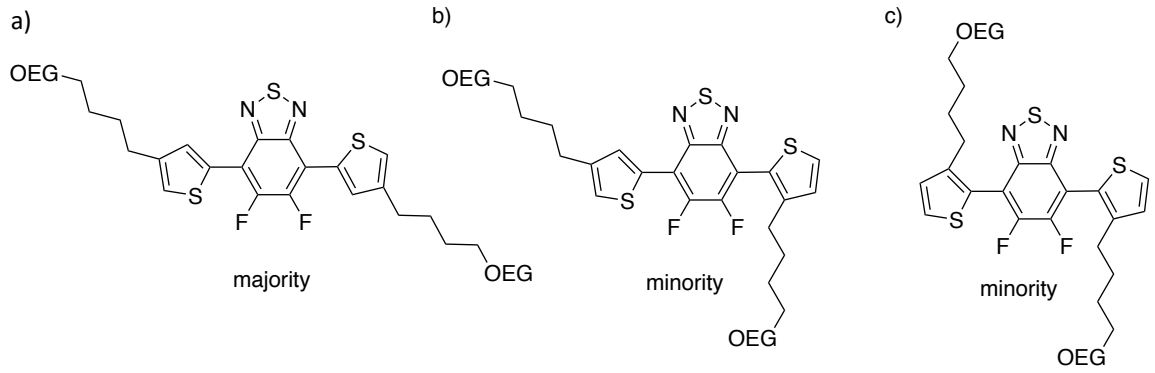

Figure 8: possible regioisomers that can be found in the chemical medium a)$\alpha\alpha$, b) $\alpha\beta$ and c)$\beta\beta$

The polymerization was then carried out by Stille cross-coupling.

The main objective of above syntheses was to synthetize new semiconductor polymers that can be easily solubilized into common low boiling point organic solvents such as $CHCl_3$ or THF. For that reason, we focused on analyzing first the solubility of our PF2-C_4-OEG polymer. In fact, the Soxhlet purification steps during the polymer synthesis gave us first clues. Indeed, the $CHCl_3$ fraction is much larger than usually for such polymer. Unfortunately, all our attempts to measure its molar mass

failed, both at RT in $CHCl_3$ and at 150°C in *o*-DCB. The calculated masses are too low to be correct with respect to the behavior of the polymer in solution.

Then, we performed UV-visible absorption spectroscopy in THF, $CHCl_3$ and thin-film (**Figure 9 top**). First, we compared the UV-visible spectra in thin film of both PF2 derivatives. The two spectra are less different than they appear at first glance. The standard PF2 UV-vis spectrum is know well understood in the lab. As much of D/A alternated copolymers, it exhibits two different bands relative to the π-π* transition and the ICT transition (similarly to the PBDTTPD discussed previously). The second band includes two peaks relative to two π-stacking modes. At high wavelength, the peak is attributed to a segregating stacking (high order in the π-stacking characterized by a segregation of the different comonomers across the polymer chain stack), while at lower wavelength, the peak is attributed to a mixed stacking with a shift of the polymer chains over each other [(2,5)].

In PF2-C_4-OEG, despite a general blue-shift of the absorption wavelength, signature, of a general lower delocalization along polymer chains, one can recognize the two bands. However, the second band at high wavelength, appears under the shape of shoulder, considerably less pronounced. It probably means that this new OEG derivative is less ordered in solid state than the alkylated PF2. This in an expected behavior if we considered the general consensus on the lower ordering of glycolated semiconducting polymers and the presence in our specific case of regioisomer comonomers that consequently decreases the regularity along the polymer backbone.

From the solid-state spectrum, an optical band-gap of 1.6 eV, identical to the one of the reference alkylated PF2, has been calculated.

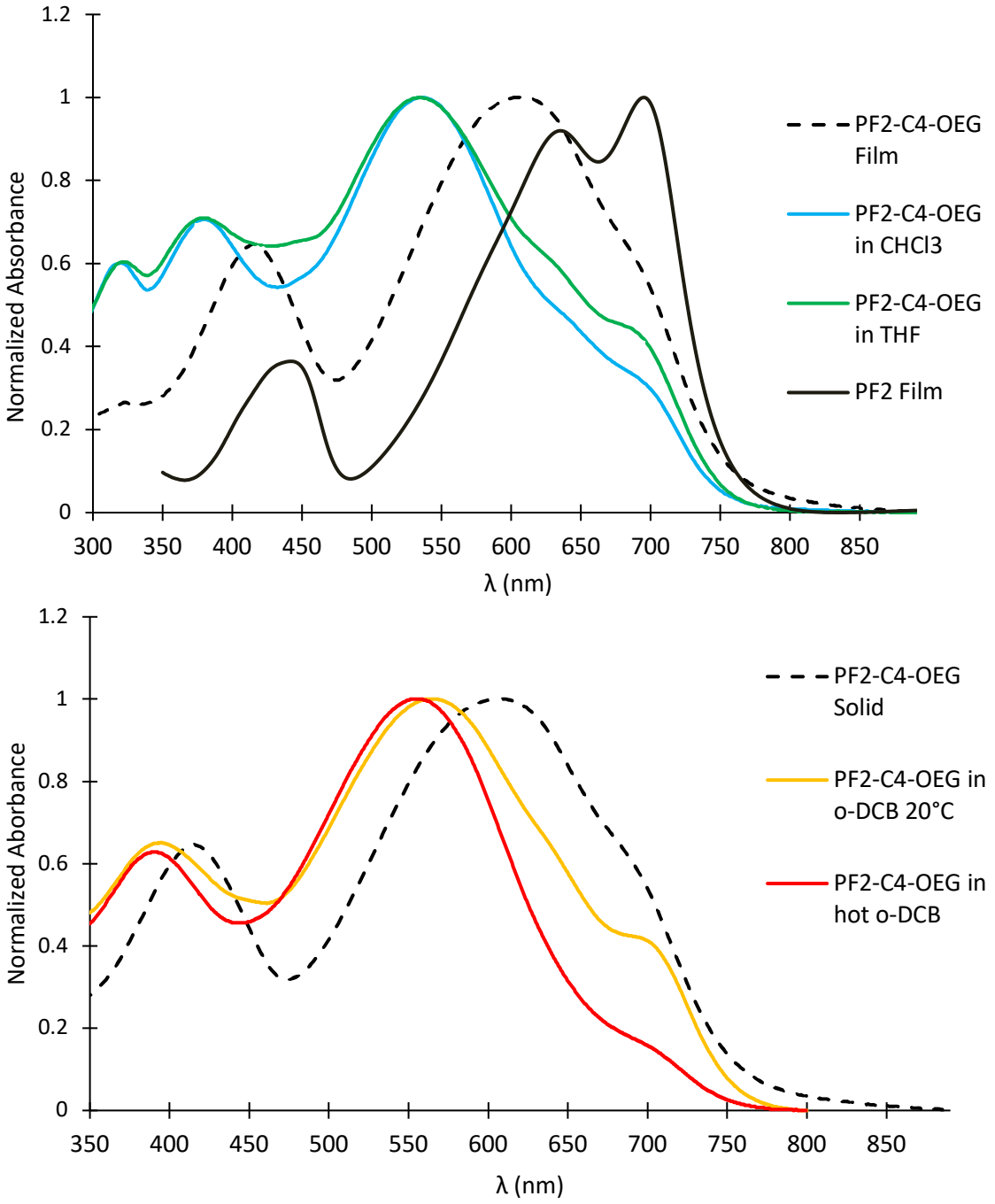

Figure 9: UV-Visible spectra of top) PF2-C_4-OEG as solid film, in $CHCl_3$ & THF– Solutions of 0.02 mg.mL^{-1}
bottom) PF2-OEG as solid film and in o-DCB at different temperature - Solutions of 0.02 mg.mL^{-1}

The strong blue-shift observed when going from solid state to solution suggests that the new polymer is quite soluble at room temperature, although not fully (**Figure 9 bottom**). Indeed, the remaining vibronic structure observed at 700 nm is a signature of the aggregated NPs in solution. This aggregation disappears when PF2-C_4-OEG solution in *o*-DCB is heated at 70°C that refers to a completed solubilization.

Moreover, cyclic voltammetry CV has been used to estimate the energy levels of the new PF2-C_4-OEG. The voltammogram only showed an oxidation wave **(Figure 10).** Any reduction has been observed for this polymer. However, it is a usual behavior for electron donor polymer that could be difficult to reduce. The oxidation potential has been measured to be of 0.9 V leading to a HOMO level of -5.3 eV. It is a 0.05 eV lower value than the one already reported for the alkylated PF2. Such a difference is within the error margin and suggests that the OEG segment does not significantly modify the energy levels of this new polymer. The butyl segment used as spacer helps to move the OEG segment away from the conjugated backbone, which is positive as it allows to keep a deep HOMO level.

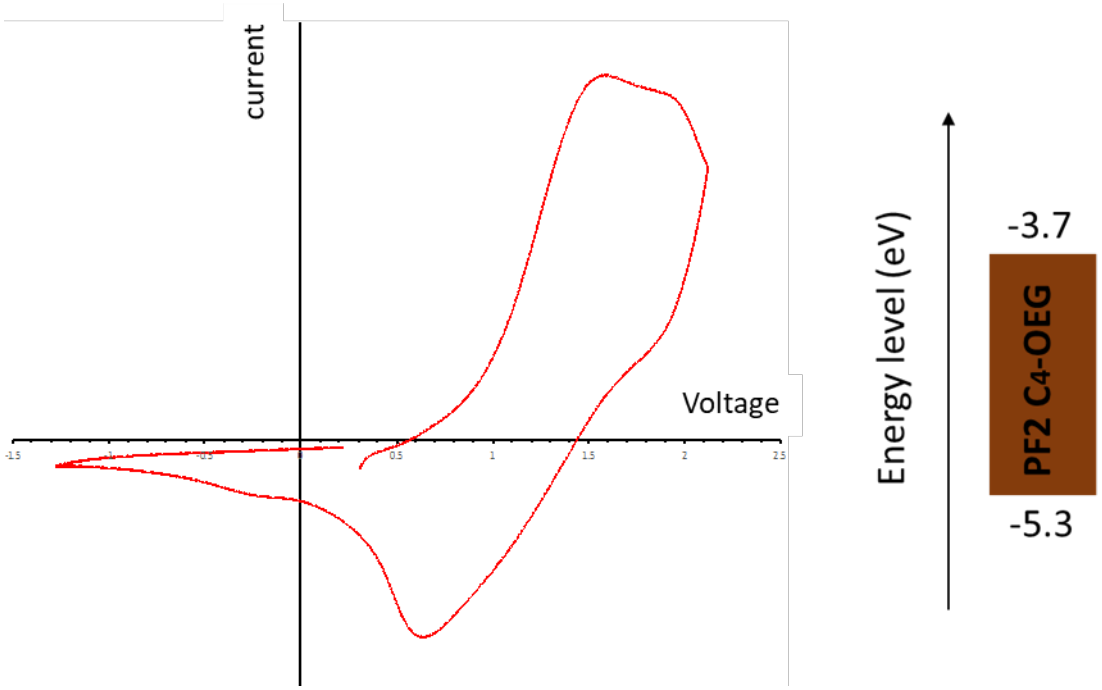

Figure 10: Cyclic voltammogram of PF2-C_4-OEG with its HOMO-LUMO values

As conclusion for this part, we synthesized a new semiconductor polymer containing a hybrid alkyl-OEG chain. This approach leads to an enhance solubility even in low BP solvents. The nanoprecipitation process leading to the elaboration of NPs will take place in the next part. We will particularly focus on the benefits of these new side chains on the NPs elaboration and suspension stabilization, without surfactant addition.

III. Nanoprecipitation:

The nanoprecipitation, also called dispersion by "Ouzo effect", usually takes place by rapidly adding a large quantity of non-solvent, water or alcohol, to a solution of semi-conductor materials in a solvent miscible with previous non-solvent. Thus, precipitation occurs by a process of nucleation and growth due to a supersaturation of the system and particles of uniform size are then obtained, in the absence of surfactant and without significant energy input. In this process, the size and morphology of the particles depend on the concentration of the organic molecule, the organic molecule/solvent/non-solvent interactions, and the mixing speed [6,7]. However, as shown in **chapter I**, the concentration zone in the binodal region where the formation of stable NP occurs can be difficult to find and corresponds to very low polymer concentrations. This process thus leads to a much lower concentration of the final NP dispersions than by the miniemulsion technique[8]. Moreover, the aggregation-driven growth of the NP sometimes continues over several hours leading to very large aggregates[9].

As for the miniemulsion, we tried to integrate electron acceptors into particles by elaborating composite particles or a mixture of separate particles.

III.1 Nanoprecipitation in water or alcohol for PF2, PBDTTPD or $PC_{71}BM$:

III.1.A Without surfactant:

In the first time, preliminary attempts for PF2, PBDTPD, $PC_{71}BM$ or eh-IDTBR NPs elaboration using diluted solutions was done in pure water or in alcohol solutions (methanol, ethanol, isopropanol or butan-2-ol). Up front, materials were solubilized in THF or chlorinated solvent depending on nanoprecipitation non-solvent destination. For alcohol solution, nanoprecipitation can be processed using both initial solutions since THF and *o*-DCB/$CHCl_3$ are miscible with above listed alcohols. In contrast, nanoprecipitation in water can only be accomplished using THF solution due to the immiscibility between water and $CHCl_3$.

Standard solutions concentrations were used in the first step, from 1 $mg.mL^{-1}$ to 0.05 $mg.mL^{-1}$ in order to nanoprecipitate these materials in pure water or alcohol solutions. A summary of the different conditions is given in **Table 1**. Stable NPs dispersions (200 ± 50 nm average diameter) were only obtained for eh-IDTBR. For the other tested materials, none of these attempts led to stable NP dispersions. In fact, a normal precipitation phenomenon takes place leading to extremely large particles.

Material	Concentration ($mg.mL^{-1}$)	Solvent	Non – solvent	Results
$PC_{71}BM$	1	THF	water or ethanol	Small Aggregates
		$CHCl_3$ or *o*-DCB	ethanol, methanol or butan-2-ol	
eh-IDTBR	1	THF	Water	200 ± 50 nm
PF2	1	*o*-DCB	ethanol, methanol or butan-2-ol	Very large Aggregates
	2.5 1 0.5 0.1 0.01	THF	water ethanol, methanol, isopropanol , butan-2-ol	
		$CHCl_3$	ethanol, methanol, isopropanol or butan-2-ol	
PBDTTPD	2.5 1 0.5 0.1	THF	water ethanol, methanol, isopropanol , butan-2-ol	Medium Aggregates
		$CHCl_3$	ethanol, methanol, isopropanol or butan-2-ol	

Table 1: Nanoprecipitation conditions tested for the different materials using a ratio of solvent/non-solvent 1/2.

Many parameters were changed, for example the ratio between the solvent and the non-solvent of the materials. As before, nanoprecipitation did not take place even by decreasing the solvent/non solvent volume ratio from 1/4 to 1/8.

Besides that, we also investigated the effect of the temperature. We supposed that heating the initial solution at 50°C may increase the solubility of these polymers and could minimize the quantity of already existing aggregates (**see UV-Visible spectra above**). In addition, heating of the non-solvent solution could also increase the solvent evaporation rate, thus decreasing Ostwald

ripening. However, none of these parameters were useful to elaborate NPs in water or alcohol solutions.

As conclusion for this study, these first results were not very encouraging, since large particles have been obtained even by starting from extra diluted solution (0.05 mg.mL^{-1}), precipitating in high non-solvent quantity (8 mL of water to 1 mL of material solution) or/and modulating the medium temperature.

III.1.B Using PF 127 as non-ionic surfactant:

Recently, Xie *et al.*[10] have reported a surfactant-assisted nanoprecipitation method, based on the use of Pluronic F127 (**PF127 - Figure 11**), a triblock copolymer of poly(ethylene oxide) and poly(propylene oxide), which allows a control of the NP aggregation phenomenon and leads to more stable suspensions. In comparison to SDS, this surfactant has two advantages: it is non-ionic and it can be easily removed from the surface of the particles by playing with its temperature sensitive critical micellar concentration (cmc)[11]. Indeed, its solubility in water increases at low temperature, allowing it to desorb from the NPs surface, resulting in more efficient dialysis steps.

We thus decided to study the nanoprecipitation of our materials in the presence of PF127.

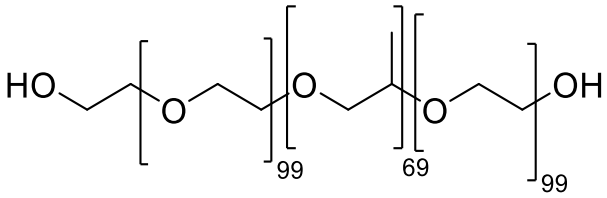

Figure 11: structure of PF127

Experimentally, material solution in THF was injected rapidly into an aqueous surfactant solution at 20 mg.mL^{-1}, followed by ultrasonication in order to improve the mixing.

With the help of PF127, particles of PF2 and PBDTTPD could be obtained as shown in in **Table 2** and **Table 3**, and their average diameter depends on initial materials concentration. Indeed, a decrease of the average diameter for PBDTTPD particle from 560 ± 110 nm to 230 ± 50 nm is observed when its initial concentration in THF is decreased from 2.5 to 1 mg.mL^{-1}. This decrease in the particles size could be attributed to the lower density of nuclei in the solvent mixture which decreases the probability for the formation of larger particles by aggregation and/or to a better solubilization of the material at lower concentration in the initial solutions[12]. However, the decrease of initial material solution also results in a very low final suspension concentration. For that reason, lower concentrations were not studied. The same trend was also observed for the PF2 nanoprecipitation, by applying the same experimental conditions as for PBDTTPD.

Besides that, particles diameter did not change significantly when the volume of non-solvent was doubled (samples 3 & 6), remaining in an average range of 200-300 nm regardless of the ratio between solvent and non-solvent.

Samples	[PBDTTPD] in THF mg.mL^{-1}	Surfactant	Ratio Solvent / Non-solvent	Hydrodynamic diameter (nm)
1	2.5	PF127	1/2	560 ± 110
2	1	PF127	1/2	230 ± 50
3	1	PF127	1/4	220 ± 60

Table 2: PBDTTPD NPs elaboration by nanoprecipitation. Diameter measured by DLS.

Samples	[PF2] in THF mg.mL^{-1}	Surfactant	Ratio Solvent / Non-solvent	Hydrodynamic diameter (nm)
4	2.5	PF127	1/2	360 ± 110
5	1	PF127	1/2	250 ± 70
6	1	PF127	1/4	230 ± 50

Table 3: PF2 NPs elaboration by nanoprecipitation. Diameter measured by DLS.

Finally, the use of PF127 contributes to the formation of stable NP dispersions even if their diameter remained quite high, and not adjustable. This could be attributed to the low solubility of PF2 and PBDTTPD in THF, as described in the first part of this chapter. It is however worth noting that particles in the same diameter range were also reported by Xie *et al.*[10] for the various materials tested in their article.

In PBDTTPD and PF2 case, the elaboration of NPs by nanoprecipitation approach was difficult and only possible with the assistance of a nonionic surfactant. This surfactant will have to be removed before preparing optoelectronic devices.

By using our synthesized PF2-C_4-OEG, a polymer showing a higher solubility in THF and having oligoethylene glycol chains that could help the stabilization of the nanoparticles in water, we hope to be able to obtain nanoparticles by precipitation in pure water, without any surfactant. Indeed, as shown in **chapter II**, PF2-C4-OEG has a similar surface free energy as PF2 of around 30 mN.m^{-1}, but with a much higher polar component than PF2 (13.3 mN.m^{-1} compared to 0.1 mN.m^{-1}), thus increasing its interactions with water.

III.2 Nanoprecipitation in pure water using PF2-C_4-OEG as donor material:

The nanoprecipitation of PF2-C_4-OEG from THF solution in pure water was studied. Separate particles were first prepared, followed by donor-acceptor composites NP in combination with $PC_{71}BM$ or eh-IDBTR.

III.2.A Separate NPs:

In contrast to PF2, stable NP dispersions were obtained by nanoprecipitation of the PF2-C_4-OEG in pure water, confirming our intuition that introducing oligo(ethylene glycol) side chains would help the process.

- **PF2-C_4-OEG concentration in THF solution:**

Table 4 shows the hydrodynamic diameters of NPs elaborated by nanoprecipitation of PF2-C_4-OEG at various polymer concentrations for a solvent/non solvent ratio of 1/4. As previously a slight decrease in hydrodynamic diameter from 180 ± 90 nm to 120 ± 70 nm is observed when the initial concentrations decrease from 1 mg.mL^{-1} to 0.1 mg.mL^{-1}. However, as the difference was not significant, we decided to continue the study by fixing the initial material amount at 1 mg.mL^{-1} in order to keep a reasonable final NP dispersion concentration.

PF2-C_4-OEG concentration in THF mg.mL^{-1}	Hydrodynamic diameter (nm)
1	180 ± 90
0.5	160 ± 60
0.1	120 ± 70

Table 4: Hydrodynamic diameters measured by DLS for PF2-C_4-OEG separate NPs, solvent/non solvent ratio = 1/4.

III.2.B Composites NPs:

Composites NPs containing PF2-C_4-OEG as electron donor material and $PC_{71}BM$ or eh-IDTBR as electron acceptor materials, were then prepared.

Influence of different parameters on composites NPs diameter:

- **concentration in THF solution:**

Here, we studied the effect of initial materials PF2-C_4-OEG:$PC_{71}BM$ 1:2 concentration. Unlike the case of separate PF2-C_4-OEG NPs, no change in particle diameter was reported. The average diameter measured by DLS was around 150 nm ± 100 regardless the initial concentration (1mg.mL^{-1}, 0.5 mg.mL^{-1} and 0.1 mg.mL^{-1}).

Besides that, the large standard deviation of the NP diameters distribution**,** show that during nanoprecipitation, particle diameter is not uniform and cannot be controlled.

- **Ratio PF2-C_4-OEG: $PC_{71}BM$ or PF2-C_4-OEG: eh-IDTBR**

Table 5 represent the effect of changing the donor:acceptor ratio on the average diameter of PF2-C_4-OEG:$PC_{71}BM$ or PF2-C_4-OEG:eh-IDTBR composites NPs, keeping the total materials concentration in THF at 1 mg.mL^{-1}.

Ratio D:A	Hydrodynamic diameter (nm) for PF2-C_4-OEG: $PC_{71}BM$ NPs	Hydrodynamic diameter (nm) for PF2-C_4-OEG: eh-IDTBR NPs
2:1	140 ± 80	130 ± 30
1:1	140 ± 100	110 ± 70
1:2	190 ± 100	100 ± 80

Table 5: effect of PF2-C_4-OEG:eh-IDBTR ratio on NPs composites diameters 1mg.mL^{-1} materials/THF solution precipitated into 4 mL of pure water (V Øorga = 20%).

As for separate PF2-C4-OEG NPs, polydisperse NPs were obtained for both composites, the standard deviation of the NPs diameter slightly increasing with the amount of $PC_{71}BM$ in the PF2-C4-OEG NPs. This could be due to the poor solubility of $PC_{71}BM$ in THF leading to the presence of aggregates already before nanoprecipitation. However, it is interesting to notice that it is possible to obtain composite NPs containing $PC_{71}BM$ in pure water with diameter in the range of 140 to 190

nm, while no $PC_{71}BM$ separate NPs were obtained of in pure water. The PF2-C_4-OEG probably plays the role of a surfactant surrounding PCBM aggregates, thanks to its oligo(ethylene glycol) chains.

In order to confirm that both materials are indeed in the same particles, fluorescence measurements of the PF2-C_4-OEG:$PC_{71}BM$ composites NPs were performed and compared with the separate PF2-C_4-OEG NPs (**Figure 12**). As was the case for the PF2:$PC_{71}BM$ composites NPs elaborated by miniemulsion approach, the fluorescence intensity is also quenched whatever the D:A ratio between 1:2 and 2:1. This quenching indicates that that both materials are located within the same particle, allowing charge transfer between donor and acceptor. In the literature, as discussed in **Chapter I**, mixed morphology with smaller donor and acceptor domains were observed in nanoprecipitated NPs as compared to the core-shell morphology observed in NPs prepared by miniemulsion. In our case it would be interesting to observe the morphology by STXM to see if we also obtained mixed NPs with small domains or a core-shell structure due to the presence of the oligo(ethylene glycol) stabilizing chains.

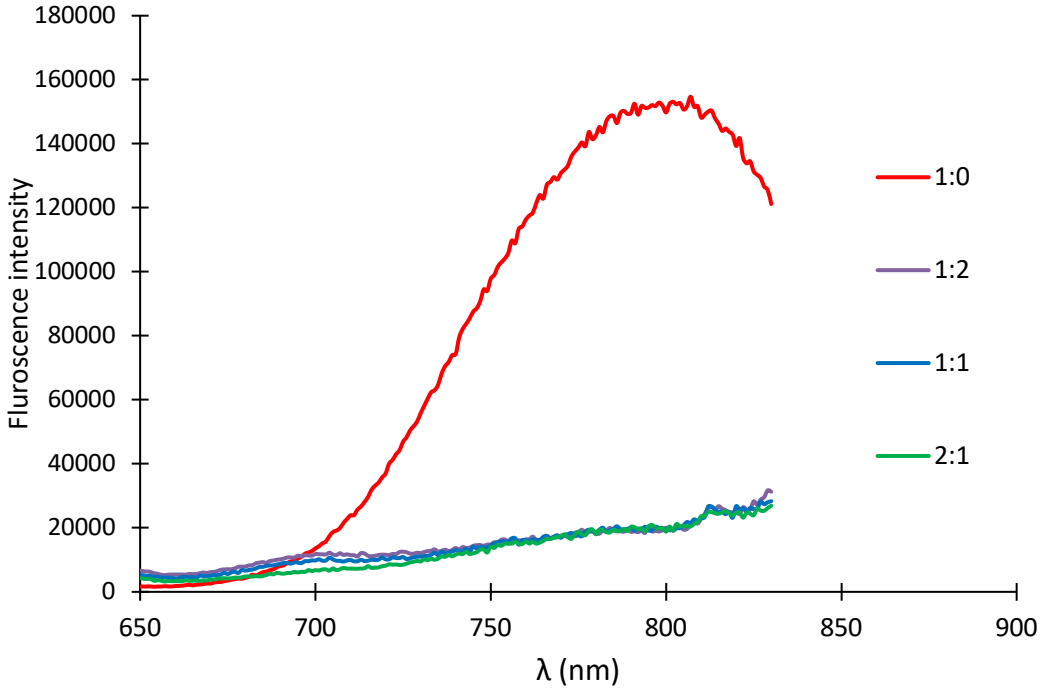

Figure 12 : Fluorescence spectroscopy of PF2-C_4-OEG:$PC_{71}BM$ composites NPs and PF2-C_4-OEG separate NPs. Excitation at λ = 600 nm, suspension concentration 0.002 mg.mL^{-1}

In the case of composite NPs with eh-IDTBR, slightly smaller and less polydisperse composite NPs are obtained (**Table 5**), compared to PF2-C_4-OEG:$PC_{71}BM$ composite NPs, probably thanks to the better solubility of eh-IDTBR in THF. It is probably facilitated by the fact that, eh-IDTBR separate NPs could also be obtained in pure water even in the absence of PF2-C_4-OEG as already shown in **Table 1**.

- **Effect on changing solvent / non-solvent ratio**:

As observed in **Figure 13**, increasing the amount of non-solvent has no remarkable effect on composites PF2-C_4-OEG:PC_{71}BM 1:2 NP diameter. Therefore, a ratio of solvent/non-solvent of 1/2 will be kept as best condition for the nanoprecipitation, in order to obtain the less diluted NP dispersion as possible. Indeed, we have shown in **Chapter IV** that a NP dispersion concentration of 17.5 mg.mL^{-1} was necessary to obtain homogeneous thin films by spin coating.

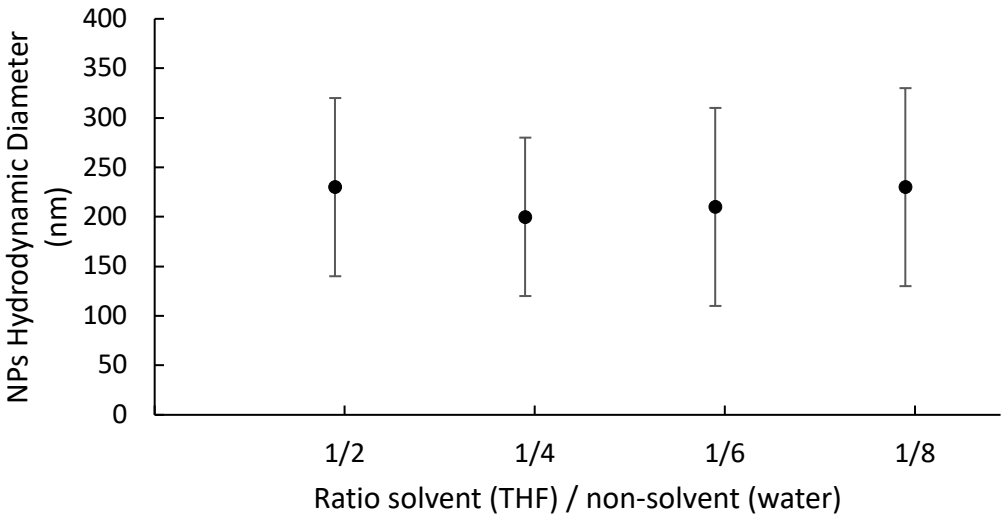

Figure 13: hydrodynamic diameter measured by DLS for PF2-C_4-OEG:PC_{71}BM 1:2 composites NPs. 1mg.mL^{-1} solution injected into different non-solvent ratio.

IV. Conclusion:

The objective of this chapter was to elaborate nanoparticles by nanoprecipitation in order to avoid the presence of ionic surfactant. Starting from the PF2 structure, which is only poorly soluble in THF and chloroform, we designed and tested different strategies to synthesize a semi-conducting donor polymer that should be more soluble in low boiling point solvents. Even if the multi-step syntheses and purifications were not as easy as expected due to the polarity brought by the oligo(ethylene glycol) moieties, we successfully synthesize the PF2-C_4-OEG. This new polymer has the same backbone structure as PF2, but the ethylhexyl side chains are replaced by oligo(ethylene glycol) groups separated from the backbone by a C_4 chain. As expected, this polymer has a much better solubility in chloroform and THF as PF2. Moreover, its OEG groups are expected to help the stabilization of the NPs in water. Indeed, while the nanoprecipitation of PF2 was only possible in the presence of Pluronic F127, PF2-C_4-OEG stable NPs were obtained in pure water without any surfactant. Moreover, it was possible to elaborate composite PF2-C_4-OEG:$PC_{71}BM$ and PF2-C_4-OEG:EH-IDTBR composite NPs by nanoprecipitation. Further characterization of their morphology and optoelectronic properties still have to be performed.

V. References:

1. Rammal, M., Lévêque, P., Schlatter, G., Leclerc, N. & Hébraud, A. Recent advances in the green processing of organic photovoltaic devices from nanoparticle dispersions. *Mater. Chem. Front.* 10.1039.D0QM00361A (2020) doi:10.1039/D0QM00361A.
2. Olla, T. *et al.* Benzothiadiazole Halogenation Impact in Conjugated Polymers, a Comprehensive Study. *Macromolecules* 52, 8006–8016 (2019).
3. Kim, T. *et al.* Flexible, highly efficient all-polymer solar cells. *Nat. Commun.* 6, (2015).
4. Zhong, Y., Biniek, L., Leclerc, N., Ferry, S. & Brinkmann, M. Segregated versus Disordered Stacking in Two Low Bandgap Alternated Copolymers for Photovoltaic Applications: Impact of Polymorphism on Optical Properties. *Macromolecules* 51, 4238–4249 (2018).
5. Schmode, P. *et al.* The Key Role of Side Chain Linkage in Structure Formation and Mixed Conduction of Ethylene Glycol Substituted Polythiophenes. *ACS Appl. Mater. Interfaces* 12, 13029–13039 (2020).
6. Lepeltier, E., Bourgaux, C. & Couvreur, P. Nanoprecipitation and the “Ouzo effect”: Applicationto drug delivery devices. Advanced Drug Delivery Reviews 71, 86–97 (2014).
7. J. E. Millstone, D. F. J. Kavulak, C. H. Woo, T. W. Holcombe, E. J. Westling, A. L. Briseno, M. F. Toney and J. M. J. Fréchet, Synthesis, Properties, and Electronic Applications of Size-Controlled Poly(3-hexylthiophene) Nanoparticles, Langmuir, 2010, 26, 13056–13061.
8. S. Subianto, N. Dutta, M. Andersson and N. R. Choudhury, Bulk heterojunction organic photovoltaics from water-processable nanomaterials and their facile fabrication approaches, *Advances in Colloid and Interface Science*, 2016, 235, 56–69.
9. F. Wang, M.-Y. Han, K. Y. Mya, Y. Wang and Y.-H. Lai, Aggregation-Driven Growth of Size-Tunable Organic Nanoparticles Using Electronically Altered Conjugated Polymers, J. Am. Chem. Soc., 2005, 127, 10350–10355.
10. C. Xie, T. Heumüller, W. Gruber, X. Tang, A. Classen, I. Schuldes, M. Bidwell, A. Späth, R. H. Fink, T. Unruh, I. McCulloch, N. Li and C. J. Brabec, overcoming efficiency and stability limits in water-processing nanoparticular organic photovoltaics by minimizing microstructure defects, *Nature Communications*, 2018, **9**, 5335.
11. Bohorquez, M., Koch, C., Trygstad, T. & Pandit, N. A Study of the Temperature- Dependent Micellization of Pluronic F127. *J. Colloid Interface Sci.* **216**, 34–40 (1999).
12. L. Parrenin, G. Laurans, E. Pavlopoulou, G. Fleury, G. Pecastaings, C. Brochon, L. Vignau, G. Hadziioannou and E. Cloutet, Photoactive Donor–Acceptor Composite Nanoparticles Dispersed in Water, Langmuir, 2017, 33, 1507–1515.

GENERAL CONCLUSION

This PhD work aimed at studying the eco-friendly nanoparticles aqueous dispersion route for the preparation of OPV devices. It is at the interface between organic semiconductor and colloid science. Consequently, it is based on three very different topical fields:

- ***Polymer synthesis***:

We have synthesized several polymers, from the standard PF2, the laboratory's reference polymer for its performance in OPV devices, to a more soluble version, called PF2-C_4-OEG, using original hybrid chains of the alkyl-oligo(ethylene glycol) type, as well as various new polymers. Unfortunately, we have not yet found the miracle material that combines high performance and good solubility in low-boiling organic solvents. However, the new PF2-C_4-OEG seems a promising conjugated polymer that probably deserves to be further studied.

- ***NPs elaboration by miniemulsion or nanoprecipitation***:

The miniemulsion process has allowed the synthesis of different types of NPs, single component or composite, based on the use of standard PF2. Two kind of electron acceptor materials have been investigated, $PC_{71}BM$ and eh-IDTBR. In particular, a core shell structure of composites NPs made up of PF2:$PC_{71}BM$ was confirmed by several techniques such as fluorescence, TEM and STXM. In this case, PF2 occupies the shell and the $PC_{71}BM$ the core as predicted by the surface energy values of the two materials, respectively of 30 and 47 $mN.m^{-1}$. We succeeded to elaborate NPs exhibiting promising diameter of 60 ± 20 nm which is compatible with the film thicknesses targeted for active layers in OPV devices. However, the miniemulsion required the use of ionic surfactant, SDS, to stabilize the NP suspension. Despite the numerous dialysis steps applied, we have shown that a significant amount of surfactant still remains in the final suspension, before its use as an aqueous ink.

Therefore, we also implemented the nanoprecipitation approach that can be performed without ionic surfactant. For nanoprecipitation, we used our new polymer, the PF2-C_4-OEG, soluble in $CHCl_3$ and THF at RT and bearing oligo(ethylene glycol) side chains that help the NPs stabilization in water. We succeeded to precipitate it in pure water as single component, or in blend with electron acceptors ($PC_{71}BM$ or eh-IDTBR). Composite NP with 150 nm of diameter have been thus obtained and will be soon investigated in OPV devices.

- ***Thin-film and optoelectronic devices elaboration and characterization***:

the production of thin films from aqueous suspensions required a long development process. However, we succeeded to find proper conditions allowing to obtain satisfying homogeneous thin-films with a thickness that can be tuned from 70 to 200 nm approximately. This optimization of conditions was performed on composite PF2:$PC_{71}BM$ NPs, obtained by miniemulsion and with a final solid content of 1.75 wt%. From these thin-films, we characterized the charge transport properties by SCLC and OFET method. Promising hole and electron mobilities of about 10^{-3} $cm^2.Vs^{-1}$ were measured. As expected from literature, we have seen an impact of the post-deposition thermal annealing, related to a structural and morphological changes upon temperature. Indeed, at 120°C a coalescence of neighboring NPs appears, while above 140°C, a phase change in the NPs film structuration takes place that seems to be related to the co-crystallization of both materials. Finally, a 1% of PCE has been obtained in preliminary OPV tests. Although promising, this result shows that further optimization is necessary to still increase this efficiency.

This thesis project is very new in our laboratory. Therefore, each point required a laborious clearing. However, we succeeded in reaching a functional OPV device, which demonstrates that this research makes sense and that the use of NP suspensions in non-toxic and environmentally friendly solvents can be an interesting way towards the industrialization of organic optoelectronics technologies. However, there are many perspectives that need to be further explored.

Starting from the miniemulsion elaborated NPs, the optimization of the OPV device elaboration will be performed in order to reach better PCEs. For instance, the thickness of the active layer or the $PC_{71}BM$:PF2 ratio could be varied. Moreover, as the NPs approach allows multilayer deposition, which is not possible for the solution processed active layer, we could try to better control the charges driving towards the corresponding electrode by varying the vertical D:A composition of the active layer, with interlayers of separate PF2 NPs on the anode side and separate $PC_{71}BM$ NPs on the cathode side as proposed by Gärtner *et al* [(1)]. When the OPV device made of PF2:$PC_{71}BM$ will be optimized, the preparation of OPV devices from the composite PF2:eh-IDTBR will also be prepared. For these particles, the role of the SDS ionic surfactant in the functioning of the OPV device will also be studied.

In parallel, we could also study the behavior of our nanoprecipitated NPs containing our new PF2-C_4-OEG polymer in OPV devices. The molecular design of such polymer already proved to be interesting as it helped the nanoprecipitation process by stabilizing the NPs in water, without changing significantly the energy levels of the PF2. Other polymers could be designed with a similar strategy, which could serve as real surfactant in the nanoprecipitation or miniemulsion process.

However, the difficulties that can be encountered during the polymer synthesis due to the molecule polarity have to be anticipated.

Finally, all polymer blend (donor and acceptor) could also be tested in order to see if a core-shell structure is still found in NPs and if a kind of higher stability of device can be reached.

1. Gärtner, S., Reich, S., Bruns, M., Czolk, J. & Colsmann, A. Organic solar cells with graded absorber layers processed from nanoparticle dispersions. *Nanoscale* **8**, 6721–6727 (2016).

RESUME EN FRANÇAIS

I. Introduction :

L'électronique organique est un domaine de recherche en pleine explosion depuis une petite trentaine d'année, aussi bien d'un point de vue fondamental qu'appliqué. Ainsi les semi-conducteurs organiques trouvent aujourd'hui des applications dans le domaine des diodes électroluminescentes, des lasers, des capteurs, des photodétecteurs ou encore des cellules solaires organiques. Les connaissances associées, tant du point de vue chimique que physique ne cessent de progresser. Ces matériaux sont extrêmement prometteurs. Cependant, leur mise en œuvre se fait actuellement essentiellement en solution dans des solvants organiques toxiques, ce qui représente un frein à leur industrialisation. Dans ce cadre, ce travail de thèse s'est fixé pour objectif de développer des nanoparticules (NPs) de matériaux semi-conducteurs organiques (SCO) dispersées dans des milieux aqueux ou alcooliques inoffensifs.

Les dispersions de NPs organiques ne représentent pas à proprement parler un sujet innovant. Cependant, leur application au SCOs est un champ disciplinaire relativement inexploré et représente un beau défi dans la mesure où les SCOs sont des matériaux de faible solubilité dans des solvants organiques usuels et que leur utilisation en dispositifs nécessite le contrôle de leur auto-assemblage en film mince, en particulier dans les cellules solaires organiques constituées de deux matériaux complémentaires.

En conséquence, l'objectif de ce travail thèse repose principalement sur la préparation et la caractérisation de nanoparticules de polymères conjuguées, présentant des propriétés à l'état de l'art dans le domaine du photovoltaïque organique et synthétisés au laboratoire. Les nanoparticules ont été préparées par deux méthodes différentes : la miniémulsion et la nanoprécipitation. Enfin, ces NPs ont été utilisées pour élaborer des films minces à partir de ces particules, optimisés afin de constituer les couches actives de cellules photovoltaïques organiques (**Figure 1**).

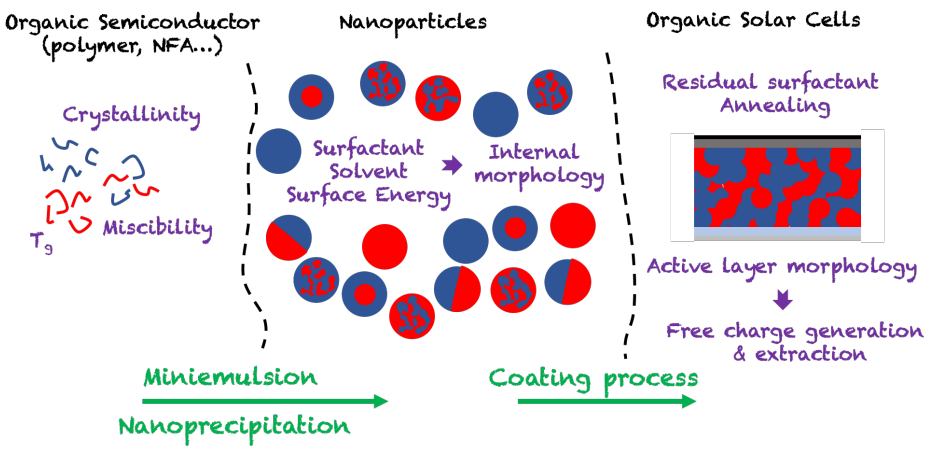

Figure 1 : Des matériaux SCO au dispositif OPV via la préparation de NPs et leur mise en œuvre sous forme de films fins.

Concernant la miniémulsion, deux phases non miscibles sont préparées : une phase organique contenant le SCO solubilisé dans un bon solvant et une phase aqueuse contenant un tensioactif. La phase organique est ensuite dispersée dans la phase aqueuse par ultrasonification puis le solvant organique est finalement évaporé. L'avantage de cette technique réside dans la facilité de mise en œuvre d'un grand nombre de polymères, cependant, elle nécessite l'utilisation d'un tensioactif souvent ionique tel que le dodecylsulfate de sodium (SDS). Plusieurs cycles de dialyses sont ensuite nécessaires pour enlever ce tensioactif qui risque de piéger les charges dans le dispositif optoélectronique final.

En conséquence, la nanoprécipitation a été également explorée. Cette technique permet d'éviter l'utilisation d'un tensioactif ionique. Il s'agit de préparer une solution diluée des matériaux SCOs dans un solvant organique et de l'ajouter rapidement à une grande quantité de non-solvant du polymère (de l'eau ou des alcools principalement) miscible avec le solvant organique initial. Le mélange se trouve alors sursaturé en SCOs, ce qui provoque la formation de nanoparticules par un mécanisme de nucléation-agrégation. Le solvant organique est ensuite rapidement évaporé.

II. Synthèse des polymères organiques semi-conducteurs donneurs :

Pour lancer ces études, nous avons choisi dans un premier temps le PF2 (**Figure 2**), un polymère semi-conducteur contenant deux atomes de fluor, récemment élaboré et étudié au laboratoire pour la fabrication des cellules solaires à hétérojonction volumique (type BHJ) dont un rendement de conversion moyen (Power Conversion Efficiency, PCE) élevé, supérieur à 10%, a été obtenu [(1)]. L'efficacité de ce polymère repose sur les propriétés d'auto-assemblage induites par la présence des atomes électronégatifs de fluor, qui outre l'abaissement des niveaux d'énergie, favorise

également les interactions de π-stacking entre macromolécules voisines. Ce PF2 présente ainsi des mobilités de trous élevées dans la direction perpendiculaire au plan du substrat.

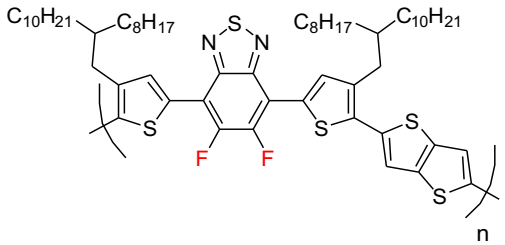

Figure 2 : structure du PF2

LE PF2 a été synthétisé par couplage de Stille entre deux monomères préalablement synthétisés au laboratoire. Ce polymère de masse molaire importante, n'est malheureusement soluble dans l'*o*-dichlorobenzène qu'à des températures supérieures à 90°C (**Figure 3**). En dessous de cette température, des agrégats ayant un diamètre d'environ 440 nm se forment. Or les procédés que nous utilisons pour préparer les NP nécessitent de partir de solutions homogènes de polymères. De plus, le solvant doit être évaporé après l'élaboration des particules afin d'obtenir des suspensions aqueuses. Or la température d'ébullition de l'*o*-dichlorobenzène est plus élevée que celle de l'eau ou des alcools, donc son évaporation est particulièrement délicate et longue. Afin de résoudre le problème, le même polymère ayant une plus faible masse molaire, plus soluble dans le chloroforme, a été synthétisé en diminuant la durée de la polymérisation de 20 h à 20 min (Schéma 1), puis la fraction obtenue par extraction au Soxhlet dans le chloroforme est utilisée. Elle présente une masse molaire de 53 kg.mol^{-1}.

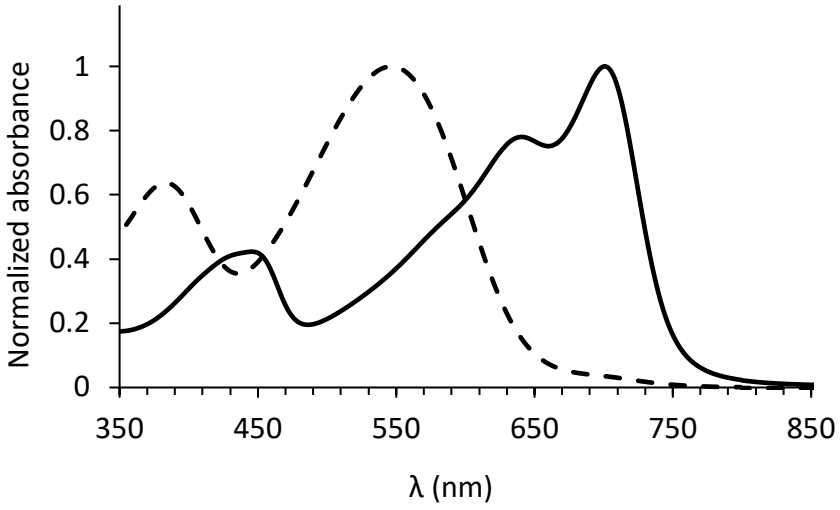

Figure 3 : Spectres UV Visible du PF2 (masse molaire élevée) dans l'oDCB à 25°C (trait plein) – et 95°C (pointillés)

Afin de pallier la faible solubilité du PF2, un deuxième polymère, issu de la littérature a été choisi, le PBDTTTPD (**Figure 4**). Celui-ci est décrit comme étant soluble dans le $CHCl_3$, THF et le CH_2Cl_2. De plus, ce polymère a retenu notre attention, car il peut être utilisé en combinaison avec un polymère accepteur, le P(NDI2HD-T2), disponible au laboratoire, pour élaborer des cellules solaires « tout polymère » présentant des PCEs de l'ordre de 6% [22]. Alternativement, un PCE de 6% est également obtenu en mélange avec le $PC_{71}BM$.

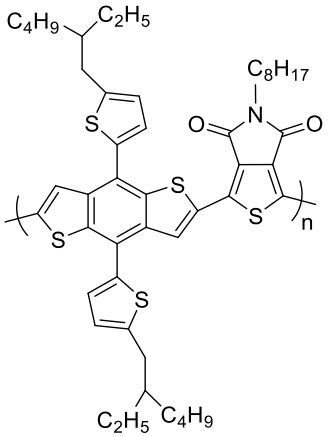

Figure 4 : structure du PBDTTTPD

III. Élaboration des nanoparticules et leur caractérisation :

Les techniques de nanoprécipitation et de miniémulsion ont été utilisées pour préparer des NPs simples contenant le polymère donneur d'électrons (PF2 ou PBDTTTPD) ou le matériau accepteur d'électrons ($PC_{71}BM$ ou eh-IDTBR) ainsi que des NPs composites, contenant les deux SCOs à la fois.

II.A Miniémulsion :

Des NPs simples de PF2, de $PC_{71}BM$, d'eh-IDTBR, ainsi que des particules composites associant le PF2 à l'un des deux accepteurs d'électrons ont été préparées par miniémulsion. La quantité de SDS permet de contrôler le diamètre de ces NPs. Ainsi, des NPs de diamètre compris entre 60 ± 20 nm et 200 ± 70 nm ont été obtenues. Pour les NPs composites obtenues, nous avons également montré que le ratio donneur:accepteur utilisé n'avait pas d'influence sur le diamètre des particules. Des mesures spectroscopiques en UV-visible, fluorescence et photoluminescence résolue en temps ont ensuite été réalisées, permettant de confirmer que dans le cas des particules composites, les deux matériaux, PF2 et $PC_{71}BM$ ou bien PF2 et eh-IDTBR se trouvent bien ensemble dans la même particule. Enfin, la morphologie cœur-coquille des NPs de PF2:$PC_{71}BM$ a été déterminée par microscopie électronique à transmission (MET). Elle a également été confirmée par microscopie à transmission des rayons X (Scanning transmission X-ray microscopy, STXM). De plus, cette technique nous a permis de cartographier la composition chimique des plus grosses NPs, grâce à la

différence de contraste entre les deux spectres C K edge NEXAFS (near-edge X-ray absorption fine structure) des deux matériaux PF2 et $PC_{71}BM$. Dans un premier temps, les images de STXM nous ont permis de montrer que la coquille est composée d'une phase riche en PF2 contenant 75% de PF2 et 25% de $PC_{71}BM$ alors que le cœur de la particule contient une phase riche en $PC_{71}BM$ qui contient 10% de $PC_{71}BM$ et 30 % de PF2 (**Figure 5**). De plus, nous avons montré que lors d'un recuit de 10 min à 150°C, le $PC_{71}BM$ diffuse dans la coquille de PF2, jusqu'à atteindre une concentration de 42 ± 8 %pds. Bien que la morphologie cœur-coquille n'est pas la plus adaptée pour l'application photovoltaïque car les domaines accepteurs et donneurs doivent pouvoir former des chemins de percolation pour transporter les charges jusqu'au électrodes, la concentration initiale en $PC_{71}BM$ dans la coquille doit permettre la mobilité des électrons vers les électrodes même sans recuit. En revanche, dans le cas des nanoparticules PF2:eh-IDTBR, la morphologie interne des nanoparticules n'a pas pu être identifiée du fait du peu de contraste entre les deux matériaux au MET ou au STXM.

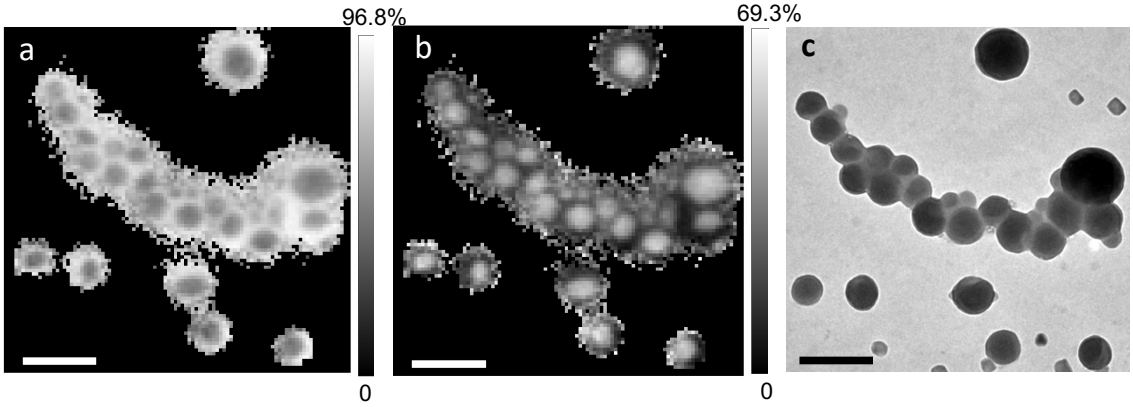

Figure 5 : a-b) Images STXM d'un assemblage de NPs, a) cartographie de la composition en PF2 (%pds), b) cartographie de la composition en $PC_{71}BM$ (%pds). c) image MET du même assemblage. La barre d'échelle représente 400 nm.

III.B Nanoprecipitation :

Les premiers essais de nanoprécipitation du PF2 et du PBDTTTPD ont systématiquement conduit à la formation de grosses particules peu stables dans le temps. L'utilisation d'un tensioactif non ionique, le Pluronic F127, (Xie *et al.* ont recours à ce tensioactif, sur d'autres polymères)[(3)] a toutefois permis d'obtenir des nanoparticules ayant un diamètre d'environ 240 nm.

Cependant, afin d'éviter totalement l'utilisation de tensioactifs durant la procédure de préparation des NPs, nous avons décidé de synthétiser un dérivé du PF2 plus soluble. Pour ce faire, nous avons cherché à remplacer les chaînes alkyles standards par des chaînes hybrides présentant un espaceur alkyle terminé par un segment oligo(ethylène glycol) (OEG) (**Figure 6**). Ces extrémités OEG sont susceptibles en outre d'améliorer la stabilité des particules dans l'eau ou les alcools. Cependant, cette synthèse multi-étapes (9 étapes) s'est révélée bien plus complexe qu'imaginée, du fait de la

faible sélectivité de certaines étapes de réactions sur le thiophène et de la difficulté de séparation des sous-produits de réaction, dès lors qu'une chaîne OEG, très polaire, est fixée sur le polymère. Néanmoins, nous avons abouti à un polymère nommé PF2-C_4-OEG.

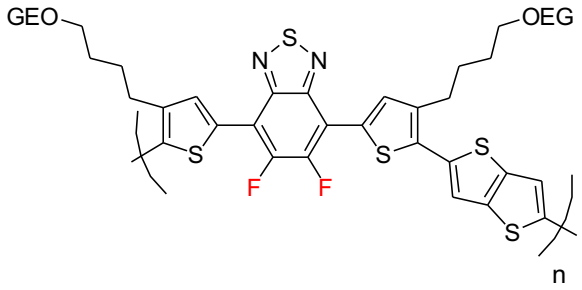

Figure 6 : structure du PF2-C_4-OEG

Le polymère synthétisé présente une bonne solubilité dans le $CHCl_3$ ou le THF, cela nous a permis de procéder à la nanoprécipitation dans l'eau (**Figure 7**).

Des NPs contenant uniquement du PF2-C_4-OEG ont été premièrement élaborées. Des solutions polymères/THF allant de 0,1 mg.mL^{-1} à 1 mg.mL^{-1} ont été préparée. Leurs précipitations dans l'eau pure, sans l'intervention d'un tensioactif, aboutissent à l'obtention de NPs ayant un diamètre de l'ordre de 150 ± 70 nm après évaporation du THF à 60°C pendant 3h.

Comme pour la miniemulsion, nous avons ensuite élaboré des NPs composites PF2-C_4-OEG:$PC_{71}BM$ et PF2-C_4-OEG:eh-IDTBR. A nouveau, des NPs ayant un diamètre proche 150 nm ont étaient obtenues, quelque soit la concentration initiale des matériaux dans le THF (1 ; 0,5 ; 0,1 mg.mL^{-1}), le ratio D/A (1/2 ; 1/1 ; 2/1) ou bien le ratio entre le THF et le eau (1/2 ; 1/4 ; 1/6 ; 1/8) .

D'autre part, l'extinction de fluorescence observée dans les NPs composites PF2-C_4-OEG:$PC_{71}BM$, en comparaison de la fluorescence mesurée dans des NPs composées de PF2-C_4-OEG uniquement, est une indication de la présence de ces deux matériaux dans la même particule. Comme pour les miniémulsions, des techniques, telles que STXM, pourraient être utilisées pour déterminer la localisation des matériaux à l'intérieur des nanoparticules.

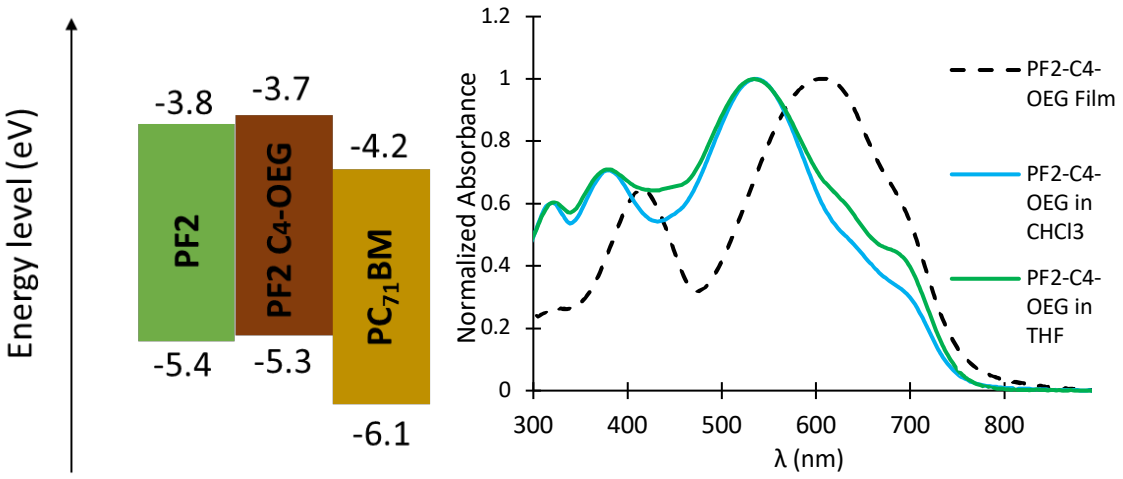

Figure 7 : Comparaison des niveaux d'énergie du PF2-C4-OEG, du PF2 et du $PC_{71}BM$ (gauche). Spectres UV-Visible du PF2-C4-OEG en film mince et en solution à 0,02 mg.mL^{-1} dans le $CHCl_3$ et le THF.

IV. Préparation des films à partir de suspensions de NPs :

Les NPs produites par miniemulsion ont ensuite été dialysées afin d'enlever le maximum de SDS avant l'élaboration des films minces pour les dispositifs optoélectroniques. Malgré ces nombreuses étapes de lavage (jusqu'à 16 étapes successives), une quantité estimée à 20 wt% minimum de SDS, correspondant approximativement à la monocouche de SDS adsorbée à la surface des nanoparticules, se trouve toujours dans la suspension de NPs (une mesure ATG permet de quantifier cette quantité de SDS présente).

La formation de films minces à partir des suspensions de NPs est une étape compliquée qui a nécessité de nombreux essais pour être maitrisée. En particulier, elle est rendue complexe par la faible viscosité des suspensions et l'évaporation lente de l'eau lors du dépôt. Néanmoins, des films homogènes ont été préparés par spin-coating. L'influence de la concentration des suspensions, du nombre de couches déposées sur un même substrat (jusqu'à 3) et du recuit sur l'épaisseur et la morphologie des films, ont été étudié par AFM et GIWAXS. Finalement, des films de 70 à 215 nm d'épaisseur ont pu être obtenus après dépôt de 1 à 3 couches de NPs de 60 ± 20 nm de diamètre. La rugosité des films est de l'ordre de 20 nm. L'AFM permet d'observer une diminution de la rugosité du film à 10 nm, ainsi qu'une coalescence des NPs dans le film lors d'un recuit de 10 min à 120°C. En revanche, un recuit de 10 min à 150°C conduit à une séparation de phase visible en AFM accompagnée d'une augmentation de la rugosité à 100 nm. L'analyse GIWAXS montre qu'à 150°C une nouvelle phase apparaît, qui semble correspondre à une co-cristallisation du PF2 et du $PC_{71}BM$. Des dispositifs SCLC, OFET et des cellules solaires ont été ainsi préparés. Les dispositifs SCLC et OFET nous ont permis de mesurer la mobilité des électrons et des trous et de tenter de rationaliser leurs

évolutions en fonction de la température de recuit post-dépôt (**Tableau 1**). La mobilité des électrons augmente légèrement à 100 et 120°C, probablement grâce à la diffusion du $PC_{71}BM$ vers la coquille des NPs et la coalescence de ces dernières, permettant d'améliorer les chemins de percolation permettant le transport des électrons vers les électrodes. Cependant, la mobilité des électrons diminue fortement à 150°C avec la séparation de phase observée dans le film. La mobilité des trous a été mesurée perpendiculairement aux électrodes par SCLC. Elle diminue lors des recuits dès 120°C. Cela est probablement dû à un changement de phase et d'orientation des molécules de PF2, celles-ci passant d'une orientation mixte et équilibrée du type lamelles à plat (face-on) et lamelles sur la tranche (edge-on), par rapport aux électrodes, à une orientation majoritairement edge-on impliquant un transport de charges préférentiel dans la direction parallèle aux substrats. Dans le même temps, la mobilité des trous mesurée par OFET parallèlement aux électrodes, augmente fortement avec la température de recuit.

T°C	**μ_{e-} SCLC ($cm^2/V.s$)**	**μ_{h+} SCLC ($cm^2/V.s$)**	**μ_{h+} OFET ($cm^2/V.s$)**
Sans récuit	$(5 \pm 2)x10^{-3}$	$(1,3 \pm 0,4)x10^{-3}$	$(6,7\pm0,8)x10^{-7}$
100	$(6 \pm2)x10^{-3}$	-	$(7,7\pm0,1)x10^{-6}$
120	$(7,5\pm 3)x10^{-3}$	$(0,8 \pm 0,2)x10^{-3}$	$(1,9\pm1)x10^{-5}$
140	$(2 \pm 2)x10^{-3}$	$(0,5 \pm 0,4)x10^{-3}$	$(1,0\pm0,2)x10^{-4}$
160	$(2 \pm 2)x10^{-3}$	-	$(2,6\pm0,4)x10^{-4}$

Tableau 1 : Mobilités des électrons & trous pour les NPs composites PF2:$PC_{71}BM$ 1:2 (Épaisseur de films 140 nm / 2 couches)

Finalement, un PCE de 1% (**Tableau 2**) a été obtenu dans des cellules OPV ayant une couche active d'environ 70 nm d'épaisseur, à base de NPs composites PF2:$PC_{71}BM$ à une ratio de 1:2 (initialement, des diamètres de 60 nm ont été mesurés pour ces NPs). Un recuit thermique post-dépôt à 120°C s'est révélé indispensable pour favoriser la coalescence de NPs et induire la bonne mobilité des charges et un fonctionnement décent des dispositifs photovoltaïques. Cependant, au-delà de 140°C, le changement de phase probablement dû à la co-cristallisation du PF2 et du $PC_{71}BM$, altère les performances des dispositifs. Il s'agit de résultats préliminaires tout à fait prometteurs et de nouvelles séries de dispositifs sont actuellement en cours de préparation.

Conditions	V_{OC} (mV)	J_{SC} (mA.cm^{-2})	FF %	Epaisseur de la couche active (nm)	PCE %
BHJ solution – sans recuit	760	17.8	66	235	9
NPs – 120°C	790	3	40	70	1

Tableau 2 : Caractéristiques des cellules OPV du PF2:$PC_{71}BM$ 1 :2 préparés à partir de solution dans l'o-DCB ou de NPs dans l'eau.

V. Conclusion :

En conclusion, au cours de cette thèse, différents aspects de la préparation de cellules photovoltaïques à partir de suspensions de NPs dans l'eau ont été abordés, depuis la synthèse de polymères π-conjugués jusqu'aux dispositifs optoélectroniques. Nous nous sommes néanmoins focalisés principalement sur la préparation et l'étude de NPs de semi-conducteurs organiques par miniémulsion et par nanoprécipitation. Ainsi, des NPs composites à base du polymère PF2 et de $PC_{71}BM$ ou d'eh-IDTBR ont été élaborée, de structure cœur-coquille et possédant un cœur riche en $PC_{71}BM$ et une coquille riche en PF2 dans le cas des NPs PF2:$PC_{71}BM$. La structure n'a en revanche pas pu être définie dans le cas des NPs PF2:eh-IDTBR . Ces NPs ont été utilisées pour élaborer des films minces qui ont été caractérisés par différentes techniques (GiWAXS, AFM,…). Des résultats préliminaires encourageants ont été obtenus aussi bien en OFET et SCLC qu'en cellules solaires. Cependant, de nouveaux essais sont en cours afin d'optimiser les couches actives et les protocoles de préparation des dispositifs.

Enfin, nous avons également étudié la technique de nanoprécipitation et montré que le remplacement des chaînes alkyles du PF2 par des chaînes hybrides incluant des extrémités OEG permet d'augmenter la stabilité des NPs obtenues. Il s'agit là aussi de résultats prometteurs que l'on devrait prochainement appliquer à la préparation de films minces.

VI. Références :

1. Ibraikulov, O. A. *et al.* Face-on orientation of fluorinated polymers conveyed by long alkyl chains: a prerequisite for high photovoltaic performances. *J. Mater. Chem. A* **6**, 12038–12045 (2018).
2. Kim, T. *et al.* Flexible, highly efficient all-polymer solar cells. *Nat. Commun.* **6**, (2015).
3. Xie, C. *et al.* Overcoming efficiency and stability limits in water-processing nanoparticular organic photovoltaics by minimizing microstructure defects. *Nat. Commun.* **9**, (2018).

- Communications -

Publications :

- Participation à la rédaction d'un chapitre d'un livre publié par CNRS Editions dans le cadre de l'année de l'Ingénierie verte : « Des procédés écocompatibles pour des panneaux photovoltaïques organiques », A. Hébraud, T. Heiser, M. Rammal, I. Rodriguez-Donis, S. Thiebaud-Roux.
- Rammal Mohammad, Patrick Lévêque, Guy Schlatter, Nicolas Leclerc, and Anne Hébraud. "Recent Advances in the Green Processing of Organic Photovoltaic Devices from Nanoparticle Dispersions." *Materials Chemistry Frontiers*, 2020, 4(10), 2904-2931.
- Deux articles supplémentaires sont en cours d'écriture concernant d'une part :
    - La miniémulsion et l'élaboration des dispositifs optoélectroniques vertes basés sur les NPs.
    - La synthèse de nouveaux polymères et leurs nanoprécipitation.

Conferences :

- « Nanoparticules de polymère conjugué pour la mise en œuvre éco-efficiente de films minces » Science et Technologie des Systèmes pi-Conjugués (SPIC 2019) – Arras/France - Présentation Orale.
- Internationale : Nous avons envoyé des demandes pour plusieurs conférences (Macro 2020 en Corée – Euchem 2020 Portugal - …) mais à cause de la situation sanitaire (covid-19), toutes ces conférences ont été reportées à des dates ultérieures.

Mohammad Maxime RAMMAL

Nanoparticules de polymère conjugué pour la mise en œuvre éco-efficiente de cellules photovoltaïques organiques

École doctorale
Physique, chimie-physique
ED 182
Université de Strasbourg

Résumé

Les performances des cellules photovoltaïques organiques ne cessent de progresser grâce notamment au développement de nouveaux polymères π-conjugués à faible bande interdite. Cependant, ces polymères peu solubles doivent être mis en œuvre à partir de solutions à chaud dans des solvants chlorés toxiques. Nous avons étudié la dispersion de ces polymères sous la forme de suspensions aqueuses de nanoparticules (NPs), servant ensuite d'encre pour la mise en œuvre plus écologique des cellules solaires par des techniques d'impression classique. Par la technique de la miniémulsion, des NPs simples contenant le polymère donneur d'électron, le PF2, et une molécule acceptrice d'électron, le PCBM ou l'eh-IDTBR, ainsi que des particules composites contenant les deux matériaux à la fois ont été obtenues. Leur morphologie a été étudiée par TEM et STXM et dans le cas des NPs composites PF2 :$PC_{71}BM$, des particules de type cœur-coquille ont été obtenues avec un cœur riche en $PC_{71}BM$ et une coquille riche en PF2. La miniémulsion présentant l'inconvénient d'utiliser un tensioactif ionique, qui doit être éliminé par dialyse avant la fabrication des cellules photovoltaïques, nous avons également préparé des NPs par nanoprécipitation sans tensioactif. Pour cela, un dérivé du PF2 contenant des chaînes latérales oligo(ethylène glycol) a été synthétisé afin d'aider à la stabilisation des NPs en l'absence de tensioactif. Enfin la formation de couches actives à partir de ces suspensions a été optimisées afin de préparer des dispositifs électroniques, permettant de mesurer leurs propriétés optoélectroniques.

Mots clés : *Nanoparticules (NPs) de polymère conjugues, miniémulsion, nanoprécipitation, optoélectronique, chimie verte.*

Abstract

The performance of organic photovoltaic cells is constantly improving, thanks to the development of new π-conjugated low-bandgap polymers. However, these poorly soluble polymers must be processed from hot solutions in toxic chlorinated solvents. We have studied the preparation of aqueous suspensions of nanoparticles(NPs) of these polymers, to be used as inks for the eco-friendly production of solar cells using conventional printing techniques. By the miniemulsion technique, simple NPs containing the electron-donor polymer, PF2, and an electron-acceptor molecule, $PC_{71}BM$ or eh-IDTBR, as well as composite particles containing both materials were obtained. Their morphology was studied by TEM and STXM and in the case of the composite NPs PF2:PCBM, core-shell particles were obtained with a $PC_{71}BM$-rich core and a PF2-rich shell. However, the miniemulsion technique has the disadvantage of using an ionic surfactant, which must be removed by dialysis before the manufacturing of the photovoltaic cells. Therefore, NPs were also prepared by nanoprecipitation without surfactant. For this purpose, a PF2 derivative containing oligo(ethylene glycol) side chains was synthesized to enhance the stabilization of the NPs in the absence of surfactant. Finally, the formation of active layers from these suspensions has been optimized in order to prepare electronic devices, allowing the measurement of their optoelectronic properties.

Keywords: *Conjugated polymer Nanoparticles (NPs), miniemulsion, nanoprecipitation, optoelectronic, green chemistry.*